Coupled CFD-Population Balance Modelling of Soot Formation in Laminar and Turbulent Flames

Petros Akridis

Thesis submitted for the degree of
Doctor of Philosophy
of
Imperial College London

Department of Mechanical Engineering
Imperial College London

October 2015

Abstract

In this thesis, a discretised Population Balance Equation (PBE) model is coupled with a detailed in-house Computational Fluid Dynamics code to study soot formation in axisymmetric diffusion flames with comprehensive gas-phase chemistries for C_2H_4 and CH_4 fuels. The main aim of this study is to predict the complete Particle Size Distribution (PSD) of soot particles in turbulent non-premixed flames via a transported Probability Density Function approach. The PSD is obtained from the solution of the PBE without any prior assumption on its shape, using volume or diameter to describe the size of soot particles. However, due to a great number of uncertainties that appear from the turbulence interactions with chemistry, radiation and particle formation, the main objective is divided into smaller tasks where these complexities are avoided. Initially, the performance of the PBE is assessed under several numerical methods on an initial distribution-convection test, 0D reactors and 1D flamelet framework. The PBE has been originally discretised via a collocation type finite element method, and in the present work Finite Volume (FV) methods are used. The PBE with Total Variation Diminishing (TVD) scheme demonstrates better performance. The FV-TVD PBE with suitable soot kinetics is employed in 2D laminar flames where overall good agreement is achieved for the velocity, temperature, mole fraction of C_2H_2 and OH species and the mean properties of PSD (i.e. total number density and soot volume fraction). However, the temperature and soot volume fraction profiles on the turbulent flames do not exhibit similar accuracy as the laminar flames and there is still room for improvement. The evolution of the PSD is computed for both flames in the entire flame region exhibiting weak bimodal distribution in some points. The performance of complex coupled phenomena in PBE modelling via soot kinetics, detailed chemistry, radiation and turbulence interactions is explored.

Declaration of originality

I declare that the thesis presented herein, entitled 'Coupled CFD-Population Balance Modelling of Soot Formation in Laminar and Turbulent Flames', is the outcome of my own original work. It has not been submitted in any form for any other degree or diploma. Information that was used from other published or unpublished sources has been acknowledged and cited appropriately where a list of references can be found in the Bibliography.

Petros Akridis, October 2015

Copyright declaration

Acknowledgements

I would like to express my sincere appreciation to my supervisor Dr. Stelios Rigopoulos for his continuous support and beneficial discussions throughout this endeavour. Those have been a great inspiration to me in order to achieve the targets of this project. The opportunity of being part of his research group has been a real pleasure for me and I would like to thank all my colleagues for that. As such, a big thank you to my graduated colleagues Dr. Andrea Stefan and Dr. Salem Elbahloul and the rest of the group Fabian Sewerin, Panayiotis Koniavitis and Lucas Franke who are still working hard to finish their PhD.

Moreover, I want to give my special thanks to my graduated colleague and friend in my research group, Dr. Athanasios Chatzopoulos for exchanging information with me that was crucial in finding a way to overcome certain dead ends during my research.

I am most grateful to my family for their advice, continuous support and unconditional love. Without them, I would be not be able to pursuit my goals in life. Last, but not least, I would like to thank with all my heart my beloved girlfriend Afroditi for her patience and support when dealing with me and my concerns with the PhD, and encouraging me in difficult times.

Furthermore, I would like to acknowledge the financial support of the EPSRC and the ARCHER UK national supercomputing service which made all this possible.

Contents

List of Tables

List of Figures

Nomenclature

Roman Symbols

A_{factor}	Pre-exponential factor	(varies)
A_s	Surface area of each particle	m^2
A_T	Total surface area of particles per mixture volume of gas	m^2/m^3
b	Integer values to set the non-uniform grid of Litster's PBE	-
B	Net generation by Birth events (e.g. nucleation rate, coagulation birth)	(varies)
$\bar{B}$	Transformed Birth function in moment equation	(varies)
B_0	Nucleation rate in the dynamic PBE	(varies)
B^0	Nucleation rate in moment transport equation	$m^{-3}\ s^{-1}$
c	Species concentrations as a function of growth rates	(varies)
c_i	Convection CFL number in the i^{th} component	-
c_{mix}	Mixing CLF number	-
C_D	Mixing coefficient	-
C_{mass}	Mass of a single carbon atom	kg
C_p	Specific heat capacity of the mixture	$J/(kgK)$
C_{rad}	Soot radiative power density constant	$m^{-1}K^{-1}$
C_s	Soot nucleus (incipient) diameter	m
C_α	Coagulation constant (can take values 1, 3 or 9)	-
$C_{\epsilon 1,2}$	Dissipation rate energy constants	-
C_μ	Model constant of eddy viscosity	-
df_i	Diffusion CFL number in the i^{th} component	-
d_p	Particle diameter	m
d_i	Collision diameter of i^{th} PAH	m

dt	Global time step	s
dt^{PDF}	PDF internal time step	s
dW_i	The increment of Wiener process in the i^{th} direction	$\sqrt{s}$
D	Net generation by Death events (e.g. coagulation death)	(varies)
$\bar{D}$	Transformed Death function in moment equation	(varies)
D_{eff}	Effective CFL (dynamic plus turbulent) diffusion coefficient	m^2/s
D_k	Mixture-averaged diffusion coefficient of species k	m^2/s
D_{lk}	Binary diffusion coefficient of l^{th} and k^{th} species	m^2/s
$D_{T,k}$	Thermal diffusion coefficient of species k	$kg/(ms)$
D_α	Damköhler number	-
E_α	Activation energy	$J/kmol$
f_v	Soot volume fraction	-
$f_{v,int}$	Integrated soot volume fraction	m^2
g_i	Gravitational acceleration in the i^{th} direction	m/s^2
g_k	Consumption term of a gas-phase species k due to soot formation processes	$kg/(m^3 s)$
$G(L)$	Linear growth rate	m/s
$G(v)$	Volumetric growth rate	m^3/s
G_0	Constant growth rate	m/s
G_i	External coordinate velocity in the i^{th} direction	m/s
G_l	Internal coordinate velocity in each l^{th} section	(varies)
h_k	specific enthalpy of k^{th} species	m^2/s^2
H	Total specific enthalpy of mixture	kJ/kg
H'_k	Specific enthalpy of the k^{th} species	kJ/kg
$J_{k,i}$	Species diffusion flux vector in the i^{th} direction	$kg/(m^2 s)$
k	Turbulent kinetic energy	m^2/s^2
k_α	Reaction rate constant of NSC oxidation	$g/(cm^2\ atm\ s)$
k_β	Reaction rate constant of NSC oxidation	$g/(cm^2\ atm\ s)$
k_{growth}	Reaction rate constant of surface growth	$m^3/(m^2 s)$
$k_{n,N}$	Reaction rate constant of Nucleation	$1/s$
$k_{n,sg}$	Reaction rate constant of Surface Growth	$kg/(m^2\ atm\ s)$

k_L, k_A, k_v	Shape factors of diameter, surface area and volume respectively	-
k_{oxid}	Reaction rate constant of oxidation	$m^3/(m^2 s)$
k_T	Reaction rate constant of NSC oxidation	$g/(cm^2\ s)$
k_z	Reaction rate constant of NSC oxidation	atm^{-1}
k_B	Boltzmann constant	$m^2 kg/(s^2 K)$
K_p	Total mean absorption coefficient of gas-phase	m^{-1}
Le_k	Lewis number of k^{th} species	-
L_T	Total particle diameter of particles per unit volume of gas	m/m^3
m_b	Number of carbon atoms of the fuel size found in the global reaction	-
$m_{d_p,\delta}$	Diameter-based moment of number δ	(varies)
m_j	Moment of j^{th} number (transport moment equation)	(varies)
$m_{v,\delta}$	Volume-based moment of number δ	(varies)
M	Mass of fluid contained in a computational cell	kg
M_r	Moment of any r number	$kmol/kg$
M_s	Molar mass of soot particles with a constant value 12.011	$kg/kmol$
M_{tot}	Total mass of fluid in the entire system	kg
n	Temperature exponent in Arrhenius equation or population density	(varies)
n_b	Number of Hydrogen atoms of the fuel size found in the global reaction	-
$n(d_p, t)$	Number density function of soot particles (diameter size)	m^{-4}
$n(v, t)$	Number density function of soot particles (volume size)	m^{-6}
n_s	Number density function at each inlet and outlet s streams	(varies)
n_l	Number density of soot particles with discrete size l	m^{-3}
N	Total number of particles found in the system	-
N_A	Avogadro constant ($6.02214 \cdot 10^{26}$)	$kmol^{-1}$
N_{cells}	Total number of computational cells in the system	-

$N_{C,PAH}$	Number of carbon atoms in the incipient PAH species	-
N_{pc}	Number of particles per cell	-
N_{pdf}	Number of PDF cycles	-
N_s	Total number of soot particles per unit mass	$kmol/kg$
N_{sec}	Total number of PBE sections	-
N_{sp}	Total number of species in the system	-
N_{tot}	Total number of stochastic particles in the system	-
p	Pressure	$kg/(ms^2)$
p_k	Partial pressure of k^{th} species	atm
p_{mass}	mass of fluid represented by a single stochastic particle	kg
p_{mix}	Probability of a pair of particles to interact with each other	-
Pr	Prandtl number	-
$P(\psi)$	Probability density function in the sample space ψ	(varies)
P_k	Production of turbulent kinetic energy	$kg/(ms^3)$
$\dot{Q}$	Radiation source term of enthalpy equation	$J/(m^3s)$
Q_s	Volumetric flow rate of s inlets and outlet streams	m^3/s
r_l	Internal coordinate property of l^{th} section	(varies)
r_i^+	Upwind ratio of two consecutive number density functions gradients	-
R	Universal gas constant (value 8.314)	$J/(molK)$
R_e	Reynolds number	-
R_{growth}	Surface growth rate expression	$kg/(m^3s)$
R_h	Universal gas constant not in SI units (1.9859)	$cal/(mol\ K)$
R_1	Finite sub-region of particle phase space S	(varies)
R_{Nuc}	Nucleation rate expression	$m^{-3}s$
R_{oxid}	Surface oxidation rate expression	$kg/(m^3s)$
S	Phase space of PBE	(varies)
S_α	Source term of any scalar property α in composition PDF	(varies)
Sc_k	Schmidt number of k^{th} species	-
t	Time	s

T	Temperature	K
u^c	Correction diffusion velocity	m/s
u_i	Velocity component in the i^{th} direction	m/s
u_k^n	Normal (Ordinary) diffusion velocity of k^{th} species	m/s
u_k^T	Thermal diffusion velocity of k^{th} species	m/s
$\vec{v}_E$	Velocity vector in the physical coordinates	m/s
$\vec{v}_I$	Velocity vector in the internal coordinates	(varies)
V	Volume of the system	m^3
$V_{k,i}$	Complete diffusion velocity of k^{th} species in i^{th} direction	m/s
$V_{s,i}$	Thermophoretic and ordinary diffusion velocity of soot in i^{th} direction	m/s
V_T	Total volume fraction of particles	-
$V_{T,i}$	Thermophoretic velocity of soot in the i^{th} direction	m/s
w^P	Weight of each stochastic particle p	-
$\bar{w}$	Mean weight of stochastic particles	-
W_k	Molar mass of k^{th} species	$kg/kmol$
$\bar{W}$	Mean molar mass	$kg/kmol$
x_i	Position in physical space in the i^{th} direction	m
X_l	Mole fraction of l^{th} species	-
Y_k	Mass fraction of k^{th} species	-
Y_s	Mass fraction of soot particles	-
Z	Mixture fraction	-
Z_k	Mass fraction of k^{th} element	-

Greek symbols

$\vec{\alpha}$	Vector that contains a set of internal and external coordinates	(varies)
α_f	Fraction of surface sites on soot particles available for a given reaction	-
α_s	Strain rate	$1/s$
$\beta_\alpha(v, v')$	Size-dependent coagulation kernel	m^3/s
$\beta_{\alpha,0}$	Size-independent coagulation kernel	m^3/s

γ	Uniformly distributed random number to control the extent of mixing with values between 0 and 1	-
Γ_Φ	Diffusivity of a transported quantity Φ	$kg/(ms)$
ΔL	Interval between two particle diameter points	m
δ_{ij}	Kronecker delta function	-
δ_{max}	Maximum number of moments considered	-
ϵ	Turbulent dissipation rate	m^2/s^3
ζ	Increment factor of the PBE exponential grid	-
η	Special factor to distribute particles to neighbouring points	-
κ	Constant found in a piecewise interpolation formula	-
λ	Mixture thermal conductivity	$W/(mK)$
λ_k	Thermal conductivity of species k	$W/(mK)$
λ_p	Mean free path of a particle	m
μ	Dynamic mixture viscosity	$kg/(ms)$
$\mu_{i,j}$	Reduced mass of i^{th} and j^{th} PAH species	kg
μ_T	Turbulent viscosity	$kg/(ms)$
ν_{O_2}	Stoichiometric coefficient of molecular oxygen	-
ξ	Size property of soot particles	(varies)
Ξ	Flux limiting function	-
π	The ratio of a circle's circumference to its diameter (3.14159)	-
ρ	Mixture density	kg/m^3
ρ_s	Soot density	kg/m^3
σ	Stefan-Boltzmann constant	$W/(m^2K^4)$
σ_k	Prandtl number of turbulent kinetic energy	-
σ_ϵ	Prandtl number of turbulent dissipation energy	-
σ_t	Turbulent Prandtl number in diffusion	-
τ_{ij}	Viscous stress tensor component	$kg/(ms^2)$
τ	Residence time	s
τ_t	Turbulent time scale	s
τ_{ij}	Component of the viscous stress tensor	$kg/(ms^2)$

ϕ_α	Composition variables used in the PDF function	(varies)
ϕ_j^e	Lagrange basis function	-
ϕ	Any transported quantity (e.g. velocity, species mass fraction)	(varies)
Φ_{kj}	Correction factor of the Wilke formula	-
$\dot{\Phi}_{mix}$	Micro-mixing process	(varies)
χ_1	Parameter of NSC oxidation	-
$\chi_{C_{soot}-H}$	Number of saturated sites per unit surface area	m^{-2}
$\chi_{C_{soot}}$	Number of dehydrogenated sites per unit surface area	m^{-2}
ψ	Sample space variable corresponding to ϕ	(varies)
$\dot{\omega}_k$	Mass production rate of k^{th} species	$kg/(m^3 s)$
$\dot{\omega}_\Phi$	Source term of any Φ transported quantity	(varies)
$\dot{\omega}_\alpha$	Source term of any α scalar property	(varies)
$\dot{\omega}_{N_s}$	Soot number density source term	$kmol/(m^3 s)$
$\dot{\omega}_{Y_s}$	Soot mass source term	$kg/(m^3 s)$
$\dot{\omega}_{M_r}$	Source terms of any moment number r (in MoMIC)	$kmol/(m^3 s)$

Subscripts, Superscripts and Operators

$\sim$	Density weighted or Favre-averaged quantity
$\vec{}$	Vector
$-$	Unweighted mean or Reynolds-averaged quantity
$''$	Favre Fluctuation of a quantity
∇	Gradient
$(p), (q)$	Pair of notional particles
max	Operation to find the maximum value
nc	number of collocation points within each element
e	Each element
$+, -$	Right and left face fluxes respectively

Abbreviations

ABF	Appel-Bockhorn-Frenklach
BOFFIN	Boundary Fitted Flow Integrator

CD	Coalescence Dispersion
CFD	Computational Fluid Dynamics
CFL	Courant Friedrichs Lewy condition
CHEMKIN	Chemical Kinetics
CPU	Central Processing Unit
CSP	Computational Singular Perturbation
CSTR	Continuously Stirred Reactor
DNS	Direct Numerical Simulation
DOM	Discrete Ordinates Method
DQMOM	Direct Quadrature Method of Moments
EIA	Energy Information Administration
EMST	Euclidean Minimum Spanning Tree
FE	Finite Element method
FV	Finite Volume method
GDE	General Dynamic Equation
GRI	Gas-Research Institute
HACA	Hydrogen-Abstraction C_2H_2-Addition
HP	Hewlett-Packard
IEM	Interaction by Exchange with the Mean
ILDM	Intrinsic Low-Dimensional Manifold
JANAF	Joint Army-Navy Air Force
JSR	Jet Stirred Reactor
LES	Large Eddy Simulation
LII	Laser Induced Incandescence
LHS	Left Hand Side
MoMIC	Method of Moments Interpolative Closure
MPI	Message Passing Interface
MOC	Method of Characteristics
NSC	Nagle-Strickland-Constable
ODE	Ordinary Differential Equation
OTA	Optically Thin Approximation
PAH	Polycyclic Aromatic Hydrocarbon

PBE	Population Balance Equation
PDF	Probability Density Function
PFR	Plug Flow Reactor
PSD	Particle Size Distribution
PSR	Perfectly Stirred Reactor
ppm	parts-per-million (10^{-6})
QMOM	Quadrature Method of Moments
RANS	Reynolds Averaged Navier-Stokes
RCCE	Rate-Controlled Constrained Equilibrium
RHS	Right Hand Side
SIMPLE	Semi-Implicit Method for Pressure Linked Equations
SLFM	Steady Laminar Flamelet Model
TCI	Turbulence-Chemistry Interactions
TDPT	Thermocouple Particle Densitometry Technique
TEM	Transmission Electron Microscopy
TNF	Turbulent Non-premixed Flame
TRI	Turbulence-Radiation Interaction
TVD	Total Variation Diminishing
USC	University of Southern California (origin of gas-phase mechanism)
WF	Wang and Frenklach
WSR	Well Stirred reactor
0D, 1D, 2D	Zero, One, Two spatial dimensions
2TEM	Two-Transport Equation soot Model

Chapter 1

Introduction

1.1 Motivation

Currently, fossil fuel combustion accounts for the greatest share of generation in the UK (approximately 86%) and the global energy market according to the U.S. Energy Administration (EIA) between 2001-2012 [1]. Combustion of fossil fuels is the most dominant source of power for humankind and will remain for some time. The energy is stored in the chemical bonds of the fuel atoms and is released in the form of thermal energy through combustion. An alternative is to produce electrical energy by a chemical reaction process (fuel cell). Home heating, electricity, almost the entire transportation system and industrial processes to produce commercial products from raw materials all rely on burning petroleum components, coal and natural gas. Unfortunately, combustion is accompanied by the release of greenhouse gases (e.g. CO_2) and air pollutants (e.g. particulate matter) that can be detrimental to human health and to the environment. The continuous consumption of fossil fuel resources - and the prospect of their depletion - makes the importance of understanding the fundamentals and application of combustion clear. This has spurred remarkable research efforts to obtain greater control over combustion processes and design less polluting, more efficient engines [2].

Many years ago, the development and optimisation of a combustion engine relied exclusively on theoretical work and on small-scale experimental methods to replicate the actual device or process. Unfortunately, theoretical work is restricted to very simple geometries and physics, and deals mostly with linear problems. On the other hand, experimental methods suffer from scaling problems, measurement difficulties, and operating costs; setting up the experimental equipment was sometimes difficult and very time-consuming [3]. Each one of these problems

is alleviated by using advanced numerical fluid dynamic models to perform simulations for a variety of geometries and operating conditions. Unfortunately, even these computational methods have several restrictions. An important numerical barrier is our inability to express and accurately model some of the complex fluid dynamic phenomena mathematically (e.g. mixing in turbulent reacting flows). Truncation errors [3] associated with discretisation are also an issue. Another more important restriction is that a detailed simulation of a combustion process is infeasible due to computational limitations. To overcome the speed and storage capacity restrictions, major simplifications are made in the description of the problem (e.g. simplification of chemistry) to reduce the computational expense, sometimes compromising the accuracy of the model. Unfortunately, those simplifications are necessary in the numerical study of most practical devices (e.g. industrial furnaces, gas turbines, internal combustion engines) as they are usually turbulent, time dependent and inherently multidimensional [4].

With today's advancements in computer technology, more detailed processes can be applied in simulations. This is now possible through the use of parallel processing in certain time-consuming elements of the CFD code (e.g. detailed chemical reactions), distributing the workload to several processors to solve those parts simultaneously and resulting in a significant increase in speed. An example to highlight the significance of the parallel programming is the chemistry of aviation and diesel fuels. Their fuel chemistry is a mixture of a high number of hydrocarbons, requiring hundreds of species and thousands of chemical reactions to be correctly represented [4]. Increasing the speed of the simulation by using more than one CPU is supremely important in avoiding as many of these simplifications as possible. Even so, the advances in computer technology still leave Direct Numerical Simulations (DNS) of practical devices out of reach [5] and is mainly applied to academic problems.

Combustion is a group of complicated, highly non-linear phenomena that interact with each other; these include complex transport mechanisms, radiative heat transfer, multiphase flow and detailed chemical kinetics [2]. Each of these phenomena individually constitutes a challenging topic to explore. These phenomena occur simultaneously at different temporal and physical scales that may vary by several orders of magnitude. This wide range of scales is primarily due to the nature of the chemical reactions, and the appearance of eddies in turbulent flows that result in a system of stiff equations [6]. Examples of this broad range of scales include nanoseconds for the fast reactions (e.g. radical species) and milliseconds for transport mechanisms and the very slow reactions (e.g. NO formation). The complexity can be further increased if a

system operates in turbulent conditions due to turbulence-chemistry and turbulence-radiation interactions, and through additional complications from the particulate dynamics of aerosols like soot particles. As such, the coupling of all these phenomena along with their combined effects is more feasibly explored in simplified cases instead of using the complex geometry and conditions of a practical device used in industry. Many relevant choices of simple laminar and turbulent experimental cases exist and can be studied in the laboratory under a controlled environment.

An axisymmetric co-flow non-premixed flame configuration is an ideal platform to model soot formation in laminar and turbulent conditions. Instead of solving in a 3D environment, the axisymmetry simplifies the model to 2D domain - radial and axial - and significantly reduces the computational effort required. It should be noted that the steady state condition and axisymmetry, which can be easily visualised on a laminar flame, cannot be treated exactly the same in turbulent flames. The instantaneous turbulent flame shape is constantly changing through time due to the random and chaotic motion of turbulence. Turbulent flames are considered axisymmetric only when time averaging is performed among the transported quantities [7]. Laminar and turbulent experiments of this kind, for which a vast amount of data is available for comparison, can be found in [8, 9] and [10] respectively. The relatively simple geometry and flow field of both experiments allow the application of detailed chemical, physical and complex particulate models.

However, the behaviour and performance of soot formation models should initially be evaluated in the absence of any complexities and uncertainties arising from fluid dynamics, especially turbulence. As such in this thesis, soot implementation via a detailed Population Balance Equation (PBE) is first assessed in homogeneous 0D reactors (i.e. Batch and Perfectly Stirred Reactor (PSR)) where there is no spatially dependency and in 1D laminar flamelet with mixture fraction coordinate.

Soot is an aggregate of mainly solid carbon particles and a relatively small number of hydrogen atoms. It is usually a product of the incomplete combustion of hydrocarbon species in fuel-rich zones. Soot has been observed in experiments [11, 12] to have a fractal shape, a pearl necklace (e.g. chain-like) structure of almost equally-sized spherule particles. Soot particles are invisible to the naked eye, but their presence can easily be detected from a flame's yellow luminosity. The yellow colour of the flame is created because soot particles are heated to incandescence and emit radiation. The generation of soot particles can be identified in quotidian

applications by this yellow colour characteristic, in such phenomena as lighting a match, a candle's flame, forest fires, jet engines and so on.

Soot is a hazardous particulate that has a negative impact on the environment and causes adverse health effects in human physiology. According to a recent study [13], black carbon (e.g. a component of soot) could be the second major contributor to global warming behind carbon dioxide emissions (CO_2) because it can strongly absorb more light than it reflects. Black carbon concentration is not uniformly distributed with altitude and its profile varies vertically in the atmosphere. According to [13] soot measurements indicate that in polluted regions a declining concentration profile is observed up to 4 km altitude. Above this height the profile remains relatively constant up to troposphere. However, in remote regions black carbon concentration is influenced from transport mechanisms and peaks in the troposphere or above. Black carbon has shorter lifetime (on the scale of weeks) unlike the much longer timescales of CO_2 [13]. As such, an immediate reduction in soot production could result in a quick positive feedback effect in global warming. Furthermore, soot has been classified as carcinogenic and mutagenic particulate matter as it is made up by PAH; prolonged exposure can cause lung cancer, premature death, bronchitis, asthma and other negative outcomes [14]. Additionally, sufficient soot concentration in the atmosphere can result in reduced visibility. This is especially important in confined places (e.g. inside a building) where evacuation can be impeded in case of a fire. From a commercial point of view, soot has also great importance in such applications as jet engines. Soot deposition and continuous radiation is the main driver of heat load to critical combustor (like the igniter and injector) and flow components, decreasing their durability and lifespan [15, 16]. In summary, soot emission and inhalation should be avoided whenever possible.

For these reasons, stricter legislation is constantly applied to industries (primarily automotive and aviation) that have significant contributions to soot production. These rules prohibit soot emission from exceeding certain limits in terms of particle size and concentration (soot volume fraction). These green initiatives are imposed by the governments of the United States, Canada and European Union, among others [17]. However, in controlled combustion environments, carbon black is generated similar to soot formation processes. It is actually useful in applications including black pigment in printing, automotive tyres, reinforcing agents in rubber products, ribbon inks and in industrial furnaces where the enhancement of radiation due to soot particles is a desired outcome [18].

Accurate numerical modelling of soot formation is a formidable task. The modelling of soot production and destruction processes is highly complex because they involve several homogeneous and heterogeneous reactions, as well as other physical processes such as coagulation and aggregation [19]. Moreover, the time scales of soot formation processes are larger than the time scales of the gas phase reaction [20]. An additional complexity derives from the influence of soot on the flow field of the mixture through the absorption and emission of radiation energy. This radiation effect reduces the temperature of the flame, altering the density of the mixture and the local gas-phase composition. In reality, most of the practical reacting systems are of complex geometry, operate in turbulent conditions and non-premixed combustion. As a result, detailed simulations of those practical systems are prohibited by the very computationally intensive processes and the lack of complete understanding of soot behaviour [21]. Detailed model development must be validated in simplified sooting systems by incorporating these various phenomena successfully, and assessing their performance and behaviour against simplified experimental cases.

Typical values of soot volume fraction in a laboratory non-premixed flame (e.g. CH_4 or C_2H_4 fuel) range from roughly 0.1 to 10 parts-per-million (ppm). Even, modern experimental equipment has major difficulties in measuring those low concentration levels and the incipient sizes of soot particles. This difficulty is also present for the small-scaled turbulent methane flame described in [10]. At large scales, however, this is not an issue as methane fuel produces soot quite heavily due to increased time scales. Unfortunately, this measuring difficulty prevents the full observation of soot physics. Numerical models are needed to provide greater insight into this type of problem.

Generally, soot formation is still an active combustion topic of on-going research; many aspects remain unresolved, including soot's inception process and universal kinetics. The investigation of soot in turbulent and laminar reacting flows is one of the most challenging subjects in engineering science, whether the approach be theoretical, experimental or numerical.

Soot particles are introduced in the system by having an initial size distribution or by a nucleation process which generates soot particles of the smallest possible size. The incipient soot particles are commonly modelled by assuming to have a spherical shape as observed in Megaridis and Dobbins experiment [11]. Their size is increased by surface growth and coagulation processes. In later states, the soot particles continue to collide with each other; beyond a certain point, they are unable to fully merge (coagulate) and keep their spherical shape, as

they stick together instead (aggregation). Eventually, these particles become fractals until they shrink or completely destroyed by oxidation. Their size varies across the flame region from their incipient diameter (e.g. 1 nm) up to several microns due to surface and coagulation/aggregation processes. From this range of sizes, a subset of particles can be small enough to allow them to penetrate the respiratory system and be deposited on the lungs, or even infiltrate the blood-stream. This generated size polydispersity of a population of particles through a combustion process is quantified as Particle Size Distribution (PSD).

Soot formation processes depend largely on this size range of particles, and on their morphology. In other sciences, the quality of the crystals used in pharmaceutical industries is dependent on the crystal size distribution [22], as it is often desirable to predetermine their final size distribution. Similarly, the scientific interest in soot research has recently shifted from studying the mean properties of PSD to investigating soot particle nanostructure and detailed size distributions [23]. A complete PSD is a prerequisite for computing the morphology of soot aggregates and highlighting dominant soot formation mechanisms. An example is a bimodal distribution of soot particles, usually observed due to the competition between nucleation and coagulation processes.

1.2 Objectives

The main aim of this study is to couple a discretised Population Balance Equation (PBE) with a comprehensive in-house Computational Fluid Dynamics (CFD) code to study soot formation in laminar and turbulent flames. The PBE allows the computation of the complete PSD via its solution in the entire flame region. So far, the majority of the numerical studies have implemented a two-transport equation model (2TEM) approach by assuming monodisperse shape distribution to predict the total number density and mass fraction of soot, ignoring the polydispersity of particles. However, this thesis accounts for the polydispersity of particles through a detailed PBE model. Very few studies have implemented a detailed CFD-PBE model to laminar flames. To the author knowledge no PDF-PBE model has been implemented to study soot formation in turbulent flames and obtain the PSD which is the ultimate goal of this thesis. As such certain objectives are set to assess the performance of the PBE in the most simplified systems (0D reactors). Later, more complex systems are combined with the PBE such as 1D flamelet, CFD and PDF models to study soot formation and the evolution of PSD

in laminar and turbulent flames.

The first objective is to solve the discretised PBE in a simple initial distribution test (convection process) and to implement the discretised PBE into 0D reactors and 1D flamelet equation in mixture fraction space. In the initial distribution test and 0D reactors, the solution of the PBE is obtained using several numerical methods. The original PBE is discretised by a finite element method [24] and extended to a finite volume method in this thesis with a TVD scheme. Both numerical schemes are assessed and validated by transforming the PBE into a series of moment equations that provide an exact solution for the moments, and the method of characteristics that yields an exact solution of the PSD. Later, the finite element and finite volume PBEs are applied to 1D flamelet, and the moments of PSD are compared with the exact solution of the transformed PBE.

The second objective is to compare the PBE with other widely used approaches, such as the 2TEM and the Method of Moments with Interpolative closure (MoMIC) in a 1D flamelet framework to identify suitable soot kinetics for the PBE. Most of these kinetics are used earlier in the 2TEM (acetylene-based) studies, or the MoMIC code (PAH-based). It should be noted that neither 2TEM and MoMIC codes obtain the complete PSD, whereas the PBE is capable of such a prediction.

The third objective in this thesis is to apply the PBE with the best possible performance according to the first and second objectives in order to predict soot formation in laminar flames that have been investigated both numerically and experimentally. An ideal axisymmetric laminar diffusion flame is selected [9, 25], where a large amount of data important to soot formation is available for comparison, including velocity fields in the axial and radial directions, temperatures, soot volume fractions and the concentrations of major species. The laminar diffusion flame is solved by coupling the discretised PBE with an in-house CFD code. This is an imperative objective, as the laminar case provides a more fundamental analysis without any additional complexities related to turbulence-chemistry interactions found in turbulent flames. Moreover, parallel computing was found to be essential in order to speed up the simulations.

The fourth objective is to use appropriate soot kinetics found in the laminar flames, as intended in the third objective, and to couple the PBE with the in-house CFD code (BOFFIN) to predict soot formation in turbulent flames. This is the ultimate challenge in this thesis as major problems caused by turbulent effects such as the turbulence-chemistry, turbulence-particle formation and turbulence-radiation interactions. In this study, these problems are

resolved via a transported PDF-PBE approach. The integration of the chemistry ODEs is parallelised to speed up the computations.

1.3 Outline of thesis

- Background information and mathematical expressions of the governing equations driving each system, 0D reactors, the 1D laminar flamelet and multidimensional laminar and turbulent flames are shown in Chapter 2. All these systems will be numerically investigated, as is briefly explained in the objectives section. Moreover, a variety of soot kinetics (including acetylene and PAH-based) with the transport equations describing the 2TEM and MoMIC approaches are shown which will be used in the upcoming simulations along with an introduction to the PBE.

- A literature review is developed in Chapter 3, based on several numerical schemes that were used to obtain a solution of the PBE in various scientific fields other than soot formation studies. In addition to the PBE review, the derivation of finite volume scheme for the PBE is shown as well as an efficient scaling methodology to speed up computations. Furthermore, a simple convection test case is conducted to examine the accuracy of finite volume methods compared to other numerical schemes and analytical solution.

- Computations of two homogeneous 0D reactors and 1D flamelet are performed in Chapter 4. Several PBE model parameters (e.g. grid size) and soot kinetics are tested in order to find the optimum formulation. The results are compared with a moment transformation PBE and a method of characteristics, as well as with the 2TEM and MoMIC approaches.

- Three laminar cases of Santoro's jet burner experimental series [8] are numerically investigated in Chapter 5. The first case study is a non-smoking flame, while the second and third cases exhibit smoking flame characteristics.

- Two turbulent flame simulations are compared with [10] experiment in Chapter 6. The turbulence-chemistry, turbulence-particle formation and turbulence-radiation interactions are incorporated on the original in-house CFD code by including a transported PDF approach.

- Finally, this thesis concludes with Chapter 7, including a summary of results and suggestions for future work.

Chapter 2

Background theory

2.1 Combustion modes

Combustion science involves the intimate interactions of many fundamental disciplines, including thermodynamics, fluid mechanics, transport phenomena, turbulence, chemical kinetics, and heat and mass transfer. It is clearly a complex, multidisciplinary topic. It should be noted that even a detailed numerical adaptation of one of the aforementioned disciplines (e.g. detailed chemical kinetics instead of few-step chemistry) could result in an intractable simulation. An accurate numerical analysis of a combustion process requires the combination of all these phenomena, and depends largely on the level of the detail that is applied to describe each mechanism. In practise, high detail is usually avoided by employing several well-grounded simplifications whenever possible in order to constrain the computational expense of a combustion simulation. Unfortunately, these simplifications are not global. They are not applicable for every combustion problem, and their validity must be examined according to the problem specification. Nowadays, these simplifications could be relaxed up to a point due to the advancements in computer technology [26].

The major simplifications are associated primarily with the reduction of the gas-phase chemical mechanism. Even so, the same assumptions that work well for certain cases may not be valid for some others. For example, the unity Lewis number is a common assumption in turbulent flames. However, it is not valid for laminar flames where the differential diffusion effects play an important role. Thus, the variety of combustion problems has been classified as combustion modes; this divides the analysis for each system according to applicable assumptions and simplifications. A summary of the combustion modes is sketched in Figure (2.1).

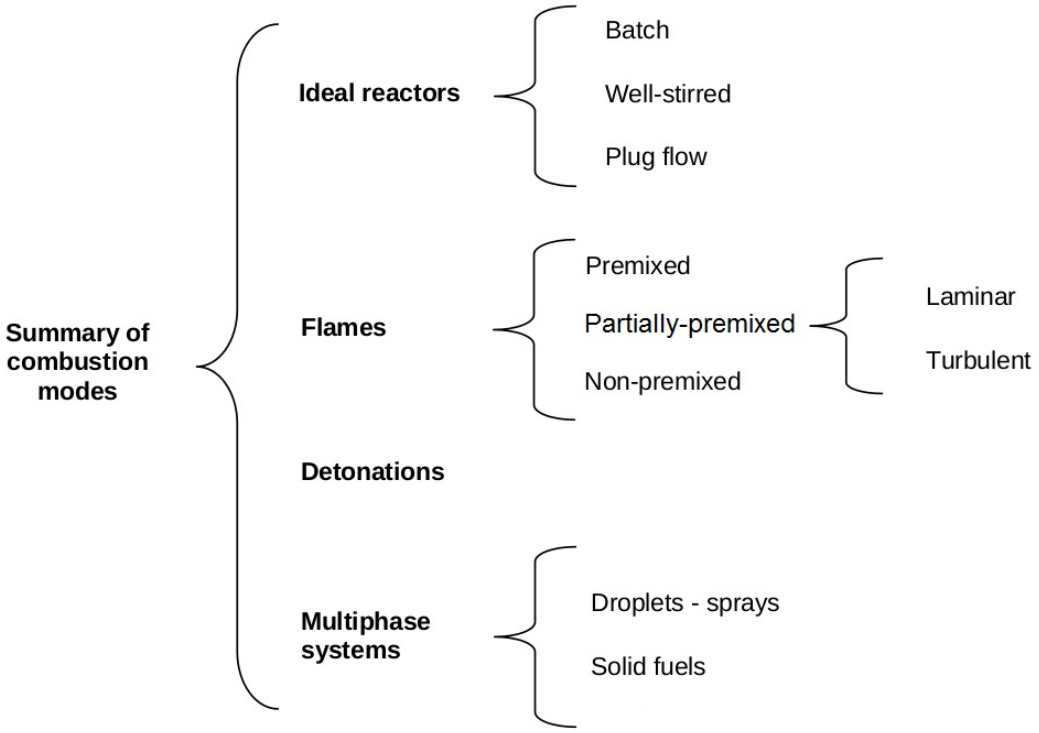

Figure 2.1: The different modes of combustion [27]

2.1.1 Ideal reactors and other modes

Within a region of unburned mixture, rapid oxidation reactions can take place in several locations without waiting for the arrival of a flame front. An example is the autoignition in spark-ignition combustion engines (e.g. engine knock) which can be investigated using an ideal reactor concept [28]. Combustion can be performed in special chemical devices properly designed to let reactions occur in the entire volume of the vessel simultaneously under a controlled environment [29]. These vessels are called ideal or homogeneous reactors, and are classified as batch (or discontinuous) and continuous processing. The concept of the ideal reactor is useful because transport phenomena and heat transfer are neglected or highly simplified, focusing mainly on parts related to chemical kinetics (gas-phase) and particle dynamics (crystals, aerosols etc.).

Another example of combustion mode is the detonation where a shock wave is usually generated by igniting a combustible mixture. The combustion shock wave propagates instead of a flame at supersonic velocity, initiating a rapid combustion process that immediately turns the reactants into products. If the same wave propagates with subsonic velocity, the process is called deflagration. Both these waves exhibit different characteristics and are beyond the scope of this thesis. The reader can find a further explanation in [28].

Multiphase flow is another category that belongs to the context of fluid mechanics. Multi-

phase non-reacting flow is the simultaneous flow of materials through a medium with two or more distinct phases. The most common class of multiphase flow is the two-phase, which has a combination according to the state of the different phases. These include liquid-solid (e.g. sediment transport of sand in the sea), gas-liquid (e.g. gaseous bubbles in a liquid) and gas-solid. In addition, materials or fluids of the same phase but with different chemical properties belong to this category (e.g. liquid-liquid system of oil droplets in water) [26].

Multiphase flows could also be accompanied by chemical reactions. Examples are found in the combustion of solid fuels, spray or droplets. The combustion of liquid droplets or solid fuels happens primarily in the gas phase region. Gaseous species are produced from heated vaporised liquid or devolatilisation of solid fuel pyrolysis; these react, and form a surrounding diffusion flame. This is a homogeneous combustion process governed by the diffusion of fuel vapour and oxidiser species. At times, heterogeneous reactions occur on the surface of solid particles or within a liquid droplet.

2.1.2 Flames

The final and most important category is the flame mode. The chemical kinetics of the reaction zone change the molecular structure of the species by converting the reactants into products and releasing energy. It is divided into three different types: the premixed, partially-premixed and non-premixed flame. All flame types could be of laminar or turbulent type, and in steady or unsteady state. The three flame types are defined according to the initial state of the mixture.

In premixed flames the initial unburned mixture is fully mixed at the molecular level prior to entering the reaction zone. Moreover, this type of flame is dominated by chemical kinetics where the generated flame propagates towards the unburned mixture with a finite velocity. Two velocities are of primary interest: the unburned gas velocity, and the flame speed. The latter is dominated by the chemistry of the mixture. When the flame speed is higher than the unburned gas velocity, the flame will propagate upstream and in some occasions cause the flashback phenomenon (the flame travels inside the fuel mixture jet origin tube).

In contrast with premixed systems, the non-premixed flame has its reactants (the fuel and the oxidant) initially separated; they mix in the same region where the reaction zone appears. This reaction region is fixed to the vicinity of the interface between the reactants, brought together by a diffusion process. The products and the energy released generally diffuse away from the reaction zone into the fuel and oxidiser areas [30]. The shape and structure of a diffusion flame

is determined by the mass flux of air or fuel entering the reaction zone under stoichiometric conditions: greater mass flux of oxygen entering the reaction zone requires the consumption of more fuel, and the reaction zone will move towards the fuel side. This application is favourable to the experimenter mainly for safety reasons and because the burning rate is limited and dominated by the transport and mixing processes rather than chemical kinetics. Greater flame stability can be obtained in diffusion flames with no flashback compared to premixed flame types [31].

The last flame type exhibits similar features with both the premixed and non-premixed flames. The partially-premixed flame is more realistic and often to be encountered in practical combustion applications rather than pure premixed on pure non-premixed flames [26]. In general, partially-premixed flames are considered to be premixed flames with non-uniform equivalence ratios. Examples of this type of flame can be found in situations such as when an additional oxidiser or fuel stream is introduced to a premixed system or in a situation where lifted non-premixed flame occurs as the reactants are partially mixed prior to ignition. The partially-premixed flame is not considered is this thesis and will not be explored further.

2.2 0D and 1D reacting systems

The batch process is perhaps the simplest reactor used in chemical engineering. Two examples of a batch process application can be found in the fermentation and pharmaceutical industries where actual batch reactors are widely used for a variety of processes including product mixing, chemical reactions and small (batch) or large-scale (PSR) production. The process involves a device with a closed thermodynamic system operating under unsteady conditions. No mass comes into or out of the device until the chemical process is completed. The batch process can be represented by two different methods of operation. The first operation is that of fixed-mass constant volume, and the second is a fixed-mass constant pressure process. In the latter, both temperature and reactor volume will increase with time during a reaction process. This model can be used as an initial analysis for modelling more complex systems. An example is given in [28] where the autoignition effect of an internal combustion engine is explored by resolving the explosion on a small time scale using the batch process with a constant volume hypothesis.

An extension of the batch process is the continuous processing, which can be found in many studies under a variety of names. The following names describe essentially the same reactor:

well-stirred (WSR), continuously-stirred (CSTR) or perfectly-stirred (PSR). Occasionally, the system is also called the Longwell or Zeldovich reactor in recognition of their work. Here, the name PSR will be used for this type of reactor. The PSR is similar to the batch process, as no gradients of composition and temperature exist inside the vessel. For both PSR and batch processes, a uniform composition is assumed in the entire volume of the vessel (homogeneity). The PSR is an open system that can be either steady or unsteady state, including inflow and outflow conditions. The reactants can be injected in the system from multiple inlets, but have a single exit. The PSR is an ideal reactor where, due to the perfect mixing assumption, the output is identical to the inside composition of the reactor. Both batch and PSR may have heat transfer through the vessel walls; this can be neglected completely for adiabatic investigations [28].

Another type of continuous processing is the Plug Flow reactor (PFR), involving several assumptions: constant velocity (plug flow) across each cross section, perfect instantaneous mixing perpendicular to the flow, no mixing in the direction of the flow, ideal frictionless flow and ideal gas behaviour. The plug flow reactor is considered as 1D with steady state flow, whereas the previous reactors are 0D models with no spatial dependency. Moreover, many PSR in series can actually approximate a single PFR [32]. These ideal reactors are sketched in Figure (2.2).

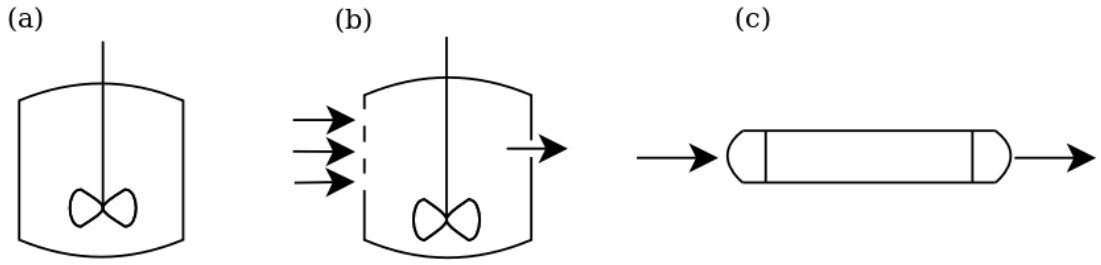

Figure 2.2: Ideal reactors a) batch, b) PSR, c) plug-flow

2.2.1 Batch and PSR operating conditions

In practise, it is difficult to match the assumed ideal requirements in an actual experimental reactor. These requirements can be met up to a point by identifying the limiting conditions of a reactor's operation, available in the table 2.1. In this thesis, the primary focus is on the following homogeneous 0D reactors: the batch and the PSR. The operating conditions of both systems are categorised according to mass exchange, heat exchange, an assumption of a

mechanical variable in order to derive the governing equations and time dependency. With no mass exchange, the reactor is a batch process whereas with inflow and outflow terms it is considered as PSR. Regarding the heat exchange, a constant temperature (isothermal) can be set to both reactors or adiabatic where the temperature is changing through the chemical process but there is not any form of radiation or heat transfer to the surroundings. In contrast to batch, in the PSR reactor another parameter appears: residence time. The residence time term shows the amount of time that species or particles spend inside the reactor undergoing chemical rate processes. The residence time in PSR is usually an arbitrary finite number, and the longer the residence time period is set, the input and output stream effects are reduced and the closer the PSR system becomes to a batch process operation. Both systems are assumed to be well-mixed, and they can be easily expressed by mass and energy balance equations on a control volume inside the vessel in order to derive the governing equations.

Event	Limiting conditions	
Mass In/Out	Batch	PSR
Heat In/Out	Isothermal	Adiabatic
Mechanical variables	Constant volume	Constant pressure
Time-dependence	Transient	Steady

Table 2.1: Ideal reactor operating conditions [32]

2.2.2 Batch and PSR governing equations

The equation governing the batch reactor is a partial differential equation of the chemical reaction rate terms. However, additional terms appear in the species differential equation due to soot formation. These new terms are the consumption and production rates of certain species that react with the soot surface area, such as C_2H_2 and OH species. Moreover, an additional differential equation which solves the PBE is added to the system to describe soot formation. The differential equation of the PBE solves the number density function of multiple soot particle discrete sizes. The governing equations of species and number density function along with the adiabatic energy balance are shown for the constant-pressure batch formulation in equations (2.1), (2.2) and (2.3) respectively.

$$\frac{\partial Y_k}{\partial t} = \frac{\dot{\omega}_k + \dot{g}_k}{\rho} \quad , \quad k = 1, N_{sp} \tag{2.1}$$

$$\frac{\partial n_l}{\partial t} = \dot{N}_l + \dot{G}_l + \dot{S}_l + \dot{C}_l \quad , \quad l = 1, N_{sec} \tag{2.2}$$

$$\frac{\partial T}{\partial t} = -\frac{\sum_{k=1}^{N_{sp}} H'_k \dot{\omega}_k}{\rho C_p} \tag{2.3}$$

On the left hand side (LHS) of equation (2.1) the Y_k describes the mass fraction of each k^{th} species. On the right hand side (RHS) of this equation, the chemical source term of each k^{th} species is $\dot{\omega}_k$; the other term $\dot{g}_k$ is the consumption or production of species due to soot formation processes. The equation (2.2) is the temporal evolution of the number density function - the population density, which is determined by four source terms. The source terms on the RHS are nucleation ($\dot{N}_l$), surface growth ($\dot{G}_l$), oxidation ($\dot{S}_l$) and coagulation rates ($\dot{C}_l$) at a discrete size l of a soot particle. The batch reactor is homogeneous, and the governing equations are not functions of any physical coordinate. Thus, the population density is a function of only discrete sizes of particles and time. The temperature of the system is found by the energy balance expression in equation (2.3). Adiabatic conditions are assumed, and therefore no radiation model or any other heat transfer mechanism is included. On the RHS of (2.3) ρ is the mixture density, C_p is the specific heat capacity at constant pressure and H'_k is the specific enthalpy of k^{th} species. The thermodynamic properties of each species used in equation (2.3) can be determined by a JANAF polynomial table where a polynomial expression is solved as a function of temperature.

The governing equations of the spatially homogeneous PSR are similar to the equations of the batch reactor. However, in the PSR, additional mass flow in/out terms appear in the governing equations of species mass fractions and number density function. This additional term between the PSR and batch reactor is also located at the adiabatic energy balance equation where the enthalpy state of the initial mixture at the inlet (H'_{k0}) is fixed and the final product's enthalpy (H'_k) are taken into account. The following equations for a constant-pressure PSR are shown in equations (2.4), (2.5) and (2.6).

$$\frac{\partial Y_k}{\partial t} = \frac{\dot{\omega}_k + \dot{g}_k}{\rho} + \frac{Y_{k0} - Y_k}{\tau} \quad , \quad k = 1, N_{sp} \tag{2.4}$$

$$\frac{\partial n_l}{\partial t} = \dot{N}_l + \dot{G}_l + \dot{S}_l + \dot{C}_l + \frac{n_{l0} - n_l}{\tau} \quad , \quad l = 1, N_{max} \tag{2.5}$$

$$\frac{\partial T}{\partial t} = -\frac{\sum_{k=1}^{N_{sp}} H'_k \dot{\omega}_k}{\rho C_p} + \frac{\frac{\sum_{k=1}^{N_{sp}} Y_{k0}\left[H'_{k0} - H'_k\right]}{C_p}}{\tau} \tag{2.6}$$

The new term compared to the batch reactor's equations contains τ, located in the denominator of the last term on the RHS of equations (2.4), (2.5) and (2.6); this is called the residence time. The τ term is equal to the ratio of a reactor's capacity to the flow rate of particles through the system. The residence time is calculated as $\tau = \frac{\rho V}{\dot{m}}$. The mass fractions Y_{k0} and specific enthalpies H'_{k0} terms have a 0 symbol, which refers to their initial state value at the inflow boundary of the PSR prior to ignition. The specific enthalpies and species mass fraction with the 0 symbol have fixed values throughout the entire computation. Furthermore, the number density function is assumed in this thesis to be 0 at the inlet (e.g. n_{l0} is set to 0).

2.2.3 Numerical and experimental study of soot in 0D-1D reactors

These 0D-1D reactor models are assumed to operate under ideal conditions and they are attractive for numerical modellers due to their simplicity. The ideal reactors are very useful in particulate technology where the fundamentals of the gas-phase and particle kinetics can be explored without the interference of a complicated flow field pattern. The batch reactor can be used to investigate ignition-delay time temperatures of gas-phase chemical mechanisms, whereas the PSR is used to compute extinction residence time and temperatures. These models can be used with very large gas-phase chemical mechanisms and detailed particulate models to obtain a solution at a reasonable computational cost. It should be noted that the batch and PSR systems are ideal to investigate the model parameters of the PBE, which are associated with the number of grid points and the type of the grid (linear or geometric) in the particle size domain. Moreover, numerical schemes under several grid parameters could be examined for convergence and accuracy.

A combination of 0D-1D ideal reactor formulation has been used in the C_2H_4/air premixed experiment of [33] where soot PSD measurements are obtained. A jet stirred reactor (JSR) is used where its output feeds a PFR tube. This experiment has been investigated by the numerical study of [34]. The JSR is modelled as PSR and a moving sectional soot model is applied to validate the soot formation mechanism. The chemistry of the reactions is represented by the Appel-Bockhorn-Frenklach (ABF) gas-phase mechanism and the soot formation is PAH-based. However, there are some uncertainties in modelling this system regarding the inlet

boundary conditions of the PFR. The JSR has some differences with the ideal PSR and the output is not the exact value for the PFR. However, this problem is overcome in [34] by calibrating the output value of the PSR to be in accordance with the inlet value of PFR. The same experiment has been investigated numerically by [35] using the same gas-phase chemical mechanism and PAH-based kinetics but with a soot model which solves stochastically the population balance equation. Moreover, in the numerical study of [35] two energy regimes (i.e. adiabatic and constant temperature) of constant pressure batch and PSR reactors are modelled to study the convergence of the PBE before investigating the JSR/PFR experiment. It is stated in [35] that the energy term of soot radiation was not incorporated in the energy balance equation of PSR due to the observed small amounts of soot volume fraction (around 0.03 ppm).

2.3 1D Laminar flames

The 0D reactors provide good fundamental analysis as they neglect the dependency of the governing equations on physical space. However, the gas-phase and PBE models have to be extended and tested in more dimensions for spatial dependency. A good option is to use a simplified 1D model. Except the 1D plug-flow reactor, laminar 1D flame models could be considered either premixed or non-premixed that are closer to practical flame configurations.

2.3.1 Numerical and experimental study of 1D laminar premixed flame

Burner-stabilised premixed flames or flat flame burners generate a floated thin flame which is close to an ideal 1D laminar flat premixed flame. The flat flame is established by adjusting a uniform velocity profile for the mixture by using a porous burner or a honeycomb section [36] at the jet burner exit. This 1D laminar premixed flame configuration is ideal to numerically model. An existing numerical code found in [37] solves this type of system for the flow field, gas-phase, particulate dynamics and temperature. However, two methods can be used for the temperature of the flame. In the first method, the 1D numerical code can receive as input the known temperature profiles prior to the computation, eliminating the need to solve for an energy equation. The temperature profiles are obtained from experimental measurements at several locations in the axial direction. The other method is to compute the temperature

through an energy equation. The former method in premixed flames is preferred as the heat losses are taken into account from the measurements within this fixed temperature profile. It should be noted that this type of experiment when the flame is close to the burner exit, fuel and burner preheating occurs. Thus, by knowing the temperature profiles in advance reduce any uncertainties regarding the prediction of the flow field, gas-phase and the particulate dynamics due to radiation and any other heat losses. As such, it is common to solve only the species transport equations and ignore the energy equation in this laminar premixed flame 1D code.

Furthermore, in premixed flames, more fundamental investigation has been undertaken both experimentally and numerically in the study of gas-phase and soot kinetics. Particle size distribution (PSD) of soot particles is measured at several locations in the axial distance above the burner using a scanning mobility particle sizer [38]. A numerical investigation has been conducted for this experiment with 1D Premix code in the study of [39] using a known measured temperature profile. On the other hand, in counterflow laminar diffusion flames, measurements of soot PSD are not yet available.

2.3.2 Laminar 1D non-premixed flame system

Diffusion flames are categorised into two types: the jet flames and counterflow flames. As noted in [26], a co-flow burner is preferred instead of counterflow due to the stability of the flame at the elevated pressures. The jet flame will be explained in a greater detail in the next section. Four types of counterflow diffusion flame are shown in [40] and will be summarized here. Counterflow diffusion flame types are classified into a) opposed concentric jets consisting of oxidiser and the fuel separately, b) flat flame between two opposed matrix burners, c) spherical porous and d) cylindrical porous burners.

This thesis focuses on the counterflow type (opposed concentric jets) and the reader can seek more information for the rest diffusion flame types in [40]. A schematic of the counterflow configuration is shown in Figure 2.3. After combustion is initiated, a thin flame is generated and is stabilised at a location that depends primarily on the composition of the fuel and the velocity of both jets. A stagnation region is formed somewhere between the two opposing burners. The effect of aerodynamics on a flame is strain rate and is estimated from the velocity gradient. The inverse strain rate is the characteristic time scale of the problem [41]. It should be noted that as the distance between the opposing jet burners is decreased or their velocities are increased, the strain rate is increased and the flame departs from the chemical equilibrium.

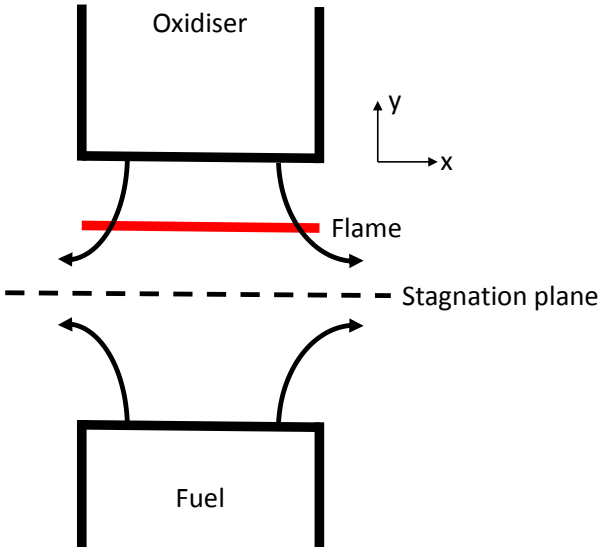

Figure 2.3: Opposed jet diffusion flame

It is possible to derive a 1D counterflow flame structure by taking into account several assumptions, starting from a steady 2D axially symmetric (or planar) counterflow configuration. Two methods can be used to reduce the 2D into 1D. The first method is to use a similarity coordinate to the 2D governing equations [41], and the second is through using the Prandtl's boundary layer theory assumption, which neglects diffusion in the direction orthogonal to the stream line (x-axis) [30]. With the Prandtl assumption, the system is reduced to 1D governing equations in diffusion flames which are functions of a single physical coordinate. This spatial distance is described by the y-coordinate, referring to vertical axial direction.

2.3.3 Flamelet equation

This kind of geometry is often used in experimental and numerical investigations because the 1D counterflow configuration can be simplified into an even simpler 1D flame structure, called the flamelet. In the flamelet configuration the momentum equations are no longer necessary to be solved.

The governing equations of the flamelet are obtained by replacing the physical coordinate (y-coordinate) with a conserved quantity, called mixture fraction coordinate. The mixture fraction is denoted by Z and is the mass fraction of the mixture that originated in the fuel inlet stream. Any element from the fuel region could be used to represent mixture fraction, as they are conserved quantities (e.g. hydrogen element). The carbon element is preferred, though, because in most cases no carbon is located at the oxidiser (e.g. air) except in situations such

as where CO_2 is available in the oxidiser region. The mixture fraction value ranges from 0 to 1 assuming that the carbon element exists only on the fuel side and not on the oxidiser side. As such, at the oxidiser stream the mixture fraction is 0, and at the fuel stream the mixture fraction is 1. Also, the mixture fraction can be normalised to vary between values 0 (oxidiser stream) and 1 (fuel stream) using the equation (2.7) for available numerical or experimental data of mass fractions according to Bilger's formula mixture fraction definition found in [41].

$$Z = \frac{Z_C/(m_b W_C) + Z_H/(n_b W_H) + 2(Y_{O_2,2} - Z_O)/(\nu'_{O_2} W_{O_2})}{Z_{C,1}/(m_b W_C) + Z_{H,1}/(n_b W_H) + 2Y_{O_2,2}/(\nu'_{O_2} W_{O_2})} \tag{2.7}$$

The $Z_{C,1}$ and $Y_{O_2,2}$ terms denote carbon element mass fraction from the fuel stream and mass fraction of O_2 from the oxidiser stream respectively. W_C, W_H and W_{O_2} are the molecular weights of each species and m_b and n_b are the number of carbon and hydrogen atoms of the fuel species. The 1D formulation with a mixture fraction coordinate can represent a counterflow or an infinite mixing layer of a coflow. The temporal and spatial derivatives of physical coordinates can be replaced with the new independent variable, Z, using a Crocco transformation. Introducing further assumptions to the system, such as that all the species mass diffusivities are equal (Lewis number equals to 1) excluding differential diffusion, the flamelet equation can be derived. The species transport equation of the flamelet with the mixture fraction coordinate is shown in equation (2.8).

$$\frac{\partial Y_k}{\partial t} = \frac{\chi}{2}\frac{\partial^2 Y_k}{\partial Z^2} + \frac{\dot{\omega}_k}{\rho} \tag{2.8}$$

The species mass fraction is represented by the term Y_k for a specific k^{th} species and χ is the scalar dissipation rate. The Lewis (L_e) number is set to 1 to omit differential diffusion and to get the simplify expression of (2.8). In case the Lewis number is not equal to 1 then additional terms are needed to the flamelet equation (2.8). The scalar dissipation rate as shown in equation (2.9) is an important parameter in non-premixed flame and especially in flamelets because it provides the necessary coupling between the mixing of the fuel and combustion modelling. By analogy with a simple species transport equation, the scalar dissipation rate can be thought as a diffusion term in the mixture fraction space as can be seen in the equation (2.8).

$$\chi = 2D\left|\frac{\partial Z}{\partial x_j}\right|^2 \tag{2.9}$$

The term D is the mass diffusivity. In this case, the mass diffusivities of all species are

assumed to be equal, and the index j refers to the different physical coordinates of the system. In the flamelet system the scalar dissipation rate can be represented by a simple algebraic form through mathematical manipulation and transformation by assuming constant density as found in [41] and shown below in Equation (2.10) for the laminar counterflow diffusion flame configuration. No energy equation is introduced to this numerical methodology, yielding only adiabatic temperatures. The scalar dissipation rate is a function of the mixture fraction alone and is calculated (prescribed) prior to the computation by the following expression found in equation (2.10) [41, 42]. The planar configuration and the axial configuration of laminar counterflow problems' mathematical framework can be found in [41].

$$\chi(Z) = \frac{\alpha_s}{\pi} e^{-2[\mathrm{erfc}^{-1}(2Z)]^2} \tag{2.10}$$

where α_s is defined as the strain rate, erfc^{-1} is the inverse complementary error function and Z is any value of mixture fraction between 0 and 1. The equation (2.10) is found by assuming constant density in the momentum equation and unity Lewis numbers in a counterflow configuration. Additional terms and modifications should be added to include non-unity Lewis numbers and non-constant density [41]. Scalar dissipation rate is obtained for every point in the known mixture fraction space. Introducing a non-dimensional (similarity) coordinate η the analytical expression of the scalar dissipation rate in equation (2.10) was found. The solution of the mixture fraction is obtained for this non-dimensional coordinate in the equation (2.11) which is inverted to yield equation (2.10).

$$Z = \frac{1}{2}\mathrm{erfc}(\frac{\eta}{\sqrt{2}}) \tag{2.11}$$

This flamelet equation is discretised by the finite difference method for a non-uniform mesh, and the diffusion-chemistry part is solved via a fractional step. Fractional step is a numerical method for solving stiff equations by decoupling the diffusion from the chemistry. This means that on the first stage the diffusion term of Equation (2.8) is solved without including the chemical source term. On the second stage, the solution of the diffusion term is used to compute the reactions of the chemical source term, updating the final solution of each species mass fraction.

This flamelet formulation and analytical solution which is derived from counterflow geometry [41] can be joined by an energy equation where the radiation properties of soot particles can

be examined. However, in this thesis an energy equation in the flamelet configuration is not included leading to adiabatic temperatures. Due to the many ODEs that exist in the system from the chemistry, this formulation can be used to conduct numerical investigations on the stiffness of the gas-phase chemical mechanisms and particulate dynamics. It can test the performance of the PBE before implementing it into an actual multidimensional flame. Another important use of this method is in creating a flamelet library to represent the chemistry in a turbulent flow case with an assumed probability density function (PDF). Mean values of species are obtained using the presumed PDF of the mixture fraction, which is determined by statistical moments (e.g. mixture fraction variance) [26].

The scalar dissipation rate is the inverse time of a diffusion time scale. As such, the scalar dissipation rate represents a diffusivity term that is different at a given point of mixture fraction space. The scalar dissipation rate is the same space for all species when the assumption of unity Lewis numbers is made. An important dimensionless quantity associated with diffusion flames is the Damköhler number; it is the ratio of a characteristic mixing time scale against a characteristic chemical reaction time scale. When chemical reactions are much faster than the diffusion rates of the gaseous products, the consequence is a high Da number [26]. In turbulent flames, however, the infinitely fast chemistry assumption (large Damköhler number) can be replaced by the solution of the laminar flamelet model incorporating some finite-rate chemistry effects (lower Damköhler number). The model fails to capture significant non-equilibrium effects such as re-ignition and extinction, and is reasonably predicting slow chemistry processes (e.g. NOx and soot formation) [43, 44].

2.3.4 Steady and unsteady flamelet

The coupling between the laminar chemistry stored in a flamelet library and turbulent flow field is achieved by using a statistical method, for example a presumed beta probability density function. Transport equations of the mixture fraction without any source terms and mixture fraction variance are solved. The scalar dissipation rate is a function of mixture fraction and can be computed from equation (2.9). According to [45] libraries through the Steady Laminar Flamelet Model (SLFM) where the time derivative is neglected contain the species mass fractions, which are functions of mixture fraction and are stored under a specific scalar dissipation rate. Later, SLFM was extended to unsteady combustion where the species mass fractions are now functions of scalar dissipation rate and mixture fraction. In unsteady reacting flows

the scalar dissipation rate varies during reaction history. Thus, it may be not appropriate to represent the chemistry with the SLFM, but rather with the unsteady flamelet.

In non-premixed combustion, flamelet refers to a thin reaction zone in physical space where the effects of turbulence are negligible and the eddies do not enter the flame structure. The scalar dissipation rate is the only variable that transfers the turbulence information of the flow field to the reaction zone [45]. Normally, scalar dissipation rate is the only variable that connects the physical space with the mixture fraction space (see equation (2.9)). In simple configurations such as infinite mixing layer or counterflow flame, the scalar dissipation rate can be determined by an analytical solution derived in [41]. The steady laminar flamelet is not appropriate for predicting extinction and re-ignition events and slow-formation pollutants such as NOx and soot formation; the unsteady flamelet is found to be more appropriate to model the transient effects in turbulent flames. Unsteady effects have been investigated in [46, 43] where the unsteady flamelet approach is used as post processing mode to predict NO concentrations with reasonable agreement. The unsteady flamelet captured the extinction quite accurately whereas re-ignition is not [44].

2.4 Laminar flames

Several experiments of both laminar flame types (premixed and diffusion) have been performed. A large amount of data is measured, and is available for comparison against numerical sooting studies. The diffusion flame configuration is a good choice for performing numerical investigation among other systems, such as premixed flames. This is because the majority of practical large-scale industrial applications are non-premixed configurations.

2.4.1 Laminar and turbulent diffusion flames

Examples of diffusion flames in commercial applications are the gas turbine and diesel engines that operate primarily in turbulent conditions. The study of soot formation in these applications may not be possible numerically and experimentally due to the significant computational effort required, as well as complex geometry and difficulties in measuring soot properties for validation purposes. A very efficient way to reduce the computational expense of chemistry is to represent it by the laminar flamelet concept [26]. Many studies of reacting turbulent flows model the chemistry as an ensemble of laminar flamelets. The laminar flamelet libraries are produced from

a 1D counterflow burner, providing an additional reason to investigate laminar flames. The steady laminar flamelet model is a widely used approach for computing the complex chemistry of the turbulent non-premixed flames [47].

On the other hand experimentally, in the case of an unsteady turbulent non-premixed flame, the experiment measures the spatially and temporary resolved soot concentrations; these are not usually reliable and are difficult to obtain [17], especially at elevated pressures. Thus, laminar flame experiments are much easier to set up and control in order to obtain any measurements. The results of the laminar computation can be validated and projected to turbulent flames through the flamelet hypothesis [17].

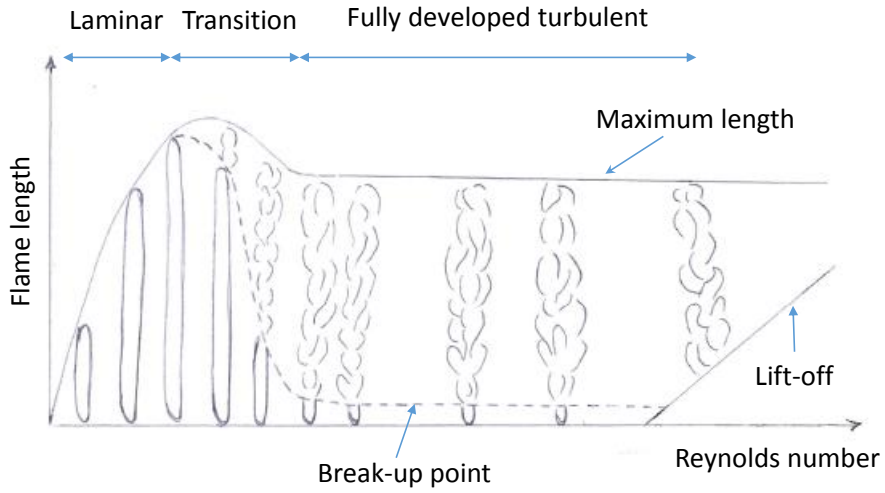

Figure 2.4: Coflow jet diffusion flame characteristics

The jet configuration of fuel injected in ambient air is qualitatively displayed in Figure 2.4 [48]. The Reynolds number depends significantly on the inlet fuel flow rate. The flame length of the illustrated laminar flames in Figure 2.4 is a function of the Reynolds number. As the Reynolds number is increased, the laminar flame length is increased almost linearly up to a critical transition point. A transition state between laminar and turbulent states occurs, and the flame length starts to drop. For a sufficient high flow rate a fully turbulent flame rises until it reaches a lift-off point, and finally its blow-off point [48]. In certain experiments the oxidiser is specified with an initial velocity. In laminar diffusion flames with an appropriate oxidiser velocity and fuel dilution, such as in [49], a lifted laminar coflow flame could be achieved avoiding fuel preheating issues.

The most straightforward approach for solving laminar or turbulent reacting cases is the Direct Numerical Simulations (DNS). In DNS all the characteristic length and time scales are

resolved [48]. The full instantaneous governing equations are solved without any turbulence model. Even so, DNS simulations are intractable and limited to academic situations [48] of fairly low Reynolds numbers (like laminar reacting flows) with simple geometries. As such, several assumptions are introduced to alleviate the computational burden. These approximations are usually constant density (incompressible flows), low Mach-number (where density may change due to temperature variations but remains independent of pressure variations [48]), constant transport properties such as constant species heat capacities, few-step instead of detailed chemistry.

An over-ventilated laminar diffusion flame is considered in this thesis. This means that excess air is available in the surroundings in order to fully react with the fuel issued from the central jet. In this type of flame, the flame boundary converges towards the axis as a result of buoyancy acceleration; the steady laminar flame has a final closed conical shape. If air is not found in excess and is not sufficient to burn all the fuel coming from the jet, the flame surface is expanded away from the axis of symmetry and is called an under-ventilated flame. This is also called an inverted flame [36].

2.4.2 Governing equations for reacting flows

The next instantaneous governing equations describe the laminar and turbulent jet systems. The continuity equation is shown (2.12), conservation of momentum (2.13), species conservation (2.14) and total enthalpy conservation - sensible plus chemical enthalpy - (2.15).

$$\frac{\partial \rho}{\partial t} + \frac{\partial \left(\rho u_i\right)}{\partial x_i} = 0, \quad i = 1, 2 \tag{2.12}$$

$$\frac{\partial \left(\rho u_i\right)}{\partial t} + \frac{\partial \left(\rho u_i u_j\right)}{\partial x_j} + \frac{\partial p}{\partial x_i} = \frac{\partial \tau_{ij}}{\partial x_j} + \rho g_i \tag{2.13}$$

$$\frac{\partial \left(\rho Y_k\right)}{\partial t} + \frac{\partial \left(\rho u_i Y_k\right)}{\partial x_i} = -\frac{\partial J_{k,i}}{\partial x_i} + \dot{\omega}_k, \quad k = 1, N_{sp} \tag{2.14}$$

$$\frac{\partial \left(\rho H\right)}{\partial t} + \frac{\partial \left(\rho u_i H\right)}{\partial x_i} = \frac{Dp}{Dt} + \tau_{ij}\frac{\partial u_i}{\partial x_i} + \frac{\partial \left(\frac{\lambda}{C_p}\frac{\partial H}{\partial x_i}\right)}{\partial x_i} - \frac{\partial}{\partial x_i}\left[\mu \sum_k^{N_{sp}} \frac{1}{Pr}\left(1 - Le_k\right) h_k \frac{\partial Y_k}{\partial x_i}\right] + \dot{Q} \tag{2.15}$$

These equations can be applied to reacting and non-reacting flows in both laminar and turbulent systems. The $\dot{Q}$ is the heat source term (e.g. radiative flux), ρ is the mixture density, p is the static pressure, u is the velocity field containing the components of Cartesian, cylindrical or spherical coordinates and $J_{k,i}$ is the diffusion mass flux vector of k^{th} species and is given in equation (2.16).

$$J_{k,i} = \rho V_{k,i} Y_k \tag{2.16}$$

The variable Y_k denotes the mass fractions and it should be noted that k index is reserved as an indicator to refer to the k^{th} species and will not follow the summation rule. H is the total enthalpy, μ is the mixture viscosity, λ is the thermal conductivity of the mixture and Le is the Lewis number of species k. $V_{k,i}$ in equation (2.16) is the complete diffusion of each species k. This format is appropriate when ordinary, thermal and correction diffusion velocities are considered. These equations can be found in more detail and different forms in [48, 50]. In the above equations several terms are neglected. For example, for low Mach numbers, the pressure and viscous heating terms of enthalpy are negligible and can be neglected. Also, gravitational effects can be neglected for high Froude numbers [50]. In case of laminar flames, though, the gravity term is essential for buoyancy-driven flames, and should be included in the momentum equations. The governing equations can be transformed from a Cartesian to a curvilinear system as defined in [51].

The benefit of using an axisymmetric geometry is that the computational model can be represented by a rectangular 2D domain instead of a full 3D simulation, significantly reducing the computational effort. The Navier-Stokes equations are solved for the axial and radial momentum, and a gravity term is included only in the axial momentum equation in order to take the buoyancy effects into account. All, the previous governing equations could be represented for simplicity by the same general transport equation. The general transport equation that is used for all the transported quantities is shown in equation (2.17).

$$\frac{\partial(\rho\phi)}{\partial t} + \frac{\partial(\rho u_j \phi)}{\partial x_j} = \frac{\partial}{\partial x_j}\left(\Gamma_\phi \frac{\partial \phi}{\partial x_j}\right) + \dot{\omega}_\phi \tag{2.17}$$

The first term is the unsteady term. The second represents the convection of the fluid flow, the third is the diffusion, and the last term is the source term of each transported quantity. ϕ is the scalar transport quantity (e.g. scalar velocity, mixture fraction, species). Γ_Φ represents the

mass diffusivities of each transported species transport and the transport coefficients (mixture viscosity) in momentum equations. In soot transport equations the diffusion term is omitted due to the negligible contribution of the molecular diffusivity of the heavy soot particles. Instead of the diffusion term, a thermophoresis term (Soret effect of soot particles) is included which will be explained with a more detail in the next section in equation (2.20), whereas the enthalpy equation includes the divergence of the radiative flux.

Even in laminar flows, the computational cost can be dramatically increased by the direct computation of the chemical source term without any of the simplifications or assumptions that occur in turbulent flows. The computational cost in this laminar flame depends on three factors. The first is the number of the chemical species that are transported throughout the computational domain; the second is the computation of the chemical source terms, and the third is the computation of the transport coefficients, such as mixture viscosities and mixture-averaged mass diffusivities of each species. The convection and diffusion timescales in the laminar flows are relatively large, but the chemical timescale is very small; the global time step is significantly dropped because smaller scales require smaller time step to be captured. The length scales of species and soot particles require more grid points in some areas [2]. As such, parallel computing is crucial to reducing the computational cost in order to ensure all the previous factors can be treated in a manageable amount of time. Scaling study of the laminar 2D case is shown in Chapter 3.

2.4.3 Modelling of laminar flames

The modelling of laminar diffusion flames start by the discretisation of the governing equations listed in the previous section. In this thesis the governing equations are discretised with a finite volume scheme. The finite difference approximations are computed in a flow domain in which a mesh is generated. The Navier-Stokes, gas-species, total enthalpy and all soot size class equations are solved in cylindrical coordinates in each mesh cell. An algorithm related to the Semi-Implicit Method for Pressure Linked Equations (SIMPLE) is used to handle the pressure and velocity coupling. The continuity equation is used to model the pressure correction equation to enforce mass conservation. The convection terms of all the transported quantities are computed using upwind configuration. Gravitational term is applied only to the axial momentum equation to take into account the buoyancy effects. To enhance the conservation properties of the finite volume technique, TVD scheme is applied using Van-Leer method. All

the transport equations are solved in a segregated manner using a conjugate gradient solver.

However, during the solution process across the CFD domain mass conservation constraints should be satisfied for any reacting case. The most widely used constraint is to lump all the conservation errors of the species into an inert (diluent) species of the chemical mechanism, which is usually nitrogen or argon. This simple method should be applied only in strongly diluted flames, otherwise non-physical (negative) values of the inert species could appear in the computational domain. The nitrogen is usually ideal because the chemical mechanisms do not have any reactions regarding this species, and is considered to be inert. Also, in diffusion flames, air is usually specified as the oxidiser where nitrogen is found in excess. Implementing this method for the nitrogen species then N_{sp} - 1 transport equations are solved as the nitrogen conservation equation is no longer necessary. This conservation error appears due to Fick's law approximation of diffusive fluxes. The second constraint that could be used is that the sum of the diffusive fluxes should be equal to 0, and the third requires that the sum of the chemical source terms should be equal to 0 as well [4] and is usually satisfied automatically by the chemical mechanisms. The constraints are shown in equation (2.18).

$$\sum_{k=1}^{N_{sp}} Y_k = 1, \quad \sum_{k=1}^{N_{sp}} Y_k V_{k,i} = 0, \quad \sum_{k=1}^{N_{sp}} \dot{\omega}_k = 0 \tag{2.18}$$

The laminar flame that arises through a jet flame is conical. The buoyancy effect is essential and its strong role in some laminar diffusion flames is indicated in Santoro's experimental study [9] as the heated gases are accelerating upwards due to mixture density gradients. The pathlines of the particles via this acceleration converge towards the centre of the flame. This is typical in the Santoro laminar diffusion flame experiments [8, 9]. Differential diffusion of all species is considered. The mass diffusivity of each species is computed from CHEMKIN library from a transport and thermodynamic database, which is provided by the gas-phase chemical mechanism. The mass diffusivity of each species is determined as a mixture-averaged diffusion. The following equations are applied to compute the mass diffusivity of each species k.

$$D_k = \frac{\sum_{l \neq k}^{N_{sp}} X_l W_l}{\overline{W} \sum_{l \neq k}^{N_{sp}} \frac{X_l}{D_{lk}}} \tag{2.19}$$

The expression (2.19) is behaving well as the pure species limit is approached. However, if the mixture is a pure species the formula is still undefined. Thus, an insignificant amount is added to the mole fraction of all species to overcome this problem [52]. X_l is the mole

fraction of species l, W_l is the molecular weight of each species l and D_{lk} are the binary diffusion coefficients. Also, thermophoretic diffusion could be applied. The thermophoresis is determined via the following relationship:

$$V_{T,i} = -0.55 \frac{\mu}{\rho T} \frac{\partial T}{\partial x_i} \tag{2.20}$$

The 0.55 value is a common constant used in the majority of the studies to compute thermophoretic effects. Other studies such as [53] used 0.67 as the coefficient. Thermophoresis is a force that is acting opposed to the gradient of temperature. The thermophoretic velocity is added to the gas fluid velocity for the transport equations of soot as shown in equation (2.109). The thermophoresis diffuses the soot particles radially inward to the flame.

Normally, Wilke's formula should be used to calculate the mixture thermal conductivity which is a complicate expression and computationally expensive according to [4]. Therefore, the following semi-empirical formula in equation (2.22) is usually used to compute the mixture thermal conductivity λ. Moreover, the viscosity of the mixture (μ) is computed by the Wilke formula in equation (2.21). These models can be found in a greater detail in [52, 30] where their accuracy is discussed.

$$\mu = \sum_{k=1}^{N_{sp}} \frac{X_k \mu_k}{\sum_{j=1}^{N_{sp}} X_j \Phi_{kj}} \tag{2.21}$$

$$\lambda = \frac{1}{2} \left(\sum_{k=1}^{N_{sp}} X_k \lambda_k + \frac{1}{\sum_{k=1}^{N_{sp}} X_k / \lambda_k} \right) \tag{2.22}$$

The μ_k and λ_k are the viscosity and thermal conductivities of each species respectively which can be found in the CHEMKIN libraries. The Φ_{kj} is the correction factor of the Wilke formula which depends on the coefficients of viscosities and molecular weights of each species as shown in equation (2.23).

$$\Phi_{kj} = \frac{1}{\sqrt{8}} \left(1 + \frac{M_k}{M_j} \right)^{-\frac{1}{2}} \left[1 + \left(\frac{\mu_k}{\mu_j} \right)^{\frac{1}{2}} \left(\frac{M_j}{M_k} \right)^{\frac{1}{4}} \right]^2 \tag{2.23}$$

The diffusion model plays a significant role in estimating the correct transportation of the species. The diffusion velocity $V_{k,i}$ of the flux vector in equation (2.16) can be computed either by a full multicomponent diffusion model or by several simplifications. The equation (2.24)

is the full multicomponent diffusion model where the body forces acting on each species are assumed to be equal otherwise an additional term will appear.

$$\nabla X_k = \sum_{l=1}^{N_{sp}} \frac{X_l X_k}{D_{lk}}(V_l - V_k) + \sum_{m=1}^{N_{sp}} \left[\frac{X_l X_k}{\rho D_{kt}} \left(\frac{D_{T,l}}{Y_l} - \frac{D_{T,k}}{Y_k} \right) \right] \left(\frac{\nabla T}{T} \right) + (Y_k - X_k)\frac{\nabla p}{p} \tag{2.24}$$

The multicomponent diffusion model in equation (2.24) relates in the first term of the RHS the gradients of mole fraction to the relative diffusion velocities, in the second term the thermal diffusion (Soret effect) and in the third term and pressure gradients [4]. The most accurate model is the multicomponent diffusion, which is a generalisation of the Maxwell-Stefan equations. However, for a standard hydrocarbon flame, this diffusion model is unnecessarily detailed and time-consuming [4]. Thus, the following simplification of the complete diffusion velocity of each species is described in the following relationship (2.25) by assuming that the diffusion velocity vector is composed of three parts.

$$V_k = u_k^n + u_k^T + u^c \tag{2.25}$$

The following simplification of the diffusion model in equation (2.25) is widely used: Fick's law with mixture-averaged diffusion coefficients as shown in equation (2.26).

$$Y_k u_k^n = -D_k \nabla Y_k \tag{2.26}$$

This is the simplest diffusion model where the gradient mass fraction can be implemented directly, because the transport equations are usually in terms of mass fractions. The other simple model is the Hirschfelder and Curtis first-order approximation with mixture-averaged diffusion coefficients and related to mole fraction as shown in equation (2.27).

$$X_k u_k^n = -D_k \nabla X_k \tag{2.27}$$

This approximation is similar to Fick's law and very convenient to use as the mixture averaged diffusion coefficients can be easily related to kinematic viscosity and some imposed Schmidt numbers; the binary diffusion coefficients are complex functions of collision integrals. As such, the binary diffusion coefficients do not need to be computed. The Fick's law and Hirschfelder

and Curtis model are exact when a binary mixture is applied with no pressure gradients and no volume forces [54]. The latter simplification is usually not the simplest because the gradients of the mole fraction are needed, and should be transformed from mass fractions which are usually directly available. The Hirschfelder and Curtis method is the best first-order approximation to the solution of the Stefan-Maxwell equations in conjunction with a correction velocity [4] as shown in equation (2.28).

$$u^c = -\sum_{k=1}^{N_{sp}} Y_k(u_k^n + u_k^T) \tag{2.28}$$

Still, even by using the diffusion model of equation (2.26) or (2.27) which are significant simplifications of the full multicomponent diffusion model shown in equation (2.24), a significant amount of computational cost is spent for the calculation of the mixture-averaged diffusion coefficients of each species. In the case of imposed Schmidt numbers for each species, the computational effort is alleviated. The terms in the energy flux are related through the Fourier law. Finally, the mixture density is connected to the other thermodynamic variables by the equation of state [4]. The density is related to other thermodynamic variables for an ideal gas using equation (2.29).

$$\rho = \frac{p\bar{W}}{RT} \tag{2.29}$$

Differential diffusion is also called as preferential diffusion. Due to differential diffusion effects, the lighter species (like H_2) diffuse faster than the heavier species. The differential diffusion between the gas-phase species and soot particles is found to be important in few turbulent reacting flows studies [55]. However, their effects are more pronounced for slower jets [26], and need to be considered in laminar flames. In turbulent reacting flows, it is common to omit these effects as they are considerably expensive and sometimes negligible. Differential diffusion effects have been examined in laminar flames, and their importance in predicting correct temperatures at the upstream region and at the tip of the flame is apparent [56].

Moreover, other transport mechanisms such as Dufour effects where an energy or heat flux appears in the energy equation due to mass concentration gradients is typically negligible in combustion processes [4] and is omitted in this thesis. Thermal diffusion or Soret effect of species is another transport mechanism that appears in the species transport equations due to the different diffusivities of light species subjected to a temperature gradient. The Soret

mechanism is more significant for light species such as hydrogen molecules. A numerical soot formation study is performed with the Soret effect mechanism and is found not to be important to the C_2H_4-air/argon diffusion flame configuration [57].

2.5 Turbulent combustion

2.5.1 Modelling approach for turbulent flames

Several numerical approaches exist to simulate a turbulent reactive case. These numerical models have been found to be Direct Numerical Simulation (DNS), Large Eddy Simulation (LES) and Reynolds-averaged Navier-Stokes (RANS) [58]. Each category has its own benefits and drawbacks. The numerical investigation of a turbulent reacting flow requires the same governing equations listed in the previous laminar flame section. However, this will be very computationally intensive, as it requires a very fine mesh to capture all the time and length scales. Therefore, a DNS simulation for turbulent reacting flows is intractable and is restricted to low Reynolds number and academic flows with simple geometries. RANS or LES could be used to alleviate the computational cost problem. It should be noted that by performing a Favre-averaged operation on the governing equations, their final form will be very similar to those of the DNS with the exception of some extra fluctuations terms. There are several advantages and drawbacks when using each one of these models; these are summarised in the following table 2.2. Generally, in turbulent flows of high Reynolds numbers with RANS, the mean molecular transport of momentum and molecular diffusion fluxes are omitted from the averaged equations because they are negligible. They may be included by simply adding the turbulent diffusion term with the molecular diffusion term.

Approach	Advantages	Drawbacks
RANS	• Coarse computational grid • Complex geometries • Reduced computational effort	Mean transported quantities Modelling is required for all scales
LES	• Unsteady features • Less modelling than RANS	3D simulations are required Modelling of small scales
DNS	• No models are needed • Numerical “experiment”	Very fine grids Limited to simplified geometries

Table 2.2: Model advantages

Due to limited computational resources, the cost of the DNS and LES computations is still a major issue and is generally prohibitive. As a result, in most commercial CFD software today, RANS formulation is widely used in industry due to the advantages listed in the table 2.2. DNS simulation is performed to establish the fundamentals of chemistry and other physical processes through a simple laminar flame, which is tractable prior to investigating a similar turbulent configuration. Several experiments are performed with a variety of fuels, such as C_2H_4 and C_3H_8; most of them utilised a CH_4 fuel (natural gas) [10] because of the high commercial usage in the energy sector and lower polluting impact. Compared to laminar modelling, turbulence modelling is much more complex and poses greater numerical challenges where simplifications are needed in order to conduct appropriate simulations.

One of the main challenges in turbulent reacting flows is the treatment of turbulence-chemistry and turbulence-radiation interactions (TRI). If these are neglected, it could result in a loss of accuracy. If TRI are included, for example, the radiation emissions have been found to increase by around 30-60% according to [59] affecting significantly the flame structure. Turbulent flow is characterised by velocity, temperature and species local fluctuations. These scalar fluctuations increase the difficulty in the numerical modelling and the need for robust, stable models free from artificial diffusion is apparent [60]. The incorporation of those models is usually complex and time-consuming. To reduce the computational cost of a numerical investigation in turbulent flames, combustion models and several turbulence models are used to model the unclosed terms arising from turbulent fluctuations; this is instead of conducting a full DNS simulation.

DNS solves the full instantaneous Navier-Stokes equations without applying any turbulence model. DNS is a powerful tool for investigating a real physical problem, and can provide very useful information about the problems' physics. Sometimes DNS is considered to be a numerical "experiment", and can be used to calibrate models of other approaches [58]. In this case all the temporal and spatial scales are resolved (from the smallest scale, Kolmogorov, up to the largest scale) by using an extremely fine mesh to capture all the effects. Due to the dense grid that is required, the computational cost of this method is prohibitive, requiring a tremendous amount of memory and number of processors in turbulent reacting flows. This is why DNS remains mainly as a research tool, and is not used for practical systems. Appropriate simplifications are applied to alleviate the problem of computational cost as has been explained in section 2.4.1.

The alternative is to use LES instead of DNS. LES is based on the idea of separating the large

turbulence scales from the small turbulence scales. The large-scale structures are more affected by the geometry, flow characteristics and boundary conditions, and can be solved explicitly. On the other hand, the small scales exhibit more universal features and homogeneity, as they are less dependent on boundary conditions. As such, the instantaneous governing equations are spatially filtered where the large scales are spatially and temporary resolved explicitly, whereas the small scales are not resolved directly and are considered by a sub-filter closure model [58]. LES has been used and validated mainly for non-reacting cases. In turbulent reacting flows, the complexity and computational expense is further increased because chemical reactions are taking place at very small scales that need to be modelled. As a result, in combustion applications the quality of an LES simulation is highly dependent from the effects of the sub-filter fluctuations. In general, LES is less expensive than DNS simulation, but is still expensive for industrial combustion applications and it is not a widely used approach yet; a 3D simulation is required for axisymmetrical problems, where a 2D formulation is possible for DNS and RANS modelling [58].

The last model to be discussed is the RANS application. The instantaneous governing equations are time averaged. With the time averaging, the dynamic range of scales is significantly reduced, and the evolution of the averaged quantities is solved. It should be noted that by using RANS in a turbulent flame, the average flame thickness is wider and much larger than the instantaneous flame region. As such, a larger mesh size can be employed appropriately compared to LES and DNS where the flame thickness is smaller, and a smaller mesh size is required to capture it [61, 58]. RANS models employ coarser grids than LES and DNS. Therefore, with the aforementioned description, it is clear that RANS solves only the mean flow field, and the mesh does not necessarily need to be very fine. For this reason, RANS is widely used in engineering applications due to the reduced computational effort. RANS has the great advantage of being more easily applicable to complex geometries than LES and DNS, and various operating conditions can be studied at a lower computational cost [61].

To derive the RANS model, two approaches can be used: Reynolds decomposition and Favre averaging. Reynolds averaging is used to separate the fluctuation term from the mean flow field, while the Favre is a density-weighted averaging procedure. In this study, the following Favre-averaged governing equations are used in the simulations. In the RANS model all the turbulence scales are modelled except the mean flow properties which are computed directly. Unfortunately, the averaging process may reduce the number of degrees of freedom of the

investigation, but the averaging of the non-linear terms in instantaneous equations produces unclosed terms which need to be modelled. The Favre-averaging is preferred over Reynolds averaging in variable-density combustion flows due to the induced density fluctuations, and because it reduces the number of the unclosed terms. Unfortunately, the most time consuming portion is spent on the smallest scales (e.g. where combustion and mixing occurs) and not at the large scales, as the fluid bulk motion is not affected directly (by the small scales) [58].

2.5.2 Governing equations for turbulent flames

The Reynolds averaging operation is denoted with a bar on top of each variable, and the Favre averaging process is denoted by a tilde on top of each variable. In the conventional Reynolds averaging, no Favre terms are encountered; however, with the Favre averaging, both operations are found in certain variables. For any transported quantity ϕ the relationship to link the two averaging operations (e.g. Reynolds and Favre averaging) is shown in equation (2.30).

$$\tilde{\phi} = \frac{\overline{\rho\phi}}{\bar{\rho}} \tag{2.30}$$

The Favre-averaged transport equations of continuity, momentum, species and enthalpy conservation are shown in equations (2.31), (2.32), (2.33) and (2.34) respectively.

$$\frac{\partial \bar{\rho}}{\partial t} + \frac{\partial \left(\bar{\rho}\tilde{u}_i\right)}{\partial x_i} = 0 \tag{2.31}$$

$$\frac{\partial \left(\bar{\rho}\tilde{u}_j\right)}{\partial t} + \frac{\partial \left(\bar{\rho}\tilde{u}_i\tilde{u}_j\right)}{\partial x_i} + \frac{\partial \bar{p}}{\partial x_j} = \frac{\partial \bar{\tau}_{ij}}{\partial x_i} - \frac{\partial \left(\bar{\rho}\widetilde{u_i'' u_j''}\right)}{\partial x_i} \tag{2.32}$$

where $\bar{\rho}\widetilde{u_i'' u_j''}$ is the unclosed Reynolds-stress term. This term is modelled by employing a turbulence model. The most common approach to close this term is to apply two balance equations for the turbulent kinetic energy (k) and turbulent dissipation rate (ϵ). This is a two-equation turbulence model. Other alternatives include a one-equation turbulence model, the Prandtl mixing length (e.g. zero equation) or the Reynolds stress model [62].

$$\frac{\partial \left(\bar{\rho}\tilde{Y}_k\right)}{\partial t} + \frac{\partial \left(\bar{\rho}\tilde{u}_i\tilde{Y}_k\right)}{\partial x_i} = -\frac{\partial \left(\overline{J_{k,i}}\right)}{\partial x_i} - \frac{\left(\bar{\rho}\widetilde{u_i'' Y_k''}\right)}{\partial x_i} + \bar{\dot{\omega}}_k \tag{2.33}$$

where $\bar{\rho}\widetilde{u_i'' Y_k''}$ is the an unclosed transport term of the chemical species, which appears due to

turbulent fluctuations. This term is modelled by the gradient diffusion hypothesis. The other unclosed term, $\bar{\dot{\omega}}_k$ is the highly non-linear chemical source. Modelling of the chemical source term is of paramount importance, and will be explained at the end of this section in detail.

$$\frac{\partial\left(\bar{\rho}\tilde{H}\right)}{\partial t}+\frac{\partial\left(\bar{\rho}\tilde{u}_i\tilde{H}\right)}{\partial x_i}=\frac{D\bar{p}}{Dt}+\overline{\tau_{ij}\frac{\partial u_j}{\partial x_i}}+\frac{\partial\left(\overline{\frac{\lambda}{C_p}\frac{\partial H}{\partial x_i}}\right)}{\partial x_i}-\frac{\partial\left(\bar{\rho}\widetilde{u_i''H''}\right)}{\partial x_i}+\bar{\dot{Q}} \tag{2.34}$$

where the $\overline{\rho u_i'' H''}$ is equal to $\bar{\rho}\widetilde{u_i'' H''}$ [48]. This term appears due to enthalpy turbulent fluctuations, and is the same as the species transport equation unclosed term. A gradient diffusion hypothesis is used to obtain closure. It should be noted that the drawback of the gradient diffusion hypothesis is that it cannot predict turbulent flames where there is a counter gradient turbulent transport (the turbulent scalar fluxes have a direction opposite of equation (2.39)). This phenomenon could occur in flames of weak turbulence as explained in [48]. The last remaining unclosed term is the $\bar{\dot{Q}}$ which acts as a sink term to enthalpy due to radiation from species and particulate matter. The closure of this non-linear term is treated in a similar manner to the species chemical unclosed source term. A further explanation will be given in a later section.

2.5.3 Turbulence modelling

Following the turbulence viscosity assumption proposed by Boussinesq, an expression for Newtonian fluids is given that introduces a turbulent viscosity term. This turbulent viscosity term needs to be modelled. Several approaches have been proposed; the zero-equation model (Prandtl mixing length model), one-equation models such as Prandtl-Kolmogorov and the two-equation models category where the most famous one is the k-ϵ [48]. Two transport equations are used to describe the turbulent kinetic energy (k) and turbulent dissipation rate (ϵ). These balance equations are shown in (2.35) and (2.36).

$$\frac{\partial\bar{\rho}k}{\partial t}+\frac{\partial\left(\bar{\rho}\tilde{u}_i k\right)}{\partial x_i}=\frac{\partial}{\partial x_i}\left[\left(\mu+\frac{\mu_t}{\sigma_k}\right)\frac{\partial k}{\partial x_i}\right]+P_k-\bar{\rho}\epsilon \tag{2.35}$$

$$\frac{\partial\bar{\rho}\epsilon}{\partial t}+\frac{\partial\left(\bar{\rho}\tilde{u}_i\epsilon\right)}{\partial x_i}=\frac{\partial}{\partial x_i}\left[\left(\mu+\frac{\mu_t}{\sigma_\epsilon}\right)\frac{\partial\epsilon}{\partial x_i}\right]+C_{\epsilon1}\frac{\epsilon}{k}P_k-C_{\epsilon2}\bar{\rho}\frac{\epsilon^2}{k} \tag{2.36}$$

where P_k is the production of turbulent kinetic energy, and is given by the expression found in equation (2.37).

$$P_k = -\bar{\rho}\widetilde{u_i'' u_j''}\frac{\partial \tilde{u}_i}{\partial x_j} \tag{2.37}$$

Gathering all the unclosed terms of the Favre-averaged equations except the chemical and radiation source terms, their closure is obtained with the following expressions. The turbulent species and enthalpy fluxes are modelled with the classical gradient diffusion assumption. Starting with the unclosed term of the momentum equations, the Reynolds-stress term is modelled via Boussinesq approximation [48]:

$$\bar{\rho}\widetilde{u_i'' u_j''} = -\mu_t\left(\frac{\partial \tilde{u}_i}{\partial x_j} + \frac{\partial \tilde{u}_j}{\partial x_i} - \frac{2}{3}\delta_{ij}\frac{\partial \tilde{u}_k}{\partial x_k}\right) + \frac{2}{3}\bar{\rho}k \tag{2.38}$$

$$\bar{\rho}\widetilde{u_i'' Y_k''} = -\frac{\mu_t}{Sc_{kt}}\frac{\partial \tilde{Y_k}}{\partial x_i} \tag{2.39}$$

$$\bar{\rho}\widetilde{u_i'' H''} = -\frac{\mu_t}{Pr_H}\frac{\partial \tilde{H}}{\partial x_i} \tag{2.40}$$

The assumption of the gradient diffusion hypothesis is applied for species and enthalpy unclosed turbulent flux terms as shown in equations (2.39) and (2.40). This model requires knowledge of an effective turbulent viscosity term μ_t. The following parameters have the same values for any k^{th} species and enthalpy $Sc_{kt} = 0.7$ and $Pr_H = 0.7$. The viscosity term is also applied to the two transport equations of k-ϵ turbulence modes. The turbulent viscosity is estimated by the following expression:

$$\mu_t = \bar{\rho}C_\mu\frac{k^2}{\epsilon} \tag{2.41}$$

The model constants are usually modified to tune the turbulence levels according to the experiment specifications [58]. Their usual standard values are shown below.

$C_\mu = 0.09$	$\sigma_k = 1.0$	$\sigma_\epsilon = 1.3$	$C_{\epsilon 1} = 1.44$	$C_{\epsilon 2} = 1.92$

Table 2.3: Turbulence modelling constants and parameters

An improvement to the turbulent predictions used in this thesis is the modification of $C_{\epsilon 2} = 1.8$ to predict the right-spreading jet rates due to round jet anomaly. Other studies include a more complex formulation of the model constants to predict the spreading rates by expressing them as functions of certain variables, such as distance from the burner. Moreover, an additional

third term could be added to the dissipation rate; it is called a round jet correction term, and is proposed by Pope [20].

For the non-reacting case these models and closures are sufficient to predict with a reasonable accuracy the flow field and the level of turbulence in an experiment. Unfortunately, for turbulent reacting flows the source terms of the species transport (chemical source term) and enthalpy transport (radiation) pose a great problem and are challenging to predict from the turbulent combustion community. It is shown in a review of turbulent reacting flows [63], that the averaged chemical source terms are assumed to be described by the following equality in equation (2.42).

$$\dot{\bar{\omega}}(Y, H, p) = \dot{\omega}(\bar{Y}, \bar{H}, \bar{p}) \tag{2.42}$$

The mean chemical source term is a non-linear function of certain instantaneous variables, such as species mass fractions, enthalpy and pressure. These input parameters are averaged in order to compute the chemical source term. This essentially eliminates the turbulence-chemistry interactions, introducing significant errors as illustrated in [63] due to the high non-linearity of this term. This equality should be represented as an inequality as shown in (2.43).

$$\dot{\bar{\omega}}(Y, H, p) \neq \dot{\omega}(\bar{Y}, \bar{H}, \bar{p}) \tag{2.43}$$

2.5.4 Modelling turbulence-chemistry interaction

As such, the turbulence-chemistry interactions are a major problem that must be addressed as accurately as possible. A formulation to achieve a satisfying prediction of turbulence-chemistry interactions is to couple the CFD with a joint probability density function (PDF) approach. The benefits of using PDF via a Monte-Carlo approach are significant. The most important of these is in the computational effort of the simulation. With the Monte-Carlo PDF approach, by adding species or extra scalars the computational cost is increased linearly and the solution is stochastic; with common discretisation schemes, such as finite differencing, the cost is increased exponentially and the solution is deterministic, making the simulation intractable. Moreover, the chemical source term with either a stochastic or deterministic PDF approach appears in closed form, and can be predicted directly with finite-rate chemistry in its Arrhenius form without any combustion models such as eddy dissipation or eddy break-up models. Except

chemical source terms, other one point nonlinear sources are treated exactly (in closed form); they are dependent on local scalar parameters such as radiation emission and soot kinetics. Radiation emission and soot kinetics are functions of temperature, soot volume fraction and certain gas-phase compositions.

The PDF approach has been categorised into the scalar (composition) PDF, and two other more advanced methods (velocity-composition and velocity-frequency-composition PDF approach). The composition PDF solves the evolution of the mass fraction of species, and sometimes enthalpy, as random variables using the Monte-Carlo method. The composition PDF contains all the necessary information to determine the structure of the flame, and quantifies the probability of having a specific gas composition and enthalpy anywhere in the computational domain. The other more advanced PDF methods include additional independent variables to the species composition, like velocity and turbulent dissipation rate. The velocity-composition PDF approach takes into account the velocity fluctuations of the system, and the gradient diffusion hypothesis is eliminated. The approach contains the essential information for describing both the flow and the structure of the flame. The composition and velocity-composition formulations are not grid-free models, and still require a CFD solver to supply the turbulence time scale information necessary to perform mixing. Those two methods are one point, one time PDFs that do not contain any further information on the time and length scales of turbulent motions. The other PDF approach is the velocity-frequency-composition PDF approach, which can be used as a stand-alone method without the need to couple it with a CFD domain. However, this method poses significant robustness issues, is more complex [58] and usually requires the mean pressure gradients to be supplied by solving the Poisson equation.

The most common approach to derive the transported PDF is to use the instantaneous conservation equations along with an ensemble averaging of the fine-grained density function [62], which is defined as the product of Dirac delta functions [63] according to the number of independent variables. The derivation of the PDF is shown in detail by [63] using a fine-grained Eulerian velocity-composition joint PDF. The derivation can also be accomplished by starting from a fine-grained composition PDF [64].

$$p(\underline{\psi}; x, t) = \prod_{\alpha=1}^{N_{sc}} \delta(\phi_\alpha(\mathbf{x}, t) - \psi_\alpha) \tag{2.44}$$

In any position x and time t the PDF is a multidimensional delta function at $\psi = \phi(x, t)$ in ψ space. This represents the PDF for a single realisation of the flow. The Eulerian PDF

transport equation is expressed below in equation (2.45) [64]. This transport equation is obtained by assuming Fickian diffusion for the molecular diffusion, and so the last term becomes the mixromixing term [65]. Moreover, molecular diffusion appears for both the physical and scalar space. Molecular diffusion in physical space can be neglected in the assumption of high Reynolds number, whereas in the scalar space cannot be neglected and Fickian diffusion is applied [62].

$$\begin{aligned}\bar{\rho}\frac{\partial \tilde{P}(\underline{\psi})}{\partial t} + \bar{\rho}\tilde{u}_i\frac{\partial \tilde{P}(\underline{\psi})}{\partial x_i} + \sum_{\alpha=1}^{N_{sc}}\frac{\partial}{\partial \psi_\alpha}\left(\dot{\omega}_\alpha(\underline{\psi})\tilde{P}(\underline{\psi})\right) = \\ -\frac{\partial}{\partial x_i}\left(\bar{\rho}\left\langle u_i''|\underline{\phi}=\underline{\psi}\right\rangle\tilde{P}(\underline{\psi})\right) \\ +\sum_{a=1}^{N_{sc}}\sum_{\beta=1}^{N_{sc}}\frac{\partial^2}{\partial\psi_\alpha\partial\psi_\beta}\left(\left\langle\frac{\mu}{Sc}\frac{\partial\phi_\alpha}{\partial x_i}\frac{\partial\phi_\beta}{\partial x_i}|\underline{\phi}=\underline{\psi}\right\rangle\tilde{P}(\underline{\psi})\right)\end{aligned} \tag{2.45}$$

The equation (2.45) is a joint transported PDF, where all the one-point statistics, moments and variances can be obtained. One point, one time statistics are obtained where the quantities are local and are not related to any other points in space or time [66]. The one point, one time formulation provide the statistics only on the individual points of x and time t [66]. The terms of the equation above have the following significance. The first term is the rate of change of $\tilde{P}(\underline{\psi})$. The second term is the mean convection of $\tilde{P}(\underline{\psi})$ in physical space coordinates. The third term is the chemical production rate in the scalar composition space. The fourth term with the minus sign refers to the turbulent transport in physical space, and the last term denotes the molecular mixing that arises from molecular diffusion in the scalar composition space. It is clear that the last two terms are unclosed (e.g. conditional expectations) and require modelling to continue with this methodology, whereas the first terms on the LHS appear in closed and exact form and do not require any modelling [64].

For the unclosed turbulent transport term in the physical space, a gradient diffusion hypothesis is introduced [64, 65]. The information of the turbulent viscosity is supplied by the external CFD solved through the turbulence k-ϵ models.

$$-\frac{\partial}{\partial x_i}\left(\bar{\rho}\left\langle u_i''|\underline{\phi}=\underline{\psi}\right\rangle\tilde{P}(\underline{\psi})\right) \approx \frac{\partial}{\partial x_i}\left[\frac{\mu_t}{\sigma_t}\frac{\partial\tilde{P}(\underline{\psi})}{\partial x_i}\right] \tag{2.46}$$

The other unclosed term, the micromixing term, requires a mixing model for evaluation.

By introducing the gradient diffusion hypothesis (2.46) and a mixing model (e.g. EMST), the unclosed terms can be evaluated. The final form of the transported PDF equation (equation (2.45)) where all the terms are closed is shown in equation (2.47) [64].

$$\bar{\rho}\frac{D\tilde{P}}{Dt} + \sum_{\alpha=1}^{N_{sc}} \frac{\partial}{\partial \psi_\alpha}\left(\dot{\omega}_\alpha(\underline{\psi})\tilde{P}(\underline{\psi})\right) = \frac{\partial}{\partial x_i}\left(\frac{\mu_t}{\sigma_t}\frac{\partial \tilde{P}(\underline{\psi})}{\partial x_i}\right) + \dot{\Phi}_{mix}(\underline{\psi};\mathbf{x},t) \tag{2.47}$$

where the first term is the material derivative and the Φ_{mix} represents the mixing model. It should be noted that the Eulerian equation (2.47) can be solved with a Monte Carlo method. It can be solved also with a Lagrangian formulation, which is equivalent to the Eulerian PDF approach and is proven to be second-order accurate. In the hybrid model of RANS-scalar PDF method there is a need to ensure consistency between the Eulerian (CFD grid) and Lagrangian formulations (particle method). The scalar values are represented by each notional particle. As the stochastic particles are transported in the computational domain, control algorithms are used to ensure that those particles behave according to the boundary conditions and are sorted out within the limits of each computational cell [63]. The PDF at a position $\mathbf{x}$ is given in equation (2.48).

$$P(\underline{\psi};\mathbf{x},t) = \frac{1}{N_{tot}}\sum_{p=1}^{N_{tot}} \frac{w^{(p)}}{\bar{w}}\delta(\underline{\phi}^{(p)} - \underline{\psi})\delta(\mathbf{x}^{(p)} - \mathbf{x}) \tag{2.48}$$

where N_{tot} is the total number of particles, $w^{(p)}$ is the weight of each particle and $\bar{w}$ is the mean weight defined by $\bar{w} = \frac{1}{N_{tot}}\sum_{p=1}^{N_{tot}} w^{(p)}$. The modelled PDF equation is then solved stochastically by allowing the particle representations (chemical species) to evolve [64] throughout the domain. The position of each stochastic particle is tracked and is expressed by the relationship found in equation (2.49).

$$dx_i^{(p)} = \left(\tilde{u}_i + \frac{1}{\bar{\rho}}\frac{\partial(\frac{\mu_T}{\sigma_t})}{\partial x_i}\right)dt + \left(\frac{2}{\bar{\rho}}\frac{\mu_t}{\sigma_t}dt\right)^{1/2} dW_i \tag{2.49}$$

where the asterisk denotes each particle's position and dW_i denotes the increment of Wiener process of component i, which is the stochastic process. The increments are Gaussian random variables [20]. The mean velocity and the turbulent mixing values are determined by the RANS finite-volume method, and are used as an input to the PDF approach.

2.5.5 Mixing models and chemical reaction

In PDF methods, the unclosed micro-mixing term which appears due to the effect of molecular diffusion on the composition can be modelled by various proposed mixing models; these include the Interaction by Exchange with the Mean (IEM), modified Curl model, Euclidean minimum spanning tree and few others which can be found in detail in the following mixing model review [67]. The mixing of particles, which is a transport equation in the scalar space ϕ, is expressed by equation (2.50). In this study, the transported joint-PDF is solved without any prior assumption on its shape.

$$d\phi_{\alpha}^{(p)} = \dot{\Phi}_{mix}^{(p)} + S_{\alpha}^{(p)} dt \tag{2.50}$$

The IEM or linear mean-square estimation (LMSE) relaxes the particle compositions towards the local mean composition, which is determined by the notional particles residing in each grid cell. The IEM mathematical expression where each notional particle changes its properties [64, 65] is shown in equation (2.51).

$$\frac{d\phi^{(p)}}{dt} = -\frac{C_d}{2}\frac{\epsilon}{k}\left(\phi^{(p)} - \tilde{\phi}\right) \tag{2.51}$$

The LMSE model is a linear deterministic mixing model, and is continuous in time. The other mixing model is a stochastic one, and is a modified version of the original Curl model to yield continuous PDFs [67]. In this mixing model the probability of a pair of particles interacting with each other in a time interval δt is computed by the equation (2.52).

$$p_{mix} = C_d \delta t \frac{\epsilon}{k} N_{pc} \tag{2.52}$$

The other equations determine the new concentration from the mixing of a random selection of a pair of particles $\phi^{(p)}(t)$ and $\phi^{(q)}(t)$ from the ensemble within each computational cell. The extent of mixing on each mixing event is controlled by the uniformly distributed random number γ which takes values between 0 and 1.

$$\phi^{(p)}(t + dt) = \phi^{(p)}(t) + \frac{1}{2}\gamma\left(\phi^{(q)}(t) - \phi^{(p)}(t)\right) \tag{2.53}$$

$$\phi^{(q)}(t + \delta t) = \phi^{(q)}(t) - \frac{1}{2}\gamma\left(\phi^{(q)}(t) - \phi^{(p)}(t)\right) \tag{2.54}$$

Both IEM and Curl models have advantages and disadvantages [63, 67]. The IEM model preserves the shape of the PDF, whereas with the modified Curl model, the shape is not preserved. In both models the shape of the PDF does not relax into a Gaussian distribution, and according to [63] they do not perform well with high Damköhler numbers as they are non local in composition space. There are numerous desirable characteristics of the mixing models, but three stand out as most essential. These three essential characteristics that the mixing models should satisfy are: 1) the mean scalar quantities should not change after a mixing process, 2) scalar variances should decay at the correct rate, and 3) scalar quantities should remain inside their physical bound limits (e.g. mixture fraction should be between 0 and 1) [63]. In addition, the mixing models should be consistent with the linearity, satisfy the independence principles and should cause the PDF of conserved scalars to relax to a joint normal (Gaussian) distribution in statistically homogeneous systems. They should also respect the notion of locality in composition space [63] because without the locality concept particles are allowed to mix across the reaction zone without burning. The IEM and Curl models satisfy the first three most essential features of mixing modelling, but do not have the other criteria including locality. On the other hand, linearity and independence properties are not satisfied with the EMST but it possesses the first three essential characteristics and localness criteria.

Other key features and limitations of the mixing models are that the IEM is the easiest to implement, but is unable to predict extinction. The modified Curl model performs better than the IEM model, but there are problems when there is moderate extinction. Finally, the EMST model is local in composition space as pairing particles for mixing is more likely to occur for those particles which are closer in the composition space. However, the EMST is more computationally expensive compared to IEM and Curl models [58] and not consistent with linearity. Few studies have been performed to examine the performance of the mixing models in jet flames. It has been found out that EMST mixing model is capable of calculating accurately the burning indexes and mixture fraction variance compared to IEM and Curl mixing models and actually predicts an attached flame (correct flame shape) where the other mixing models do not as Curl model predicts a lifted flame and IEM yields to extinction [68, 69]. Generally, the EMST is resistant to global extinction compared to IEM and Curl model. Moreover, it should be noted that the EMST can also lead to spurious results and that the localness property may not be sufficient to ensure physically realistic prediction [67].

Chemical reactions and the mixing processes change the scalar values of each notional par-

ticle. The S_ϕ denotes the source term in the species ϕ (2.50) equation. This source term represents the radiation for the enthalpy scalar due to soot particles and gas-phase species emissivity, and the source terms of the each size class of soot particles. Soot source terms are mainly the following mechanisms: nucleation, surface growth, oxidation and coagulation processes. The transported PDF method alleviates the problem closure of the source terms of chemistry, soot and radiation emission (due to the averaging procedure) and can be computed directly without any closure assumptions. In the end, the particle means in each cell are time-averaged over 1000 iterations to reduce statistical error [20]. Normally, the molecular diffusion of species and particles in the scalar space are represented by a mixing model. However, soot particles have negligible molecular diffusion, and much smaller mixing compared to the gas-phase species. This Lagrangian formulation is assumed to be with unity Lewis numbers where all the species, enthalpy and each size class of soot particles have the same mixing. To remedy this problem the turbulent mixing of soot particles is reduced by a hundredfold compared to the species mixing. This crude approximation method has been used by [20] where the soot particle representations are mixed in a much slower rate than the gas species. The chemical reaction source terms of all scalars are described by equation (2.55).

$$\frac{d\phi_\alpha^{(p)}}{dt} = \frac{\dot{\omega}_\alpha(\underline{\phi}^{(p)})}{\rho(\underline{\phi}^{(p)})}, \qquad \alpha = 1, ..., N_{sp} \tag{2.55}$$

There are other PDF approaches in the literature, as discussed previously. With the particle approach (Monte-Carlo) the PDF could be Eulerian for a fixed number of particles in the middle of a computational cell, or Lagrangian where the particles move freely. Other types of PDF include using the Eulerian PDF approach with stochastic fields. With this method a stochastic term is included in the conservation equations and can be implemented into CFD codes with less difficulty compared to particle methods [5].

2.5.6 CFL condition, particle control and time averaging method

The hybrid CFD/Lagrangian model is applied in this thesis; several parameters need attention. One consideration of the PDF approach is the selection of the time-step. The problem arises when the CFD solver uses a global time-step (dt) for the flow field, which may not be suitable for an adequate representation of the particle field. Usually the flowfield can be solved in larger time steps than the chemical reactions and mixing process. As such, a new time step (dt^{pdf}) is

defined for solving the PDF approach. The following relationship defines the number of cycles that the PDF is performing to match the global time-step. The number of cycles essentially splits the PDF or the original CFD time step into smaller steps through the fractional method in order to capture the effects at small time scales.

$$N_{pdf} = \frac{dt}{dt^{pdf}} \tag{2.56}$$

Two time step criteria have to be satisfied in order to compute the appropriate PDF time step dt^{pdf}, and therefore the number of cycles that the PDF is going to perform. The first criterion to satisfy is that the PDF time step should not be higher than the local turbulent time scales to avoid false diffusion. The shorter PDF time step will ensure that sufficient mixing is performed [58]. The second criterion requires that the particle displacement is not large enough to skip any computational mesh cells. This is achieved by introducing a Courant-Friedrichs-Levy (CFL) condition where a convection number and diffusion number are introduced, and should be less than 1. The equation of the PDF time selection is shown in equation (2.57) from the global maximum of the convection, diffusion and turbulent time scales [62].

$$N_{pdf cycles} = max\left[\left(dt\frac{u_i}{c_i dx_i}, \quad dt\frac{D_{\text{eff}}}{df_i dx_i^2}, \quad dt\frac{C_d}{c_{mix}\tau_{min}}\right)\right] \tag{2.57}$$

The convection number c_i and diffusion number df_i are assigned with a value less than unity - 0.5 in this study - and c_{mix} is the mixing number and assigned with a value 0.25 and the $\tau_{min} = k/\epsilon$ is the minimum mixing turbulent time scale which is determined over all computational cells. An alternative is the local time stepping where a specific time step is assigned according to the CFL conditions in each cell reducing the computational effort.

The PDF formulation receives an input from the finite volume CFD code. The CFD solver supplies the PDF with the mean velocities and turbulent quantities or turbulent mixing time scale. The mean quantities are determined in the middle of each of computational cell. As such, the mean velocities are interpolated from the cell's centre to the current location of the notional particle. Several interpolations are proposed to determine a particle's velocity, such as the quadratic interpolation, but a simple linear interpolation is performed in this study [62].

Moreover, the Eulerian PDF is equivalent to the Lagrangian PDF due to the equivalence of Fokker Planck transport equation with Langevin stochastic equations [70]. This indicates that in the Lagrangian approach, an ensemble of notional particles that move and change their

composition across the domain will exhibit the same statistics as the transported Eulerian PDF approach [70]. A Monte-Carlo algorithm allows us to use both Eulerian and Lagrangian approaches. However, with the Lagrangian approach, the stochastic equations are solved only by Monte-Carlo methods; finite differencing schemes are used to solve the Eulerian approach. When the dimensionality increases in the transported PDF equation, the computational time is increased exponentially by using finite differencing; by using Monte-Carlo, it is only increased linearly.

The stochastic particles are displaced inside the computational domain, and after a time interval they are reallocated into different positions. New particles are introduced at every time step at random positions from the inlet boundary condition. These particles become unsorted (the particles need reindexing by their current host cell) as a result of advection in the physical domain, and are sometimes displaced outside the computational boundaries (e.g. symmetry, wall). Also, the mass of particles that exists in each computational cell is not preserved. Thus, particle tracking and control algorithms are employed in the PDF in order to be consistent with the Eulerian CFD code. These particle controls and tracking are explained below [62].

An equal number of notional particles were uniformly distributed across the domain. However, some small cells might contain a low number of particles and the larger cells might contain a significant number of particles. The ensemble averaging will then introduce a wasted effort in the larger cells, and will create significant statistical error for the small cells. This problem is overcome by a particle weight control and imposing a number of particles per cell [70]. To ensure the uniform distribution of particles, initial weight properties are applied to the particles.

Assuming that the total number of notional particles in the whole domain is N_{tot}, the following weight can be attributed to each notional particle p in a single cell k [70]:

$$w^{(p)} = \frac{1}{N_{pc}} \frac{M_k}{p_{mass}} \tag{2.58}$$

where M_k is the mass of fluid which is contained inside a computational fluid cell, p_{mass} is the mass of the fluid that is represented by each particle and N_{pc} is the number of particles per computational cell. It should be noted that the mass of fluid represented by a notional particle is defined as $p_{mass} = \frac{M_{tot}}{N_{cells}}$ where M_{tot} is the total fluid mass in the entire computational domain and N_{cells} is the total number of mesh cells in the whole domain. To control both weights and particle number in the domain, the following procedure is adapted to this methodology. To

control the weight splitting and clustering of the notional particles, algorithms are applied by modifying their number in each cell [70, 62]. The following two steps are applied.

- The notional particles are moving through the computational domain. The number of particles in each cell cannot be held constant and will vary. Thus, the particles are initially sorted out and their number is recorded at every time step in each cell. The total number of particles in each cell is counted and is compared to the targeted fixed number of particles per cell (N_{pc}). If the number of particles does not match the targeted number of particles then splitting or clustering of particles is performed.

- Within a cell, the splitting criteria is when the counted number of particles is less than the targeted number of particles. This splitting or cloning technique takes one notional particle and splits it into two particles while the representations of species composition and other scalar quantities remain intact. Only their weight is divided by two. The particles will keep splitting until they match the targeted number.

- On the other hand, within a cell, two particles are combined when the counted number of particles is higher than the targeted number of particles per cell. The particles are combined and their weights are added to form a new single particle. However, the representations carried by the two notional particles before clustering are different. From this merging, the representations of the first or second particle will be chosen randomly to be transferred in the new formed particle. The weights of each particle in each computational cell are modified to conserve the mass due to the combination of particles [70].

The PDF exports the ensemble Favre averaged quantities $\tilde{\phi}$ from the particle representations; these need to be time-averaged in order to reduce any statistical errors without the need to increase the number of particles and to compute the actual stationary turbulent reacting flow. The following time-averaging is performed on a mean field quantity $\bar{\phi}$ as it is found in [71]:

$$\bar{\phi}^{t+1} = \left(1 - \frac{1}{N_{PDF}}\right)\bar{\phi}^{t} + \frac{1}{N_{PDF}}\tilde{\phi}^{t+1} \tag{2.59}$$

The N_{PDF} is specified with constant values to reduce the statistical fluctuations in each computational cell avoiding an increase in the number of particles per cell [71]. $\bar{\phi}$ represents the time-averaged mean quantity and the $\tilde{\phi}$ represents the ensemble average quantity.

The number of notional particles assigned to each cell plays an important role in determining the statistical properties with accuracy. The Monte Carlo algorithms suffer from statistical

error, which is related to the number of particles per cell as can be seen at scales in the following expression: $\frac{1}{\sqrt{N_{pc}}}$ [66]. N_{pc} is the particle number per cell. Statistical error is not introduced by the dimensionality of the PDF, but by the number of particles per cell.

2.5.7 Detailed chemistry and mechanism reduction

The computation of the chemical source terms is often a difficult task, especially in turbulent reacting flows. Its computation is straightforward in laminar flames, but not with turbulent flames due to the high non-linearity (see at the end of section 2.5.3). Combustion models are needed to overcome this problem. The PDF methods are ideal as the source terms appear in close form and can be used to predict flames of low Damköhler numbers where the finite-rate chemistry effects become important. In order for these models to be applicable, gas-phase chemical mechanisms are needed. These chemical libraries contain a great number of species and chemical reactions with their respective Arrhenius parameters [61].

All hydrocarbon fuels can produce soot particles via a combustion process. In laboratory scale experiments it is common to use simple hydrocarbon fuels due to their relatively simple chemistry and sooting tendency. CH_4 fuel is the simplest hydrocarbon fuel however, it is not ideal for soot modelling because of the low tendency to form soot. As such, other fuels, such as C_2H_4 or C_3H_8, are often preferred.

Detailed chemistry models are infeasible in complex simulations with turbulent flows and are usually applied only in simplified physical models or in laminar cases. Even for a simple hydrocarbon fuel such as CH_4, a significant number of species and elementary chemical reactions are needed to successfully describe the structure of the flame. Those detailed chemistries could be up to 53 species and 325 chemical reactions for GRI 3.0 - but to describe complex hydrocarbon fuels such as an aviation fuel, the requirement could reach 300+ species and 1000+ chemical reactions [4]. To make numerical investigation feasible, aviation fuels are usually expressed as several simpler fuel components to create an overall mixture with similar physical and chemical properties. These fuels are called surrogates. Even with surrogates, a detailed chemical mechanism is needed. Therefore, reduced chemical mechanism is an attractive choice to maintain the same level of accuracy of those gas-phase mechanisms with fewer species and chemical reactions.

A way to reduce the computational effort of a combustion process is to reduce the total number of chemical reaction steps of a gas-phase mechanism by identifying which species and

chemical reactions are unimportant and do not affect the overall results. Usually skeletal mechanisms are produced by identifying reactions with minimum contribution, and omitting them from the mechanisms. Other methods of chemical reduction include singular perturbation theory, direct relation graph method, RCCE, CSP and ILDM. Each method is different and can be divided into categories of global or local chemistry reduction. The Intrinsic Low-Dimensional Manifold (ILDM) is a rigorous chemical reduction mechanism in which for a canonical reactor, the ILDM model corresponds to a batch reactor and the transport effects are not taken into account [2]. RCCE (Rate-controlled-constrained-equilibrium) is a systematic method for reducing the chemical mechanism. The chemical reduction mechanisms are usually validated by using a full-detailed direct integration chemical mechanism on the same test cases.

2.6 Soot formation

In theory, the particulate matter belongs to the multiphase flow category because of the two distinct phases involved (gas-solid). Solid particles are dispersed within a continuous phase (gas fluid), with a characteristic size and shape. The Stokes number is the ratio of the characteristic response time of the fluid and the characteristic response time of the particle. Particles with stokes number much less than 1 will follow the streamlines of the flow. This assumption is acceptable for small size particles (such as soot particles of nanometre size) [72] found in the laboratory sooting flame experiments. As such, due to the very low Stokes number, the drag forces of each solid particle are negligible and can be omitted. The solid particles in this case follow the streamlines of the fluid and can be considered as part of the single gas-phase. It should be noted, the soot particle trajectories will be different if thermophoretic effects are included. The thermophoretic velocity is independent of particle size, and can be used directly to compute a different motion of particles within the continuous phase. Despite the inclusion of thermophoretic effects, the solid particles can still be treated as part of the gas-phase. However, in the case of inertial particles with large Stokes numbers, particles should be treated with a multiphase approach by adding another dimension to the PBE - a velocity vector - describing the distribution over particle velocities as each solid soot particle exhibits different drag force. Another, problem of the multiphase approach is the phase boundaries of the dispersed phase within the continuous phase that interact with each other. An example is for inertial particles within dense flows where two-way exchange of momentum between the continuous and dispersed

phase should be considered or any other mass or energy exchange [72].

Soot formation is commonly treated as a single phase flow due to non-inertial effects. However, the combination of those two phases (i.e. soot and gas-phase) is inherently two-way coupling. Regions of high concentration levels of soot particles inside the flame significantly affect the density and temperature of the mixture through strong radiation and feedback effects due to heterogeneous reactions on particle's surface area. Gas-phase species are absorbed by the solid soot particles to grow or to reduce in size. One-way coupling, which does not change the gas velocity or the temperature fields, is proved in a sooting turbulent study [19] to be less accurate in comparison with a two-way coupling of soot and gas-phase chemistry.

Soot formation has been studied intensively over the past few years. Many experimental and numerical investigations have been conducted, contributing to our knowledge of soot formation and identifying important mechanisms. The dominant soot formation processes are found throughout those investigations, and are given in the Figure below.

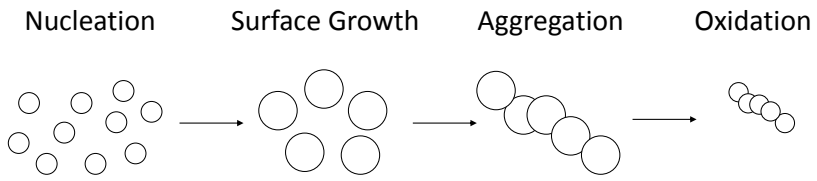

Figure 2.5: Soot formation history

According to the detailed chemistry that was mentioned previously, aromatic formation or polycyclic aromatic hydrocarbon (PAH) is produced from fuel combustion. By the continuous addition of other aromatics or alkyne species such as C_2H_2, heavier hydrocarbon species are formed; these are called PAHs. These PAHs are in planar form, and stick to each other to form dimers, trimers and so on. Initially, these PAHs are in the gas-phase until too many carbon atoms with a minor number of hydrogen species are stuck together. This transition, due to their heavy weight, eventually forms a spherical solid soot particle of approximately 1 nm consisting of around 100 carbon atoms [2]. The shape of the incipient soot particle is assumed to be spherical. There are different hypotheses of soot nucleation, including ionic species, polyacetylenes and the aforementioned PAH physics. The most widely accepted theory of soot inception is the PAH-based concept. After the inception of a soot particle, its size increases by surface growth mechanisms. This surface growth mechanism is a heterogeneous reaction because the solid soot's particle surface reacts with several gas-phase species, in this case C_2H_2. Another form of growth is the condensation mechanism, in which PAH species

and especially pyrene collide with the soot particle resulting in an increase in size. Moreover, these particles grow by the collision of two or more soot particles. This is called coagulation or aggregation. There is confusion about the terminology of these two mechanisms. Assume that two soot particles of equal spherical volume size collide with each other. If the result of this collision is a single spherical particle twice the volume of the original particles, then this is called coagulation. If the result of this collision is a cluster particle, with fractal shape, then this is called aggregation. The coagulation and aggregation mechanisms are described by the dynamics of soot particles (Smoluchowksi equation [72]). For the coagulation process the number density of soot particles is reduced, but the volume or mass remains constant.

More specific, the co-annular diffusion flame configuration is a widely performed experiment by many researchers (see section 5.1). From these studies the main soot formation zones have been identified across the entire length of the flame. According to [11], the evolution of soot's morphology in a co-annular diffusion flame proceeds as follows. On the lower part of the flame, close to the burner and towards the wings of the flame, near-spherical nucleus soot particles are observed. Nucleation is the dominant mechanism is this zone. The incipient soot particles are convected upwards, where growth mechanisms start to dominate. The surface growth and coagulation mechanisms are concurrently taking place, resulting in an increase of the particle's size. It is observed that beyond a certain size limit of the soot particles, aggregation dominates coagulation. Further upwards, towards the tip of the flame, the soot particles enter a region where oxidation is dominant. Depending on the oxidation's strength in that region and the growth's strength in the previous region, three sooting flame types could appear. If the soot particles are completely oxidised, then the flame does not emit smoke. If the oxidation rates are not sufficiently high to fully oxidise them, though, then soot escapes from the flame tip.

The soot kinetics comprise nucleation, surface growth, oxidation and coagulation. The nucleation term is usually assumed to generate particles of the minimum possible sizes (1 nm nuclei diameter). Unfortunately, particle size measurements of that small range are problematic, and it is not even possible to distinguish any size ranges of the nuclei due to the insufficient resolutions of the measuring devices. Subsequently, growth and coagulation of these particles increase their sizes at a sufficient level for measurement by a device [73].

Unfortunately, despite this theory, our knowledge of soot formation is still not complete; there are still many uncertainties in understanding the full kinetics of soot formation, especially nucleation. The soot models are divided into empirical, semi-empirical and detailed models.

2.6.1 Modelling of soot formation

Empirical soot models are formulated by reaction rate constants of the soot kinetics that are correlations of experimental data [74]. The advantage of these soot models is that the agreement can be excellent with relatively simple chemistry and reduced computational effort. The drawback is that these soot models have limited applicability to other types of combustion modes, fuel and pressure conditions. The semi-empirical models solve the rate equations of soot formation with some experimental input [74]. Finally, the detailed soot models solve the rate equations of soot formation from the elementary state, keeping any experimental input to a minimum. This is the best model to generate a global soot model to work under different conditions. The majority of the soot models are semi-empirical and acetylene-based. Detailed models are represented primarily by PAH-based soot models. Examples of semi-empirical and detailed models are shown next.

The semi-empirical model of Lindstedt [75] is a simplified soot model with a monodispersed description in the free molecular regime for particle dynamics. This model is widely used in soot studies, producing accurate results but lacking the insight of a complete particle-size-distribution. A similar model to Lindstedt but with slightly modified rates is used by Fairweather [76]. These semi-empirical models belong to the category of acetylene-based structures, and do not need very detailed chemistry with aromatic formation. Only C_2H_2 and in some occasions benzene are required from the gas-phase. More semi-empirical studies can be found in a laminar co-flow non-premixed flame by Guo et al. [77]. This paper is very important to this study, as the authors simulate the same type of flame and investigate important effects such as fuel preheating and radiation very close to the burner. Table 2.4 is an example of the chemical reactions encountered in monodispersed models using C_2H_2 species as the precursor species of soot particles.

			$k = A_{factor}T^n e^{-\frac{E_\alpha}{RT}}$		
No.	Soot mechanism	Chemical reaction	A_{factor}	n	E_α
1.	Nucleation	$C_2H_2 \rightarrow 2C_s + H_2$	$0.63 \cdot 10^4$	0	21,000
2.	Surface growth	$C_2H_2 + nC_s \rightarrow (n+2)C_s + H_2$	$0.75 \cdot 10^3$	0	12,100
3.	Oxidation	$C_s + \frac{1}{2}O_2 \rightarrow CO$	$0.12 \cdot 10^6$	$\frac{1}{2}$	19,800
4.	Oxidation	$C_s + OH \rightarrow CO + H$	0.36	$\frac{1}{2}$	0

Table 2.4: Common soot formation chemical reactions [55, 78]

Detailed chemical gas-phase mechanisms and detailed soot modelling are used by Frencklach

et al. [79]. Their model contained gas-phase chemistry that includes PAH formation up to pyrene ($C_{16}H_{10}$), the heaviest hydrocarbon species in this mechanism, that acts as a soot precursor. Nucleation is defined as the collision of two $C_{16}H_{10}$ molecules; surface growth is more complex and it is described by 5 or 6 elementary reactions using HACA principles as defined by [80]. Oxidation is described by O_2 and OH species where the OH reaction is dependent on the gas kinetic theory of OH particles to the surface of soot particles. The coagulation equation is size-dependent to soot particle size. Another detailed soot kinetics mechanism is used by Smooke et al. [49]. Their mechanism differs from the ABF soot mechanism in several ways. Their soot inception is based on simple quasi-steady state expressions dependent on the molecular concentration of several species, including C_2H_2, H_2, C_6H_6 and C_6H_5. With these inception rates, the soot precursors $C_{10}H_8$ and $C_{10}H_7$ radical PAHs are computed in order to avoid any uncertainties in computing these heavy PAHs through the gas-phase chemistry (also reducing the computation effort required). Unfortunately, this model initially underpredicted the nucleation rate; according to [81]. Therefore, the nucleation rate is enhanced by a factor of 8 to improve the prediction. The surface growth that is used is the one from Harris and Weiner as stated in [49], modified by a factor of 2. The oxidation rates used are somewhat more complicated than ABF. In [49] the same OH oxidation rate is used, but the O_2 oxidation is according to the Naggle-Strickland Constable experiment [82]. The HACA mechanism found, in [79], is shown in table 2.5 illustrating a full set of growth and oxidation surface reactions that is commonly found in PAH-based soot models.

		$k = A_{factor} T^n e^{-\frac{E_\alpha}{RT}}$		
No.	Surface reactions	A_{factor} $m^3/(kmol\ s)$	n	E_α $J/kmol$
1.	$C_s - H + H \rightarrow C_s^{\cdot} + H_2$	4.17×10^{10}		54392
2.	$C_s - H + H \leftarrow C_s^{\cdot} + H_2$	3.9×10^9		46024
3.	$C_s - H + OH \rightarrow C_s^{\cdot} + H_2O$	1.0×10^7	0.734	5983.12
4.	$C_s - H + OH \leftarrow C_s^{\cdot} + H_2O$	3.68×10^5	1.139	71546.4
5.	$C_s^{\cdot} + H \rightarrow C_s - H$	2.0×10^{10}		
6.	$C_s^{\cdot} + C_2H_2 \rightarrow C_s - H + H$	8.0×10^4	1.56	15899.2
7.	$C_s^{\cdot} + O_2 \rightarrow 2CO + products$	2.2×10^9		31380
8.	$C_s - H + OH \rightarrow CO + products$	reaction probability = 0.13		

Table 2.5: HACA mechanism

The HACA mechanism is illustrated in the table 2.5. $C_s - H$ is saturated carbon atoms with joined hydrogen atoms, and the $C_s^{\cdot}$ symbol is dehydrogenated carbon atoms [79]. Other

similar HACA mechanisms are used by various authors with different reaction rates. The HACA mechanism is successfully employed in laminar premixed flames and non-premixed flames by [79, 83] respectively. Normally, the HACA mechanism is observed for PAH species (e.g. C_6H_6) that grow up to $C_{16}H_{10}$ molecules and become soot precursors. The same HACA principles are applied to the surface of the soot particles because their structure is similar to PAHs [83].

According to [81] a sectional model originating in the MAEROS program [84] is used to solve the particle size distribution. The sectional model solves the particle size distribution of spherical particles in free molecular regime and does not take into account aggregate formation (fractal shape). Moreover, an additional transport equation representing the number or the size of the aggregates could be solved as it is mentioned in [23], and thus the structure of the soot particles after the aggregation process. This methodology was made successful by applying soot kinetics, and did not use the usual chemical mechanism of [79] but rather a chemical gas-phase mechanism of [85] with some new modifications from the original model, as shown in [85]. This mechanism predicts soot precursor formation up to five-ring aromatics in methane and ethane-fuelled flames. Recently, the same model with some modifications has been extended to two other studies of an incipient smoking and smoking flame in [86]. In [86] three cases of laminar diffusion flame type - the non-smoking, incipient smoking and smoking flame - are examined with a detailed sectional model and no modifications between the cases.

The difference between incipient and smoking flames is that the former releases soot particles that are formed in the annulus region of the flame, which are large enough to survive the oxidative attack and are emitted though the flame tip; in the latter, the smoking flame emits from the flame tip a significant larger amount of soot particles which are formed in the entire flame region [8] because soot oxidation is not strong enough to destroy them.

The prediction of soot oxidation is a daunting task, as most smoking-type flames cannot be predicted accurately with the normal oxidation mechanisms that exist in the literature. A study managed to reproduce the smoking characteristics (that is, soot emission) with an acetylene-based soot model and a 2TEM approach in [74]. The oxidation rates are obtained from experimental studies. Unfortunately, with those oxidation rates no soot is emitting from the flame tip in the smoking flame, or in the incipient one. Thus, in this study those rates are modified by applying a linear increase of the collision efficiency of OH rate. A more successful implementation is applied in a different study, [53], where the correction factors are incorporated and listed in equations (2.60)-(2.63); these are dependent on local temperature to

reduce the magnitude of the oxidation rates of O_2 and OH [53]. In a more recent study [86] the smoking effects are successfully captured by modifying the surface reactivity parameter of the HACA mechanism of soot particles, which is also dependent on maximum temperature and local temperature parameters.

$$f_{O_2} = \frac{1}{1 + e^{-(T-1650)/80}} \tag{2.60}$$

$$f_{OH} = \frac{1}{1 + e^{-(T-1675)/70}} \qquad T \geq 1675K \tag{2.61}$$

$$f_{OH} = \frac{1}{1 + e^{-(T-1675)/50}} \qquad 1600K < T < 1675K \tag{2.62}$$

$$f_{OH} = \frac{0.1824}{1 + e^{-(T-1600)/85}} \qquad T \leq 1600K \tag{2.63}$$

The majority of numerical studies model soot formation with a two transport equation or a six transport equation approach (MoMIC). The two transport equations approach (semi-empirical) solves the number density and mass fraction of soot particles as shown in equations (2.64) and (2.65).

$$\frac{\partial\left(\rho N_s\right)}{\partial t} + \frac{\partial\left(\rho u_i N_s\right)}{\partial x_i} = -\frac{\partial\left(\rho V_{s,i} N_s\right)}{\partial x_i} + \dot{\omega}_{N_s} \tag{2.64}$$

$$\frac{\partial\left(\rho Y_s\right)}{\partial t} + \frac{\partial\left(\rho u_i Y_s\right)}{\partial x_i} = -\frac{\partial\left(\rho V_{s,i} Y_s\right)}{\partial x_i} + \dot{\omega}_{Y_s} \tag{2.65}$$

This is a semi-empirical model that soot formation is usually represented with acetylene-based soot models. The second and third terms of equation (2.65) are the convection and diffusion of soot particles in the physical domain. The diffusion velocity of soot particles $V_{s,i}$ includes the ordinary diffusion velocity (which is essentially close to 0) and thermophoretic velocity. The last source terms include the following terms in equations (2.66) and (2.67).

$$\dot{\omega}_{N_s} = \frac{2}{C_{min}} N_A k_1(T)[C_2H_2] - 2C_\alpha d_p^{\frac{1}{2}} \left(\frac{6k_\beta T}{\rho_s}\right)^{\frac{1}{2}} (\rho N_s)^2 \tag{2.66}$$

$$\begin{aligned} \dot{\omega}_{Y_s} = \quad & 2k_1(T)[C_2H_2]M_s + 2k_2(T)A_T[C_2H_2]M_s \\ & - k_3(T)A_T[O_2]M_s - k_4(T)A_T[OH]M_s \end{aligned} \tag{2.67}$$

The first term in equation (2.66) is the nucleation mechanism which generates new particles into the system and the second term is the coagulation term which destroys the number of soot particles in the system. In equation (2.67) the mass fraction of soot particles is added to the system by nucleation and surface growth and the particle mass is removed by O_2 and OH oxidation. Also, the reaction rate constants (k_n) of each process is set according to the number of the chemical reaction shown in table 2.4. The total surface area (A_T) of soot particles is approximated in equation (2.68) by using the first two moments as shown in [75].

$$A_T = \pi \left(\frac{6}{\pi} \frac{Y_s}{\rho_s N_s} \right)^{\frac{2}{3}} (\rho N_s) \tag{2.68}$$

A detailed soot model that incorporates PAH-based chemistry is solved with six transport equations. The transport equation of the moments that is described in the MoMIC approach is shown in (2.69).

$$\frac{\partial (\rho M_r)}{\partial t} + \frac{\partial (\rho u_i M_r)}{\partial x_i} = -\frac{\partial \left(\rho V_{s,i} M_r\right)}{\partial x_i} + \dot{\omega}_{M_r}, \qquad r = 0, 1, 2, ..., 5 \tag{2.69}$$

The source term of the MoMIC approach is the sum of the following soot mechanisms in each respective moment. It should be noted that if the MoMIC approach is set to solve only the first two moments (M_0 and M_1) then the mathematical formulation will be exactly the same with the 2TEM approach.

$$\begin{aligned}
\dot{\omega}_{M_0} &= R_{nuc,0} - R_{coag,0} \\
\dot{\omega}_{M_1} &= R_{nuc,1} + R_{sg,1} \\
\dot{\omega}_{M_2} &= R_{nuc,2} + R_{sg,2} + R_{coag,2} \\
\dot{\omega}_{M_3} &= R_{nuc,3} + R_{sg,3} + R_{coag,3} \\
\dot{\omega}_{M_4} &= R_{nuc,4} + R_{sg,4} + R_{coag,4} \\
\dot{\omega}_{M_5} &= R_{nuc,5} + R_{sg,5} + R_{coag,5}
\end{aligned} \tag{2.70}$$

More details about the formulation of each rate in the higher moments can be found in [80, 87]. It should be noted that in the 0^{th} moment the source rates are dependent only on nucleation and coagulation mechanisms. In the first moment the mass is added only by nucleation and surface processes such as surface growth, condensation and oxidation. In the rest of the moments all the mechanisms are contributing. The following equations are obtained

from [80, 87] which are used in the MoMIC approach to determine each rate in their respective moment number. These are the MoMIC equations which will be applied in this thesis [80, 87]

$$R_{nuc,r} = \frac{1}{2}\sum_{i=i_0}^{\infty}\sum_{j=j_0}^{\infty} 2.2\left(\frac{\pi k_B T}{2\mu_{i,j}}\right)^{\frac{1}{2}}(d_i+d_j)^2(m_i+m_j)^r N_i^{PAH} N_j^{PAH} \qquad r=0,1,..5 \quad (2.71)$$

$$R_{C_2H_2,r} = k_6[C_2H_2]\alpha_f \chi_{C_{soot}} \pi C_s^2 \sum_{l=0}^{r-1}\binom{r}{l} M_{l+2/3} 2^{r-l} \qquad r=1,2,..5 \quad (2.72)$$

$$R_{O_2,r} = k_7[O_2]\alpha_f \chi_{C_{soot}} \pi C_s^2 \sum_{l=0}^{r-1}\binom{r}{l} M_{l+2/3} (-2)^{r-l} \qquad r=1,2,..5 \quad (2.73)$$

$$R_{OH,r} = k_8[OH]\left(\frac{\pi k_B T}{2m_{OH}}\right)^{\frac{1}{2}} \pi C_s^2 \sum_{l=0}^{r-1}\binom{r}{l} M_{l+2/3} (-2)^{r-l} \qquad r=1,2,..5 \quad (2.74)$$

The equation (2.71) is the nucleation term where the formation of soot particles were assumed by PAH coagulation. Two PAH molecules collide with collision diameters d_i and d_j forming a dimer which is assumed to be the incipient soot particle. The equation (2.71) describes the rate of all possible collisions to form dimers of a variety of PAH molecules with different sizes. However, according to [79] the nucleation of soot particles is assumed to be initiated by the collision of pyrene species. Assuming that $C_{16}H_{10}$ is the only precursor species the equation (2.71) is greatly simplified as the double summations are dropped (see equation (4.5)). The equations (2.72) -(2.74) are part of the contributions to the surface growth rate R_{sg} where mass is added through the C_2H_2 species. The reaction rates k_6 and k_7 are determined from the Arrhenius expression and their respective constants found in table 2.5 whereas k_8 is the collision efficiency of the OH species to the surface of soot particles. The C_s is a constant parameter and represents the incipient soot diameter.

Many numerical studies in laminar and turbulent sooting flames have used a variety of soot kinetics. Currently, there are no universal soot kinetics that can be applicable to any test case. Therefore, an appropriate selection of surface and nucleation kinetics is essential for computing the correct PSD, total number density and the volume fraction of soot particles. Most of the time, the kinetics are determined by experiments where the surface and coagulation rates are

extracted. However, those rates are extracted from experiments of different conditions that may not be suitable for an application to different experiments. As such, some mechanisms in numerous numerical studies are modified from their original versions to match or obtain better agreement with experimental results.

An example is the nucleation mechanism, which cannot be measured directly by an experiment as it is difficult - nearly impossible - to observe and identify due to the small size of the incipient particles and experimental limitations. Many numerical studies commence particle formation with spherical shape at approximately 1 or 1.24 nm diameter, with 60 or 100 carbon atoms respectively, in a single soot particle [75, 78]. Similarly, several other studies modified Lindstedt's model by assuming the incipient particles to be 2.4 nm diameter with 700 carbon atoms [53] and different activation energies. In [88] the nucleation rates are assumed to generate soot particles of approximately 12 nm diameter with 90,000 carbon atoms. The nucleation mechanism is of primary importance as it greatly and explicitly affects the magnitude of the PSD and total number density, and implicitly affects the soot volume fraction where surface growth process are dominant. The nucleation rates mentioned are for an acetylene-based soot model where the 2TEM approach is employed to obtain the number density and mass fractions of soot particles. Even PAH nucleation, which is closer to reality and widely accepted throughout the scientific community, seems to be incomplete; PAH nucleation commonly uses $C_{16}H_{10}$ [83] as the only precursor species, whereas some recent studies attempt to use more than one PAH species to form nucleation. Despite nucleation rates, another example is the coagulation rate as stated in [89]; it is usually determined by an experiment using an inverse procedure to extract the necessary information. This information is very difficult to obtain due to the interference of all the simultaneous soot formation processes inside the flame, prohibiting observation of the optical equipment. As such, sometimes even the coagulation rate is modified when is extracted by the experiment [78].

2.6.2 Soot kinetics for PBE

The polydispersity of soot particles is accounted for via the discretised PBE such as the sectional model of Smooke et al. [49]. Nucleation, surface growth and oxidation rates are the soot kinetics that are used via the PBE to solve the complete PSD of soot particles. The rates of each kinetic mechanism are presented below along with their respective irreversible chemical reactions.

$$B_0 = \frac{2N_A k_1 [C_2H_2]}{C_{min}} \tag{2.75}$$

$$G(v)_{C_2H_2} = \frac{2k_2 P_{C_2H_2} A_s}{\rho_s} \tag{2.76}$$

$$G(v)_{O_2} = \frac{120 \left[\frac{k_\alpha P_{O_2} \chi_1}{1+k_z P_{O_2}} + k_b P_{O_2} (1-\chi_1) \right] A_s}{\rho_s} \tag{2.77}$$

$$G(v)_{OH} = \frac{\frac{167 P_{OH}}{\sqrt{T}} A_s}{\rho_s} \tag{2.78}$$

$$G(v)_O = 0.5 \; k_3 A_s P_O \tag{2.79}$$

The set of kinetics above was proven to be the most successful using the PBE, and is a combination two studies. The nucleation is originally used in the 2TEM approach found in [53] without any coagulation term. This nucleation expression, without any destruction terms to reduce the number density of particles, proved to be quite accurate in comparison with the experimental results. The surface rate are expressed according to the sectional model of Smooke et al. [49, 81], which in turn obtained these surface rates from original experimental studies.

The nucleation expression based on C_2H_2 is the most widely used in practise, as the PAH theory usually require huge gas-phase chemical mechanisms that are not feasible for a turbulent flame simulation. This expression is denoted for a variety of minimum carbon atoms in an incipient soot particle (C_{min}), where the minimum size of soot particles is assumed prior to the computation. The other variable is the nucleation rate k_1, which is defined with an Arrhenius rate expression and is a function of temperature and molar concentration of C_2H_2 species [53]. In this thesis, the minimum carbon atoms, pre-exponential factor and activation energy constants are found in [53].

$$k_1 = 1.7e^{-7548/T} \tag{2.80}$$

The surface growth mechanism is found in [49] where the reaction rate constants are obtained from the measured growth rates of the laminar premixed flame experiment of Harris and Weiner [90]. This surface growth rate is first-order, and is proportional to that of C_2H_2 species. An

activation energy of 31.8 kcal/mole is used, leading to the following growth rate below [81, 49] in SI units:

$$k_2 = 470e^{-16{,}004/T} \tag{2.81}$$

The other surface mechanism is the oxidation, which reduces the size of soot particles. The two major species that have been identified through experiments [82, 91] are the O_2 and OH species. The importance of the O_2 contribution to oxidation processes was found through a series of non-flame experiments in [82]. An oxidiser jet consisting of oxygen or a nitrogen/oxygen mixture struck the surface of a fixed graphite rod. The oxidation rates are determined from the surface corrosion on the graphite rod through the formulation of a mathematical expression with several reaction rates, themselves functions of temperature. These can be seen in [82] and in equation (2.82). The last oxidation rate is by radical oxygen shown in equation (2.83). Further details about this oxidation rate can be found in [77].

$$\begin{aligned} k_A =& 20e^{-30{,}000/RT} \\ k_B =& 4.46 \cdot 10^3 e^{-15{,}000/RT} \\ k_T =& 1.51 \cdot 10^5 e^{-97{,}000/RT} \\ k_z =& 21.3e^{4{,}100/RT} \\ \chi_1 =& \left(1 + \frac{k_T}{k_B P_{O_2}}\right)^{-1} \end{aligned} \tag{2.82}$$

$$k_3 = 55.4\ T^{-\frac{1}{2}} \tag{2.83}$$

In early studies of soot formation, O_2 was thought to be the major species for soot oxidation. However, another oxidation mechanism has been found to be equally and even more important which is proportional to the mole fraction of the OH. The importance of OH species and its oxidation rates are determined by laminar premixed flame experiments found in [91]. According to [91], the OH species is found to be the primary oxidant; the O_2 has been found to be secondary. The order of importance of OH and molecular species is determined according to their contribution to the soot oxidation mechanism. The oxidation rate of the OH species is physically represented as an oxidative attack where OH molecules collide at the surface of soot

particles, where the OH molecules are reacting with soot and reduce their size. The mathematical expression comes with an estimated collision efficiency between 0.28-0.13 [91] because only a fraction of OH molecules collide successfully. There is a third oxidation mechanism that is proportional to the radical oxygen. The third oxidation mechanism is of lesser importance than the previous two, and it can be found in several numerical studies such as [53].

According to the numerical soot formation modelling found in [53], coagulation is not considered due to the negligible contribution to the number density of particles. The coagulation mechanism is omitted according to the observations in [11] where the total number density of soot particles is measured to be almost constant in the growth region of the flame. Coagulation is a mechanism that essentially destroys the number density of particles and conserves mass. As such, according to the measurements, it does not have significant impact on reducing the number density of particles (that is, almost no reduction in the number density of particles).

This observation is important, as the coagulation mechanism in the detailed model of particle size distribution is a very time-consuming mechanism because it takes into account all the possible collision sizes of each particle. By neglecting the coagulation mechanism, the high computational effort is alleviated and the computation of the PBE becomes simpler as the integral terms are omitted. The remaining PBE is a partial differential equation focusing on the convection term of surface growth and the oxidation mechanism in the size space coordinate.

2.6.3 Soot kinetics in volume and diameter space

The surface (growth and oxidation) rates are denoted as volumetric surface rates, $G(v)$ terms (functions of volume size), with units of m^3/s. The surface rates were originally split into the form $G(v) = G_0 A_s(v)$, which is incorporated into the PBE. G_0 is the constant surface growth or oxidation rate with units m/s and $A_s(v)$ is the surface area of each particle, which is determined by its volume (spherical assumption). The volumetric surface rate expression can be further elaborated by expressing it in a more suitable form $G(v) = G_0' v^{2/3}$. G_0' is originally the G_0 term, but with the addition of the shape factor coefficients that are used to determine the surface area according to the volume size of each particle. It should be noted that the G_0 term is dependent on environmental variables such as temperature and species. If volume size is considered as the internal coordinate, the surface rates of each particle size are given by $G(v) = G_0' v^{2/3}$. Beyond the volumetric method, the other method is to use the linear surface rates (diameter as the internal coordinate) where the growth and oxidation mechanisms are

size-independent, avoiding the convection size-dependent problem. The relation that links the volumetric growth rate to a linear growth rate is shown in equation (2.84).

$$G(v) = \frac{dv}{dt} = \frac{d(\frac{\pi}{6}d_p^3)}{dt} = 3k_v d_p^2 \frac{dd_p}{dt} = 3k_v d_p^2 G(L) = \frac{1}{2}A_s G(L) \tag{2.84}$$

With linear surface rates, any dependency on the size of the particles disappears here and with the spherical particle assumption. The volumetric growth rates are transformed on the particle diameter space resulting in the final form $G(L) = 2G_0$. Those growth and oxidation rate expressions are written for atmospheric pressure systems. In cases where the pressure of the system is increased or decreased, the mole fractions are normally the partial pressures of each species in units of atmosphere [81]. In different pressures the kinetics should be modified accordingly. Substituting equation (2.76) into equation (2.84) the following expression is derived. Similar expressions are yield for the oxidation rates.

$$G(L) = \frac{2G(v)}{A_s} = \frac{4k_2 P_{C_2H_2} \cancel{A_s}}{\rho_s \cancel{A_s}} = \frac{4k_2 P_{C_2H_2}}{\rho_s} \tag{2.85}$$

2.6.4 Modelling of radiation in sooting flames

Another important effect that can be studied in laminar and turbulent sooting flames is the radiation model. Soot particles have a significant impact on the flowfield due to their strong radiation properties. The importance of using the assumption of optically thin media, where energy is emitted and not re-absorbed, is shown in [92]. Another study using the simple optically thin approximation (OTA) against a more detailed radiation model - the Discrete Ordinates method (DOM) - is shown in [53]. Both studies found that the OTA radiation model produced significant discrepancies with respect to the oxidation zone of soot particles. The discrepancies are not very important in the non-smoking flame, but the radiative model effects are more apparent in the smoking flame where the flame length is longer and the re-absorption of energy will alter the soot volume fraction profiles. The radiation models provide the divergence of the net radiative flux in the energy equation. The advantage of the OTA model is its easy implementation and fast computation. The other radiation models for computing re-absorption require that a radiative heat transfer equation needs to be solved. Usually, the radiating species of this flame are selected to be CO_2, CO, H_2O and soot particles as they are the most important radiating species for a hydrocarbon flame [93]. Equation (2.86) is implemented for an OTA

approximation. The radiation model has a higher impact on flames producing soot, and if the fuel is of a high hydrocarbon content, it produces a higher amount of soot volume fraction; this significantly increases the role of the radiation process. For example, it is expected that the role of soot radiation will be smaller on CH_4 flames, but much stronger on C_2H_4 flames.

$$\dot{Q} = \nabla q = -4\sigma K_p \left(T^4 - T_0^4\right) \tag{2.86}$$

K_p is the Planck mean absorption mixture coefficient, found from the sum of four mean Planck absorption coefficients of each species and their partial pressures and soot.

$$K_P = K_{CO_2} p_{CO_2} + K_{CO} p_{CO} + K_{H_2O} p_{H_2O} + K_{CH_4} p_{CH_4} + K_{soot} \tag{2.87}$$

The absorption coefficient of soot is calculated as $K_{soot} = C_{rad} f_v T$ giving a fifth power temperature dependence in the equation (2.86) as shown in [94]. C_{rad} is the constant taken according to several studies to connect soot radiation into the energy equation. An example of soot formation study that used 2370 $(m^{-1}K^{-1})$ is found [95] as a C_{rad} value, while another example that used 1370 $(m^{-1}K^{-1})$ is found in [94]. The radiation model affects the flame temperature, which in turn affects the chemical reaction of each species and the mixture density.

2.7 An introduction to the PBE

Population balance modelling is a widely used mathematical tool in chemical and mechanical engineering, with applications to crystallisation, granulation, pharmaceutical science, cell populations, polymerisation and aerosols. The Population Balance Equation (PBE) is used to quantify the dynamics of particulate processes in each application. These processes are characterised by a continuous phase and a dispersed phase. The continuous phase can be visualised as the fluid that carries the dispersed phase (discrete entities) with a distribution of properties (particle size). The dispersed phase may or may not affect the continuous phase. The latter is called one-way coupling, whereas the former, where the dispersed phase affects the continuous phase by mass transfer from gas to solid (and vice-versa) and by means of heat transfer of the discrete entities to the surroundings, is called two-way coupling. As analytical solutions are available only for very simplified cases, for more complex systems the numerical solutions are sought [73]. In addition, the main reason for analytical solution unavailability is that aggregation and breakage mechanisms are expressed as integral functions [96], and the derivation of

analytical solutions regarding the kernels of aggregation and breakage that actually represent a real physical system is highly complex.

The Population Balance equation (PBE) is a conservation equation, similar to the well-known mass and energy balance equations. The PBE describes the temporal change of a particle's property distribution, and can be thought as a balance law of the number of an individual property of a population. The difference between the PBE and the normal conservation equations are the mechanisms that comprise the PBE. The PBE can have the same or similar convection and diffusion terms as any other mass conservation equation in physical coordinate space. Additionally, the change of the particle population could be described by more convection and diffusion terms in size space [73], increasing the dimensionality.

The same methodology applied by using the PBE can be found in some applications under a different terminology. For example, in atmospheric science studies, the term General Dynamic Equation (GDE) is used instead of PBE. Furthermore, in many studies the term "Smoluchowski equation" is used instead of PBE when coagulation or aggregation mechanisms alone describe the dynamics of particles. It should be noted that the theory of population balance modelling has its origin in the early work of Smoluchowski [72]. Later, more mechanisms - including growth terms - were added to the coagulation mechanism, expanding the Smoluchowski framework into the current PBE form that resembles a conservation equation [89].

The solution of the PBE is not an easy task, as it is usually described by a complex integro-differential equation. The parameters of the PBE that affect the formation and shape of the distribution are the rates of each process (e.g. growth rates, coagulation rates). The kinetics that describe these rates are usually measured or extracted from experimental data such as dynamic PSDs on relevant experiments (inverse problem). The solution of the PBE is the number density $n(S,t)$ - a function of spatial coordinates and particle properties, or, more precisely, of particle phase space S and time t [89].

2.7.1 Internal and external coordinates of PBE

Particle phase is a vector space with the minimum number of independent coordinates that are required to obtain a complete description of the distribution [97]. The particle phase space contains the vectors of the internal and external coordinates. The external and internal coordinate terminology has been established by Hulburt and Katz in [98]. To further elaborate, the internal coordinate describes the size of the particle in this case. A single particle is

characterised by a distinct size. A group of these particles forms a distribution of their size property that can vary in the actual physical space depending on the axial and radial position in an inhomogeneous mixture. As such, the number density will be a function of two spatial or external coordinates (e.g. radial and axial position) and multiple internal coordinates (including particle size) [99].

It should be noted that in the homogeneous systems (e.g. 0D reactors) the mixture and particles are well-mixed inside the vessel, and the dependency of the number density on the external coordinates is no longer necessary and is dropped. In the homogeneous system the PBE is greatly simplified, as the number density is a function of the multiple internal coordinates and time alone. The internal coordinates refer to the distribution of properties that describe a particle's state. Internal coordinates are the properties that can describe a particle's size, such as mass, volume, diameter, or a particle's state such as age. The age property of soot particles is associated with their surface reactivity [97].

In a sooting reacting flow, the soot particles are constantly changing their positions in the particle phase space. This means that the particles are moving through the external coordinate axis (physical domain) by a convection process. Similarly, these particles are also convected along the internal coordinate axis or size space. The conventional velocity components related to the external coordinates are not always equal to the bulk fluid velocity due to the addition of thermophoresis and for other reasons such as inertia. This new convection velocity of soot particles results in a slightly different trajectory than the gas-phase species. On the other hand, the velocity components related to the internal coordinates describe the rate change of the internal properties of the particles. An example is that the internal velocity is determined by the surface growth processes that increase the size of soot particles, or decrease their size by an oxidation process. Both surface rates may be constant or size-dependent of the internal property. In addition, the surface rates may be constant, or dependent on environmental properties that lie outside the internal coordinate regime (such as temperature and species concentration). An example of the mathematical description of both velocities in external and internal coordinate space is shown in equation (2.88) [98, 99].

$$\begin{aligned} \frac{\partial x_i}{\partial t} &= u_i(x,t) = v_E & i &= 1,2,3 \\ \frac{\partial r_l}{\partial t} &= G_l[c(x,t), T(x,t), r] = v_I & l &= 1,2,...,N_{sec} \end{aligned} \tag{2.88}$$

In Equation (2.88), the first partial derivative denotes the conventional velocity in physical space of three external coordinates (axial, radial and azimuthal). The $\vec{v}_E$ is the velocity vector of the external coordinates u_i. The second partial derivative is the internal velocity, and G is the surface growth rate. G is a function of multiple parameters, including species concentrations (c) and temperature (T), and is sometimes a function of an internal property (r) of a total number of sections N_{sec}. The v_I is the vector velocity of an internal property r. The other parameters, $\mathbf{x}$ and t, are the physical space vectors and time respectively [98].

2.7.2 Spatially distributed and spatially homogeneous forms of the PBE

The derivation of the PBE is split into two parts: the spatially distributed (or local) form, and the spatially homogeneous (or integrated) form. In some occasions the spatially distributed form is denoted as micro-distributed form and the spatially homogeneous as macro distributed forms [97]. In the spatially distributed form the number density of the PBE is defined as a function of external coordinates and internal coordinates suitable for inhomogeneous mixtures, whereas in the spatially homogeneous form the spatial variation is neglected. The latter is more suitable for studying the global behaviour of the system (well-mixed) [89]. The derivation of the PBE for spatially homogeneous systems can be found in a more detail in [97] and is basically the same as the derivation of Equations (2.94) and (2.95) where in the latter the external velocities are neglected, by integrating the spatially distributed form over the spatial coordinates.

Assuming a finite subregion of coordinates R_1 of the particle phase space S, the total number of particles N found in that subregion is computed by Equation (2.89) [89].

$$N(R_1) = \int_{R_1} n(R_1, t) dR_1 \tag{2.89}$$

Choosing an arbitrarily fixed subregion R_2 coordinates (including external and internal) of the particle phase space S the following population balance statement is satisfied:

$$Accumulation = Inflow - Outflow + Net\ generation \tag{2.90}$$

The accumulation term is the effect of the input, the outflow terms and the net generation of the subregion R_2. The input and output terms account for the physical inflow and outflow

of particles into and out of the system in external coordinate space. Additionally, in internal coordinate space, mechanisms like growth or shrinkage are treated as the convection of particles into or out the subregion of size space. The net generation is the difference between the birth and death events generating new particles in the system or decreasing them. The birth events are leading to an increase of number of particles whereas the death events results in a decrease of number of particles in particle phase space. By assuming that no fluxes are present at the boundaries of the subregion R_2, the only remaining terms are the birth and death events comprising net generation. The accumulation (time derivative) term of Equation (2.90) is stated as the following [89]:

$$\frac{d}{dt}\int_{R_2} n(R_1,t)dR_1 = \int_{R_2}(B-D)dR \tag{2.91}$$

where $B(R_1,t)$ and $D(R_1,t)$ are the birth rates and death rates respectively, which in turn are functions of subregion coordinates R_1 and time respectively. The time derivative term in Equation (2.91) can be expanded to account for the conventional fluxes in external coordinates and the fluxes in the internal coordinate space such as growth.

$$\frac{d}{dt}\int_{R_2} n(R_1,t)dR_1 = \int_{R_2}\left[\frac{\partial n}{\partial t} + \nabla\cdot(n\frac{d\alpha}{dt})dR_1\right] \tag{2.92}$$

where the arguments of the number density function are not included in the RHS of Equation (2.92) for clarity, and the α vector contains a set of internal and external coordinates [97] of the phase space R_1. The time derivative, or the rate of change of the α vector, describes the convection of particles in the phase space R_1. These velocities can be seen in the Equation (2.93), and in more detail in (2.88).

$$\frac{\partial\alpha}{\partial t} = \mathbf{v}_E + \mathbf{v}_I \tag{2.93}$$

The divergence term as observed in Equation (2.92) is split into two parts in external (v_E) and internal (v_I) velocities according to their respective coordinate system. Finally, substituting Equations (2.93) and (2.92) into (2.91), the differential spatially distributed form of the PBE is obtained for an arbitrary region R_2 (that is, the integral of the R_2 region is dropped); this is shown in Equation (2.94) where using Equations (2.93) in the expanded version of Equation (2.92), the PBE is obtained in its spatially distributed form.

$$\frac{\partial n}{\partial t} + \nabla \cdot (nv_E) + \nabla \cdot (nv_I) = B - D \tag{2.94}$$

By integrating the spatially distributed form over the three spatial coordinates or volume of the system, the spatially homogeneous form is obtained in (2.95). For spatially homogeneous systems [89] with a number of inlet and outlet streams s, the PBE takes the following form:

$$\frac{\partial n}{\partial t} + \nabla \cdot (nv_I) + n\frac{d(logV)}{dt} = B - D + \sum_s \frac{Q_s n_s}{V} \tag{2.95}$$

2.7.3 Coagulation terms and complete PBE

The dynamic PBE describes the continuous evolution of particle size distribution (PSD) or other distributions of more than one property, and any changes regarding the population of any property are described via different particle mechanisms. These are mathematical expressions for quantifying the distributions of the internal coordinates of discrete entities in a continuous phase [89]. The particle mechanisms that determine the PSD could be nucleation, surface growth, oxidation, coagulation, deposition, aggregation or fragmentation. The dominant mechanisms in the soot field have been identified to be the first four. The continuous PBE with those four mechanisms is a hyperbolic integro-partial differential equation PBE, as can be seen in Rigopoulos and Jones [24]. The continuous spatially homogeneous form is shown in Equation (2.96).

$$\begin{aligned}\frac{\partial n(v,t)}{\partial t} = &- \frac{\partial \left(G(v) \cdot n(v,t)\right)}{\partial v} + B_0 \delta(v - v_0) \\ &+ \frac{1}{2}\int_0^v \beta_\alpha(v - v', v') n(v - v', t) n(v', t) dv' \\ &- n(v,t) \int_0^\infty \beta_\alpha(v, v') n(v', t) dv'\end{aligned} \tag{2.96}$$

The first term in the LHS of the equation (2.96) is the unsteady or accumulation term. On the RHS of this equation, the first is the surface growth combined with the oxidation mechanism; the second is nucleation. The last two terms are the coagulation birth term and the coagulation loss term, respectively. As can be seen from (2.96), the internal coordinate is chosen to be the volume (v) of particles. An alternative choice could be the particle diameter or mass, but for the sake of simplicity of the coagulation term, the volume size is retained. In addition, the $\frac{1}{2}$ in the coagulation birth term is placed in front of the integral to prevent double counting of

all possible particle collisions. Furthermore in (2.96), the $n(v,t)dv$ represents the probability per unit volume of mixture that a soot particle whose particle size volume lies between v and $v+dv$ can be found at time t [100]. This statement could be re-phrased as saying that $n(v,t)dv$ is the mean density of soot particles between volume size v and $v+dv$. The total number and total volume fraction of particles at a specific point in time are given by the following moment expressions:

$$m_{v,\delta}(t) = \int_0^\infty v^\delta n(v,t)dv \quad , \quad \delta = 0,1 \tag{2.97}$$

Further elaborating, Equation (2.96), $n(v-v',t)n(v',t)dv'$ is the probability of a collision at time t of a particle with size $v-v'$ with another particle of size v' in a unit volume mixture, forming new soot particles of size v. The β_α term, is the coagulation kernel; it describes the frequency and the efficiency of these collisions. The integral indicates the sum of all these collisions from particles with the smallest possible size to particles of size v. The coagulation birth term of the continuous PBE in equation (2.96) could be written in a different way, where the upper integral limit v from the original range of integration 0 to v is written as $v/2$ instead as it is mentioned in [101]. This formulation removes the need to add $\frac{1}{2}$ in front of the coagulation birth event integral, as it prevents double counting of all collisions. Clearly, the v' varies from 0 to particles of volume size v. The same goes for particles $v-v'$. As such, each pair collision in the set is considered twice [102]. The integral limits from 0 to v take into account all the possible collisions that can occur. In other words, the possibilities for all the collisions of size v and $v-v'$ are proportional to the product $n(v-v',t)n(v',t)$. From a physical point of view, collision order is irrelevant (symmetry property) and the coalescence kernel as a function of $v-v'$ and v' is the same as v' and $v-v'$ [89].

During the coagulation process, the particles will either coalesce and form new particles of increased size, or they will rebound and no successful merging will occur. This behaviour is accounted for by the coalescence kernel. In general, the choice of internal coordinates could be either particle diameter or volume. This choice is usually determined by the dominant growth processes. For example, if the coagulation process is more important, it would be much easier and more useful to use volume as the internal coordinate as the volume size is additive in coagulation terms [89], and is a more naturally conserved quantity. On the other hand, if the dominant growth mechanism is through the surface growth terms, then particle diameter

could be more appropriate as the grid in the particle size domain requires less points than the volume size domain and also size-dependencies of the growth terms could be dropped making the computations easier to perform. An example of the latter statement is that the surface growth terms of spherical soot particles are usually proportional to their surface area. The resulting growth term is size-independent of the surface area when the number density function is described by a diameter domain but size-dependent in its volume domain. When the surface growth terms are size-dependent the formulation is not that simple as the growth rate is non-linear and continuously changes across the particle size domain. Size-dependent growth rates are computed for any cell face in the particle size domain and careful attention is needed as the numerical schemes may not produce a conservative solution. The transformation of the surface growth rates is explained in detail in section 2.6.3.

The coagulation death term describes the loss of the original particles of volume fraction between v and $v + dv$ [89] that participated in a successful collision and merging. The initial two particles that were used to form a new single particle are destroyed by the death term. A new particle is formed, whereas the previous two initial particles no longer exist and should be removed from occupying a position in the size space. The newly formed particle is added to a location in the size space by the coagulation birth term. Moreover, the coalescence kernels are non-negative and symmetric because they obey the same physical laws [89, 99]. The coagulation frequency is decomposed into collision frequency and coalescence efficiency. The coagulation efficiency can be interpreted as the probability of one pair of particles forming a single particle [89]. The coagulation kernel could be a constant (independent of size), or size-dependent. In other words, the coagulation kernel is a measure of the frequency of collisions between particles v and $v - v'$ that are successful in producing a new particle of size v [103].

Normally, the coagulation kernel is split into the coagulation rate term and the dependence of the kernel on the size of particles. There are several coagulation kernels types regarding the dependence on the size of particles that could be used in the coagulation term of the PBE [89]. However, in the study of soot formation only two coagulation kernels are appropriate to describe this collision mechanism. The first coagulation kernel which has been applied with a two equation approach method for the free molecular regime can be found in [78, 55]. This size-independent coagulation kernel is described by the equation (2.98).

$$\beta_{\alpha,0} = 2C_a \bar{d}_p^{1/2} \left(\frac{6k_B T}{\rho_s} \right)^{\frac{1}{2}} \tag{2.98}$$

where C_a is a coagulation constant with different value in different studies, such as three or nine [78], and ρ_s is the soot density 1900 kg/m^3. The different collision regimes are the free molecular regime ($Kn >> 1$), transition and continuum regime ($Kn << 1$). The collision factor β expressions according to each collision regime depending on the Knudsen number (Kn) which is defined as the ratio of the mean free path between two collisions of a gas molecule and particle radius ($Kn = 2\lambda_p/d_p$) [104, 105]. The next equation shows the coagulation kernel that is particle size-dependent and in the free molecular regime.

$$\beta_\alpha(v, v') = 2.2 \left(\frac{3}{4\pi}\right)^{\frac{1}{6}} \left(\frac{6k_B T}{\rho_s}\right)^{\frac{1}{2}} \left(\frac{1}{v} + \frac{1}{v'}\right)^{\frac{1}{2}} \left(v^{1/3} + v'^{1/3}\right)^2 \tag{2.99}$$

The dynamic PBE has to be supplied with an initial condition in the time domain, and with boundary conditions in the volume size domain. The conditions that were followed in all simulations are as follows. The particle size distribution at time 0 (at the beginning of the experiment) can take an initial (starting) size distribution or can be set to 0.

$$n(v, 0) = n_0(v) \tag{2.100}$$

$$n(0, t) = n(\infty, t) = 0 \tag{2.101}$$

The boundary conditions in Equation (2.101) means that there are no particles of 0 volume size at any time step. Moreover, all the particles have a finite size [89], and the grid in the size domain should be sufficiently large in order for the last grid point to have a number density function equal to 0 to avoid any clipping of the distribution. Depending on the problem, location of the last grid point may change according to how large the PSD domain has to be in order to capture the entire particle size spectrum.

2.7.4 Moment integrals of the PBE

The mean properties are the moments of the distribution (e.g. the total number density of particles and total surface area). The moment integrals associated with the particle diameter are listed below [103].

$$m_{d_p,\delta}(t) = \int_0^\infty d_p^\delta n(d_p, t) dd_p \quad , \quad \delta = 0, 1, ..., \delta_{max} \tag{2.102}$$

There are an infinite number of moments $\delta_{max} = \infty$. However, the first four are most important and of physical significance. They define the total particle number density (N_T), particle diameter (L_T), particle surface area (A_T) and particle volume fraction (V_T) per unit volume.

$$N_T = m_{d_p,0} \tag{2.103a}$$

$$L_T = k_L m_{d_p,1} \tag{2.103b}$$

$$A_T = k_A m_{d_p,2} \tag{2.103c}$$

$$V_T = k_v m_{d_p,3} \tag{2.103d}$$

The average particle diameter, the mean surface area and mean volume size of a particle are defined by the following expressions using the moments listed in (2.103).

$$\bar{d}_p = \frac{L_T}{N_T} \tag{2.104a}$$

$$\bar{a}_p = \frac{A_T}{N_T} \tag{2.104b}$$

$$\bar{v}_p = \frac{V_T}{N_T} \tag{2.104c}$$

The values of the shape factors k_L, k_A and k_v depend on the assumed particle shape and type. For example, for spherical size particles, the shape factors are $k_L = 1$, $k_A = \pi$ and $k_v = \pi/6$ [103, 106]. Alternatively, choosing the volume internal coordinate, the 0^{th} and first moments of the distribution describe the total number density of particles and total particle volume fraction respectively per unit volume of mixture as shown in equation (2.97). The second moment from using volume as the internal coordinate is noted in [107] to be useful in predicting the onset of gelation.

2.7.5 Moment transformation of the PBE

Consider particle phase space in two dimensions in physical space (axial and radial). Furthermore, consider a case where the soot particles in the system are described by the distribution of one or more ξ properties ($\xi > 0$); the range of values of each property is subdivided into

a number of sections l to describe the level of detail of the distribution of each property (ξ). For soot formation studies, the size of primary particles ($\xi = 1$) and the size of aggregates ($\xi = 2$) could be assigned to obtain a complete description of the soot particles. By increasing the dimensionality to $\xi = 2$ two transport equations are solved for each size l grid point [83]. In this situation, the resulting number of equations to be solved can be enormous; By ignoring the size of the aggregates and assuming that there is only one particle property ($\xi = 1$) which is diameter (size of primary particles), this property is split by 400 diameter sections ($l = 400$). The discretised PBE is expressed as 400 transport equations where each one represents a particle diameter section which should be solved at every point in the 2D space. As such, the total amount of soot transport equations that should be solved to obtain the particle size distribution in each grid point of the computational domain is in general $\xi * l$ and in our case is $1 * 400$ transport equations. As such the total amount of transported size equations solved in the entire computational domain is $\xi * l * N_{cells}$.

In many engineering systems it is unnecessary to solve for the detailed distribution of each internal property and simplifications are made to the PBE. Instead of obtaining the complete PSD, it is sometimes more convenient and more computationally feasible to represent the distribution with a few averaged quantities. The internal coordinate property vanishes by integrating the PBE m times for every particle property reducing the dimensionality to that of transport equations. However, the procedure to form moment forms of the PBE often leads to terms that cannot be reduced to moments. These terms consist of fractional moments or an unclosed set of moment equations [89].

The transformation of a PBE into moment equations can be found in detail in [97]. Assuming that the spatially distributed process shown in equation (2.94) is described adequately by a single internal coordinate, size diameter as shown below.

$$\frac{\partial n}{\partial t} + \nabla \cdot v_e n + \frac{\partial}{\partial d_p}\left(G(d_p)n\right) = B - D \tag{2.105}$$

Assuming that the growth rate is constant and size-independent $G(d_p) = G_0$. Then the PBE is averaged by integrating equation (2.105) as shown below.

$$\int_0^\infty d_p^\delta \left(\frac{\partial n}{\partial t} + \nabla \cdot v_e n + \frac{\partial}{\partial d_p}\left(G_0 n\right) - B + D \right) dd_p \tag{2.106}$$

By substituting the moment integral terms of (2.102) to the integrated spatially distributed

form equation (2.106) can be transformed into the following complete set of moment equations:

$$\frac{\partial m_\delta}{\partial t} + \nabla \cdot v_e m_\delta = 0^\delta B^0 + \delta G_0 m_{\delta-1} + \bar{B} + \bar{D} \qquad , \qquad \delta = 0, 1, 2.. \tag{2.107}$$

The substitution of the first two terms of equation (2.106) is straightforward whereas the third term which contains the internal coordinate is integrated by parts. Equation (2.107) can be solved for an infinite number of moments. However, keeping down to four moments is usually found to be sufficient to fully describe the main properties of a particle system. The second term on the LHS is the convection of the moments in the external coordinates (i.e. physical space). The first term on the RHS is the nucleation of particles with initial particle size diameter of 0. The B_0 term appears in equation (2.107) through the integration by parts of the third term and denotes the number flux of particles entering the internal coordinate region from 0 size (nucleation rate). Moreover, the Birth and Death terms are assumed that can be expanded in terms of moments. The bar on top of Birth and Death terms denotes moment integration. This term could include the size of small incipient particles (usually negligible) if the nucleus size is known prior to use, such as 2.4 nm instead of 0 for the soot particle's initial diameter. The second term on the RHS express the effect of the growth term of particles. The δ index number of moments in the front of the growth term restricts the addition of surface growth to the 0^{th} moment, because nucleation and coagulation processes affect only the number of particles. The infinite set of moment equations as can be seen in Equation (2.107) is compatible, and of the same dimensionality as the governing equations. They can be solved as normal transport equations. The advantage of this transformation is its easy implementation and fast computation. The main drawback is that the complete PSD cannot be obtained directly.

The Equation (2.107) is obtained by integration over the internal coordinate dimension (size space) and assuming that the growth mechanism is constant (size-independent). Ignoring any Birth and Death events the equation (2.107) is simplified further and the moment solution is exact for any order of moment. The standard method of moments describes the evolution of the moments which involve only functions of the moment themselves. However, in soot formation even the SMOM requires closure for some missing moments (fractional moments) which appear in the coagulation and surface growth mechanisms when the internal coordinate is described in volume size space (see equation (2.67) the A_T dependence to solve the first moment). To obtain a closed set of moments equations in the volume size space the shape of the distribution

is often assumed prior to the computation, such as monodisperse (2TEM model), log-normal or gamma distribution [89]. In the following equations, though, a transformation of the PBE from volume space to diameter space eliminates the dependence of surface growth terms to surface growth area (A_s) and the moment set of equation is exact. The moment equations can be further implemented in batch and PSR reactors. A PSR system is described by the following equation [97]:

$$\frac{\partial m_\delta}{\partial t} + \frac{m_\delta - m_{\delta,in}}{\tau} = 0^\delta B^0 + \delta G_0 m_{\delta-1}, \qquad \delta = 0, 1, 2, ... \tag{2.108}$$

where the new second term on the LHS refers to the residence time τ of the PSR system. The moment concentrations of output and input of the system are taken into account. For a batch reactor the output and input terms are neglected.

It should be noted that by using the moments, the PSD is not calculated. In theory, the PSD could be retrieved by using an infinite set of moments. This is impossible from a computational perspective. In practise the number density function should be retrieved with a small number of moments [97].

2.8 Summary of the PBE model

This thesis couples the in-house CFD code (BOFFIN [51]) with a detailed PBE to predict soot formation in laminar and turbulent diffusion flames. The predictive power of this framework and soot formation kinetics are examined as the complexity of the flow field is progressively increased throughout the Chapters 3-6.

The discretised PBE model (shown in detail in Chapter 3) that is employed to all the simulations is univariate (1D) of the particle size property ξ. In this thesis, the particle size property ξ is assigned as the particle diameter (d_p) in Chapters 4,5,6 or in a few test cases with volume size (v) of soot particles in Chapter 4. The coagulation mechanism of the PBE is ignored in the laminar and turbulent multidimensional flames (Chapters 5 and 6) according to the observations mentioned at the end of soot formation section in 2.6.1. However, coagulation mechanism has been implemented in a few test cases of Chapter 4 to test its performance.

The transport equation of the spatially distributed continuous PBE form for the laminar flames (Chapter 5) is shown in equation (2.109).

$$\frac{\partial n(\xi,x,t)}{\partial t}+\frac{\partial([u+V_T]\cdot n(\xi,x,t))}{\partial x}-\frac{\partial}{\partial x}\left(D_p\frac{\partial n(\xi,x,t)}{\partial x}\right)= -\frac{\partial\left(G(\xi,\phi)\cdot n(\xi,x,t)\right)}{\partial\xi}+B_0'(\phi)\delta(\xi-\xi_0) \tag{2.109}$$

On the LHS of equation (2.109) the first term is the time derivative of the number density function. The other two terms are the convection and diffusion terms of the number density function in the physical domain (external coordinates) respectively. The V_T term is the thermophoretic velocity which is applied only to the laminar diffusion flames of Chapter 5 and not in the turbulent diffusion flames of Chapter 6 as it is assumed to be negligible according to [7]. The expression of thermophoresis (V_T) that is used for the laminar flames is shown in equation (2.20). The terms on the RHS are solved in the particle size diameter space of soot particles. However, the number density function requires soot kinetics to compute the particle surface rates ($G(\xi;\phi)$) and the nucleation rates (B_0'). The nucleation rate (B_0') corresponds to the rate given by equation (2.110) which is scaled appropriately to compute the number density of particles with units $m^{-3}s^{-1}$ in the nucleus size. The reaction rate constant parameters of the original form of soot kinetics (volumetric surface rates) that are used for the 0D reactors, flamelet, laminar and turbulent diffusion flames are shown in section 2.6.2. However, the soot kinetics in section 2.6.2 are originally given in the volume size domain (see [81]) and for reasons of high computational expense they have been transformed to the particle diameter space according to section 2.6.3. The final soot kinetic expressions that have been implemented to the PBE are shown for the diameter space in equations (2.80)-(2.114).

$$C_2H_2\rightarrow 2C_s+H_2 \quad , \quad B_0=\frac{2N_Ak_1[C_2H_2]}{C_{min}} \tag{2.110}$$

$$C_2H_2+nC_s\rightarrow(n+2)C_s+H_2 \quad , \quad G(d_p)_{C_2H_2}=\frac{4k_2X_{C_2H_2}}{\rho_s} \tag{2.111}$$

$$C_s+\frac{1}{2}\rightarrow CO \quad , \quad G(d_p)_{O_2}=\frac{240\left[\frac{k_\alpha X_{O_2}\chi_1}{1+k_zX_{O_2}}+k_bX_{O_2}(1-\chi_1)\right]}{\rho_s} \tag{2.112}$$

$$C_s+OH\rightarrow CO+H \quad , \quad G(d_p)_{OH}=\frac{\frac{334X_{OH}}{\sqrt{T}}}{\rho_s} \tag{2.113}$$

$$C_s + O \rightarrow CO \quad , \quad G(d_p)_O = 0.5\ k_O X_O \tag{2.114}$$

These expressions are transformed from the volume to diameter size space and the dependence on the surface area is crossed out. Also, the partial pressures of the species as shown in the original soot kinetics in section 2.6.2 are replaced by mole fractions of their respective gas species as the majority of the simulations is conducted in atmospheric pressure flames. However, at elevated pressures the mole fractions have to be multiplied by the new pressure (in atm). For example in the elevated turbulent diffusion flame ($3atm$) of Chapter 6 the mole fractions are multiplied by 3.

It should be noted that for the Batch and PSR reactors the surface growth rate in equation (2.111) is decreased by a factor of two to reduce the range of the PSD and the number of grid points which are required to cover the entire particle size spectrum. The batch and PSR are simplified reactor systems with no spatial dependence and are suitable for the examination of numerical schemes and to test the PBE performance for different grid parameters.

The turbulent case is solved using the hybrid CFD-PDF method. The transported PDF method solves the scalar representations of the mixture fraction, species mass fraction, enthalpy and discrete sizes of soot particles. The momentum equations are solved by the in-house CFD code ([51]) along with the k-ϵ turbulence model. The CFD model supplies the mean velocities and turbulent time scale to the PDF method. The transport PBE shown in Equation (2.109) is solved in a Lagrangian framework via a Monte-Carlo method. The stochastic particles are changing their position in the psychical domain and scalar space (particle size diameter space) as shown in the equations (2.115)-(2.117).

$$dx_i^{(p)} = \left[\tilde{u}_i \frac{1}{\bar{\rho}} \frac{\partial \Gamma_T}{\partial x_i}\right]_{(p)} dt + \left[2\frac{\Gamma_T}{\rho} dt\right]_{(p)}^{\frac{1}{2}} dW_i \qquad i = 1, 2 \tag{2.115}$$

$$d\phi_k^{(p)} = \dot{\Phi}_{mix,k}^{(p)} dt + \dot{\omega}_k^{(p)} dt \qquad k = 1, ..., N_{sp+2} \tag{2.116}$$

$$dn_l^{(p)} = \dot{\Phi}_{mix,soot,l}^{(p)} dt + \dot{\omega}_{Nuc,l}^{(p)} dt - \dot{\omega}_{Growth,l}^{(p)} dt + \dot{\omega}_{Oxid,l}^{(p)} dt \qquad l = 1, ..., N_{sec} \tag{2.117}$$

The micro-mixing term is modelled and applied in this thesis by the EMST. All three mixing

models have been employed to this thesis and similar to the study of [68] the flame could not be stabilised and global extinction was occurred. Only the EMST could predict a stabilised and attached jet diffusion flame to investigate the experiments of [10]. Moreover, due to the negligible molecular diffusion of soot particles ($D_p = 0$) the micro-mixing term for soot particles is also neglected ($\dot{\Phi}_{mix,soot} = 0$).

Chapter 3

Numerical Methods

3.1 Review of numerical methods for the solution of PBE

The dynamic PBE equation (2.96) is a hyperbolic partial integro-differential equation of mixed dimensions, for which an analytical solution might be available only in simplified systems such as chemically homogeneous systems. Computational methods are needed to approximate the integral and differential terms of this equation especially in spatially distributed systems. To obtain the number density function (or population density), the PBE equation is discretised in the physical coordinates via a computational mesh and the internal property domain (particle size) via a second grid of several sections. The PSD of soot particles covers a large size range, from 1 nm up to 1 μm. As such, a flexible grid (e.g. uniform or exponential) is necessary; it should have the minimum number of grid points sufficient for an accurate description of a particle property, minimising the computational effort.

Many problems are encountered during the process of solving the internal property of the PBE equation. One of these arises from the hyperbolic form, due to the growth and oxidation terms appearing in the equation. The convection term describes the motion of particles not only in one way direction, but two, due to the opposite sign of the oxidation term. As such, greater attention and accurate numerical models are needed to capture this two way movement of convection successfully to conserve the number of particles. The conservation of particles becomes more difficult when the hyperbolic form is size-dependent and not a constant flux. Moreover the complexity of the integral form and the non-linearity associated with the coagulation term

are also issues [89]. It should be noted that coagulation and aggregation mechanisms require kernels to describe the collision and sticking efficiency of the particles. Sometimes these terms are not available, as they are quite difficult to extract from experimental data (i.e. solving the inverse problem). Another problem is the nucleation term. The nucleation term results in a sudden rise in the number of particles with a specific size. The shape of nucleation in the PSD domain is similar to a spike. The peak value of the triangular shape spike is located on the nucleus (first) particle size point.

So far, many numerical techniques used to discretise the PBE and their PSD and mean properties have been reviewed [22, 108, 109]; these reviews illustrate the merits of each technique when solving for the number density function. The PSD solved by each numerical scheme is compared against analytical solutions to test the accuracy of each technique. That was essential in order to find out the most appropriate and accurate method of solving the PBE. The performance of each numerical method is observed for several test cases that exhibit steep moving fronts and sharp discontinuities [22], where a number of problems appear in a convection-diffusion process. Some of the numerical methods employed that are found in the literature are the method of moments, stochastic, finite difference, specialised discretisation techniques, finite element and finite volume methods.

3.1.1 Moment-based methods

The method of moments is a widely used approach in modelling soot formation in laminar and turbulent flames. The 2TEM and MoMIC approach described in section 2.6.1 employ the method of moments by solving two and six transport equations respectively to obtain directly the moments of the PSD at a very low computational cost. The approaches that attempt to model soot formation while using the method of moments need assumptions to obtain closure. At times, the unclosed terms require the knowledge of few moments that lie outside the set of moment equations. Moreover, there is the inherent difficulty in reconstructing the PSD; this is commonly known as the inversion problem. To obtain closure on the PBE, and especially in coagulation terms, the most approximate and simplest method of all is to assume that the PSD is monodisperse. This greatly limits the smallest number of moments required to solve the moment equations. Assuming a monodisperse PSD, the only moments necessary to obtain a solution are the 0^{th} and the first moment of the distribution, providing the mean value of some size property (e.g. surface area). This is the two transport equation model which

essentially ignores the PSD of soot particles. Another strategy is to assume that the PSD is log-normal. With this assumption, the smallest number of moments that required is the first three moments of the distribution. These three moments are used to compute the geometric mean and standard deviation of the PSD in order to compute the rest of the moments when needed to obtain closure [110]. A more general approach is to use Lagrange interpolation between the logarithms of the moments. With this technique, fractional moments are computed and used to obtain closure on surface mechanisms and coagulation mechanisms of the moment equations. The method of Lagrange interpolation is described in Frenklach [87]. This method is called the method of moments of interpolative closure (MoMIC), and six moments are solved to predict soot formation. However, Frenklach did not extend his formulation into aggregation problems and into reconstructing the PSD from the six moments.

There is an alternative approach to discretising the PBE for obtaining the moments of the PSD directly. This approach is an improved version of the standard method of moments, and is called Quadrature Method of Moments (QMOM), where the accuracy could be on the same order of magnitude as the discretised PBE procedures while using very few scalars [111]. This method is similar to the standard method of moments where the internal coordinate is integrated out [112]. It should be noted that the standard method of moments is limited, and is accurate only for size independent growth terms, size independent aggregation and breakage kernels [112]. It is in fact the size dependency of each process that could cause problems in the standard method of moments, as the size dependent terms of each process are unclosed terms. However, these terms are closed by a set of moment equations and a few assumptions on the shape of the distribution [112]. Compared to the standard method of moments, the closure of the moments is achieved in the quadrature method of moments by transforming the PBE into a set of moments by approximating the number density function with a quadrature approximation. The QMOM can be thought as a method in which the PSD is assumed prior to the computation, such as monodisperse or log-normal distribution; in QMOM's case, though, the number density is assumed to be made by delta functions [112], and the final closed form of the moment equation is in terms of abscissas and weights evaluated from finding the eigenvalues and eigenvectors from a sophisticated matrix algorithm [111]. The main disadvantage of this approach is that the complete PSD is not directly accessible, and its reconstruction is not an easy task. [112].

However, an alternative method to QMOM is instead of solving the transport equations

for the moments, it is possible to solve the transport equations directly for the weights and abscissas. This is known as the DQMOM method. This method is described and the equivalence between the QMOM and DQMOM is demonstrated in [113]. Another detailed soot model that implements a hybrid higher order method of moments is applied in [114]. It combines the advantages of the method of moments with interpolative closure (MOMIC) and the direct quadrature method of moments (DQMOM). This is a multi-dimensional method of moments that takes into consideration the volume and the surface of the particles [114].

In addition, the reconstruction of a number density function from the knowledge of very few moments is a severely ill-posed problem. As stated in [115], reliable algorithms for solving this problem and generating a complete PSD are still not available. So far, these methods are limited and successful in simple cases; however, they may have not the same success for a variety of test cases. This method is difficult from theoretical and practical points of view for reconstructing the PSD successfully for all cases. In theory this method is difficult because all moments should be available for a correct retrieval of the PSD. From the practical point of view, this method is an ill-posed inverse problem [116].

Three different methodologies of reconstructing the PSD from a finite set of low-order moments are shown in [116]. The first and most popular method for reconstructing the PSD is by knowing in prior the shape of the distribution (e.g. Gaussian distribution). This approach is widely used, and is numerically fast and accurate even for bimodal distributions if the assumption on the shape of the distribution is the correct choice. However, this method is not recommended if the distribution is not known prior to the computation. The other two approaches that do not require any assumption regarding the shape of the distribution are the discrete method and spline functions. The discrete method is an accurate one, but has only been used for simple PBEs of nucleation and surface growth mechanisms without any oxidation, aggregation and breakage terms. The discrete method is proposed by Randolph and Larson [97]. The other method used spline approximations. It is a general and flexible approach. This approach proved to be successful in smooth distributions, but with sharp peaks the reconstruction fails to capture all complexities [116]. The reconstruction of the PSD it is well-known as the Stiljies problem where numerous PSDs could possess the same moments [117].

3.1.2 Stochastic and finite difference methods

Another brief review of the solution of the PBE can be found in [118]. A review conducted regarding the different numerical methods for solving the PBE, one of them is the stochastic PBE. The benefit of using stochastic models is more profound in multidimensional PBEs where the solutions are retrieved at a reasonable numerical cost for a significant number of internal coordinates; the other numerical methods require increased computational effort, with the addition of internal coordinates [118]. Like PDF methods for turbulent flows, the stochastic approach differs from the common finite difference methods by performing realisations of the system behaviour through a generation of random numbers. These random numbers are used to compute the required probability functions that govern system behaviour [118]. A stochastic algorithm for coagulation and breakage mechanisms is shown in [119], and a method of population balance modelling with nucleation, growth and coagulation mechanisms is presented in [120]; it is solved stochastically in PSR and PFR reactors by using jump processes, where a real volume of particles is approximated by a sample volume of computational particles.

The finite difference technique is a widely used method for approximating the partial derivatives, using the Taylor's expansion series. Finite difference schemes tend to flatten (broad) the sharp discontinuities due to numerical diffusion. Also, they tend to smooth out the solution, as any sudden changes are not well-captured due to inadequate resolution. This technique can conserve the number of particles and mass only in the limit of infinite resolution, requiring a great amount of grid points. The computational effort is significantly increased by the addition of grid points. Examples of finite difference methods in PBE can be found in the review study of Mesbah et al. [22].

3.1.3 Discretised PBEs

Throughout the literature, greater focus has been made to specialised algorithms that have been used to discretise the PBE method. They are also known as the method of classes [121]. Sectional methods are developed that discretise the continuous particle size distribution with a set of independent functions; these can be categorised as 0^{th} or higher-order [121]. Higher-order methods are preferred if any convection terms in the internal coordinate space are considered, and lower-order methods are preferred when breakage or coalescence is considered [121]. Sectional methods are performed by numerous studies with different discretisation procedures.

In general, the discretisation of the PBE is categorised as an M-I approach or M-II approach;

these were first defined in [122]. In the M-I approach, the mean value theorem for integrals is used on the coalescence frequency [89]; in the M-II approach, the mean value theorem is used in population density functions defined in terms of Dirac delta function concentrations.

The sectional method is applied in the early work of Bleck [123, 121], where it is suggested that it is unlikely to derive analytic solutions with kernels that will be realistic in practical problems. The discretised PBE of the Bleck study [123] achieves closure by employing the M-II approach [89]. As such, the continuous size distribution has to be solved numerically to permit more realistic choices of the kernel. The continuous size distribution of cloud droplets in Bleck's study [123] is expressed by the coagulation term alone. A mean field approximation is applied to the number density function [121], and a set of ordinary differential equations is derived that includes double integrals and is computed by a simple quadrature. The drawback of this approach was the complexity of the method - it is computationally intensive to compute the double integrals [121].

Later, Batterham [124] described the coalescence process alone by a discretised equation. Unfortunately, in Batterham's study [124], the PBE was discretised on a coarse fixed geometric grid. Despite the methodology's good accuracy, Batterham's method is not correctly predicting the total number of particles but the particle volume is well captured [103, 122]. Initially, Batterham discretised the coagulation term with a uniform volume grid domain. The number of equidistant intervals, which was defined as 30 or below, was very large in the volume size spectrum; consequently, no information could be found for small size particles according to the diameter space. As such, a geometric series is applied for the volume size where each grid point is twice the size of the previous point [121]. Both Bleck and Batterham [123, 124] applied a geometric discretisation only on the coagulation mechanism.

A similar discretisation technique to Batterham's study [124] was developed by Hounslow et al. [103], where the continuous PSD is split into discrete intervals using a geometric discretisation. In Hounslow et al. [103], a complete form of the general PBE was shown; it includes nucleation, surface growth and coagulation mechanisms. The PSD was discretised by a piecewise constant approximation [121] (or stepped population density [125]) using the same geometric series as Batterham [124]. However, this method was successful in conserving the number of particles but not the mass during aggregation process [121]. As such, a correction factor of an arbitrarily constant value was implemented to the aggregation term in order to correctly account for the mass conservation; the change in the number of particles proved to

be independent for any value of this correction factor [103]. Another similar applications of a discretised PBE, known as the method of classes or sectional method, is found in [126] and [127].

It should be noted that Hounslow et al. [103] contributed significantly to the advancement of the numerical solutions of the PBE by introducing a new discretised form of the PBE. The new discretised form, and especially coagulation, is influenced by Batterham [124]. The results of the first four moments of the PSD are compared, and agree well with the experimental results of a batch process where the one-dimensional PBE describes the particle's size in diameter space. A constant PSD is assumed within each size interval, and any integrals (e.g. coagulation) are replaced with summations. The drawback of this model is that the discretisation of the domain is accurate only for a coarse fixed geometric (for example, exponential) grid with an increment ratio between the discrete points of $v_{i+1}/v_i = 2$ [128].

The drawback of Hounslow et al. study [103] is dealt with by extending the original formulation to an adjustable geometric discretisation grid domain for $v_{i+1}/v_i = 2^{1/b}$ in Litster et al. [128]. In [128], it is described that in practise, a much finer resolution is frequently needed to accurately capture and check for the convergence properties of the PSD. It should be noted that in the improved version of PBE in [128], the original PBE model of [103] with the fixed geometric grid was examined; despite its initial great accuracy, the model exhibited significant errors in predicting the high-order moments, and the PSD was quire erroneous. Later, a similar technique was used to solve for breakage problems in [129] where the original breakage equation was modified with additional terms to guarantee the conservation of number of particles and mass for different grids.

Returning to the extended PBE model of Litster et al. [128], Kumar [130] demonstrated that the extended formulation is valid only for integer values of b below 4. The new extended approach was tested in batch and PSR reactors. The original model discretisation method of. [103] conserved the 0^{th} moment but not the higher-order moments. This was fixed by introducing a correction term within the coagulation mechanism. The original method also results in poor predictions at long periods of time [122].

A review is found in [109], where the solution of the four aforementioned discretised PBE techniques (i.e. Batterham's model [124], Marchal et al. [126], Gelbard et al. [127] and Hounslow et al model [103]), are compared to each other and with analytical solutions. The authors conclude that the best performance in terms of computational speed, number of particles and

mass conservation was achieved by Hounslow's model [103]; the second best was Batterham's model [124], which conserves the mass but underpredicts the number of particles. All four models, in general, had relatively good performance. However, all of them usually exhibited difficulties in predicting the tail of the distribution. This inaccuracy is not detrimental, though, as the particle number is too small in that region to be of significance [109]. It should be noted that in this review, only coagulation performance is evaluated. It is also stated that Batterham's model [124] double counting treatment is not obvious in the discrete equations, but is rather an inherent feature of the discretisation methodology. Higher order methods were proposed in Kostoglou's review [109] as alternatives to the zero order methods, due to the benefits of reducing the numerical diffusion errors that may actually appear on the hyperbolic form of the PBE. Zero order methods approximate the particle size distribution as a histogram, with a constant distribution between each segment; higher order methods approximate the distribution with polynomials [109]. Unfortunately, higher order methods have several limitations (including computational restrictions) and are not applicable in general [109]. In addition, the improvement of Litster's model [128] over the original Hounslow's model [103] was not valid for all values of b. For integer values over four, the formulation was not correct. This error was corrected as stated in [131].

In addition to the discretised PBEs, Kumar and Ramkrishna [122] introduced a new method of classes using a fixed and moving grid to enhance the prediction of aggregation and breakage processes. They reformulate the coagulation and breakage terms with an alternative formulation employing special factors. The new numerical method of the coagulation mechanism is more general, and exhibits better performance and accuracy than the previous coagulation mechanisms of the discretised PBEs. This pivotal method of Kumar and Ramkrishna conserves the first two moments for both an arbitrary and a geometric grid. These special factors can be considered as property balances [89]. Through coagulation, a new volume size appears due to the collision of two smaller particles. If the new size of the coagulated particle does not match a representative size point in the volume domain, the property balances assign fractions of the resulting number of particles to the neighbouring representative points (adjoining pivots) by linear interpolation [122, 89]. The fixed pivot technique on coagulation equation is shown in equation (3.1).

$$\frac{dN_l}{dt} = \sum_{v_{l-1} \leq (v_a + v_b) \leq v_{l+1}}^{a \geq b} (1 - 0.5\delta_{ab})\eta\beta_{a,b}N_aN_b - N_l \sum_{b=1}^{N_{sec}} \beta_{l,b}N_b \tag{3.1}$$

$$\eta = \begin{cases} \dfrac{v_{l+1} - v}{v_{l+1} - v_l}, & v_l \geq v \geq v_{l+1} \\ \dfrac{v - v_{i-1}}{v_l - v_{l-1}}, & v_{l-1} \geq v \geq v_l \end{cases} \tag{3.2}$$

It should be noted that the fixed pivot technique of Kumar and Ramkrishna [122] applied in the coagulation mechanism is exactly the same as Hounslow's original coagulation mechanism [103], when the fixed pivot is applied to the same geometric grid of spacing factor of two [122]. In the fixed pivot technique, the number density function is approximated by a Dirac delta function. Kumar's and Ramkrishna's fixed pivot technique [122] has been found to be easy to implement, and has relatively good conservation properties of both number and mass of particles through the use of a significant amount of grid points. Subsequently , the fixed pivot technique has been improved by proposing a moving pivot technique [132], and a cell average technique in [131, 130]. Each technique yielded better results than the previous models, and exhibited moment preservation. A moving pivot technique proved to be more accurate than the fixed pivot, but is much more complex; its discretisation results in a set of stiff differential equations that are difficult to solve [99]. Breakage discretisation will not be investigated any further here because it is not relevant to this thesis. The focus will remain on coagulation/aggregation birth and death terms.

Another interesting review in aggregation and breakage models can be found in Vanni [108]. In this review study [108], all the previous approaches, including the fixed and moving pivot techniques, are compared against analytical solutions for aggregation and breakage problems alone. Though some methodologies (including Hounslow et al. [103]) not extending their methodology to breakage problems, as they include only nucleation, growth and aggregation, Vanni [108] added a breakage term that was closer to their discretisation technique. Overall, all approaches were fairly effective in reproducing the PSD relative to the first analytical solution, but were not in close agreement with the second analytical result. The first and second analytical results form bimodal distribution functions. The models that performed better were those in Kumar and Ramkrishna [122] and the discretised zero-order method of Gelbard and Seinfeld [127]. In [108], it is also stated that the sectional model of Marchal et al. [126] and the improved discretised PBE method in Litster et al. [128] gave poor predictions and lack generality. Even by refining the grid, these models could probably not yield (converge to) more accurate solutions. All these methods are specialised algorithms for solving Population Balance equation models [133].

3.1.4 Finite element method

The higher-order methods are associated with finite element methods that approximate the PSD with a set of linearly independent functions of order greater than zero [118]

Except for the method of classes, and discretised PBEs that take discrete entities of the PSD, another method - one of the very first studied - suggests the application of two finite element approaches with good accuracy. The first involves a cubic spline collocation method where the grid point points are the collocation points; the second describes an orthogonal collocation, which is flexible to locating collocation points anywhere within each element [134].

The finite element method was later extended and applied to other studies, as in [135], using B-splines as basis functions and by using an adaptive mesh; this was helpful in reducing the size of the PSD domain. Due to the large mass spectrum of the particles, it was convenient to transform the mass coordinates into dimensionless variables in the range of -1 and 1 (scaled domain). B-splines are also used with C^2 continuity. A similar method with spline collocation was also used by [136]. Both studies used mapping methods to scale the domain. Unfortunately, the mapping methods influence significantly and alter the accuracy of the model. As such, careful selection of the mapping method parameters is required as stated in [136].

To avoid any uncertainties regarding the scaled domain, Nicmanis and Hounslow [107] employed a hybrid approach of a Galerkin finite element method and orthogonal collocation on an unscaled domain. Their work showed that the benefit of using a scaled domain over an unscaled one is that the prediction of a large number of particles at small sizes is simpler; however, it is more difficult to predict a small number of particles at large sizes. Moreover, the scaled domain method that has been applied in [135, 136] experienced difficulties in predicting the moments of the distribution (due to singular function); it also suffered from some small errors in the population density at large size ranges, because the solution was multiplied by exponential factors to transform back to its original coordinate, and introducing larger errors [107]. In addition, in the scaled domain the selection of mapping parameters is critical. This problem is avoided in the unscaled domain.

In [107], a direct comparison is performed between the new finite element Galerkin and a collocation approach with the discretised PBE of the Litster et al. [128] model. The finite element method was proven to be capable of achieving more accurate predictions and robustness, by up to two orders of magnitude, compared to the discretised PBE of Litster et al. [128]. The finite element superior performance is accompanied by even less computational effort [107].

Both collocation and Galerkin finite element methods belong to the family of weighted residuals. In collocation formulas, the weight function is defined with a Dirac delta function at selected collocation points [107], and the discretisation is similar to finite differencing. In the other formulations of weighted residuals, such as the subdomain method, the process is similar to finite volume by setting the weight function to unity. In the Galerkin method the weight functions are the same as the interpolation formulas (e.g. basis functions) [24].

Considering again the original discretised PBE in [103], the discretised form of the PBE is achieved using a geometric grid of twice the preceding size. However, this method was found inadequate for accurately computing the PSD, and was later modified and extended in [128] where a fractional geometric grid is used with more points in the volume size domain to solve the PSD [137]. In the orthogonal collocation method of [134], the PBE is divided into several elements; within each element, a number of internal collocations are specified. The number density function at each internal collocation point is approximated by the following expression [137]:

$$n(v,t) = \sum_{j=0}^{nc+1} n_j^e(t)\phi_j^e(v) \tag{3.3}$$

where the ϕ in Equation (3.3) is a Lagrange basis function, and n^e denotes the value of the number density function at the internal collocation point c of each element. The full mathematical expression of this finite element methodology can be found in [137]. An assessment is performed of the orthogonal collocation method [134], and the discretised PBE found in [128]. From the comparative study of these two models, [137] shows that the orthogonal collocation method was more accurate compared to the discretised PBE [128] for a variety of analytical solutions with functional forms of the growth rate.

Despite the better performance of the finite element collocation method, oscillations were observed in the tail and the front parts of the distribution. In situations where these oscillations are comparable in height with the peak magnitude of PSD, the model's accuracy drops - it is less robust, as it suffers from numerical instabilities. As a countermeasure to these oscillations, one might introduce an artificial diffusion term [137]. An extension of this application is found in [138]. The same methods are compared, focusing on a variety of aggregation kernels combined with constant or pulse-like nucleation terms. The nucleation term posed a real problem producing oscillations and numerical instabilities in the system. To counter this nucleation problem, a Gaussian nucleation function was approximated to improve stability. Again, the

orthogonal collocation method performed better than the discretised PBE [138].

These recent assessment studies were performed due to the absence of comparative studies between the numerical models for solving the PBE [137]. Continuing with the assessment studies, a finite element Galerkin method was introduced in [139]. Good results were produced, but as with the previous collocation finite element method, an artificial diffusion term was used to minimise the generated oscillations. In an another study, the Galerkin method, general method of moments and stochastic Monte Carlo methods were compared in batch and continuous particulate processes with nucleation, growth and aggregation mechanisms [117]. There was difficulty in reconstructing the PSD from a set of few moments, and the Galerkin method was more accurate in predicting the PSD relative to the other two methods. However, it is computationally more expensive than these alternatives. The Galerkin method is also applied to multivariate PBE as can be seen in [140].

A discretisation method with collocation on finite elements is shown in detail in Rigopoulos and Jones [24], where the model is validated against exhaustive benchmarking of numerous test cases with available analytical solutions. The accuracy of the number density function is tested for a variety of grid formulations, including exponential and uniform grids with different grid increments. The PBE grid is guaranteed to cover the entire particle size spectrum of soot particles, ensuring no loss of mass. The first two moments of the PSD and the PSD itself are compared with analytical results with very good accuracy. The collocation points are specified at the grid points of the elements where a linear Lagrange interpolation polynomial as basis function is employed. In addition, Rigopoulos and Jones [24] provide a brief review of finite element methods and discretised PBEs with some interesting conclusions. Finite element methods are more general and flexible numerical methods that can be easily applied for any PBE formulation and any grid type. They can also retrieve the complete PSD, and the moments with reasonable accuracy [24]. On the other hand, the discretised PBEs lack any generality, as they are forced to be applied in a specific grid type and are designed to accurately predict the first two moments. Higher moments may exhibit severe errors. However, compared to the finite element, discretised PBEs are easier to implement and computationally more efficient.

Furthermore, Rigopoulos and Jones [24] used a finite element scheme with collocation linear elements and an upwind propagation of growth similar to the finite difference upwind scheme. The method is computationally faster than the higher-order finite element collocation methods (cubic splines) [96], and is also used in this thesis.

3.1.5 Finite volume method

Finite volume schemes are a discretisation class well suited to solve conservation laws in a wide variety of systems [99]. The high-resolution finite volume methods are known for their general applicability and accuracy which have been developed for compressible gas dynamics. They have been gaining importance for the solution of the PBEs [133] and will be implemented and tested under different grids in a later part of this thesis, and will be compared with the finite element method. The finite volume scheme is used due to its conservation properties and the advantages of the well-known Total Variation Diminishing (TVD) scheme, which allows coarser grids to be applied. The numerical implementation of the finite volume PBE technique and TVD scheme can be found in a great detail in Qamar et al. [141]. The PBE model used in this thesis is one-dimensional, as there is only one internal coordinate that describes the particle state. In batch and PSR reactors, the particles are uniformly distributed in the physical domain; the number density function is considered to be independent of any external coordinates [101].

A more recent and interesting review was conducted by Mesbah et al. [22], where finite elements techniques, finite volume methods and method of characteristics are compared against analytical solutions. It is shown that the method of characteristics is the most accurate, as it is free of any diffusion problems due to the moving mesh and the disappearance of the convection term in the PBE [22]. On the other hand, the finite volume of first-order joined by flux limiting techniques are applied and compared for the same test cases, with finite elements of orthogonal collocation and Galerkin methods. It is shown that the second best method after the method of characteristics is the finite volume method with flux limiters. The finite elements are less appealing according to [22], as they are more computationally intensive and suffer from severe numerical diffusion and oscillatory behaviours. In addition, when linear basis functions are applied in the collocation type finite element method, the numerical diffusion is comparable to the first-order of finite volume without flux limiters. It should be noted that in [22], the finite element methods such as Galerkin with Lagrange basis functions may yield more accurate results for the moments of the distribution than finite volume with flux limiters, but at the expense of greater computational effort.

It is clear from this recent review that the finite volume scheme with flux limiters is a very attractive choice in terms of computational power (requiring almost the same computational effort as the first-order upwind), as well as accuracy. Instead of using the previous methods, the widely used finite volume high resolution is an ideal choice for solving even multidimensional

PBEs [133]. The high-resolution finite volume scheme was initially proposed for solving PBEs by Ma et al. [142], where it was compared against a finite difference PBE method (e.g. Lax-Wendroff methods). Both models predict the convection of the size distribution with great accuracy, but the finite differencing method produced some oscillatory behaviour at the front part of the distribution. As the name high-resolution suggests, the method provides at least second-order accuracy where the solution is smooth [133]. High-resolution schemes are proposed due to their generality, and because these methods are already widely used in CFD engineering processes for compressible gas dynamics, aerodynamic and detonation waves due to abrupt shock waves [133]. This method has several benefits that include avoiding numerical diffusion (e.g. smearing or damping of the solution), which is a common problem associated with first-order methods; it also avoids numerical dispersion, which is non-physical oscillations associated with second-order methods when they encounter sudden changes or sharp gradients [133]. This approach is very efficient in handling the hyperbolic form of the equation, and especially when the growth rate is size-dependent. Applications of the finite volume high resolution schemes for analytical solutions for size independent and size dependent growth are shown in Gunawan et al. [133].

First-order discretisation schemes are diffusive, and the solution is smeared; a second-order scheme gives a higher accuracy, but produces spurious oscillations. A first-order scheme is supplemented by antidiffusion terms producing second-order accuracy and avoiding these spurious oscillations. This method is called the high-resolution method. In the literature, first-order methods usually counter the numerical diffusion by employing a finer mesh, whereas using a second-order scheme produces non-physical oscillations (called numerical dispersion) that unrealistically can take negative values [142]. Even by employing finer mesh for the second-order scheme, the oscillations produced may be unavoidable. A simple advection problem of 1D and 2D is performed, and the results of a finite difference technique are compared with first and second-order accuracy and a high-resolution scheme with a flux limiter. The first-order solution is significantly smeared, whereas the second-order eliminates the numerical diffusion but produces spurious oscillations. With the flux limiter, the solution is very well captured and no oscillations are shown [142]. Another extension of the high-resolution scheme of the finite volume is presented in [133]. It is shown that with the high resolution method, larger mesh sizes (coarse mesh) could be used with longer time steps; this can result in a faster computation of many orders of magnitude [133].

3.1.6 Summary of PBE review

The method of moments is the most widely used approach in soot formation studies such as the 2TEM and MoMIC approach due to its simplicity and low computational effort. The MOM can be employed when the low-order moments do not depend on the values of the higher-order moments. An alternative to the method of moments is the method of characteristics; it is highly efficient, especially for the hyperbolic terms, but only when the relative physics are simple. For more complex system this formulation cannot be generalised. An example of the method of characteristic limitation is on CFD applications. In CFD, the flux terms of the PBE of both the internal and external coordinates could be non-linear functions of certain parameters, such as temperature and species concentrations; these, in turn, are functions of spatial coordinates and time. As such, the method of characteristics is not easily applicable. Another method is the Monte-Carlo, which is suitable for solving a stochastic PBE. The Monte-Carlo method is computationally more expensive and of lower-order than the other methods [73]. It may be faster in multidimensional PBEs.

To summarise, the majority of population balance modelling studies involve discretisation through moment methods, finite element and finite difference techniques. Comparative and review studies have been presented to determine common problems between population balance modelling numerical techniques and the best discretisation class. Another recent class of discretised PBE is the finite volume method. The finite volume technique is widely used in fluid mechanics and aerodynamics due their conservation properties. They are very general, and can be used to many applications. Solutions of PBE are by no means trivial and efficient algorithms are needed. PBE is a highly non-linear integro-partial differential equation, where the distribution could be sharp in some occasions, not entirely smooth, and can span many orders of magnitude in the internal coordinate space (e.g. 1 nm up to 1 μm). [142].

3.2 Finite volume PBE discretisation

A good knowledge of predicting and controlling the size range of particulate processes prior to their production is of paramount importance in ensuring product development and suitability for different applications, waste minimisation and quality control [141, 143]. The finite volume high-resolution scheme seems to be an ideal numerical method for solving the PBE. It is a semi-discrete model, continuous in time but discrete in phase space [141]. In Qamar et al.

[141], the nucleation mechanism is expressed as the ratio of nucleation rate and growth rate. This ratio gives the number density of the incipient particles at 0, or at the smallest possible defined size prior to the computation. Apart from that, the PBE could be multidimensional and inhomogeneous [96]. However, in Rigopoulos and Jones [24], the nucleation mechanism is considered to be a sharp spike at the nucleus point; it is computed as the ratio of the nucleation rate with the first two points of the distribution without including any growth rate. Rigopoulos and Jones formulation allows for the study of the implementation of nucleation and coagulation problems only without the need for implementing surface growth rate mechanisms.

The PBE equation in this thesis tests the performance of discretising the PBE by a finite volume high-resolution method, and identifies the advantages of this formulation over the finite element method of Rigopoulos and Jones [24]. The PBE discretisation is shown below; for simplicity, a homogeneous system is assumed and aggregation and breakage mechanisms have been neglected, leaving only the partial hyperbolic form of the PBE equation. The derivation starts by giving the 1D homogeneous PBE, where the spatial dependency is omitted and the number density is a function of a linear size (particle diameter) [143] and not volume.

$$\frac{\partial n(L,t)}{\partial t} + \frac{\partial \left(G(L,t)n(L,t)\right)}{\partial L} = 0 \tag{3.4}$$

Equation (3.4) is a hyperbolic form of the PBE. In the finite volume discretisation, the particle diameter space should be split into several sub-domains (sections). It should be noted that the finite volume discretisation of first-order upwind scheme is the same for uniform and non-uniform mesh. A uniform mesh is assumed for the derivation of the discrete form of Equation (3.4) because it is more convenient.

Assume that the size domain is discretised into several grid points with $L_i = i\Delta L$ and with equidistant cell intervals between the grid points $\Delta L = L_i - L_{i-1}$ [141]. In the finite volume scheme, the L_i points are the cell centres and the locations $L_{(i\pm1/2)}$ (e.g. $L_{i\pm1/2)} = L_i \pm \frac{\Delta L}{2}$) are the cell faces or edges. An illustration of the grid cells and their centres on the 1D size domain is shown in Figure 3.1.

The Figure 3.1 is just an illustration of equidistant grid points. The triangular points shown in Figure 3.1 are diameter particle sizes and represent the cell centres between the cell faces. The cell faces are drawn by a vertical thin line in the Figure 3.1. Due to uniform mesh, the length intervals ΔL are the same for both between the cell centres and between the cell faces across the PSD domain, simplifying the discretisation even further. In a non-uniform mesh,

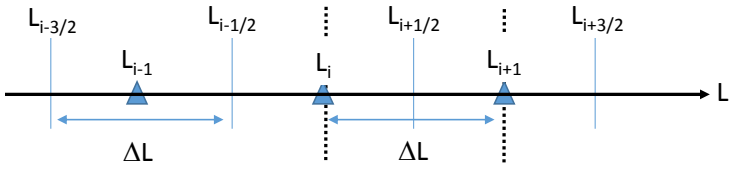

Figure 3.1: Grid size domain

these intervals are not the same between the faces and the grid points. As such, in non-uniform mesh, extra care is needed for the upwind scheme as the intervals are not constant - they change across the PSD domain. Moreover, extra care is needed for the fluxes of surface growth and oxidation terms to take into account the non-uniformity of the mesh. The surface rate $G(L,t)$ is sometimes positive and sometimes negative, depending on the magnitude of oxidation and surface growth terms. The points that carry the information of the number density function are located at the cell centres. It should be noted that the number density functions in the following relationships are derived from integrating the PBE (3.4) in for each cell and defining n_i as the averaged number density function [141]. The discretised finite volume form of Equation (3.4) is shown in Figure (3.5).

$$\frac{\partial n_i}{\partial t} = -\frac{\left(G_{L_{i+1/2}} n_i - G_{L_{i-1/2}} n_{i-1}\right)}{\Delta L_i} \tag{3.5}$$

It should be noted that the same discretisation process is applicable to different internal coordinates, such as volume or mass, instead of diameter. The discretisation remains the same, with the only caveat that the surface rates should be computed differently at the cell faces. Furthermore, the discretisation of the internal coordinate may sometimes cover a very large range, and a uniform mesh cannot be large enough to capture the whole size span. In these cases, an exponential grid is more appropriate. For an exponential grid the interval notation ΔL_i is appropriate, and should be computed for each cell, whereas the interval in a uniform mesh the same for all cells and can be considered as a fixed constant ΔL. This is the normal definition of finite volume discretisation; another configuration exists, though, and its proof is shown in [144]. This other finite volume formulation is slightly different from the previous one, and is shown in Equation (3.6).

$$\frac{\partial n_i}{\partial t} = -\frac{\left(G_{L_i} n_i - G_{L_i} n_{i-1}\right)}{\Delta L_i} \tag{3.6}$$

This formulation is essentially the same as the finite volume upwind scheme, and its derivation can be found in [144]. The difference between Equation (3.6) and Equation (3.5) is that the surface rates can be computed at the cell centre and not on the boundaries of each cell (e.g. cell faces) [144]. This is possible according to [144] by defining a point-wise value for the surface growth velocity in each cell, or by computing the average growth velocity at each cell. In this thesis, this simple upwind formulation shown in Equation (3.6) is valid and is exactly the same as the formulation of the original finite volume scheme (3.5), because the surface growth rates in particle diameter size space are size-independent (that is, they are constants with fixed values across the entire PSD domain). Consequently, the surface rates are identical for all the cell faces and equal with all the cell centres.

So far, the discretised hyperbolic form of the PBE that includes only the surface growth and oxidation mechanism is examined. If nucleation is considered, a source term is added to the hyperbolic form of the PBE equation and is written below in Equation (3.7) where the nucleation term is expressed with a Dirac delta function.

$$\frac{\partial n(L,t)}{\partial t} + \frac{\partial \left(G(L,t)n(L,t)\right)}{\partial L} = B_0(t)\delta(L - L_0) \tag{3.7}$$

where B_0 is the newly added term and represents the nucleation mechanism with units $1/(m^4 s)$, and $\delta(L - L_0)$ is the Dirac delta function. It should be noted that there are several problems regarding this formulation. The smallest possible diameter size in the PBE is assumed to be the nucleation point. However, in some occasions the information of the number density function is propagating towards to the left boundary (particle section of 0 size) due to higher oxidation rates than surface growth, and sometimes falls outside the PSD domain. Some points are specified behind the nucleation point for consistency issues. As such, to overcome this problem, the number density function is imposed to be 0 for the points that are located behind the nucleation point. This method can be thought of as similar to a destruction term of soot particles due to oxidative attack. The nucleation term is applied only on a single point of the size domain, but requires the location of the two neighbouring grid points. The nucleation term is computed as the area of a very sharp triangle between the two adjacent grid points and the peak value of it (nucleation rate). The nucleation formulation is shown in [24]. Another possible nucleation formulation that can be used according to [141] is to define the nucleation production as the ratio of the nucleation rate and the growth rate.

Equation (3.7) is in semi-discrete form, continuous in time and discrete in size space. The

finite volume discretisation leads to the same form of (3.6) with the addition of nucleation terms. The fluxes of Equation (3.6) can be calculated in several ways in order to take into account higher-order finite volume discretisation methods, such as from simple upwind models to high-resolution methods [141]. The first-order upwind scheme can be considered by using the following approximation, shown in Equation (3.8), for calculating the fluxes:

$$(Gn)_{L_i^+} = G_{L_i^+} n_i \qquad (Gn)_{L_i^-} = G_{L_i^-} n_{i-1} \tag{3.8}$$

where the surface growth term with negative sign is the flux on the left cell face, and with the positive sign is the flux on the right cell face. For clarity, the 1/2 flux symbol is dropped. This is the simplest upwind scheme formula, where n_i is the cell averaged value located at the cell centre and $G_{L_i^+}$ are the values of size dependent growth at the right face of each cell [141]. A more complicated expression of high-order accuracy can be incorporated using a piecewise polynomial interpolation [141].

$$(Gn)_{L_i^+} = G_{L_i^+} \left(n_i + \frac{1+\kappa}{4}(n_{i+1} - n_i) + \frac{1-\kappa}{4}(n_i - n_{i-1}) \right) \tag{3.9}$$

The κ is a parameter used to define different discretisation type and order. This kind of κ-interpolation is originated in the work of Van-Leer [145]. By using κ equal to -1, a second-order upwind scheme is obtained; if κ is defined equal to 1, a standard second-order central scheme is obtained [141]. The second order central scheme is shown in equation (3.10).

$$(Gn)_{L_i^+} = \frac{1}{2} G_{L_i^+} (n_{i+1} + n_i) \tag{3.10}$$

The κ can also take any other intermediate values between -1 and 1, resulting in a blend of the second-order upwind and central schemes [141]. One example of this type interpolation is the high resolution proposed by Koren [146], with an intermediate value $\kappa = 1/3$. After some algebra, the original flux expression (3.9) is found in its final form in the following expression:

$$(Gn)_{L_i^+} = G_{L_i^+} \left(n_i + \frac{1}{2} \Xi(\theta_i^+)(n_i - n_{i-1}) \right) \tag{3.11}$$

where θ_i^+ is a ratio of the adjacent number density values at the right cell face, and is defined as $\theta_i^+ = \frac{n_{i+1} - n_i + \epsilon}{n_i - n_{i-1} + \epsilon}$. $\Xi(\theta_i^+)$ is the flux limiter, and as Koren [146] suggested, it is defined as $\Xi(\theta_i) = max(0, min(2\theta_i, min(1/3 + 2/3\theta_i, 2)))$. Using κ equal to -1, a second-order upwind

scheme can be extended to include a limiting function. There are several limiting functions that can be used according to [144] (e.g. minmod). The flux term with κ equal to -1 and including the flux limiting function is given below.

$$(Gn)_{L_i^+} = G_{L_i^+}\left(n_i + \frac{1}{2}\Xi(\theta_i^+)(n_{i+1} - n_i)\right) \tag{3.12}$$

where $\theta_i^+ = \frac{n_i - n_{i-1}}{n_{i+1} - n_i}$. The choice in this thesis is to implement Van-Leer flux limiter, which can be seen in the Equation (3.13).

$$\Xi(\theta_i) = \frac{|\theta_i| + \theta_i}{1 + |\theta_i|} \tag{3.13}$$

A major disadvantage is that the piecewise interpolation cannot be applied in a straightforward manner to the boundaries of the 1D PBE, because the high-resolution interpolation requires three number density points as inputs. An example of this kind of problem is at the nucleation point, two of the three points are located outside the current grid domain size. The inlet boundary or first grid point of the PBE is the minimum size of the particles or 0 size of particles [146], and the flux limiter formulation will search for the two points behind the nucleation non-existent points. This problem is alleviated by setting few grid points outside the computational domain, and forcing them to equal 0. In this thesis the limiter function is estimated by the Van-Leer expression. In [141], a slightly different implementation of this high resolution finite volume is examined where instead of using dummy points behind the nucleation point, at the nucleus size and the second grid point, a first-order upwind scheme is implemented at the nucleus points; on the rest of the grid points, the flux limiter implementation is applied normally. This configuration has been compared against analytical solutions and other numerical schemes. In [141], the high resolution method is less diffusive and avoids numerical dispersion under nucleation, size-dependent and size-independent growth rates, with good accuracy for relatively coarse grids.

3.3 Initial distribution test

In this section the nucleation, coagulation and breakage terms are neglected, where the PBE represents pure growth mechanisms and is a simple hyperbolic equation. This form suffers from several numerical difficulties associated with discretisation techniques. As such, many

studies have been performed to compute the convective form accurately, especially in CFD applications. In this section a distribution of particles is already specified in several initial points in the diameter size domain. The initial PSD will convect across the domain with a constant growth term towards a higher size of particles. This is the simplest problem of all, and many studies used this step function formulation to test a variety of different shapes of the number density function and its accuracy regarding the convection mechanisms in the particle size domain [22]. The initial distribution $n(d_p, t)$ is specified as follows, with growth term equal and constant at 1 m/s. The initial distribution is assumed to have a rectangular shape.

$$n(d_p, 0) = \begin{cases} 1, & 2 \leq d_p \leq 4 \\ 0, & otherwise \end{cases}$$

The initial particle size distribution (PSD) will be convected only through constant growth mechanism. In this section, the step function is an ideal case to examine several discretisation techniques. The finite volume schemes that were explored in terms of their convection accuracy are the first-order upwind, the second-order central and TVD schemes. The following methods are compared against the analytical solution of this simple step function for three uniform grid resolutions. The grid spacing (ΔL) between the points of the particle size domain is specified as 0.5 m, 0.25 m and 0.05 m for the coarse, medium and fine mesh quality respectively. The same grid parameters are applied for all the simulations of the initial distribution test. Figure (3.2) shows the PSD of the first-order upwind scheme for three different mesh configurations. It should be noted that with constant growth rates and uniform mesh size, the finite element collocation type of Rigopoulos and Jones [24] is identical to the first-order finite volume upwind scheme. The time derivative is solved for all cases with the explicit type Euler discretisation.

The first-order upwind scheme shown in Figure (3.2) for an initial rectangular number density distribution is compared with an analytical solution. The rectangular initial distribution is convected through time and should have the exact same shape and same peak value at its final time step with the distribution at the initial step. The convection processes of the PBE are performed for a total time of 6 s. However, the first-order upwind scheme was found to be very diffusive; the peak value is lower than the analytical one, and formed a wave shape instead of a rectangular structure after 6 seconds. On the other hand, in the same Figure (3.2) two improved meshes are employed, one medium and one fine. It was found that by improving the resolution of the mesh, a better prediction is achieved, and the predicted results converge

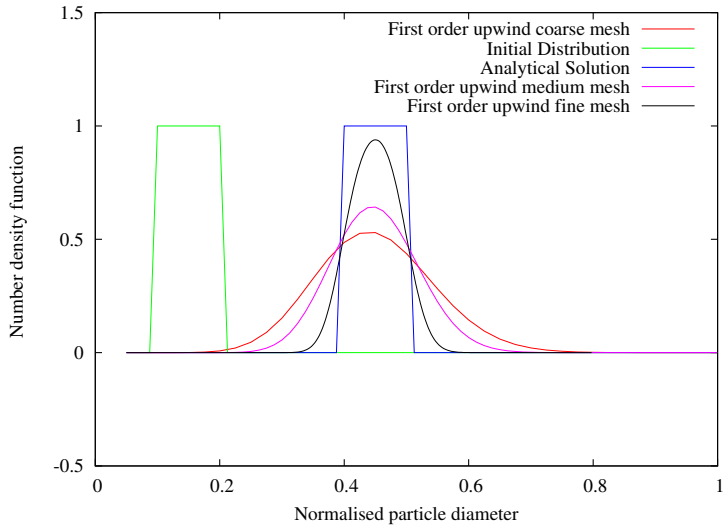

Figure 3.2: PSD upwind step function

towards the analytical solution without producing any negative values. The Figure (3.3) shows the PSD for the second-order central scheme.

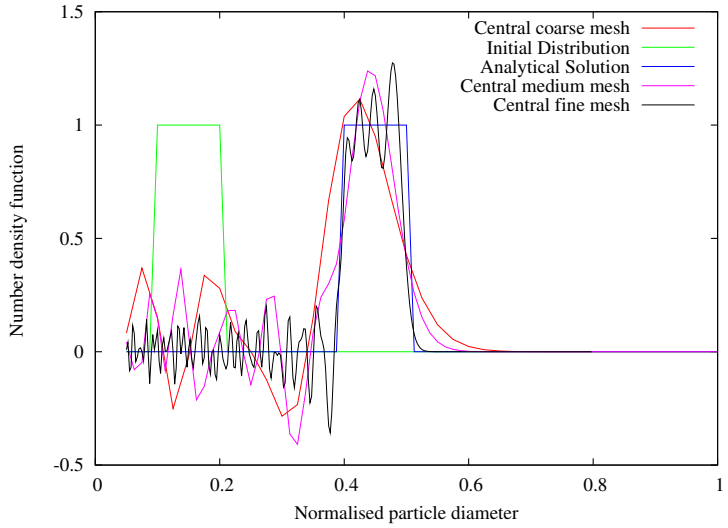

Figure 3.3: PSD second-order step function

The second-order central scheme as expected produces several oscillations, starting from the initial distribution and extending towards the middle of the PSD. As such, the oscillations produced negative values, especially in the beginning of the PSD domain. These oscillations could be reduced by filtering them out, or simply by applying a 0 value to the negative number

density values. Three different grids are tested (coarse, medium and fine mesh). The accuracy of the PSD is slightly improved by having a finer mesh, but the oscillations and negative values still remain. Even by refining the mesh, more oscillations were produced, and new oscillations appear in the peak value of the PSD. However, the moments of the distribution were more accurate with finer mesh. The Figure (3.4) shows the PSD of the finite volume scheme with Van-Leer flux limiter.

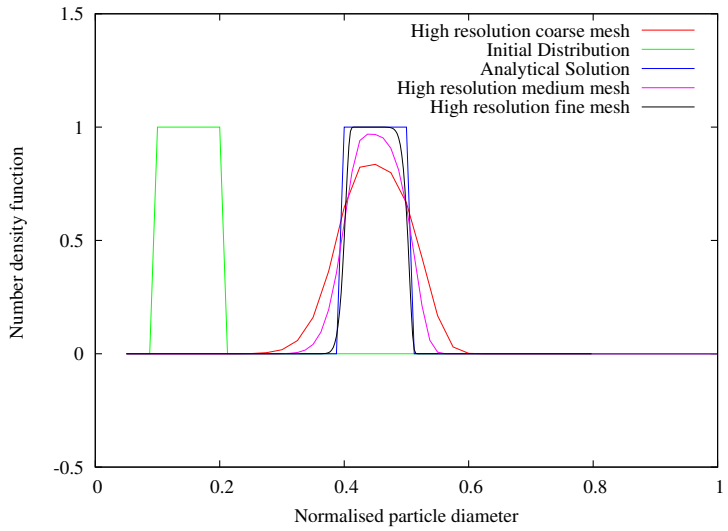

Figure 3.4: PSD TVD Leer scheme step function

No overshoots are computed at the peak values for the Van-Leer flux limiter and negligible amount of negative number density values appear along the normalised size domain at the front (upstream) part of the distribution for the fine mesh. Other flux limiters can be used as well, such as the Koren limiter as shown in Figure 3.5.

The Koren limiter has also been used in this step function formulation, and the results were found to be very similar to the Van-Leer limiter results (no overshoots) but with negligible negative number density values at the tail (downstream) of the distribution for the fine mesh. Three different grids are shown in Figure (3.4). It should be noted that these three grids are uniform, and the same mesh formulation is applied to all the discretisation techniques in this section.

Despite the underprediction of the upwind scheme where the solution is smeared and the oscillations of the second-order central scheme, the moments of the distribution are more closely predicted with the TVD scheme. As such, the PSD is more accurate with the flux limiter than

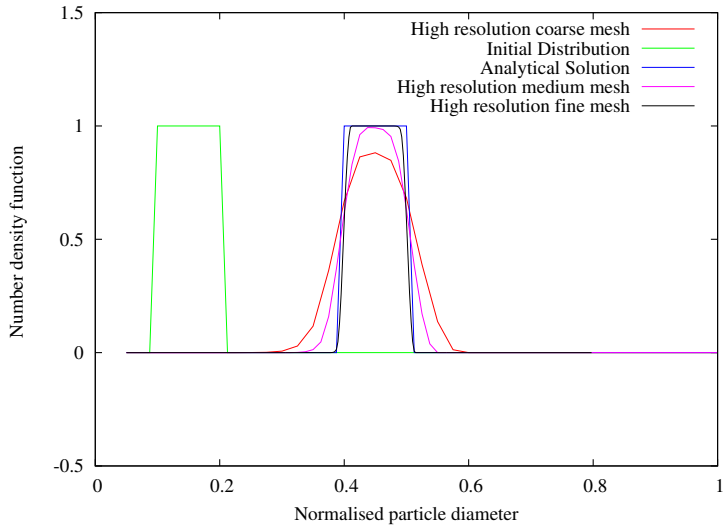

Figure 3.5: PSD TVD Koren scheme step function

the other applied methods, but still requires a sufficient mesh to capture results accurately. However, the TVD schemes (i.e. Van-Leer and Koren) can produce negative values in the front and tail part of the distribution. These negligible amounts of negative number density values can be avoided by imposing all the negative values to 0. Setting the negative number density values to 0, the PSD and the moments of the distribution of the TVD schemes are unaffected. On the other hand, the oscillations of the second order central scheme in the front part of the distribution are removed and the rest of the PSD is slightly affected by it and the relative error of the number density compared to the analytical solution is improved. However, the error of the moments of the distribution is increased. An interesting feature to compare the results of the numerical schemes is the relative error of the number density shown in equation (3.14)

$$Error = \frac{\sum_{l=1}^{N_{sc}} |n_l - n_l^{exact}|}{\sum_{l=1}^{N_{sc}} |n_l^{exact}|} \tag{3.14}$$

The relative error of the mass is computed with the 3^{rd} moment of the distribution (see equations (2.102) and (2.103d)). The table 3.1 demonstrates the errors between the different grid formulations for all the numerical schemes without imposing a 0 value to the negative number densities.

It is concluded that the TVD schemes proved to predict the PSD more accurately for the same grid formulation compared to the first and second order schemes according to the number density errors. However, the 3^{rd} moment error is lower for the second order scheme. On the

	Grid	$n(d_p, t)$ error (%)	3^{rd} moment error (%)
1_{st} order	Coarse	101.00%	36.41%
	Medium	83.77%	16.24%
	Fine	44.97%	1.22%
2_{nd} order	Coarse	91.57%	23.28%
	Medium	84.75%	10.10%
	Fine	49.69%	0.07%
Van-Leer	Coarse	49.21%	25.29%
	Medium	31.64%	10.98%
	Fine	12.37%	0.19%
Koren	Coarse	42.30%	24.50%
	Medium	26.43%	10.75%
	Fine	9.81%	0.16%

Table 3.1: Error of the number density and 3^{rd} moment

other hand, the number density errors of the second order are much higher compared to the TVD schemes because of the oscillatory behaviour. The PSDs and their peak values are more uniformly and accurately captured with the TVD scheme.

3.4 Parallelisation

3.4.1 Introduction

Modelling of soot formation in laminar and turbulent flames requires an extensive computational effort to solve the chemistry and the discretised PBE. As such, the chemistry and discretised PBE parts of the laminar flame code are parallelised, and their performance is assessed and examined in terms of numerical speed. It should be noted that the finer the mesh of the computational domain, the higher computational effort is required to perform a single time step. Therefore, it is important to distribute the workload of the chemistry and discretised PBE into several processors to enhance the speed per time step. Parallel programming divides the computationally intense parts of the code and assigns the split parts to different processors that are then solved simultaneously to speed up the simulations. The major drawback of this strategy is the excess time needed to perform the communications between the processors, which affect the total speed of the simulation. Several factors should be ensured for a successful parallel simulation.

- The new scaling methodology (parallel programming) of the CFD code should have exactly the same numerical results with the serial code (1 CPU). No error should be produced through the communications, and the results should not deviate from the serial simulation. The parallel code should be efficient and with a sufficient speed-up factor that does not compromise the numerical solution.

- An efficient strategy would be that the workload is distributed evenly among the processors. Otherwise, the slowest processor will slow down the simulation. Moreover, some parts of the code that cannot be parallelised and are executed with one CPU should be kept to a minimum.

- Excess time due to communication (overhead) should also be kept to a minimum. The overhead appears due to exchanging information between the processors.

An effective scaling was performed, and a time analysis of a simulation was carried out with one CPU. This was done to gather a record of computational times at different parts in the code in order to understand where parallelisation is needed and which processes are actually slowing down the simulation. In this thesis, the time analysis of each section of the code starts first with a fully laminar converged flame with one CPU for three time steps. The computational domain is the heaviest one performed in this thesis, where 100x200 points are used for the computational grid with a comprehensive gas-phase chemistry for ethylene combustion of 75 species and 529 chemical reactions from the University of Southern California [147] and 400 grid points in the size domain of the PBE with uniform spacing $\Delta L = 0.6nm$.

The parts of the code can be parallelised if they are independent of the other computational grid points. This means that all the necessary information for performing the computations already exists at the same grid point. Two strategies of parallelisation could be that a) each independent grid point or b) blocks of grid points are assigned to different CPUs. The most common methodology to achieve parallelisation is the second strategy via domain decomposition [14]. An illustration of both methodologies is shown in Figure 3.6 assuming that four processors are assigned to solve the computational domain.

Each cell contains the number identity of a processor. For example a cell with a number 1 means that this cell is assigned to the first CPU whereas the cells with the number 2, 3 or 4 are assigned to the second, third and fourth CPU respectively. The same numbering is similarly used for the domain decomposition (Figure 3.6b) where a whole block of cells

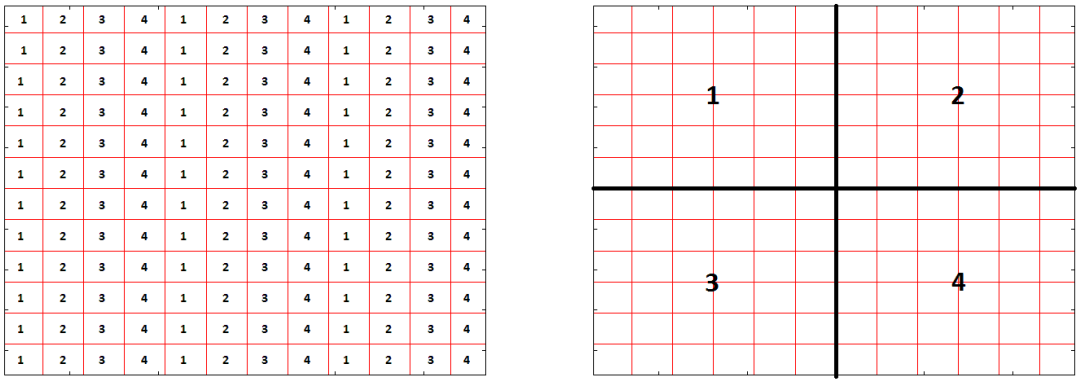

(a) Distribution in each grid (b) Domain decomposition

Figure 3.6: Parallel scheme

are assigned to different CPUs. The domain is decomposed into several smaller sub-domains (blocks), and communication occurs only at the interface of those blocks. This an advantage of the domain decomposition where less computational time is spent in communications (less overhead) between the CPUs as opposed to the first strategy where communications occur between all the mesh cells. However, a significant drawback of the domain decomposition is that a whole block could contain a larger part of the flame than the other blocks where stiffer equations appear resulting in a non-evenly distributed workload. The block with less work to execute will result the CPU to finish the calculations earlier and wait (waste time) the other CPUs to complete their calculations.

Thus, to avoid this problem the first strategy is implemented to this thesis as the workload is distributed more evenly across the processors. A time analysis is performed in the next section to investigate the overhead time of the first strategy.

3.4.2 Time analysis of the code

A time analysis is performed of the most computationally expensive laminar flame model in this thesis with 100x200 grid points in radial and axial directions with detailed chemistry, complex transport coefficients and PBE modelling. The mesh of the CFD and PBE is kept constant for all the time investigations. Time measurements are taken for different part of the code section. Three time steps are used, and the total amount of time to complete them is averaged to get the time for a single time step. Time is measured for several processes in the code: these are the complex transport coefficients (mixture viscosity and mass diffusivity of all species), the governing equations of momentum, pressure correction, species, enthalpy and discrete sizes of

soot number density. According to the time measurements all the processors require more or less the same time to complete the chemistry and PBE calculations. The Figure (3.7) shows the time analysis of the laminar flame code when 1 CPU is assigned to it.

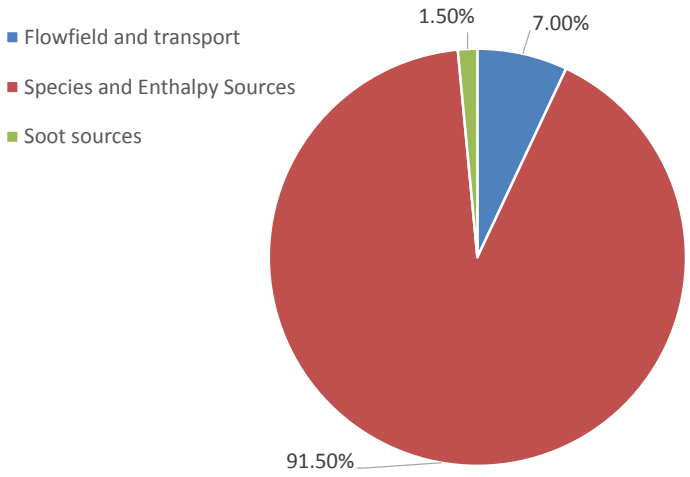

Figure 3.7: Time percentage for each section

The following percentages have been acquired for three sections across the laminar flame code with a single CPU and three time steps. It should be noted that the actual time of the simulation with a single CPU is approximately 103 s per time step and with 16 CPUs is 12 s per time step. The 91.5 % of the entire calculation is spent on the calculation of species and enthalpy (e.g. radiation) source terms in the composite domain. The remaining percentage is covered by approximately 7 %, which is the computation of the complex transport coefficients and convection-diffusion of all scalars; only around 1.5 % represents the computation of the soot sources, which essentially solves the mechanisms in the internal coordinate space. This is not very significant when compared to the species. It may not sound reasonable that soot source terms is only a very small fraction of the entire simulation, but if one considers that the PBE equation does not solve for any integrals (e.g. coagulation or aggregation) because they are omitted, then the structure is a simple hyperbolic form that is very fast to compute, even by one processor.

According to this information, it is essential to parallelise the computation of the chemical source terms that account for the largest part of the time analysis percentage. Moreover, to achieve a better scaling in this code, the computation of the transport coefficients and the PBE source terms are also parallelised by using the same parallelisation technique. As such, each processor obtains the complex transport coefficients, chemical source term and PBE source terms for a specific grid point in the domain. The diffusion-convection process is kept serial

and is not parallelised, as it is not independent of the grid points due to the consideration of several gradients. The following figure shows the scaling of the code for different numbers of processors : 1, 2, 4, 8, 12 and 16. The scaling is examined in the HP (Hewlett-Packard) workstation with 16 processors in total. The total number of grid points in all the simulations is kept constant.

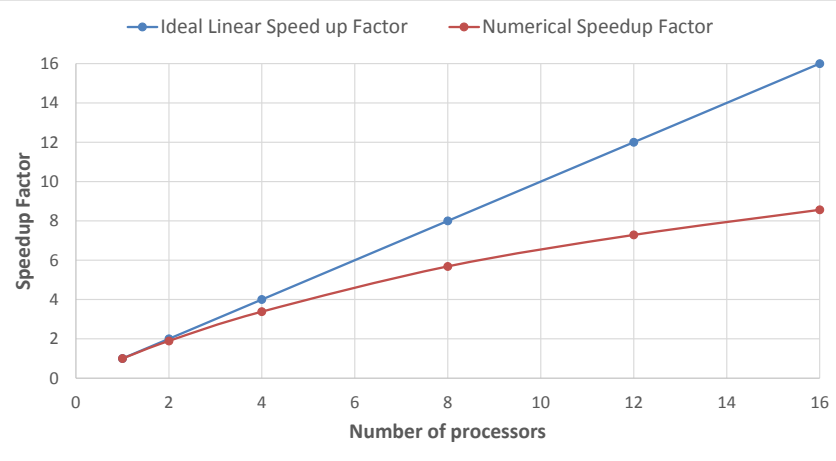

Figure 3.8: Laminar flame scaling

In Figure 3.8, the performance of the parallelised code is illustrated. The ideal linear line represents the optimum increase in speed that could be obtained by the addition of a number of CPUs. This ideal parallelisation is increased linearly with the slope equal to unity. In reality, this is not possible because of the overhead (excess computation time) that is associated with the communications between the processors to transfer the data. Another source of time waste is the computation of several parts of the code with a single CPU as they cannot easily be parallelised. The numerical speedup factor forms a curve, as can be seen in the Figure 3.8; its slope is slowly decreasing with the addition of CPUs. The reason for the drop of the parallel's efficiency is because of the overhead and the computation of the convection-diffusion processes by a single CPU. The efficiency could be further increased if the transport processes were parallelised, as well with extra care in having the fewest amount of communications as possible. A speed factor of 8.5 is achieved when 16 processors are used, reducing the computational time of each time step in 12 seconds using all the coupled phenomena for this heavy mesh. However, removing all the soot processes (i.e. the soot convection-diffusion and source terms) the speed factor that is achieved is 11 with 16 processors. This great drop of speed factor from 11 to 8.5 is found to be due to the high number (400 transport equations) of convection-diffusion

processes which are solved by a single processor and not by the communications. It should be noted that equal load distribution is achieved for this parallelisation where the processors have an almost negligible time difference (less than 1 %) when they finish the computation of transport coefficients, species and soot source terms. The same parallelisation technique is used for the turbulent flames where each CPU is assigned for a specific computational cell. The scalar information of all the stochastic particles that are located inside the same computational cell are solved by the same CPU which is assigned to.

Chapter 4

Soot kinetics and PBE in 0D and 1D models

In this chapter the simplified reactor systems are solved with greater emphasis on the study of soot kinetics and on how the different soot models behave under the same conditions of the reactors and parameters of the PBE. The two-transport equations model is usually accompanied by the implementation of acetylene-based soot kinetics and oversimplified aggregation models, because of the assumption that the PSD is monodisperse. A more detailed model is the ABF formulation, where the first six moments of the distribution are solved. So far, the ABF formulation is only accompanied by the implementation of PAH-based soot kinetics; more complicated coagulation mechanisms can be applied. No attempt has been made by the authors of the ABF formulation [79] to reproduce the complete PSD from these six moments. The mathematical description of every model is explained briefly in Chapters 2 and 3. The analysis will start with a batch reactor that will be coupled to a PBE to explore how the PSD evolves in time; later, the PSD will be examined in PSR and flamelet models. The problems are divided into two parts: the PBE formulation with volume size as the internal coordinate to include the coagulation mechanism, and the PBE formulation with particle size diameter as the internal coordinate to simplify the convection term of particles where the growth term becomes constant in this space coordinate. No coagulation is considered when the diameter is employed as the internal coordinate. The PBE grid in most of the cases is uniform in the particle diameter space and in a few others is exponential in the volume domain due to the excessive amount of volume points that are required to capture the large size spectrum of the soot particles. An illustration of both grids is shown in Figures 4.1 and 4.2.

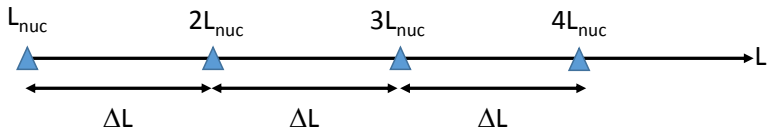

Figure 4.1: Uniform diameter domain

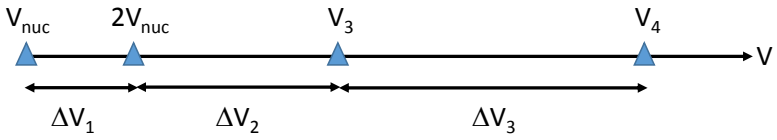

Figure 4.2: Exponential volume domain

4.1 Batch reactor simulation

In this section, the PBE is coupled to a batch reactor system. This reactor operates under adiabatic conditions at constant pressure. The conservation equations of the batch reactor (i.e. species, enthalpy and discrete sizes of soot particles) are listed in section 2.2.2. More information about the mechanisms of the PBE can be found in the equation (2.109) by dropping the spatial dependency as the batch reactor is assumed to be well mixed (homogeneous system). The soot kinetics are those listed in the summary of Chapter 2 in Equations (2.110)-(2.113). This formulation has been compared with the moment transformation Equation (2.108) for batch reactor and a method of characteristics to examine the moments of the distribution and PSD respectively. The consumption of species due to soot formation and any radiation models are ignored in these simplified systems, as the primary concern is the examination of the PBE's accuracy and performance. It should be noted that nucleation, surface growth and oxidation mechanisms are included to this model. The soot kinetics that are applied and tested in this section are those to be implemented into the multidimensional flames of Chapter 5 and 6 except the surface growth rate which has been decreased by two to reduce the large spectrum of the PSD domain. The parameters of the batch reactor are listed in table 4.1.

In Figure (4.3) the number density function is shown, and compared between the method of characteristics and two discretised PBEs (first order upwind and Van-Leer TVD scheme) with a uniform mesh and spacing (ΔL) equal to $2.41 \cdot 10^{-9}$ m. The method of characteristics yields an exact PSD, as it is free of numerical diffusion. At initial time $t = 0$ there are no particles in the system. By observing the PSDs of Figure (4.3), it is clear that for the same uniform mesh the

Equivalence ratio	3.0
Fuel	C_2H_4
Oxidiser	air
Total integration time	0.1 s
Time step	10^{-4} s

Table 4.1: Batch and PSR parameters

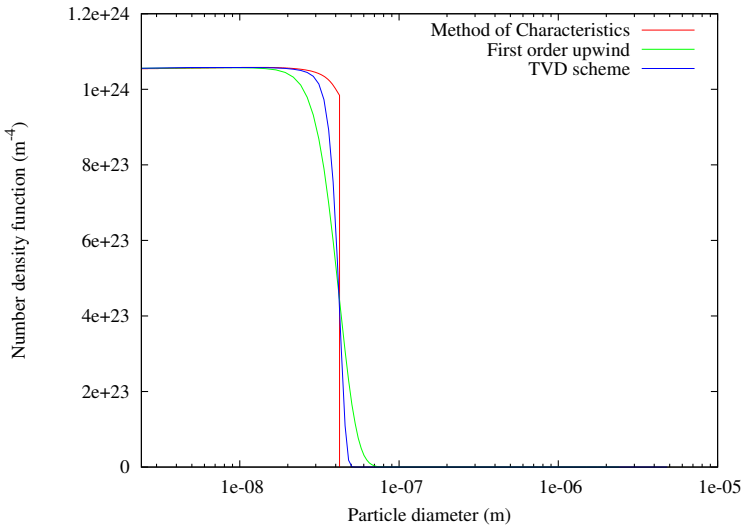

Figure 4.3: PSD from batch reactor

TVD scheme predicts a better PSD compared to the first order upwind. It should be noted that by increasing the mesh resolution even further, the PSD results of both methods are improved and converge towards the method of characteristic results. The moments of the distribution are also compared with the exact results obtained from the moment transformation. The following Figure (4.4) compares the total number of particles.

The total number of particles from the method of characteristic, first order upwind and TVD schemes are compared with a moment transformation. All the methods using the same uniform PBE mesh predict excellent agreement of the 0^{th} moment through time. The next figure (4.5) compares the same models, but for the third moment of the distribution (the soot volume fraction).

The comparison of a higher moment between the models produces some visible discrepancy. The method of characteristics has an excellent agreement with the exact solution of the moment transformation method by solving Equation (2.108), as expected. However, the first order upwind exhibits higher discrepancy by significantly overpredicting the soot volume fraction,

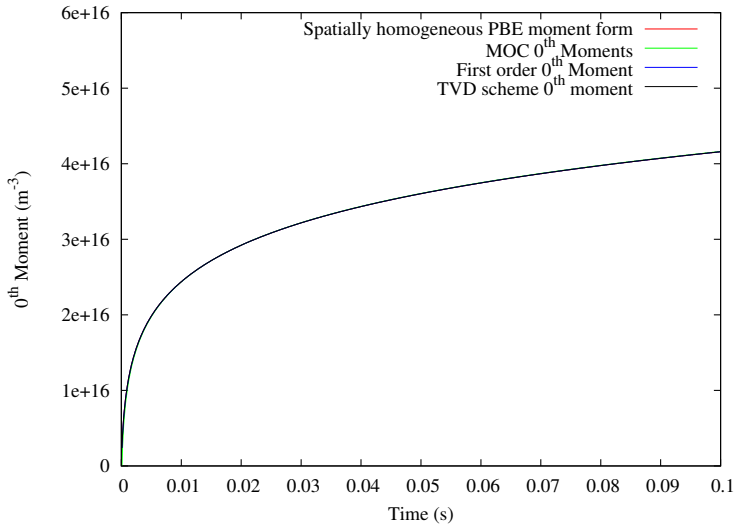

Figure 4.4: 0^{th} moment on batch reactor

whereas the TVD scheme has a closer agreement to the exact solution exhibiting a slight underprediction. With an increased mesh resolution, the moments of the distribution are predicted almost identically to the exact solution.

The other possibility that should be examined is the validation of both methods using a different internal coordinate, such as volume size. In this way, the same models are investigated under the same conditions and soot kinetics for a volume size internal coordinate. The difference, as stated before is that by using the volume size as the internal coordinate, the surface growth mechanisms are becoming size-dependent. Then also, more sophisticated numerical schemes are required to predict accurate results. With volume size as the internal coordinate the first order upwind techniques are split into the finite element and finite volume technique, as their formulations to compute size-dependent growth mechanisms are different.

Only the first order schemes are employed without the TVD schemes, and their moment results are compared against the moment transformation and the method of characteristic results. It should be noted that the method of characteristic and the moment transformation are solved for particle size diameter as the internal coordinate. For the moment transformation, if the volume coordinate is employed, the surface rates are size-dependent and the solution of the soot mass fraction requires the knowledge of the surface area (fractional moment). The surface area requires a closure assumption such as monodisperse or log-normal distribution. On the other hand, the number density function of diameter-based obtained by the MOC can be

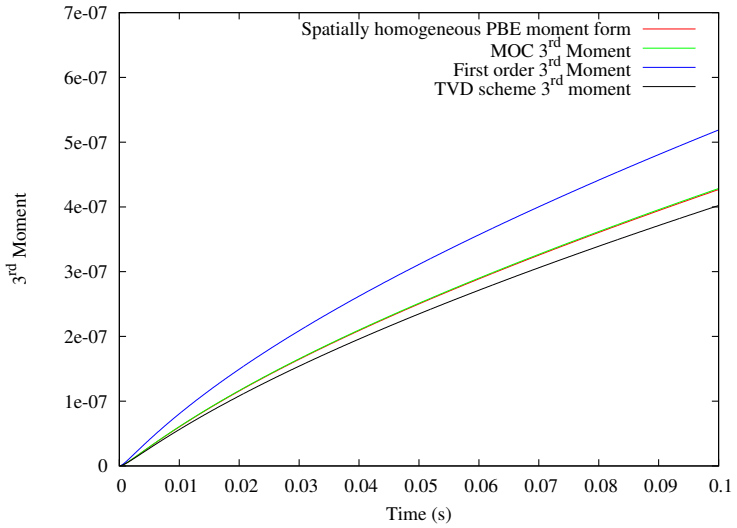

Figure 4.5: 3^{rd} moment on batch reactor

transformed into volume-based with an appropriate shape factor (spherical assumption).

The exact solution of the PSD is obtained from the method of characteristics with diameter as the internal coordinate, instead of resolving it again for the volume size internal coordinate where fluxes need to be handled differently in the volume domain. This simple method is to transform the number density as a function of particle size diameter of the method of characteristics into a number density function of particle volume size. With this transformation, the exact number density function of volume size is quickly obtained and compared against simulations of finite element and finite volume upwind schemes of uniform mesh. It should be noted that a uniform mesh of volume size requires an excessive number of grid points compared to particle size diameter (e.g. v $\sim d_p^3$). The finite element method and finite volume method of the PBE are solved with an upwind scheme and a volume grid with equidistant $\Delta V = 7.3291 \cdot 10^{-27} m^3$ (grid spacing). The following Figure (4.6) shows the number density function in terms of volume size:

Despite the excessive mesh used to discretise the number density functions in the volume size domain, the finite element of collocation type does not accurately predict the number density function; it is underpredicted compared to the transformed MOC. By using the finite volume technique in the volume size domain, though, the number density function is captured well. Therefore, the method of finite volume seems to be more appropriate for studies where the coefficient of the convection term is a variable and a function of size and not a constant and

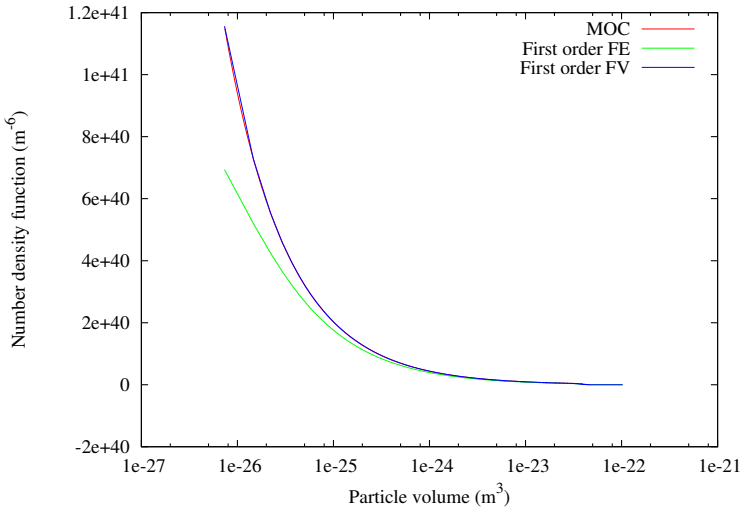

Figure 4.6: Number density functions in terms of volume size

independent of size. Moreover, the moments of both methodologies are shown and compared with the transformed PBE in Figures (4.7) and (4.8).

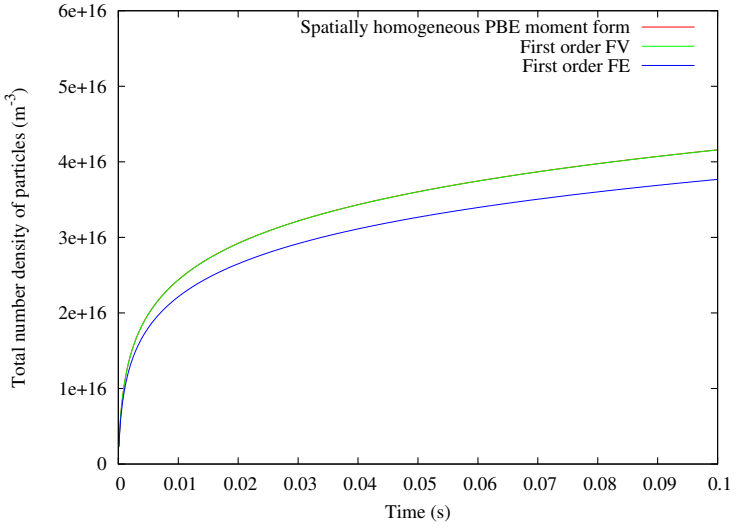

Figure 4.7: Total number density (m^{-3}) with volume as internal coordinate

By observing the moments of the distribution in Figures (4.7) and (4.8), the total number of particles is better predicted with the finite volume instead of the finite element (by which it is underpredicted). However, the first moment of the distribution is similarly well-predicted by both models relative to the exact solution. The finite volume performs a little better than

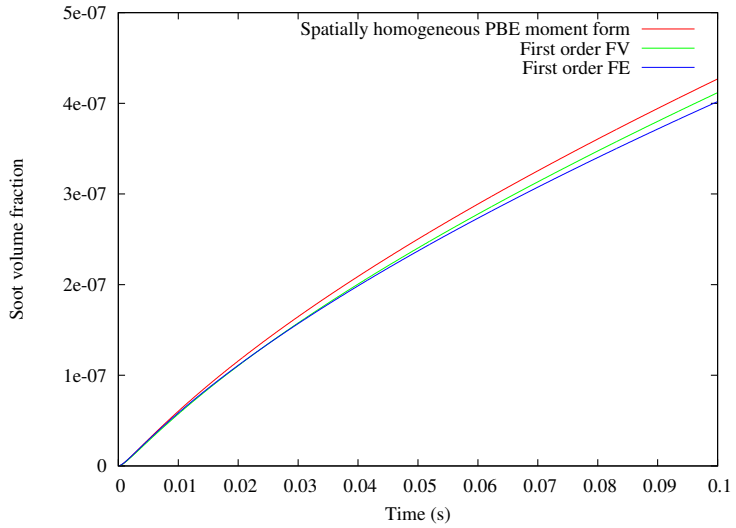

Figure 4.8: Soot volume fraction with volume as internal coordinate

the finite element for the first moment. It is clear that the MOC is better than all the models, due to the moving grid and elimination of numerical diffusion. However, the MOC method is more time-consuming than the fixed grid discretisation schemes, and problems arise around the nucleation points where they should be fixed in the size space. With the MOC, these points are moving. Therefore, MOC is suitable only for basic system simulations, and not for a fully CFD application.

In addition, the PSD is reconstructed from a set of moments (40 moments) and compared with the MOC and the TVD scheme. The reconstruction of the PSD is achieved according to the discrete method in [97] where the shape is not known prior to the computation. Several problems appeared from reconstructing the PSD and they are mentioned in Chapter 3.

Nucleation and coagulation

The PBE is further examined for nucleation and a size-independent coagulation mechanism. Two coagulation approaches are used. The original coagulation mechanism described in the finite element approach of Rigopoulos and Jones [24] and a fixed pivot technique found in [122]. The coagulation mechanism with a finite element method and the fixed pivot technique are discretised in the volume size domain with an exponential grid and an increment of $\zeta = 1.08$. The equation (4.1) is used to discretise the volume domain with an exponential grid.

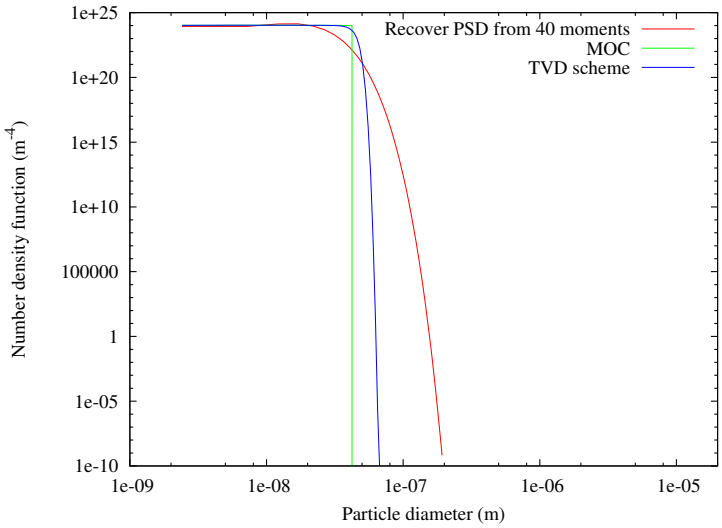

Figure 4.9: PSD reconstruction

$$v_l = v_{nuc} + v_{nuc}\frac{1-\zeta^{l-1}}{1-\zeta}, \qquad l = 3, ..., N_{sec} \tag{4.1}$$

The high mesh fixed pivot technique is discretised with uniform volume grid with spacing $\Delta V = 7.3291 \cdot 10^{-27} m^3$. Both methods are shown in Figures 4.10 and 4.11 for the volume size internal coordinate.

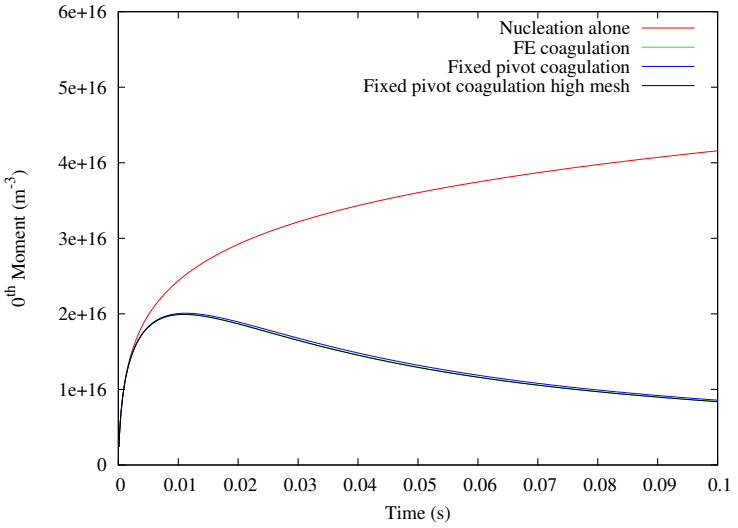

Figure 4.10: Coagulation 0^{th} moment

The total number density of particles in Figure 4.10 is reduced when coagulation mechanism

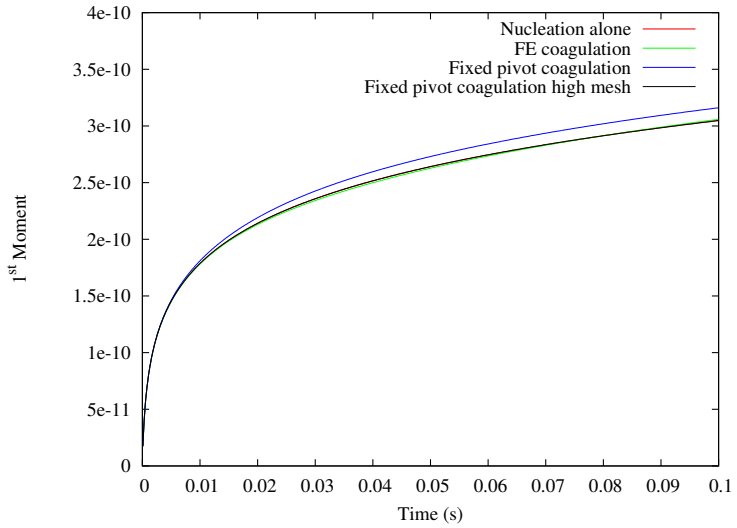

Figure 4.11: Coagulation 1^{st} moment

is applied compared to the nucleation mechanism alone. Both fixed pivot technique and finite element coagulation mechanisms have an almost identical prediction. However, in Figure 4.11 where the volume fraction is examined the exact solution should be the nucleation's volume fraction as the volume of particles should be conserved through the coagulation mechanism. The coagulation mechanism of Rigopoulos and Jones has better conservation properties than the fixed pivot technique using the same mesh. Finer mesh is required for the fixed pivot to match the conservation of the Rigopoulos and Jones model.

4.2 PSR reactor simulation

The same numerical schemes will be compared for a PSR system where there are inflow and outflow terms similar to diffusion in a computational cell. The moments of the PSDs of the PSR system are shown for a fixed residence time of 10^{-2} s. Uniform grid is employed in the PSR simulations with $\Delta L = 2.41 \cdot 10^{-9} m$.

By observing the results in Figures (4.12) and (4.13) very good agreement for the total number densities of soot particles is shown for all the models relative to the transformed PBE. The same applies for the third moment of the distribution, were some discrepancies exist for the simple upwind scheme and the TVD schemes. According to the results, the TVD scheme performs better than the first-order upwind scheme. In the PSR system no new soot particles

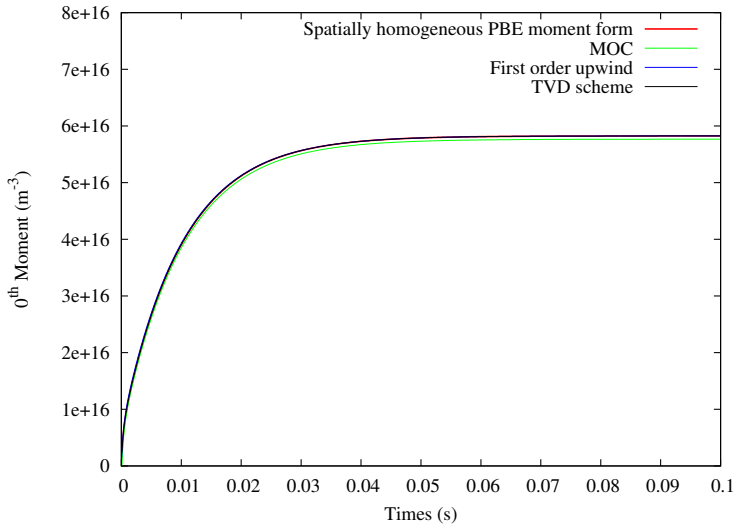

Figure 4.12: 0^{th} moment PSR

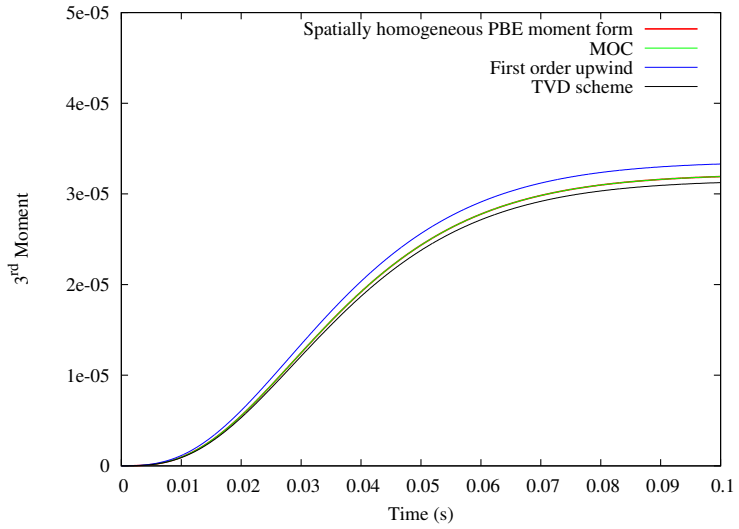

Figure 4.13: 3^{rd} moment PSR

are introduced through the inlet, and in the outlet a fraction of those particles exit the system.

The next Figure (4.14) shows the PSDs compared to the MOC prediction. It can be seen that when diameter as particle size is implemented, the numerical upwind scheme is very accurate through introducing many points into the particle size domain. Even the PSD, which is hard to address , seems to be very effectively processed by the TVD scheme as can be seen in Figure (4.14). The upwind scheme does not capture the abrupt fall (tail of the distribution) of the PSD, while the TVD scheme seems to capture it successfully. Even so, this uniform grid formulation

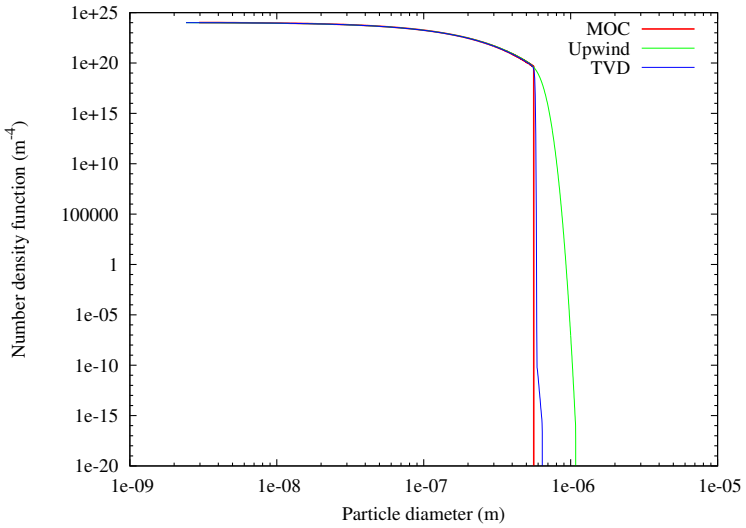

Figure 4.14: PSDs PSR

is sufficient for accurately capturing the PSD and the moments of the distribution. The TVD scheme will enhance this accuracy. It should be noted that no consumption and production terms are implemented to either batch or PSR systems in order to clearly investigate the effects of the discretisation schemes, and to find an optimum PBE grid and best parameters.

4.3 Flamelet simulation

The batch and PSR systems operated with the conditions listed in table 4.1. The surface growth rates were significantly stronger than oxidation rates and the convection term of the PBE in the one-dimensional space was basically solved in one-way direction. However, in the flamelet system, due to the stronger oxidation rates than surface growth rates at a few mixture fraction points close to the oxidiser side, the convection term of the PBE will have a two-way direction and some of the soot particles will be destroyed (completely oxidised). The moment transformation will not provide an adequate representation of the total number of particles as it does not take into account the destruction of soot particles of the oxidation process.

The flamelet code for C_2H_4 fuel and air as the oxidiser is discretised with two different uniform grids in the mixture fraction space with a total number of 100 mixture fraction points. The first uniform mesh is finer at the lower mixture fraction region (within the 0 to 0.15 range of mixture fraction) as higher temperature gradients exist in that area which are important as

the soot kinetics are highly dependent on temperature. In the second uniform mixture fraction space (within 0.15 to 1 range) the grid is coarser due to the uniform temperature profile in these regions. The first flamelet grid has a uniform spacing of $\Delta Z = 0.00224$ and the second $\Delta Z = 0.02656$. The PBE grid in the diameter space is uniform with $\Delta L = 1.205 \cdot 10^{-9} m$. The flamelet simulation is conducted with C_2H_4 as the fuel and air as the oxidiser. The total integration time is set to $0.05s$ and the time step is set to $5 \cdot 10^{-6} s$. Moreover, the flamelet equation is shown in equation (2.8) with the scalar dissipation rate equation shown in (2.10) and a strain rate (α_s) equal to $100 s^{-1}$.

Initially, only the surface growth rates (no oxidation) are implemented in order to use the moment transport equations in a 1D laminar system and obtain the exact moments of the distribution. Thus, the initial flamelet computations do not take into account the oxidation process of the soot particles in order to perform a comparison with the moment transformation. The Figure 4.15 shows the total number density of particles after reaching steady state in the mixture fraction space.

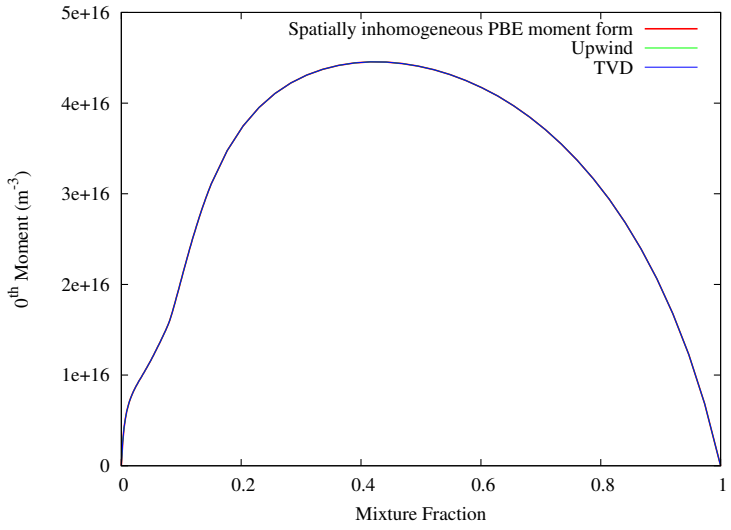

Figure 4.15: Flamelet 0^{th} moment - Nucleation + Growth rates

By observing the 0^{th} moment of the distribution by using the upwind configuration and TVD schemes, the prediction matches completely. The red line, which is the prediction of the upwind configuration, is exact identical to that of the TVD scheme; it is not possible to observe any difference in the 0^{th} moment in Figure (4.15). It should be noted that the flamelet system is the closer to the application of the multidimensional flame than the 0D systems studied previously.

The last parameter to be examined is the 3^{rd} moment, shown in the Figure (4.16).

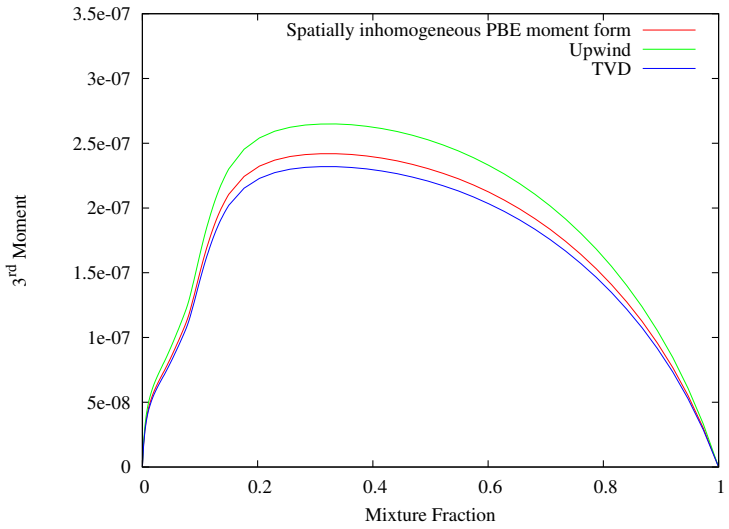

Figure 4.16: Flamelet 3^{rd} moment - Nucleation + Growth rates

By observing the soot volume fraction of all the methodologies, both the upwind and TVD schemes predict it well within reasonable accuracy. The TVD scheme predicts slightly better the soot volume fraction profiles compared to the upwind scheme. It should be further noted that a moment transformation is not used for the multidimensional flames because of the negative moments due to oxidation, and because they fail to take into account the destruction of the particles; the PBE model can handle this. For further analysis of both methodologies, PSD results are shown for this flamelet case in the Figure 4.17. Unfortunately, no analytical results of the MOC have been obtained to this model due to the complexity and computational expense arising from having a one-dimensional space (mixture fraction in this case).

The same behaviour as the previous 0D models is observed for the 1D flamelet as well. The PSD of the number density function exhibits a sudden drop at the bigger size particles, which is more accurately captured by the TVD scheme and not by the upwind scheme. Still, both models perform well in predicting the PSD and the moments of the distribution.

Before continuing to the multidimensional flame sections, it should be noted that the previous computations are performed for the soot kinetics and PBE parameters found to be the most appropriate. An investigation is performed for various soot models and kinetics, and their behaviour is examined. The findings of the soot kinetics applied to the flamelet model will be shown in the next sections.

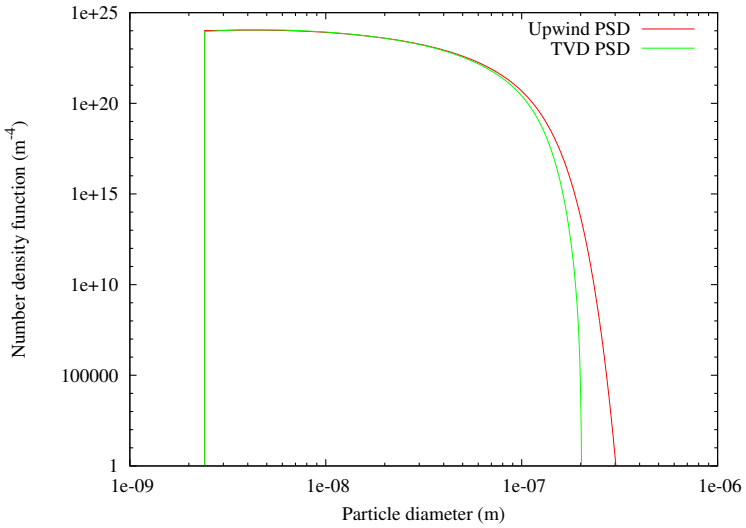

Figure 4.17: Flamelet PSD

4.4 Flamelet simulation with other soot kinetics

4.4.1 Acetylene-based soot model

In the literature, several soot kinetics are applied to both laminar and turbulent flames. Some of these are very successful. The majority of the soot models found in the literature have been applied to the 2TEM, which are acetylene-based. A number of those kinetics have been applied to the PBE model and compared with the 2TEM approach results to check if it is appropriate to apply them. Similarly to the equations (2.66) and (2.67) a simple acetylene-based soot model is applied with nucleation (4.2), surface growth (4.3) and oxidation kinetics (4.4) without the OH oxidation rate.

$$R_{nuc} = 2k_1(T)[C_2H_2]\frac{N_A}{Nc_{min}} \tag{4.2}$$

$$R_{growth} = 2k_2(T)f(A_s)[C_2H_2]M_s \tag{4.3}$$

$$R_{oxid} = k_3(T)A_s[O_2]M_s \tag{4.4}$$

These are the soot kinetics applied to the two transport equation model and PBE and their reaction rate parameters are listed in table 2.4. In the surface growth, the $f(A_s) = A_s$ is a

function of surface area. In [78] several functional assumptions have been considered for the functional dependence of soot surface growth. The surface growth by C_2H_2 and the oxidation by O_2 were implemented and are proportional to the surface area of soot particles.

The first function is the surface area of soot particles, taking into account the number of the active sites on the surface of the soot particles. A HACA mechanism is implemented in the first assumption. A second functional dependence is assumed to be directly proportional only to the surface area of soot particles, similar to what is used in the oxidation rates. This is probably the easiest way to implement in the PBE. The third assumption considered is that the surface growth should be a function of number of particles, and independent of the surface area. This assumption performed well with reasonable agreement. The fourth and final assumption which is implemented in [75] is that the surface area could be represented by the square root of the surface area of soot particles. This is a crude approximation to include the age reactivity of soot particles. For reasons of consistency, the best approximation to be investigated is the one where the surface area is proportional to the surface of soot particles both for surface growth and for surface oxidation. The next simulations are without coagulation and without the consumption terms of the species. Moreover, for the PBE the destruction of soot particles due to soot oxidation is omitted. The nucleation diameter is assumed to be approximately 1 nm according to [78]. The following models have been implemented with a volume size as the internal coordinate in order to include the coagulation terms. The simulations of this section are conducted in the the volume size domain discretised with the exponential grid shown in equation (4.1) and an increment (ζ) of 1.001. Because the soot kinetics are changed the nucleation point is also changed and set to $d_{p,nuc} = 1.04 \cdot 10^{-9} m$.

The following Figures (4.18) and (4.19) show a comparison of soot total number density and total soot volume fraction predictions respectively between the discretised PBE and the 2TEM. The results are for nucleation and surface growth only. The surface area in the 2TEM is closed by the first two moments. The same applies for the PBE, where the surface growth rate in the volume coordinate is assumed to be independent of size and is estimated by the same method as the two transport equation.

The results of the 0^{th} and 1^{st} moment, are in excellent agreement: the PBE in volume coordinate is exactly the same as the 2TEM if the surface growth rates are assumed independent of size and the PBE can be thought as monodisperse despite taking into account several volume sizes of particles. However, it is incorrect to evaluate the surface growth rates for the PBE as

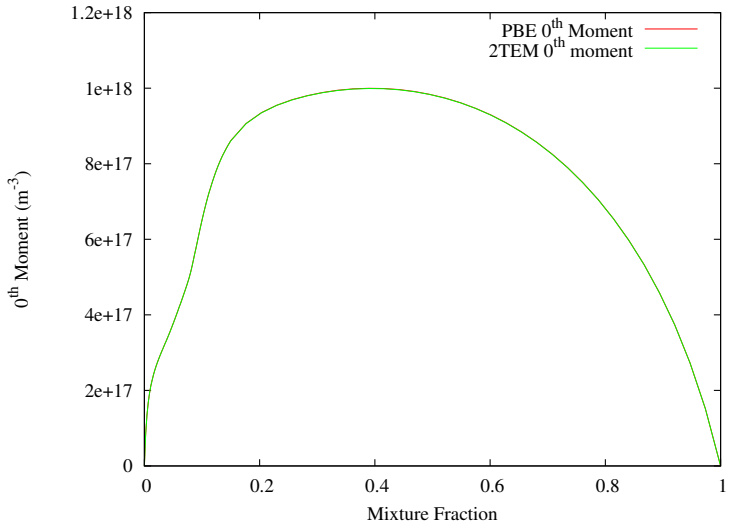

Figure 4.18: Flamelet profile of 0^{th} moment - Nucleation + Growth rates

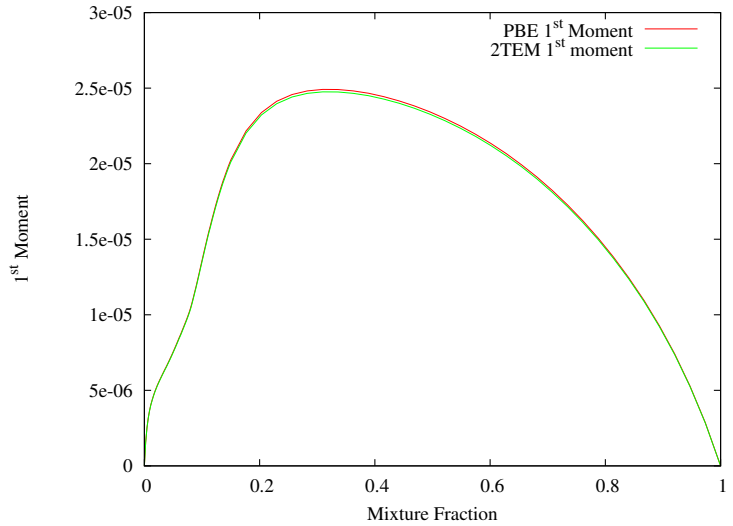

Figure 4.19: Flamelet profile of 1^{st} moment - Nucleation + Growth rates

independent of size in the volume size coordinate where according to many theoretical and experimental studies, the surface growth rate must be dependent on the surface area of soot particles. Therefore, from this conclusion also, the application of soot kinetics of any 2TEM that assumes monodispersity is incorrect and will lead to non-realistic results. In Figures (4.18) and (4.19) a significant amount of total number density of particles is observed in lean and rich mixture areas. The reason is because no oxidation model is applied to reduce the soot volume fraction in lean areas where oxidation mechanism is dominant or coagulation mechanism to

destroy the number of particles. This phenomenon will change in the next flamelet simulations as much less particles exist in lean and rich areas by including oxidation and coagulation.

Next, the full kinetics of a 2TEM and PBE are taken into account; these include nucleation, surface growth, oxidation and coagulation mechanisms. The same exponential grid is used (4.1) with $\zeta = 1.04$. Results are shown in Figures (4.20) and (4.21). The results of the first moments are compared again for the PBE relative to the 2TEM when destruction by oxidation is taken into account, and if not taken into account, as happens in the 2TEM model.

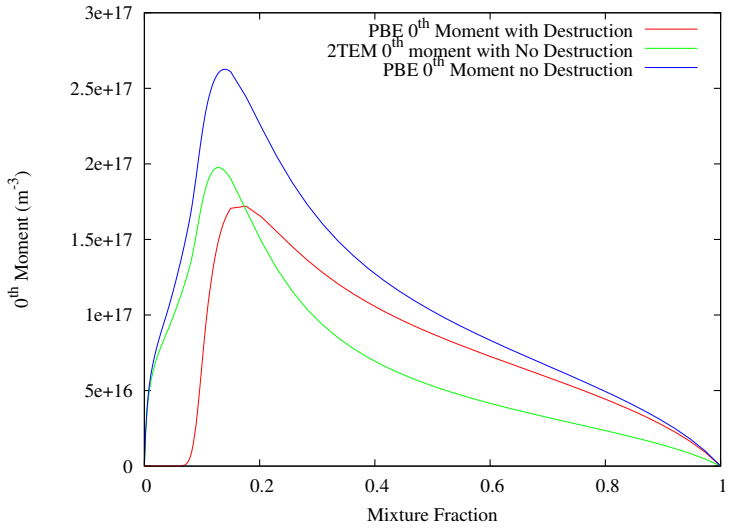

Figure 4.20: Flamelet profile of 0^{th} moment - Full soot kinetics

By observing the results, the soot number density of the 2TEM is in relatively good agreement with the PBE; if no destruction by oxidation is applied, though, the only destruction of soot number of particles is the coagulation mechanism. However, the results deviate when destruction by oxidation is taken into account and the plot of the 0^{th} moment is different. As can be seen in mixture fraction values of 0-0.1, the number density is very small or close to 0 due to oxidation. The same behaviour is observed for the volume fraction of soot particles. The predicted results of the 2TEM moments are of the same order of magnitude for all the kinetics with the PBE, and it may seem promising to apply those kinetics to the PBE where the 2TEM 0^{th} moment is very close to the PBE and the first moment is only around four times higher than PBEs. However, as shown before, the 2TEM is a monodisperse model and the kinetics may not yield the correct PSD. Even by applying those kinetics into a polydisperse PBE model in the volume internal coordinate, the predicted soot volume fraction is much lower. Therefore,

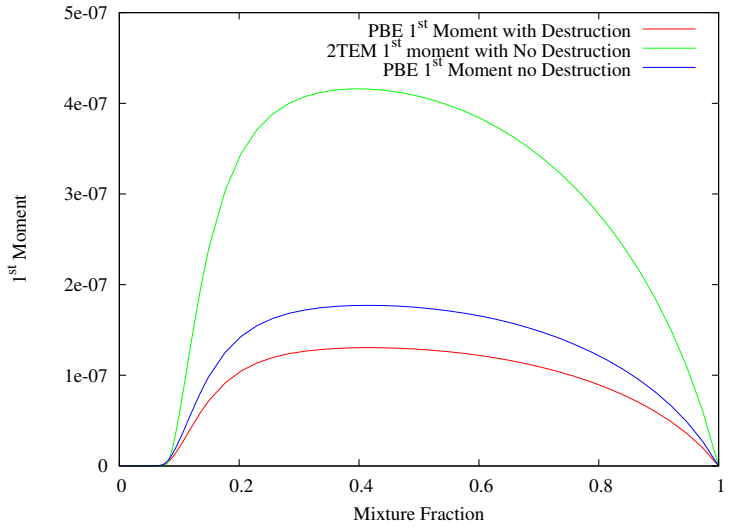

Figure 4.21: Flamelet profile of 1^{st} moment - Full soot kinetics

the great accuracy of the 2TEM exhibited in many studies, unfortunately, is not achievable in a polydisperse soot PBE model. This leaves no other choice but to investigate ABF soot modelling, or sectional soot models applied successfully in other studies.

4.4.2 PAH-based soot model

Few polydisperse models are available in the literature to conduct a numerical investigation on soot formation. Two of them are the main focus of this research. One is the soot modelling of Dworkin et al.[83], where PAH kinetics are used to describe soot formation; the other is Smooke [81], which used a simpler model for nucleation and soot growth mechanisms to describe soot formation. The investigation of the PAH kinetics will be undertaken only on the flamelet 1D model as the PAH nucleation requires a large gas-phase chemical mechanism to contain $C_{16}H_{10}$ species as the chemistry will be very time consuming in turbulent flames. An ideal well-validated mechanism is the ABF model. The kinetics used for the ABF are described below.

$$R_{nuc} = 2.2\sqrt{\frac{4\pi k_\beta T}{C_{mass} N_{C,PAH}}} d_{PAH}^2 N_A^2 [C_{16}H_{10}]^2 \tag{4.5}$$

The nucleation above differs from Lindstedt's model, as it considers the collision of two PAH molecules of equal collision diameters (namely $C_{16}H_{10}$, which is the most widely used). It could

consider other precursors than $C_{16}H_{10}$ species, but this has been found to be sufficient in some studies to represent nucleation [83]. The HACA mechanism involves many chemical reactions, shown in the table 2.5. A representative equation of the surface growth mechanism is shown below, which is similar to the oxidation mechanism by O_2 and to other mechanisms such as OH oxidative attack and PAH condensation included as well in this PBE model.

$$G_{v,C_2H_2} = 2C_{mass}k_4[C_2H_2]\alpha_f\chi_{soot}A_s \tag{4.6}$$

where χ_{soot} is the number of dehydrogenated sites per unit surface area. This value is calculated according to the elementary reactions of the HACA mechanism. It is evaluated by the following relationship:

$$\chi_{soot} = \frac{(k_1[H] + k_2[OH])\chi_{C_{soot}-H}}{k_{-1}[H_2] + k_{-2}[H_2O] + k_3[H] + k_4[C_2H_2] + k_5[O_2]} \tag{4.7}$$

The 2TEM accounts for the HACA mechanism using equation (4.6) and computing the surface area term with the first two moments. On the other hand, the MoMIC code computes the fractional moment ($M_{2/3}$) or surface area of the first moment from equation (2.72) using a Lagrange interpolation between the first six moments. The equation (4.6) is the same equation as (2.72) for the first moment. Thus, the fractional moment ($M_{2/3}$) if computed with the first two moments instead of six moments it will yield exact the same results with the 2TEM. The PBE uses the equation (4.6) to predict the surface growth rates whereas the surface area term is obtained from the fixed grid points of the size distribution prior to the simulation. The moments are compared for these three models using nucleation and surface growth mechanism due to C_2H_2 species alone. The results of model comparison follow. The models are compared to find out the how the results are affected using different modes of moment interpolation of the surface area term. Moreover, the PBE is transformed into moment transport equations in particle diameter space where the dependence on surface area is dropped; the solutions of nucleation and surface growth of the HACA mechanism are exact in the moment transformed equations and ideal to perform a comparison between all these models.

The mixture fraction grid in Figures (4.22) and (4.23) is finer at the region where the case exhibits the peak temperature value and higher temperature gradients as soot kinetics are functions and very sensitive to temperature. The mixture fraction grid is not further optimised as there is no need to improve the flamelet prediction because the main focus is the prediction

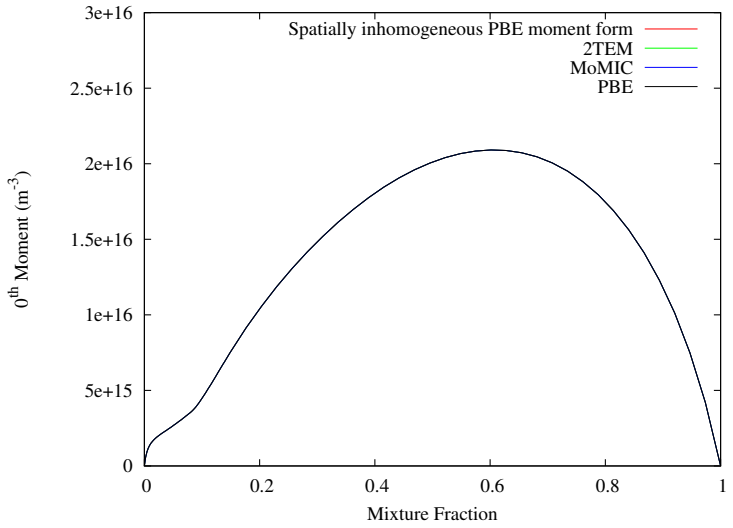

Figure 4.22: Flamelet profile of 0^{th} moment - PAH-based nucleation + Growth rates (no oxidation and coagulation)

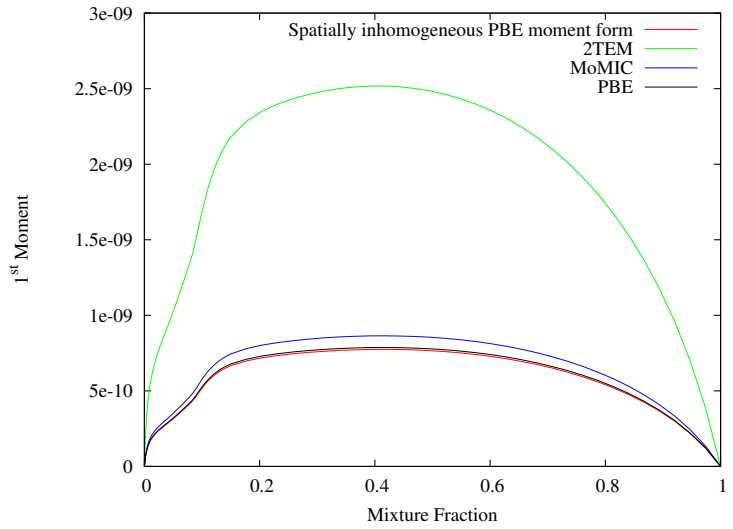

Figure 4.23: Flamelet profile of 1^{st} moment - PAH-based nucleation + Growth rates (no oxidation and coagulation)

of the moments of the distribution and the accuracy of the PBE model in 1D domain. Thus, by comparing the predictions of all models it is shown in Figure (4.22) that the 0^{th} moment is identical for any model due to the inclusion of nucleation and surface growth mechanisms alone. However, the soot volume fraction exhibits significant differences between the models. The 2TEM is highly overpredicted compared to the exact solution and the rest of the models. The

MoMIC approach offers a much more accurate solution which is not in an excellent agreement with the exact solution and there is a small discrepancy between them; the 3^{rd} moment of the PBE model with a fine uniform mesh ($\Delta L = 0.055m$) with a nucleus size $d_{p,nuc} = 0.88m$, though, is very well predicted. Also, the flamelet total integration time is changed to $0.1s$ with a time step (dt) of $10^{-6}s$.

Finally, a set of the ABF soot kinetics (i.e. PAH nucleation, surface growth and oxidation) are applied to the PBE and MoMIC. The first two moments are shown in Figures (4.24) and (4.25) with the upwind scheme. The PBE grid is uniform with $\Delta L = 0.055$ m.

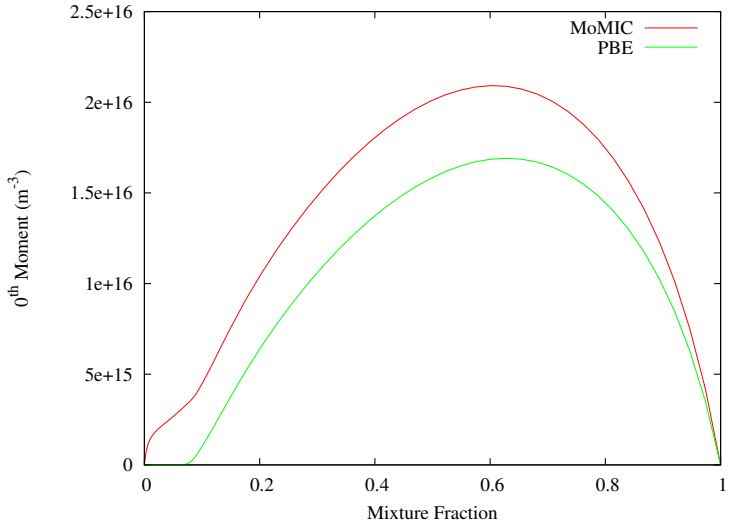

Figure 4.24: Flamelet profile of total number density of particles - All soot mechanisms except PAH condensation and coagulation

The moment results shown in Figures (4.24) and (4.25) between MoMIC and the PBE indicate that both methods seem to be in a close agreement. However, the MoMIC does not account very well for the oxidation mechanism; the number density of particles in the high oxidation regions that should be close to 0 are not showing this behaviour (Figure (4.24). Also, the surface growth rates may slightly deviate from their exact solutions, due to the interpolation closure. Also, it should be kept in mind that the PBE due to the very time consuming coagulation mechanism the mesh is not as fine as the previous simulations and the results may change as well. However, this is good first result, because those PAH kinetics were originally created for the MoMIC approach. While they were accurate for the MoMIC code, they might also be accurate for the PBE model which could take these kinetics to simulate soot formation in mutlidimensional flames.

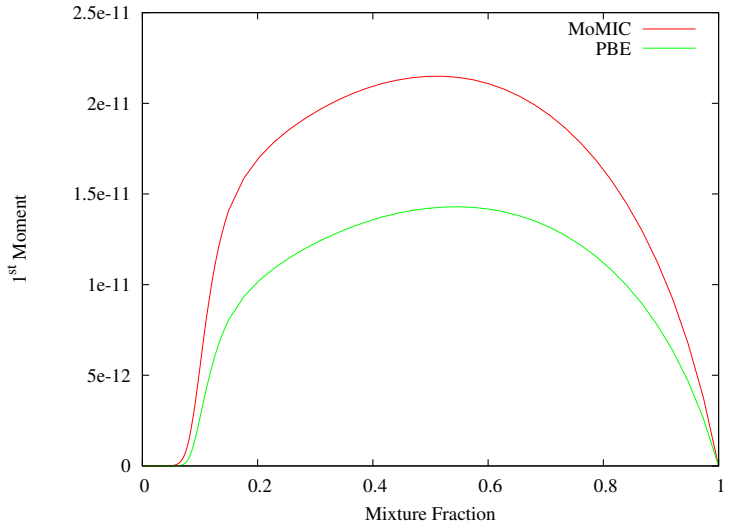

Figure 4.25: Flamelet profile soot volume fraction - All soot mechanisms except PAH condensation and coagulation

4.5 Summary and conclusions

The majority of the numerical sooting studies employed the 2TEM approach with an acetylene-based soot model or with a MoMIC approach with PAH-based soot kinetics (ABF). The 2TEM approach is a simple method that offers good predictions of soot volume fraction in non-premixed flame studies as shown in [75, 78, 55]. The MoMIC approach provides an encouraging level of agreement between the numerical and experimental results within a factor of 3 for the total number density and soot volume fractions in laminar premixed flames as shown in [79]. Therefore, in this Chapter the feasibility of using the soot kinetics originally employed in 2TEM and MoMIC approaches to the discretised PBE, is examined to test the possibility of reproducing a similar level of prediction. The implementation of the 2TEM approach to the CFD model is relatively easy compared to the MoMIC approach and the PBE model, as it solves only the first two moments of the PSD (i.e. soot number density and mass fraction). However, the results of the soot volume fraction by the implementation of the soot kinetics of both the 2TEM and MoMIC approaches are underpredicted. Hence, a series of numerical simulations were conducted to identify the source of this underprediction.

First, the accuracy of the PBE is examined in batch and PSR systems, by comparing the total number density (m^{-3}) and soot volume fraction with the analytical solutions. It is found that by employing a finite volume TVD scheme, the moments and number density function

are very well predicted with a reasonable amount of PBE grid points. Also, ignoring the coagulation mechanism, the computation of the number density function is very accurate and with significantly less amount of grid points for the diameter to be the internal coordinate. On the other hand, in volume size space, the PBE requires an enormous amount of grid points to be accurate and reach a grid independent solution. Moreover, the coagulation mechanism discretised by the finite element approach [24] is more accurate when compared to the widely used fixed-pivot technique.

The PBE with a finite volume TVD scheme is joined with the 1D flamelet along with the exact solution, the 2TEM and MoMIC approaches. All the models employ the same soot kinetics throughout the simulations. The 2TEM approach significantly overpredicts the surface growth rate and the soot volume fraction by approximately 70% compared to the exact solution (see Figure 4.23) whereas the rest of the models (i.e. MoMIC and PBE) are in a much closer agreement. Thus, the same success of the 2TEM soot kinetics could not be possibly shared by the PBE. Including the coagulation mechanism in the 2TEM approach, the soot volume fraction is underpredicted against the PBE by a factor of 3 (see Figure 4.21) despite the overprediction of the total number density function of the PBE model (see Figure 4.20). In contradistinction, the MoMIC approach is in a closer agreement with the PBE than the 2TEM.

Therefore, the ABF soot kinetics of the MoMIC approach [80, 79] might be successful by incorporating them to the PBE. The other alternative, which has been used in this thesis, is to implement soot kinetics that have been applied by similar polydispersed models (e.g. sectional models), such as in Smooke et al. [49] and Dworkin et al. [83].

Chapter 5

Modelling soot in laminar flames

The mathematical models and the discretisation of the PBE via a high resolution finite volume scheme have been described in Chapter 3. An assessment of the PBE's performance and accuracy is carried out in Chapter 4 in homogeneous and flamelet systems. The PBE with the FV-TVD method is shown to achieve the best possible performance among first and second order schemes and is implemented in the laminar diffusion flames of this Chapter. A parallelisation formulation was further implemented into the laminar flame code to speed up the simulation, as described in Chapter 4. The coupled CFD-PBE model was used to solve soot formation in a widely investigated experiment that is also one of the target laminar non-premixed flames of the International Sooting Flames Workshop [148].

The choice of the laminar diffusion flame experiment is motivated because this configuration is a simple analogue of more complex practical flame systems providing an important step in understanding soot formation [9]. The laminar co-flow diffusion flame is a multidimensional system with a relatively simple flow field. This configuration is an ideal platform for the investigation of the chemistry, radiation and soot predictions without the influence of turbulent effects. This type of experiment has a vast data available for comparison, and it offers a suitable case for conducting a numerical investigation for validation purposes. The laminar axisymmetric coflow diffusion flame configuration consists of two concentric pipes, where the fuel is issued through the central tube, and air is ejected through the outer pipe.

This target flame is a series of laminar axisymmetric co-flow diffusion flame experiments originally carried out by Santoro [8, 9]. It should be noted that in [8] many laminar diffusion flame experiments have been investigated by varying the mass inlet flow rates of the fuel and the oxidiser alone. The geometry of the two concentric pipes, fuel and air compositions were

kept the same, while varying the inlet flow rates. The majority of these experiments had pure ethylene fuel issuing from the jet burner [8, 9]. However, other fuels have been tested, as well except pure ethylene, such as methane, ethane and ethylene diluted fuel, to examine the role of the fuel structure in soot formation [8]. Generally, in flame experiments ethylene is an attractive fuel because it is the simplest of hydrocarbon fuels with moderate sooting levels. Methane is even simpler, but the levels of soot produced are significantly lower than ethylene and are usually more difficult to measure experimentally. In this thesis, three pure ethylene fuel experiments are of interest among the other configurations. Each experiment creates different sooting flame characteristics. Many other researchers replicated some of the experiments of Santoro et al. [8, 9] and provided additional data available for comparison [11]. A review of the replicated experiments conducted in the literature is shown in the next section.

5.1 Experimental studies of Santoro flames

Santoro [8], [9] has conducted a series of experiments to investigate soot formation in laminar co-flow flames using optical diagnostic techniques, including laser extinction and scattering, for particle size measurement. From these experiments, it was possible to quantify the soot volume fraction that exists in the entire region of the flame. Three types of sooting flames were identified in his experiments: the non-smoking, incipient and smoking flames. Pure ethylene fuel was used in nearly all of his experiments, with air as the oxidiser. Modifying the fuel and oxidiser flow rates causes the aforementioned types appear. By increasing the flow rates there is also a higher propensity to emit soot. The sooting flame behaviour is described by each type. In the non-smoking flame type, no soot is observed to emit from the tip of the flame. The oxidation is strong enough to completely or near-completely oxidise the soot particles within the flame. In the other two flames, the oxidation is not strong enough to completely oxidise the soot particles, and soot is emitted. When soot emission is restricted to an annular ring close to the wings of the flame, the incipient sooting type is identified, whereas when soot is emitted across the entire flame region, the system is called a sooting flame. These sooting flame characteristics are found in [8] by modifying the mass inlet flow rates of the fuel and the oxidiser.

In the first study of Santoro et al.[8], the spatial distributions of the soot volume fraction, average particle size and number density concentrations of soot particles are plotted as a func-

tion of non-dimensional height above the burner. The soot measurements were obtained using laser extinction and scattering technique. In a later study of Santoro et al. [9], axial and radial velocity profiles were measured for the heated gas flow by the laser velocimetry technique. Since these flames are significantly stable little error is resulted by the velocity measurements. In addition to the velocity measurements, radial temperature profiles at several axial points are measured by thermocouple. Temperature measurements with thermocouple wire can be affected by many sources of errors such as soot deposition on the junction. This source of error is significantly reduced in the study of Santoro et al. [9] by a rapid insertion procedure by measuring the junction temperature as quickly as possible. However, total elimination of the error cannot totally be achieved. Similar thermocouple temperature measurements within non-soot regions involve experimental uncertainties lower than 50 K [149]. Moreover, contour plots of soot volume fraction are shown in [9], providing an insight into soot distribution in the entire flame region. Further insight is provided in soot formation processes by considering the soot particle history in the flame [9]. This information is obtained by measuring the soot volume fraction along soot particle paths. The particle paths are calculated from the velocity measurements mentioned previously. The soot particle pathlines are observed to converge towards the centre of flame. This phenomenon has been attributed to gas flow acceleration due to combustion, and buoyancy effects. Soot volume fraction, number density and average particle size profiles are shown along the pathlines that exhibit the maximum soot volume fraction as a function of residence time [9]. Another observation made by these researchers is that the path of the soot particle exhibiting the maximum soot volume fraction shifts to a larger radial position (away from the axis) as the mass flow rate is increased [9]. Measurements are obtained by inserting a probe or a beam passing through machined slots on the side of the surrounded chimney wall (confined flame), providing optical access to the flame. The chimney is placed to reduce any perturbations and disturbances that could come from the surroundings. Other experimental techniques for enhancing and supplementing the optical diagnostic tools can be achieved with using thermophoretic sampling. The uncertainties between the peak values of the soot volume fraction in the Santoro et al. flames [8] are listed in [86] which are around 20-25%.

Later, Megaridis and Dobbins [11, 12] replicated the same experiment in [8, 9]. They employed a thermophoretic sampling technique, in which the phenomenon of thermophoresis is used to drive the hot soot particles on the cold wall of the probe. The sample of soot par-

ticles which is captured by the surface of the probe was examined by Transmission Electron Microscopy (TEM). Images of very small scale were formed by the TEM technique to study the soot morphology [12]. The measurements of Megaridis and Dobbins [11] were combined with Santoro et al. [9] velocity measurements, and the information on the pathlines of soot particles exhibiting the maximum soot volume fraction in the flame. Mean particle diameter, number concentration, specific growth rates and soot surface areas [11, 14] were calculated at four axial points on the pathline. The error measurement of the primary average particle diameter along the pathline for the smoking flame is around 10% as shown in [150]. This experimental configuration was later demonstrated for the same ethylene/air experiment and with methane/air and methane/oxygen compositions to examine and confirm the fractal dimension of soot and its dependence on fuel type in [151].

An experimental study of Puri et al. [152] improved upon the methodology in [9] by using the same method of laser scattering and extinction measurements in the same flame. The laser scattering technique was used to obtain measurements simultaneously at three different angles [152, 153]. This arrangement had the advantage that the light scattering measurements were less affected by small variations in the flame conditions (flame movement) [152]. As such, a more detailed analysis could be conducted where the fractal dimension of the aggregates could be determined. Moreover, in [152], a greater insight into the polydispersity of soot was obtained: the aggregate number concentration and the average number of primary particles in each aggregate were determined as a function of height or residence time along the pathline of maximum soot concentration in the flame [152]. However, the error measurements of the number density of primary particles per aggregate could be as high as 50%. According to the results of this study, Megaridis and Dobbins [12] and Santoro et al. [9], the laminar diffusion flame is established to comprise four regions of soot formation processes. Nucleation is dominant in the low region of the flame. Moreover, this small nucleation region determines the total number of primary particles in the flame. This number remains almost unchanged along the particle path. Growth of soot particles by surface processes and coagulation is next, followed by aggregation and oxidation processes. It should be noted that even the emitted soot aggregates continue to increase in size by sticking together [152]. More radial profiles of soot volume fractions in the non-smoking ethylene flame can be found in [154]. The study in [154] compared and validated their method ([154]) with the original Santoro et al. study results [8], and extended it into partially premixed flames of similar geometrical configuration.

Another experimental technique is found in [15] for a non-smoking ethylene flame but with different flows rates; this study differs from the techniques in [8, 9]. The researchers investigated an ethylene diffusion flame using laser induced incandescence (LII) to obtain spatially resolved measurements of soot volume fraction which were calibrated with laser scattering/extinction results. The LII yielded very good agreement being within 5%-10% difference at most heights in comparison with the results of laser extinction/scattering technique made by Santoro.

In Kennedy et al. [25], both experimental and numerical investigations were performed for the ethylene non-smoking and smoking flame of [8, 9]. Molar concentrations of two molecular species were measured using two different techniques. Radial molar concentration profiles were measured for both species at two different axial distances from the burner. The first stable gas-phase species was C_2H_2 concentration, is measured by mass spectrometry; the second radical species was OH, is measured by laser induced fluorescence where the error in measurements could be as high as 50%. Moreover, radial soot volume fraction profiles were measured for the smoking flame.

Measurements of the non-smoking ethylene flame and a methane counterflow flame were obtained in [155] by using a relatively simple technique with thermocouple particle densitometry. Soot volume fraction measurements were obtained. The peak values of the radial profiles of soot volume fractions were compared against their respective published laser extinction measurement results in the same flame by using the slightly different higher oxidiser flow rate of [15]. The results of [155] proved to be able to capture the shape of the soot volume fraction distributions across the flame, where the peak values are lower than the laser scattering/extinction measurements.

In an another study, the thermocouple particle densitometry technique (TPDT) results are compared with the non-intrusive laser scattering/extinction [8]. The thermocouple particle densitometry may be more suitable for combustion environments with very low soot concentrations or non-absorbing particles, according to [156]. At the lower part of the flame, the soot volume fraction is measured to be about a factor of three higher than the soot volume fraction results of [8]. This phenomenon has been attributed to the fact that that the TPDT can capture the translucent precursor soot particles [156]. Moreover, the measured soot volume fractions may be slightly lower than the laser scattering/extinction results across the centreline of the flame, except for the lower part of the flame. The estimated soot volume fraction uncertainty is 35%.

It should be noted that the majority of the experimental studies have replicated the non-

smoking ethylene experiment where valuable data is retrieved under different experimental techniques. However, only the original experimental studies of Santoro et al. [8, 9] managed to obtain few measurements in the other two types of laminar diffusion flames - the incipient and smoking flames - and even fewer numerical studies have been performed to examine these flame types.

5.2 Numerical studies of Santoro flames

Numerical modelling of soot formation has been performed on the ethylene laminar diffusion flame [8, 9] by many researchers. An early numerical attempt to predict soot formation in the laminar diffusion flame of Santoro et al. [9] was made by Kennedy et al. [157]. In [157], the addition of an energy equation and the radiation of soot particles were taken into account. The radiation term was found in this study to be quite important. This was an early attempt to predict soot formation in two flames: a laminar ethylene axisymmetric diffusion flame from [9] and a Wolfhard-Parker two-dimensional flame. The boundary layer-form of the governing equations was solved in this study [157]. However, there is a major assumption regarding soot modelling. Only the transport equation of soot mass fraction was solved in this study [157], without the need to account for particle number density. It is stated in [157] that it is unnecessary to compute the particle number density through a transport equation. As such, an empirical surface growth rate was used to predict the soot loading in the flame by assuming an average number density with a fixed value of $10^{16}m^{-3}$. This study also introduced the concept that soot oxidation rates might be too great, as no soot particles are emitted from the tip of flame as would be expected from experimental measurements [157]. However, greater oxidation rates have been attributed to the uncertainty of OH prediction, as this study [157] did not incorporate detailed chemistry.

Several years later, a much-improved study compared to [157] was presented by the same author [25]. In the new study, the boundary layer form of the governing equations was retained, but the chemistry and soot models were more detailed. A two-transport equation was employed, solving for soot number density and mass fraction of soot particles. The following soot mechanisms were employed: nucleation, surface growth, oxidation and coagulation, according to the approach in [76]. Moreover, an optically thin approximation accounted for the radiation of soot particles. However, gas-phase radiation was ignored; it was assumed that radiation of

soot particles is much more significant. In addition, a simplified gas-phase chemical mechanism was employed with 24 species and 64 chemical reactions. In [25] two laminar axisymmetric diffusion flames from [8] were examined: the non-sooting and sooting ethylene diffusion flames. In [25], the oxidation rates were concluded to be overpredicted; the authors even provided evidence from other experiments that the oxidation rate by O_2 was overestimated. This study attempted to predict the transition of the non-smoking to a smoking flame. The prediction was partially successful due to the excessive oxidation rates. The peak values of the integrated soot volume fraction were correctly predicted, but no soot was emitted in the smoking flame [25].

After the improved study of Kennedy et al. [25], Liu et al. [53] successfully employed fully elliptic governing equations and a 2TEM similar to Kennedy et al. [25], but with different soot formation rates. In [53] the same laminar diffusion flames as Kennedy et al. were investigated; this time, the soot emission was captured from the smoking flame by applying correction factors to the oxidation of O_2 and OH species. Under the same parameters, soot was not emitted from the non-smoking flame. Detailed models, such as a reduced GRI 3.0 mechanism, were applied to represent the chemistry. NOx species and other species associated with NOx and reactions were removed, leaving 36 species and 219 reactions. Two radiation models were applied. The simplified radiation model of the optically thin approximation (OTA) was distinguished from a detailed radiation model, called the discrete ordinates method (DOM). With DOM, the emission and re-absorption of radiation energy is accounted for; OTA accounts for emission of radiation energy alone. Results from both radiation models were compared to evaluate the importance of the re-absorption on the accuracy of the temperature field. DOM was found to be significant in improving the prediction for the smoking flame of the emitted soot, and much less significant in improving predictions for the non-smoking flame. The radiation models included the radiation of soot and gas-phase species. Another very important statement within this study [53] is that the coagulation term is omitted. Moreover, the soot oxidation terms were modified with correction terms to capture the emission sooting characteristics of the smoking flame.

Guo et al. [77] investigated the fuel preheating effects for a similar configuration of axisymmetric diffusion flame with different inlet velocities than Santoro et al. [8]. Two simulations were considered. In the first, the inflow boundary was set on the burner exit and the temperature was specified at ambient (no preheating is considered). In the second, the inflow boundary was extended inside the burner for a certain distance. The wall of the nozzle was extended by

4 cm, and a linear variation of temperature was specified across this length starting from 300 K to 403 K (the edge point of the nozzle wall). According to [77] this temperature distribution across the wall was not arbitrarily as it was based on measurements from an experiment. The heat transfer of conduction and convection (not radiation) between the wall nozzle to the fuel and the air streams was taken into account. It is found in [77] that the flame preheating effects influenced the velocities at the burner exit and soot formation processes. The second simulation yielded improved results for soot formation relative to first simulation. However, in [53] it is indicated that the flame preheating primarily affects the region near the burner, and the soot results are affected by a small increase of soot field by 13% . Overall, the fuel preheating will not alter the results of the non-smoking and smoking flame significantly, and it was not considered.

The numerical studies that employed two transport equation models to predict soot formation neglect the polydispersity of particles because monodisperse particle size was assumed. The next numerical study of D'Anna and Kent [158] attempted to simulate the non-smoking ethylene flame of Santoro et al. [8] with a polydisperse model. A sectional study was employed with a detailed gas-phase chemistry and PAH kinetics to describe soot formation. In [158] using a sectional model with 26 sections in the mass range and PAH kinetics, the authors were able to achieve a satisfactory centreline soot prediction (same order of magnitude), whereas the previous study of Kennedy et al. [25] with a monodisperse acetylene-based model underpredicted the value by at least an order of magnitude.

Subsequently, a sectional model with PAH kinetics was applied on the same non-smoking ethylene flame by Zhang et al. [23]. In this study, a sectional model was employed to solve not only the primary particles, but also the aggregate structure as well. The sectional model was set up on the mass range of solid soot particles with 35 sections, and a sectional spacing factor of 2.35 (the mass of each section is 2.35 times larger than the preceding section, $\frac{m_i}{m_{i-1}} = 2.35$). This study employed fully elliptic conservation equations with a parabolic velocity profile at the fuel exit and a DOM radiation model [23, 159, 53]. The numerical analysis was conducted with a non-uniform mesh independent of grid refinement, with 210 axial and 88 radial points in a computational domain of 15.24 cm in axial and 4.71 cm in radial. The implementation of this model proved to predict reasonably well the experimental results, but the average number of primary particles per aggregate was overpredicted. Moreover, in [23] the PAH condensation mechanism was clearly important - if it is neglected, significant overprediction occurs in the

soot number density and soot volume fractions. ABF gas-phase mechanism was employed with 101 species and 544 chemical reactions, and the soot kinetics were similarly applied to the ABF soot kinetics [79]. Even with a detailed sectional model and PAH kinetics, there was still an order of magnitude underprediction of soot volume fraction on the centreline [14].

Another numerical study - a continuation of [23] - simulated the same non-smoking flame [83] with uniform fuel and air exit velocities. It is pointed out that the underprediction in centreline soot volume fraction profiles is a common problem [83]. Two different gas-phase chemical mechanisms were compared against the ABF [79] mechanism. The third gas-phase mechanism was the most successful, and was therefore the mechanism suggested. It originated from the study of Slaviskaya and Frank [85], which enhanced aromatic formation in methane and ethene flames for soot modelling. However, this gas-phase mechanism was modified [83] to accurately predict soot formation. The suggested gas-phase chemical mechanism was concluded to be more accurate than the other two gas-phase mechanisms. Even the predicted soot volume fraction centreline profiles using the modified Slaviskaya and Frank [85] gas-phase mechanism were of the same order of magnitude as the experimental results, compared to the ABF gas-phase mechanism; with it, the results were one to two orders of magnitude underpredicted. Overall, all the results exhibited reasonable agreement relative to experimental results [83]. Furthermore, each mechanism resulted in a relatively good accuracy on the peak soot volume fraction values under a different constant value of the fraction of active surface sites on the soot surface area. The surface active site is a term that describes the availability of locations on the surface of each soot particle to perform chemical reactions with gas-phase species. The study concluded that this term should be explored further [83].

The latest study used the same formulation as the previous numerical study [83] and the same gas-phase chemical mechanism to attempt to simulate for the first time the three laminar diffusion flame types with the same numerical model in [86]. It should be noted that in [86], the oxidation strong rates were illustrated in the results where the smoking flame does not emit soot. The authors managed to work out this problem by modifying the single term that describes the fraction of the available surface sites specifically for the oxidation process of O_2. The surface reactivity term of the oxidation process is modified to be a function of thermal age. It is stated that by modifying the oxidation rate by OH, the peak value of soot volume fraction changes, but not the sooting characteristics of the flame. In contrast, the oxidation rate by O_2 affects the sooting characteristics of the flame, but not the peak value of soot volume fraction.

5.2.1 Flame description

Three laminar axisymmetric diffusion flames are examined in this thesis: the non-smoking, incipient and smoking flame. It should be noted that all three flames are targets of the International sooting flame workshop [148]. The three experimental flame configurations are presented in the Santoro et al. study in detail [8, 9]. The experiments are performed in atmospheric pressure and ambient temperature conditions, with pure ethylene fuel as the jet fuel and air as the oxidiser. The jet burner had an internal diameter of 11.1 mm, surrounded by a concentric pipe with 101.6 mm internal diameter. The fuel and the oxidiser issue vertically upwards. The buoyancy effects are treated numerically in the same axial direction that the fuel and air are injected. The fuel tube in the experiment was extended by 4 mm above the air annulus exit and the flame is enclosed in a 405 mm long brass cylinder to shield the flame from any air laboratory currents. In this thesis, the fuel pipe extension is not considered in the computational domain. As such, the inflow boundary is set up at the fuel pipe exit. Both the fuel and air passage contain glass beads and screens to smooth the flows and provide the experiment with uniform exit flows profiles [8]. In addition, for smoothing the flow in the air passage, a honeycomb section is placed in the final section [8] of the pipe. Each experiment has different flow rates. The non-smoking flame has a volumetric inlet fuel flow rate of 3.85 cm^3/s and a volumetric inlet air flow rate 713.3 cm^3/s. The uniform velocities are 3.98 cm/s and 8.9 cm/s respectively. The incipient sooting flame has an inlet volumetric fuel flow rate 4.6 cm^3/s and the volumetric inlet air flow rate is kept the same at 713.3 cm^3/s. The uniform velocities are 4.75 cm/s and 8.9 cm/s respectively. The smoking flame experiment has a volumetric inlet fuel flow rate of 4.9 cm^3/s and an oxidiser flow rate 1068.3 cm^3/s. The velocities are 5.06 cm/s and 13.3 cm/s respectively. All the flames have the same geometrical configuration, and are confined by a metal cylinder that functions as a chimney to provide a shield from any laboratory air currents [8]. The visible flame height of the non-smoking flame is reported to be approximately 8.8 cm [8] with a peak soot volume fraction value of around 10 ppm. The other two flames of incipient and smoking flame have an increased flame height and slightly increased peak soot volume fraction values around 13 ppm [53, 86]. A low amount of soot volume fraction is emitted for the incipient conditions, and a larger amount for the smoking flame.

Uncertainties on boundary condition

There is a diversity of opinions in the literature about the exit velocities. Some studies assume uniform profiles, and others assume fully developed flow, with a parabolic profile. However, according to the experiment of Santoro et al. [8] at the fuel exit passage, glass beads and screens are placed to smooth the flow, creating uniform velocity profiles. The same equipment with the addition of a honeycomb section is installed at the air passage to create a uniform air exit velocity profile [8]. Few studies have used parabolic velocity to describe the velocity at the fuel exit. However, in [83], it is stated that the simulations were found to be insensitive to the choice of the fuel velocity profile, resulting in the use of a flat velocity profile.

Thermal diffusion (Soret effect) of gas-phase species is neglected in this thesis, as several other studies concluded that the difference in using this mechanism is not important in the C_2H_4/air flame experiment and is only useful when light species are in excess such as helium and hydrogen [57]. With the Soret effect the species concentration is driven by a temperature gradient. Thermophoresis is the same as Soret effect, but the thermophoresis term is usually used for aerosol particles such as soot. Thermophoresis transports the soot particles radially inward, towards the axis of the flame [8]. Dufour effects describe the energy flux that arises due to concentration gradients; and their effects are usually negligible in combustion situations.

It should be noted that the C_2H_4/air flames in the experiments of Santoro et al. [8] are attached to the burner. Fuel preheating is expected as the attached flame increases the temperature of the fuel pipe which in turn increases the temperature of the fuel. Unfortunately, due to the lack of measurements in these experiments at the fuel jet exit many studies ignored fuel preheating effects. Fuel preheating effect is accounted in [83] by setting a uniform inlet temperature of 400 K. It is stated that this value is set based on trial and error process until the temperature downstream is matched with the experimental data according to the numerical study of [25]. In the study of Liu et al. [53] it is stated that fuel preheat will improve the temperature predictions and affects the soot field by 13 %. However, fuel preheat is not considered as the overall results and conclusions of his investigation will not change.

5.2.2 Computational model description

The computational domain in this thesis is kept the same for all the laminar diffusion flame configurations. Due to their axisymmetry, the computational domain can be represented by two dimensions in axial and radial directions. A schematic of this laminar diffusion flame geometry

is shown in Figure 5.1 along with the boundary conditions.

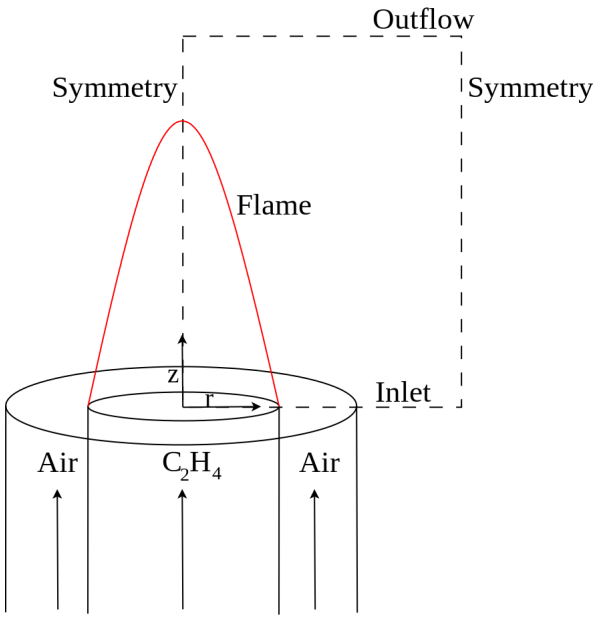

Figure 5.1: Coflow diffusion flame schematic [160]

The 2D computational domain is formed by the dashed lines (rectangular shape) as shown in Figure 5.1. The boundary conditions are applied as follows: symmetry conditions on the left and to the right planes, outflow condition on top, and inflow at the bottom. The computational domain is 0.2775 m in the axial direction, 0.0555 m in the radial direction as shown in Figure (5.2a).

The Figure 5.2b shows a part of the CFD domain drawn and the radial measurement axial locations are illustrated with blue lines. The maximum soot volume fraction that is exhibited along the pathline of the particles is shown with green and the red line indicate the flame height of the non-smoking flame.

A non-uniform mesh is applied, and is finer towards the jet burner exit (inlet boundary) where larger gradients exist in that area and coarser in the outflow boundary as shown in Figure (5.3). In the computational domain a grid is generated with 200 points in the axial and 100 points in the radial directions. In the axial direction the grid is non-uniform with a weak single expansion ratio of 1.02 and in the radial direction the single expansion ratio is 1.04. Other coarser grids are used (i.e. 50x80 and 80x120) to simulate the same scenario. It should be noted that the 100x200 mesh is found to be grid-independent, with minor differences from the 80x120 grid.

In this section the Navier-Stokes, species and enthalpy conservation equations are solved as listed in section 2.4.2. The mixture-averaged diffusion terms, mixture viscosity and mixture

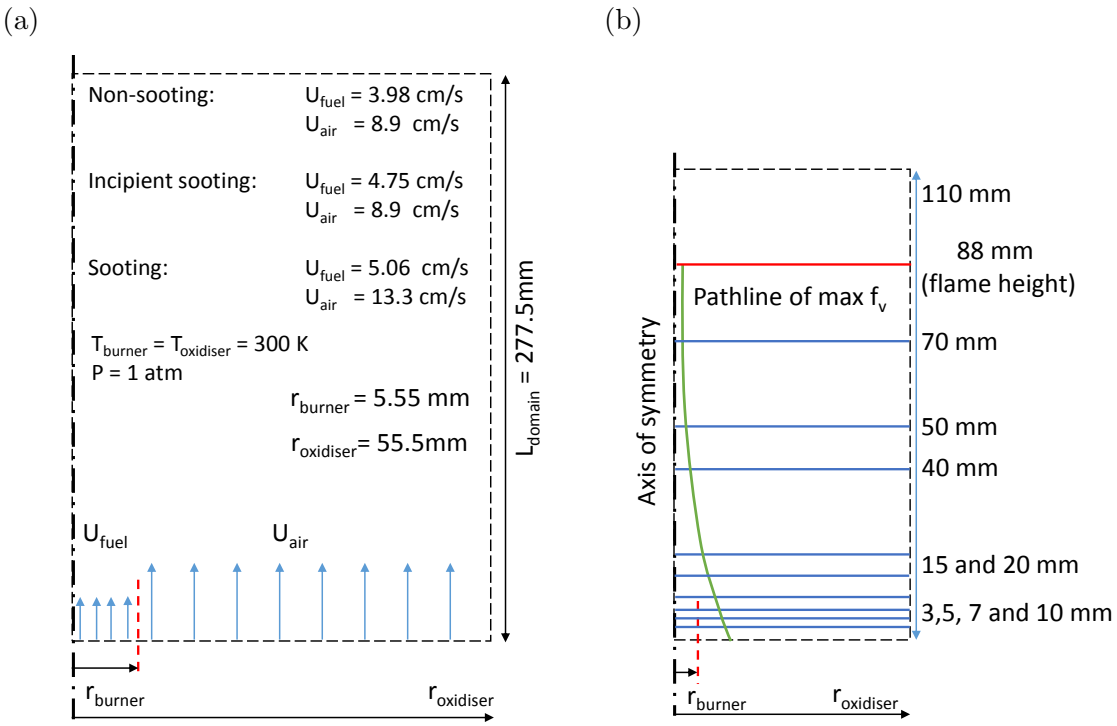

Figure 5.2: a) Detailed representation of the computational model b) Measurement locations of the non-smoking flame

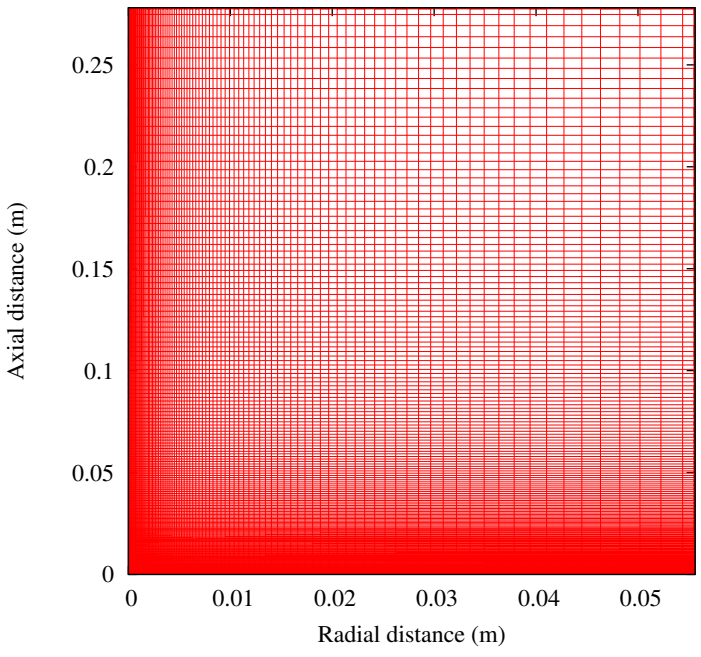

Figure 5.3: Representation of the laminar flames computational mesh

thermal conductivity are computed by the equations (2.19), (2.21) and (2.22) respectively. The PBE equation is employed to obtain the complete PSD in these laminar flames as shown in equation (2.109) and soot kinetics listed in the summary of Chapter 2.

The PBE is set up for these flames with both diameter and volume internal coordinates. However, in this thesis, the PBE with diameter as the internal coordinate is chosen to represent the size domain of soot particles due to the enormous amount of grid points to capture the entire PSD in volume size space. The size domain of the soot particles is discretised with a uniform grid. The parameters of the uniform PBE grid are 0.6 m^{-9} increment (spacing between the grid points) with 400 intervals in total. The incipient diameter size of soot particles is assumed to be 2.4 nm according to the nucleation expression found in [53]. Twelve CPUs are used for the simulations of each flame. The time-dependent governing equations of momentum (axial momentum, including a gravity term), pressure correction, enthalpy, species and discrete sizes of soot sections are solved across the entire computational domain. Finite volume schemes are applied to both the CFD and PBE model with TVD schemes to increase the conservation properties. It should be noted that the PBE is also grid independent as the change of the moments was found to be negligible for a coarser PBE mesh.

5.3 Case study 1: non-smoking flame results

The results of the non-smoking flame are presented into this section. First, the results of the flow field and temperature are compared against the experimental results.

5.3.1 Flow field

Several measurements of axial and radial velocity profiles are retrieved from [9]. The radial velocity results are compared at several axial distance points above the burner. The comparison is shown in Figures 5.4 and 5.5.

The radial velocity profiles are stronger near the burner exit, as shown in Figures 5.4 and 5.5 and they are decreased away from the burner. The predicted radial velocity profiles at 3mm and 5mm are slightly underpredicted where at 10mm the profile is in a better agreement. Away from the burner height in Figure 5.5, the radial velocities are slightly overpredicted at 20 mm and 40 mm and underpredicted at 70 mm. It should be noted that there is an uncertainty in measuring the radial velocity profiles, as the original authors could not identify the reason

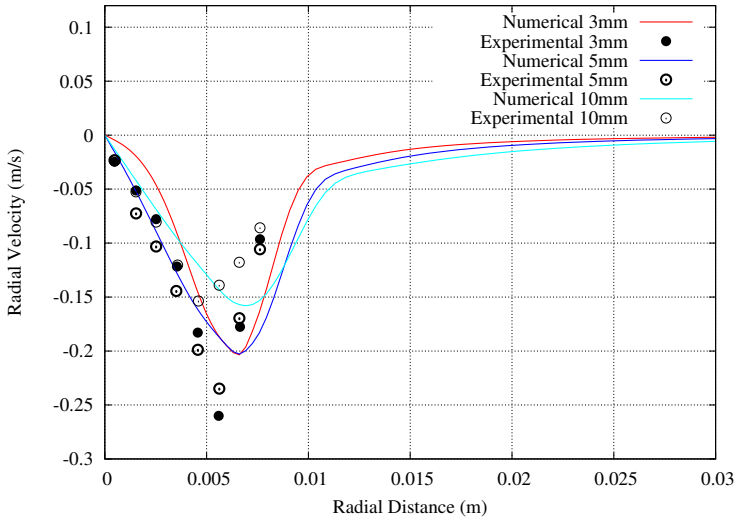

Figure 5.4: Radial velocity (m/s) plots at 3,5 and 10 mm

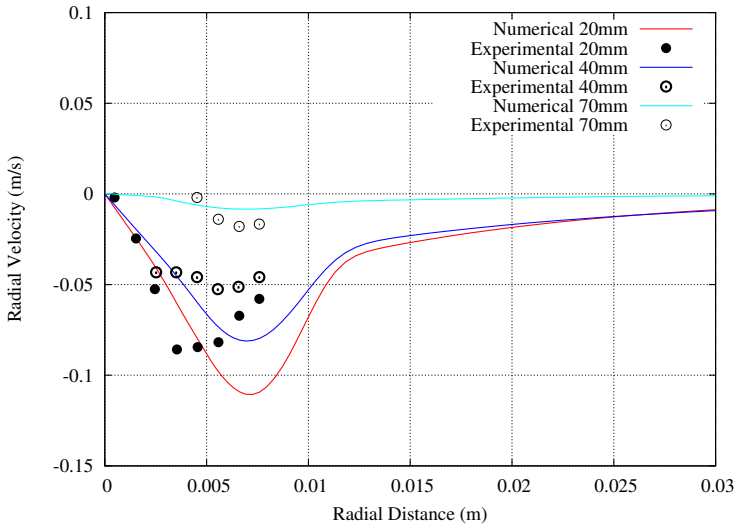

Figure 5.5: Radial velocity (m/s) plots at 20,40 and 70 mm

of a significant asymmetry [9]. They believed that this uncertainty is due to the effects of room disturbances. The radial velocity measurements exhibit a notable asymmetry between the measurements of the two opposite sides of the axis of symmetry. However, this uncertainty is not detrimental due to the much lower radial velocity magnitude compared to the axial velocity and the overall results of the flame are not strongly affected by it [9]. Moreover, the presence of substantial radial velocity indicates the convection of air into the fuel region [9].

Figures 5.6 and 5.7 display the radial axial velocity profiles for the same axial distances

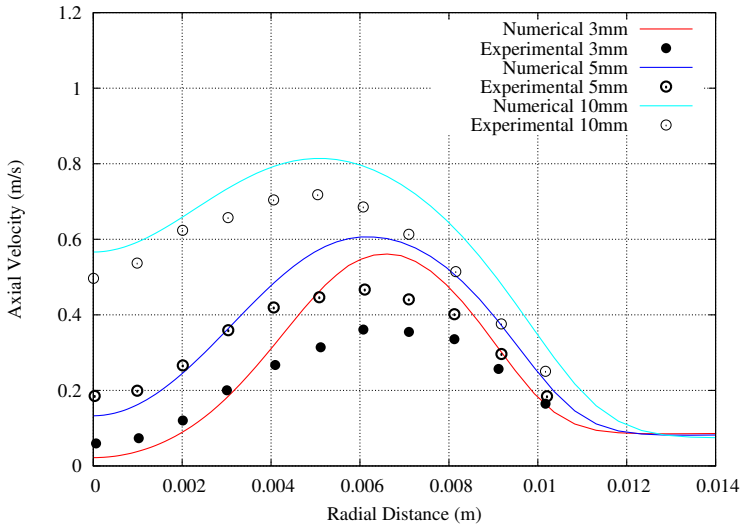

Figure 5.6: Axial velocity (m/s) plots at 3,5 and 10 mm

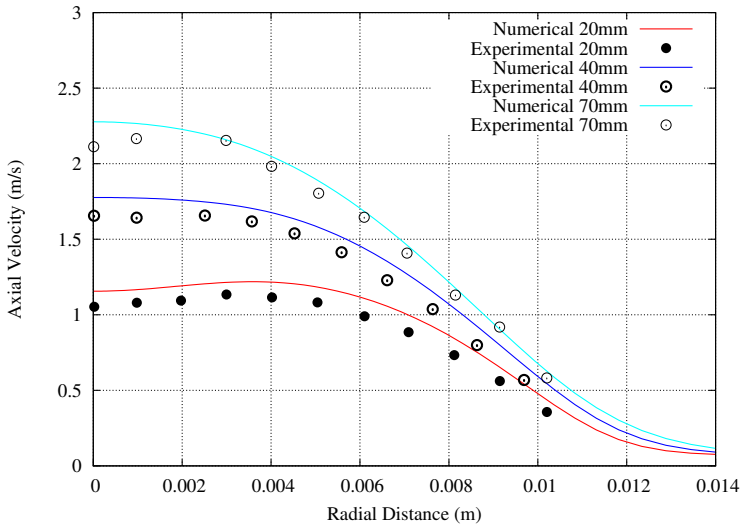

Figure 5.7: Axial velocity (m/s) plots at 20,40 and 70 mm

above the burner height. The measurements were taken by Santoro et al. [9]. Observing the axial velocity profiles close to the burner exit in Figure 5.6, the velocities at 3 mm and 5mm above the burner near the centreline are slightly underpredicted, and as the radial distance from the centreline is increased, the velocities are overpredicted. However, the trends with downstream distance of the predicted axial velocities are in relatively good agreement with the experimental values. On the other hand, very good prediction is achieved for the radial axial velocities at 20 mm, 40 mm and 70 mm above the burner height, as shown in Figure 5.7. The

axial velocities increase away from the jet burner exit due to buoyancy acceleration, which is caused by the difference in the mixture density of the hot gas flow. Moreover, away from the jet burner exit the axial velocities peak at the centreline of the flame. The next Figure 5.8 shows the centreline profile of the axial velocity. Good agreement is achieved, as can be seen in Figure 5.8.

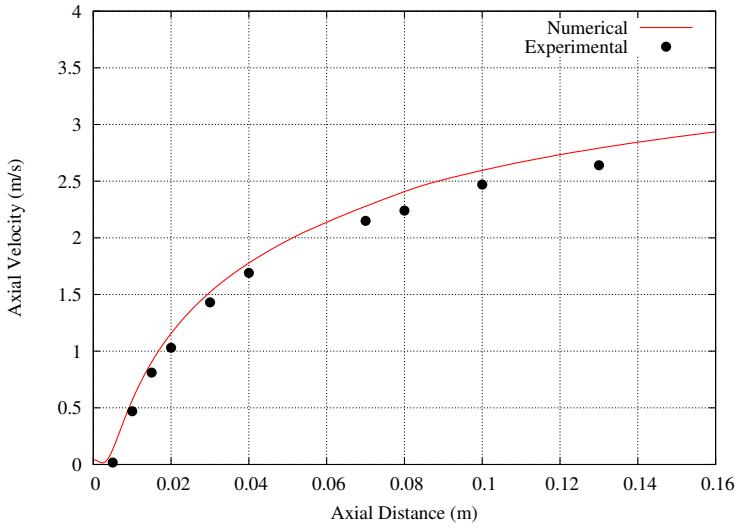

Figure 5.8: Axial velocity (m/s) on centreline

The next results illustrate the comparison of many radial temperature profiles across the flame. The comparison is conducted for the same axial distances as used for the velocity measurements.

The radial temperature profiles close to the burner exit are shown in Figure 5.9. The closest location of a measured temperature point to the burner height is at 3 mm. The temperature is underpredicted by almost $200K$ on the centreline and the peak value is overpredicted. The reason for this behaviour, especially for the underprediction, close to the centreline, probably lies in the fuel preheating which is not accounted for in this simulation. The flame of this experiment is attached to the burner. This attachment has the consequence of preheating the burner and the ejecting fuel to a higher temperature. There is an uncertainty regarding the temperature at the inlet, and the majority of studies included a uniform ambient temperature; other workers [83] have set an elevated inlet temperature profile at 400 K. However, this elevated inlet temperature profile is based on a trial and error process to match the temperature of the computations to those of the experimental data which is expected to be different for different

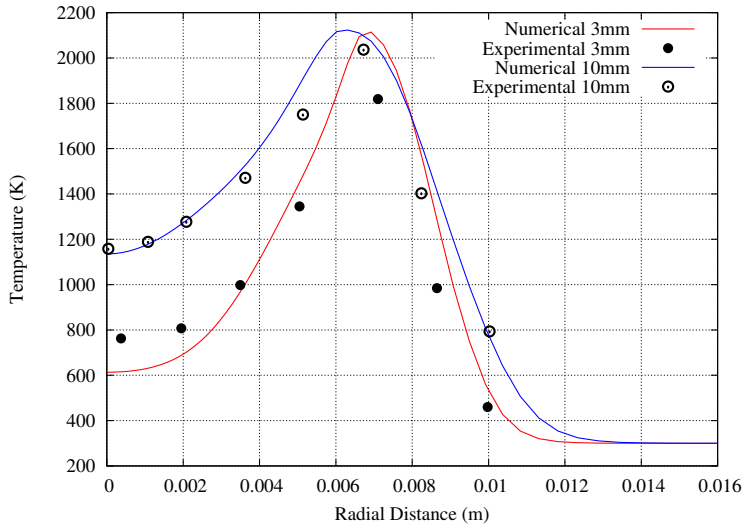

Figure 5.9: Temperature (K) plot close to jet burner exit

soot kinetics and models. The prediction of the temperature at 10 mm above the burner exhibits very good correlation with the experimental results.

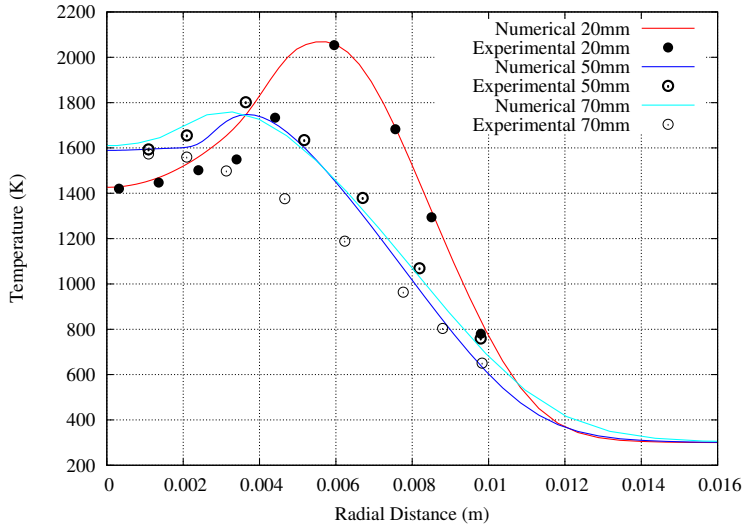

Figure 5.10: Temperature (K) plot at 3 and 10 mm

Figure 5.10 shows more radial temperature profiles at 20 mm, 50 mm and 70 mm above the burner height. Excellent agreement in the temperature profiles is observed at 20 mm and 50 mm above the burner. Moreover, the radial temperature profile prediction shown in Figure 5.10 at 20 mm has an excellent agreement and at the centreline is well predicted compared to

[53] where the centreline temperature at 20 mm is underpredicted by almost 200 K. However, the temperature profile at 70 mm above the burner exit starts to deviate from the experimental values. The temperature profile increases radially instead of decreasing. This overprediction is attributed to the strong soot oxidation in that region, where the radiation of soot is minimised by the lower concentrations of soot. As such, the radiation is not strong enough in that region to reduce the temperature. Similar phenomenon is found for the temperature profile at 70 mm in Kennedy et al. [25] and Liu et al. [53] which they used optically thin and thick radiation models respectively and could not resolve this discrepancy.

The Figure 5.11 shows the temperature profile on the centreline of the flame. The rapid rise of the temperature at the centreline of the flame is correctly captured compared to the study of [53]. This rapid rise in centeline temperature occurs via energy transfer and/or transport of hot products or reactants from the flame front to the centreline according to [9]. Thus, the flame temperature on the centreline is rapidly increased as it is heated up and reaches its peak value around 0.088 m above the burner height very similar to the soot formation study of [83].

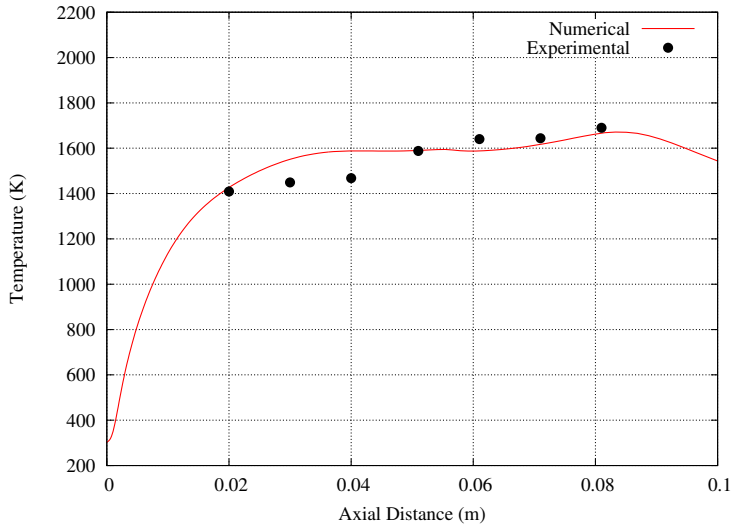

Figure 5.11: Temperature (K) profile on the centreline

A contour plot of the flame temperature is shown in Figure 5.12. Observing Figure 5.12, it is clear that the higher temperature regions in the flame are concentrated towards the sides (wings of the flame) and at the jet burner exit where the ignition occurs at the interface between the reactants. The higher-temperature regions are gradually shifted from the sides towards the centreline. The pathlines of soot particles according to the experiment [8] are

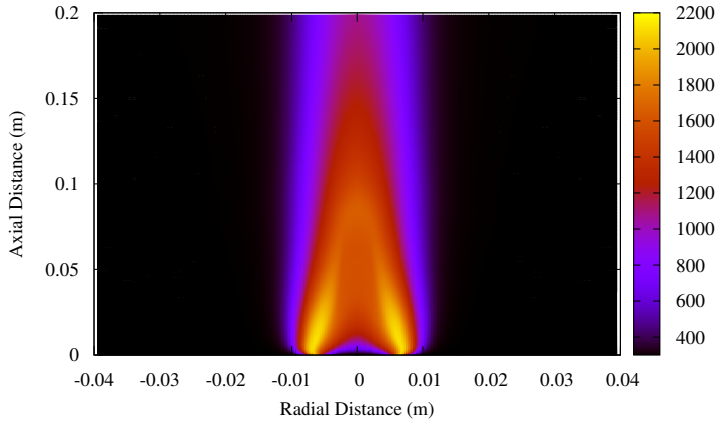

Figure 5.12: Contour plot temperature (K)

found to converge towards the centreline due to buoyancy acceleration. The visible flame length (peak temperature also shown in Figure 5.11) is found to be approximately 0.088 m, which is in accordance with the experimental observation [8], and the peak predicted temperature is around 2130 K. It should be noted that by incorporating the radiation term of gas species and soot particles, the flame shape and structure are changed significantly until they reach their final state.

5.3.2 Soot and species

The mole fraction measurements of two gas-phase species (i.e. C_2H_2 and OH) are obtained from [25]. These two species are very important; C_2H_2 is especially relevant as the main precursor of soot particle inception and the main species for soot particle growth. The OH species is also important as it has a dominant influence on the oxidation rates. A good prediction of both of these species is essential for accurately predicting the soot formation processes of nucleation and size of particles.

Figure 5.13 shows a comparison of C_2H_2 mole fraction radial profiles at two axial distances at 0.7 cm and 2 cm. C_2H_2 concentration is well captured at 2 cm above the burner and overpredicted at 0.7 cm.

Figure 5.14 shows the radial profiles of mole fraction of OH species at two axial points at 7 cm and 0.7 cm above the burner. The features of the mole fraction profile of OH species are

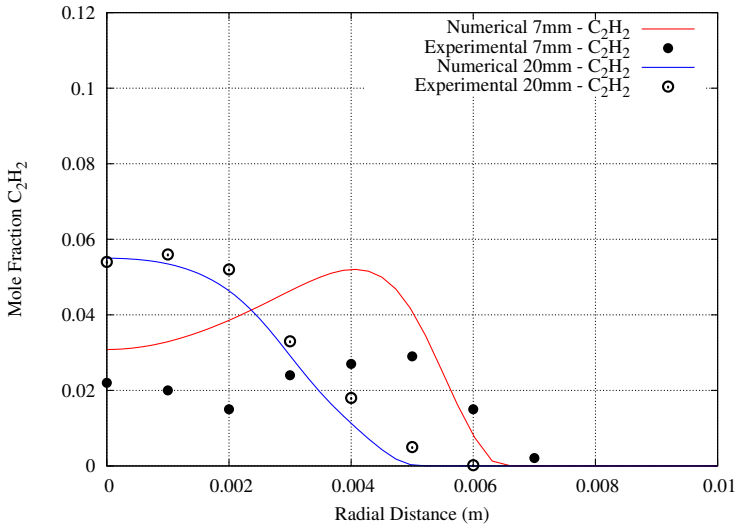

Figure 5.13: Mole fraction of C_2H_2 species

reproduced well. Both values are overpredicted, but the trends are well-captured. It should be noted that the measurement error of OH species found in [25] is estimated to be as high as 50% [159]. The prediction of OH species is essential, as it is the most dominant oxidation mechanism.

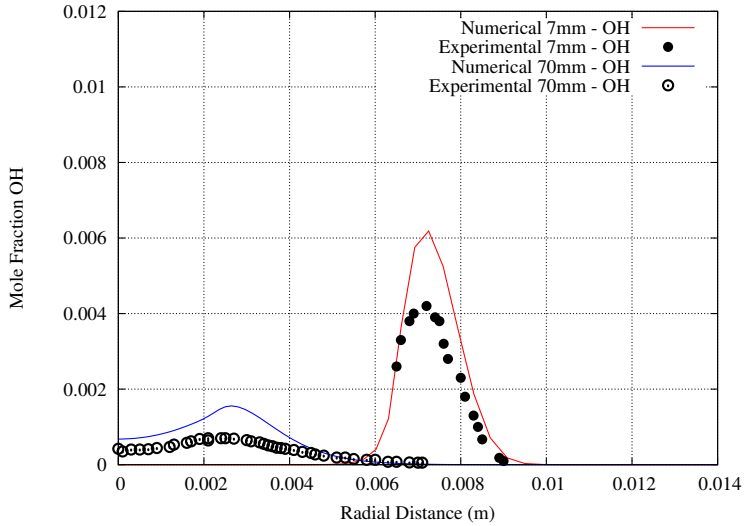

Figure 5.14: Mole fraction of OH species

Figure 5.15 shows the total number density (m^{-3}) across the entire flame region. The total number density of soot particles is predicted to have the same order of magnitude as the

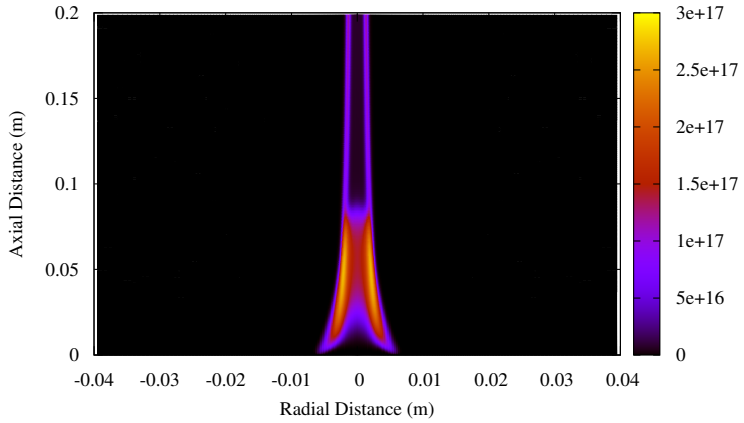

Figure 5.15: Contour plot of total number density (m^{-3}) in non-smoking flame

measurements of Megaridis and Dobbins [11]. Moreover, the bulk number of soot particles is concentrated towards the wings of the flame. The oxidation mechanism is strong enough to destroy the majority of particles with a very small (minor) fraction escaping the flame region.

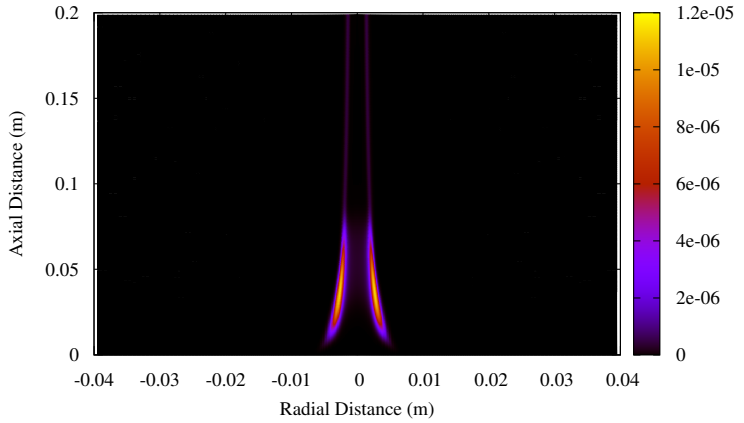

Figure 5.16: Contour plot of soot volume fraction in non-smoking flame

Figure 5.16 demonstrates a contour plot of soot volume fraction across the entire flame region. The peak value of soot volume fraction is found to be around 12 ppm in the annular region, as shown in Figure 5.16 and it is very close to the experimental result, which has been

measured to be approximately 10 ppm. The reason for this peak value overprediction is likely to be that the influence of the age of soot particles on the surface reactivity is not taken into account [49]. Moreover, the bulk of soot volume fraction is concentrated towards the wings of the flame, and not on the centreline. This is in qualitative agreement with the experiments. Furthermore, a negligible amount of soot concentration is emitted from the tip of the flame. The next Figure 5.17 shows a plot of soot volume fraction radial profiles at two axial distances: 1.5 and 5 cm.

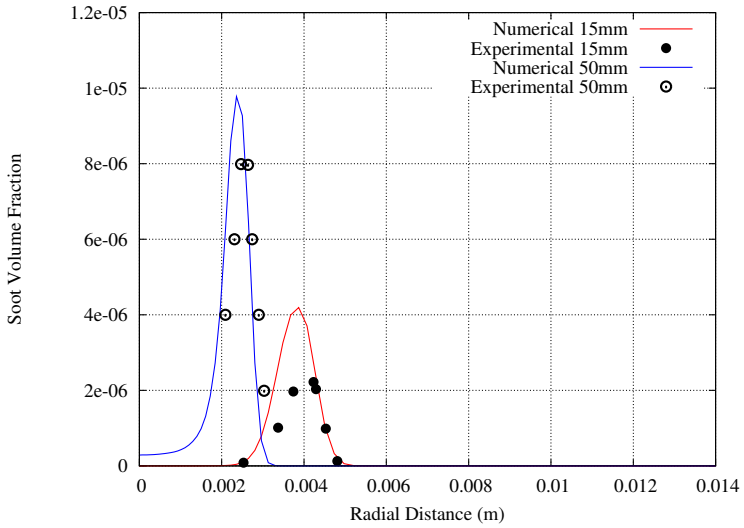

Figure 5.17: Radial profiles of soot volume fraction

Both the trend and the peak soot volume fraction profiles are reasonably predicted relative to the experimental measurements. The peak of soot volume fraction profile is slightly overpredicted at 1.5 cm.

The centreline profile is underpredicted by an order of magnitude, as can been seen in the Figure 5.18. Several soot formation studies have predicted similar underprediction of the soot volume fraction of an order of magnitude for the same flame [25, 23, 83] with different gas-phase mechanisms and soot models. However, the amount of soot prediction at the centreline was improved in [83] by using a modified gas-phase mechanism (enhancing the PAH growth rates) to increase the number density of soot particles via the nucleation process at the inception-dominated regions such as near the centreline.

The next soot measurements are taken on the annular pathline exhibiting the maximum soot volume fraction. This pathline is generated by finding the maximum soot volume fraction

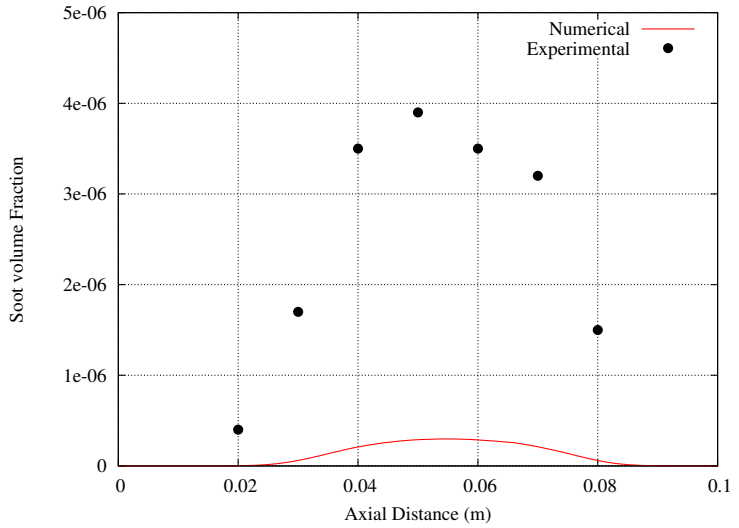

Figure 5.18: Soot volume fraction on the centreline of the flame

points in the radial profile at every axial distance location. It is mentioned in [83] that the data along the pathline is compiled at the radial positions where there is maximum soot volume fraction. These measurements are obtained from [11] as a function of the height above the burner [14].

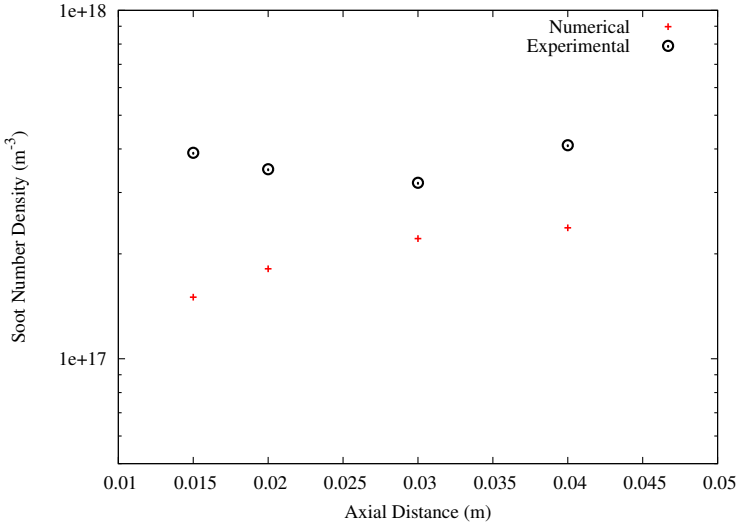

Figure 5.19: Total number density along the pathline

The total number density of soot particles in Figure 5.19 along the path of the maximum soot volume fraction is reasonably predicted, but still underpredicted. Figure 5.20 shows the

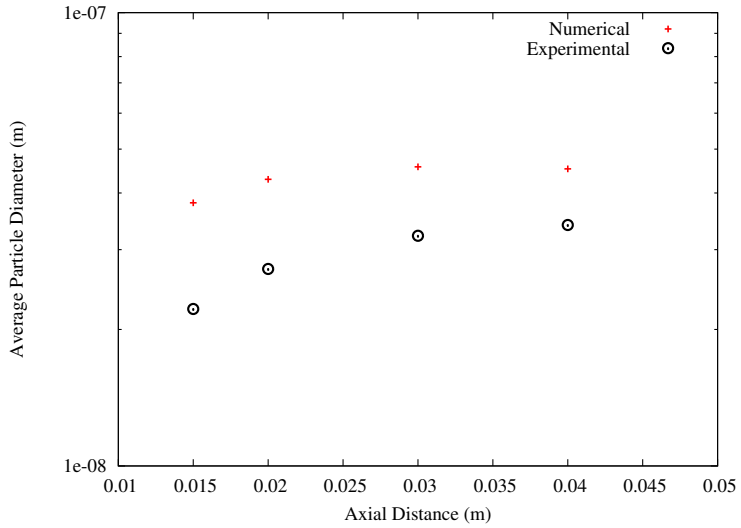

Figure 5.20: Average particle diameter along the pathline exhibiting the maximum soot volume fraction

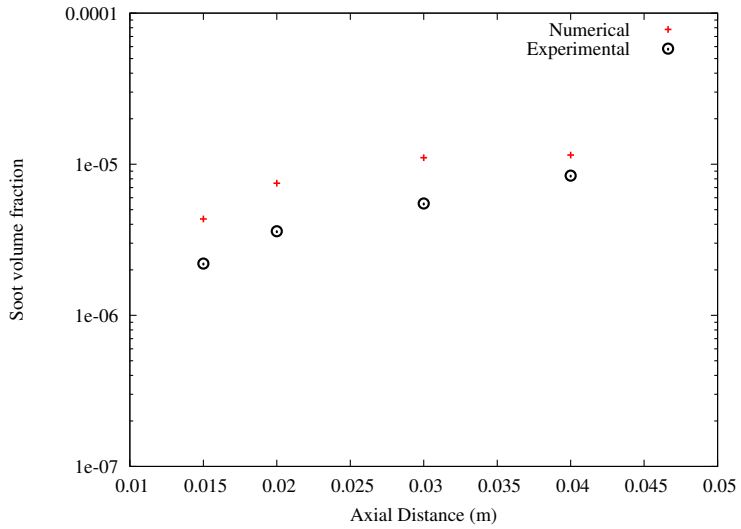

Figure 5.21: Soot volume fraction along the pathline exhibiting the maximum soot volume fraction

average particle diameter of soot particles along the same path. An overprediction is observed by approximately a factor of two. Figure 5.21 demonstrates the prediction of soot volume fraction along the same path. Similar to the previous average particle diameter, an overprediction of soot volume fraction is observed. It should be noted that coagulation's impact in this flame is still unclear and further theoretical and experimental investigations are needed to develop an

adequate particle coalescence model [159]. The Figure 5.22 shows the integrated soot volume fraction profiles along the height above the burner. The integrated soot volume fraction is given by the following expression:

$$f_{v,int} = 2\pi \int_0^\infty f_v r dr \tag{5.1}$$

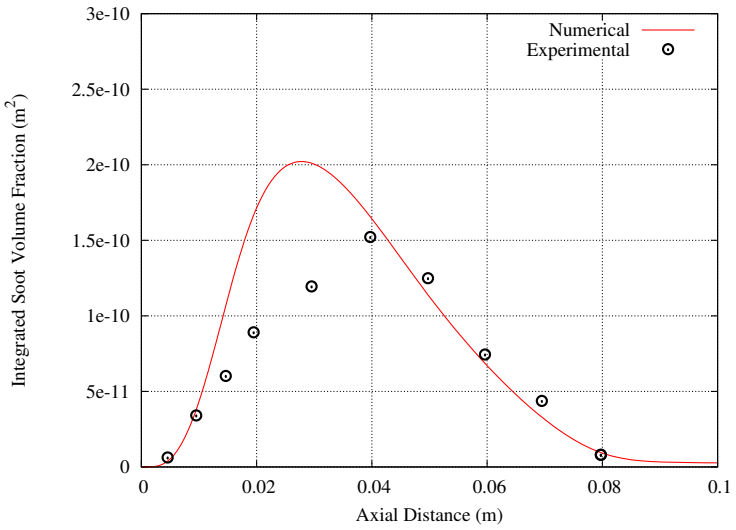

Figure 5.22: Integrated soot volume fraction (m^2)

The integrated soot volume fraction profiles are demonstrated in Figure 5.22. A relatively good prediction is observed across the flame region (e.g. 0.088 m flame length). An overprediction of the integrated soot volume fraction profile is observed, and the peak value is shifted towards the jet burner at around 0.03 m in the axial direction. Moreover, soot is almost completely oxidised at the exit of the flame tip. The Figures 5.23, 5.25d and 5.25b, display the mass fraction contour plots of C_2H_2, OH and O_2 species along with the nucleation, surface growth and oxidation rates in order to observe the behaviour of each mechanism that is established across this flame.

The contour plot in Figure 5.23 shows that the C_2H_2 species are initially formed at the annular region of the jet and gradually heads towards the centreline. The C_2H_2 species concentration is the most essential species, as the nucleation and surface growth mechanisms are solely described by the C_2H_2 concentration. The Figure 5.24a demonstrates the nucleation rate in the entire flame region, which is consistent with the mass fractions of C_2H_2 species. The

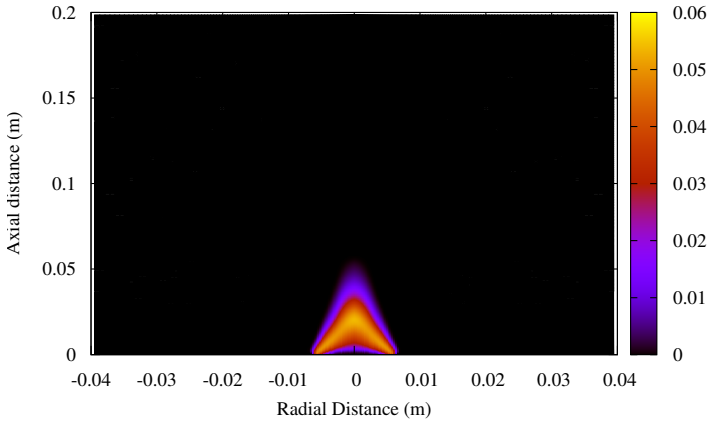

Figure 5.23: Contour plot of mass fraction of C_2H_2

(a) (b)

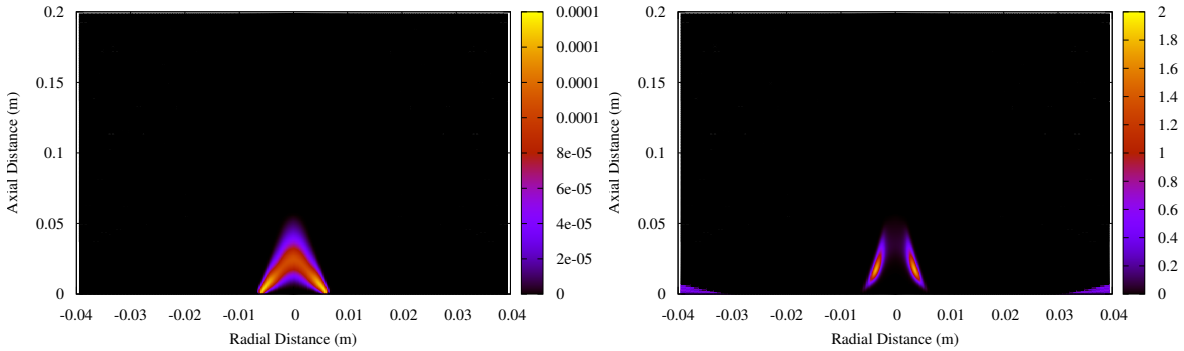

Figure 5.24: a) Nucleation rate ($\frac{kg}{m^3\ s}$) b) Surface growth rate ($\frac{kg}{m^3\ s}$)

nucleation rate in Figure 5.24a is determined by equation (2.75).

The Figure 5.24b shows the surface growth rates in the sooting flame region. The surface growth rate in Figure 5.24b is determined by equation (2.76) using the total surface area of soot particles instead of surface area of each particle. The surface growth rate is first-order dependent on C_2H_2 concentrations. Comparing Figure 5.24b to Figure 5.24a, it can be clearly seen that the surface growth rates are far more significant at the wings of the flame whereas the nucleation rates are significant on the centreline of the flame. The remainder of the soot formation processes are the oxidation mechanisms and their gas-phase species. The Figure 5.25b shows the contour plot of the O_2 mass fraction.

In Figure 5.25b, the dark area surrounding the axis of symmetry and at the beginning of the flame indicates the absence of oxygen concentration. The oxygen surrounds the flame,

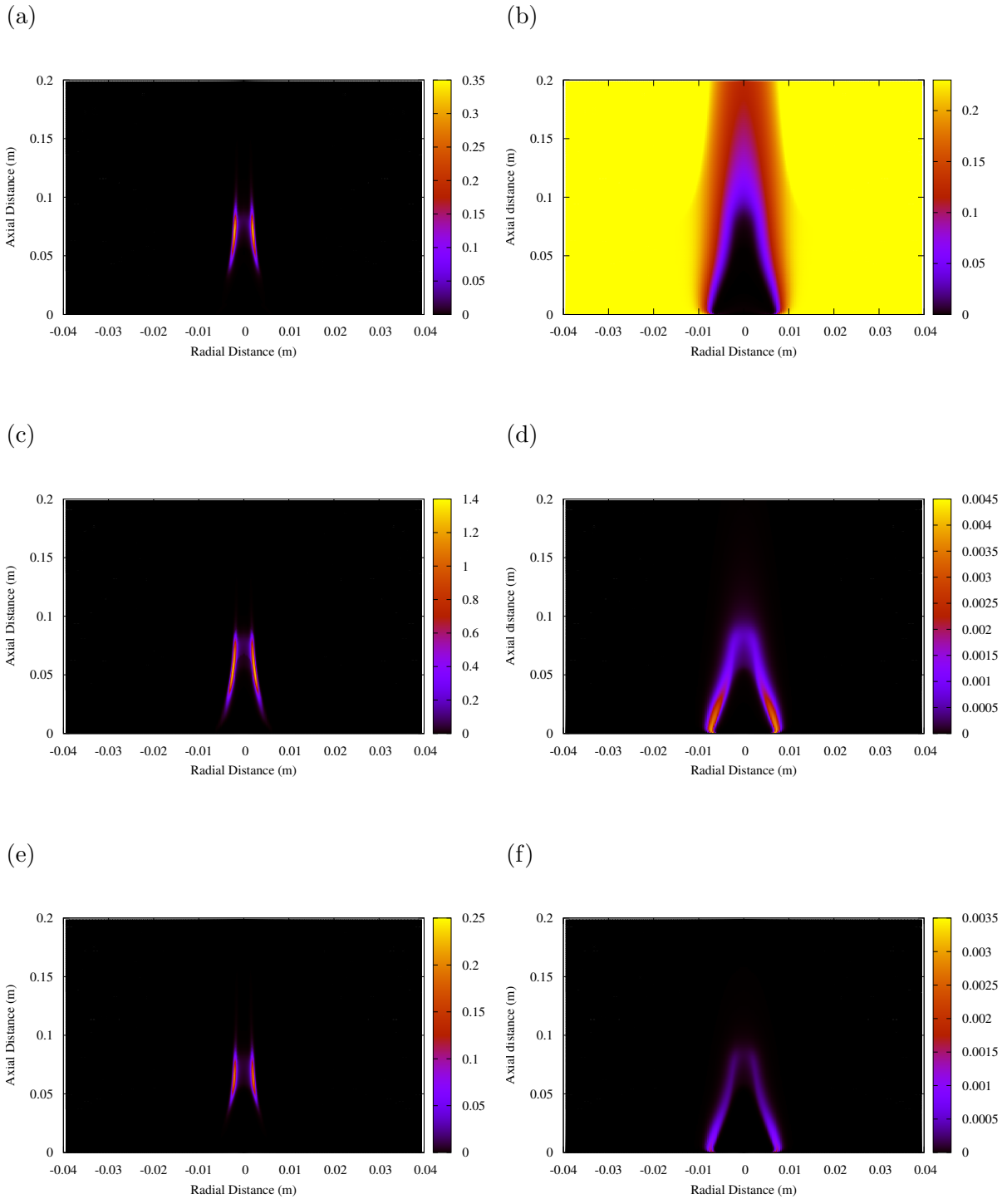

Figure 5.25: Soot oxidation rates ($\frac{kg}{m^3\ s}$) and mass fractions by a) O_2 c) OH and e) O

supplying the reaction rate zone with oxygen. The Figure 5.25a shows the oxidation rate by the O_2 that is determined by equation (2.77) replacing particle surface area with total surface area.

In Figure 5.25d, it can be seen that the OH species is not completely consumed at the tip of the flame; it survives beyond the flame region until it completely disappears. The next Figure 5.25c shows the oxidation rates by OH.

In Figure 5.25c the oxidation rates are much higher than the oxidation rates by O_2 shown in Figure 5.25a. The oxidation rate by OH species is closer the jet burner than the oxidation rate by O_2. This indicates that the oxidation rate by OH will have a greater impact on the soot volume fraction across the entire flame length at the wings of the flame.

It is clear from the oxidation rates in Figures 5.25a, 5.25c and 5.25e that the oxidation rate by OH dominates. The second oxidation rate in terms of magnitude is the O_2, and the smallest is the oxidation by the radical oxygen.

The last results shown of the non-smoking flame are the complete normalised PSDs, which are obtained by solving the PBE. The PSD of soot particles can be obtained in the entire flame region, but for reasons of clarity three axial points are chosen at the fixed radial position where the maximum soot volume fraction is found.

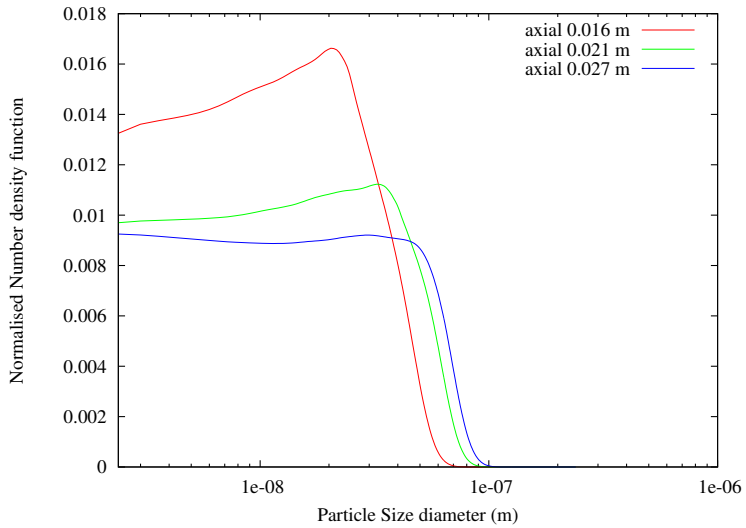

Figure 5.26: Normalised PSDs number density

By observing Figure 5.26, it is clear that, as expected, the distribution of the number density of particles is expanding with axial distance from jet burner. This is because a number of

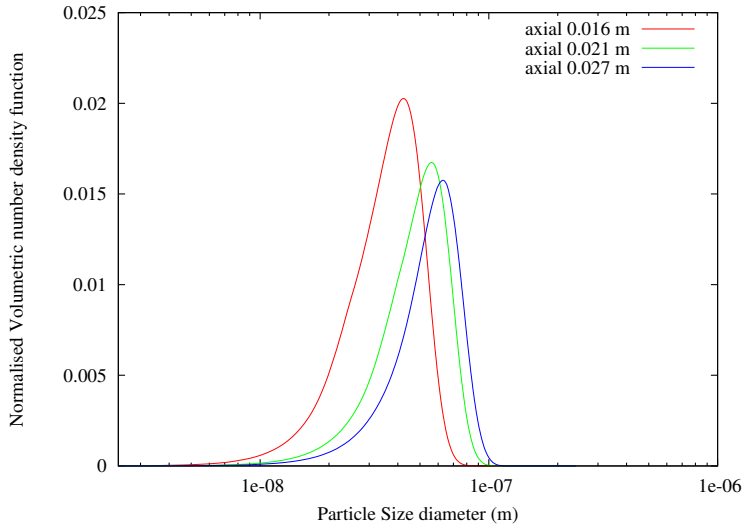

Figure 5.27: Normalised volumetric PSDs number density

particles are convected towards a region of a higher-size state, due to surface growth rate as the most dominant mechanism in that region. It should be noted that surface growth mechanisms conserve the total number density of particles (0^{th} moment) and only the mass is increased or decreased depending on the competition between surface growth and oxidation rates.

The Figure 5.27 shows the normalised volumetric PSD for the same locations as Figure 5.26. The volumetric PSD shown in Figure 5.27. The volumetric PSD is convected towards a higher size state due to surface growth processes. The nascent soot particles diameter starts at 2.4 nm and can move up to approximately 100 nm. However, the normalised PSD of the number density exhibits a weak bimodality at the axial position 0.027 m, whereas the normalised volumetric PSD exhibits only a distribution similar to log-normal. The number density and volumetric PSDs are normalised with the expressions of 0^{th} moment and 3^{rd} moment as shown in equations (2.103a) and (2.103d) respectively.

5.4 Case study 2: incipient flame results

The other flame investigated by [9] is the incipient sooting flame produced by increasing the fuel mass flow rate enough (as shown in Figure 5.2a) for a small amount of soot to be emitted from the annular region of the flame. There are not many results regarding this flame in the literature. Only the integrated soot volume fraction is measured. It should be noted that

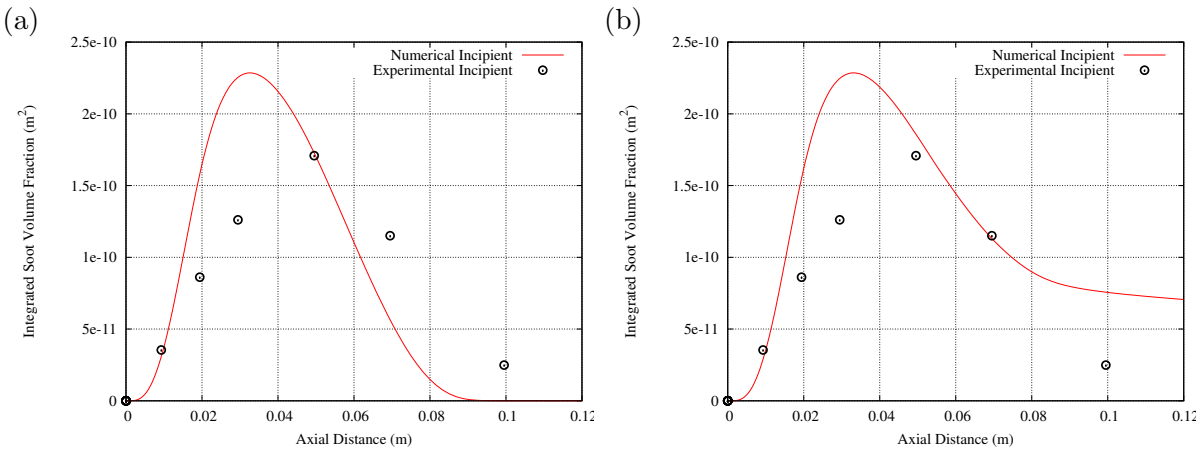

Figure 5.28: Integrated soot volume fraction (m^2) a) without correction factors b) with correction factos

so far, only the most recent numerical study [86] attempted and performed a complete set of analyses regarding the non-smoking, incipient and smoking flame. Similar to other studies [25, 53] which performed a numerical investigation of soot formation in smoking flames, the oxidation rates are much stronger than the surface growth rates. As a result no soot is emitted in the incipient smoking flame where according to the experiment [9] in incipient flame soot should not completely be oxidised and some noticeable amount should be emitted from the tip of the flame. However, holding the original kinetics will oxidise completely the soot particles and no soot will be emitted. The Figure 5.28a shows the results of the incipient flame with the original oxidation rates where soot is fully oxidised within the flame region.

The Figure 5.28b shows the effect of a modification of the original oxidation rates by applying correction factors according to [53]. With the correction factors (shown in equations (2.60)-(2.63)) as shown in Figure 5.28b, soot is emitted from the flame. The PSD predictions are shown at the same three axial points above the burner exit in Figures (5.29) and (5.30), with the correction factors.

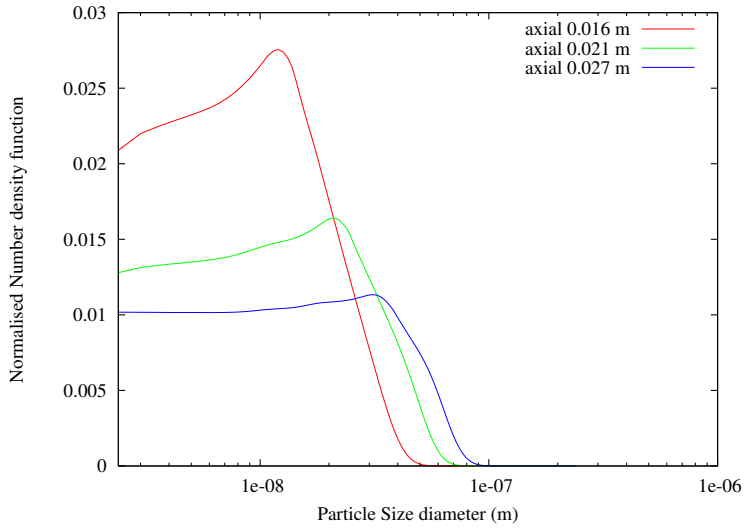

Figure 5.29: Normalised volumetric PSDs number density Incipient flame

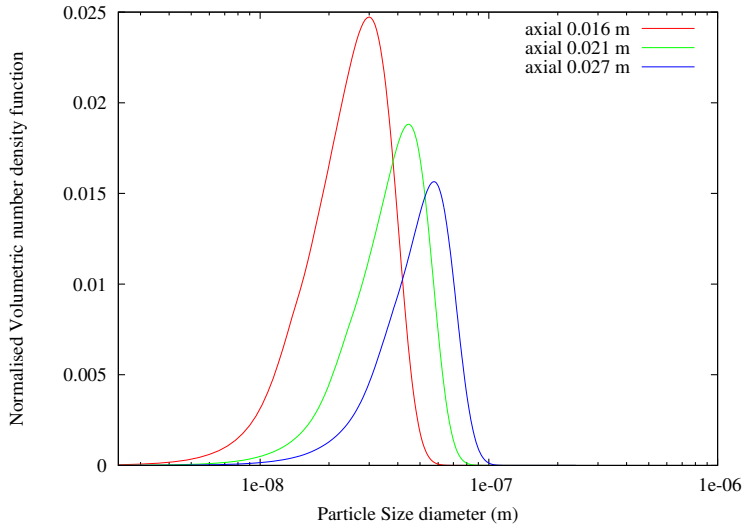

Figure 5.30: Normalised volumetric PSDs number density Incipient flame

5.5 Case study 3: smoking flame results

The last experiment is the smoking flame performed by Santoro et al. [9] by increasing the fuel and oxidiser inlet flow rates. In the smoking flame, a significant amount of soot is emitted from the tip of the flame (more soot emission than the incipient flame). The next Figure 5.31

shows the radial profiles of soot volume fractions at two axial distances, at 40 mm and 70 mm above the burner exit.

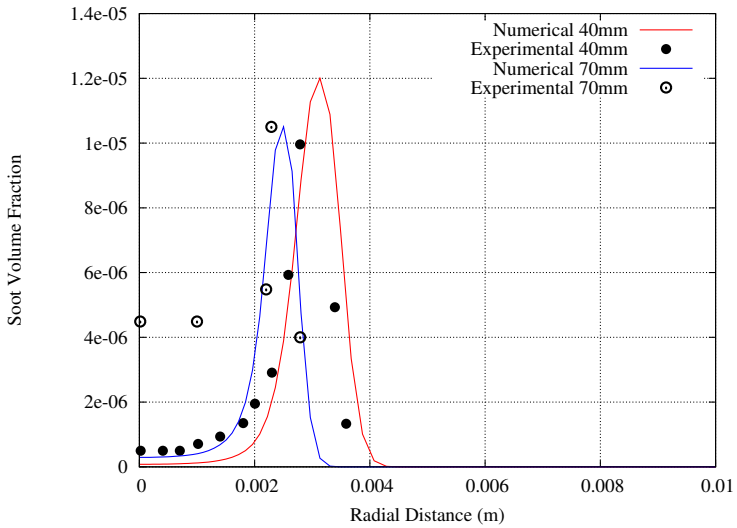

Figure 5.31: Radial soot volume fraction profiles at 40 mm and 70 mm

The radial soot volume fraction profiles in Figure 5.31 are in good agreement with respect to their peak values. However, the prediction on the centreline of soot volume fraction remains underpredicted by an order of magnitude. The centreline region has been identified in [83] as nucleation dominant region. Increasing soot nucleation by adding to the current mechanism (C_2H_2 nucleation step) a C_6H_6 nucleation step could result in an improvement. The Figure 5.32a demonstrates the total number density of soot particles along the maximum soot volume fraction pathline of the smoking flame.

Reasonable agreement is achieved for the predicted total number density of primary particles, even in smoking flame. The Figure 5.32b demonstrates the average primary particle diameter along the same path.

Observing the underprediction of the number density, and the overprediction of the average size, means that the volume fraction of particles is overpredicted as well. The Figure 5.33 shows the integrated soot volume fraction of the smoking flame.

Observing the predicted integrated soot volume fraction in Figure 5.33, it can be concluded that the trend is captured well; at the end, soot is emitted close the measured value. Moreover, similar to the non-smoking flame, the peak of the integrated soot volume fraction is slightly overpredicted and shifted towards the jet burner exit. It should be noted that without the

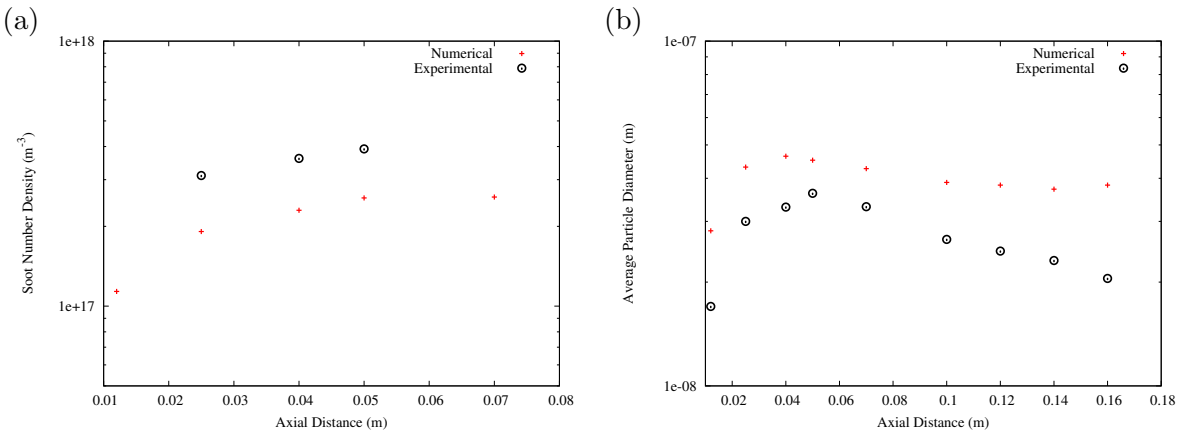

Figure 5.32: a) Total number density (m^{-3}) b) average primary particle diameter (m)

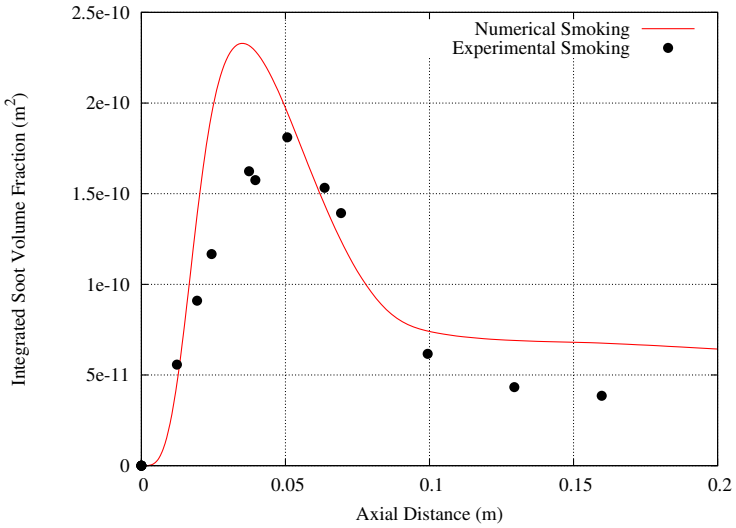

Figure 5.33: Integrated soot volume fraction (m^2) smoking flame

application of the correction factors, the oxidation rates are very strong - and even in smoking flame no soot is emitted in the model prediction as opposed to the experimental data. Finally, the last two Figures (5.34 and 5.35) show the normalised number density and volumetric distributions of the smoking flame.

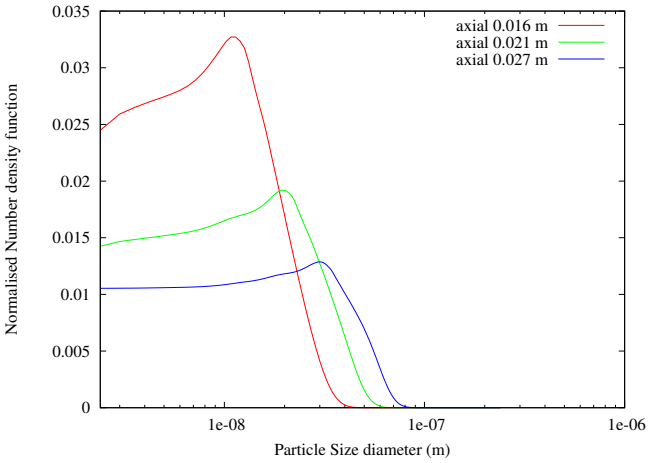

Figure 5.34: Normalised volumetric PSDs number density smoking flame

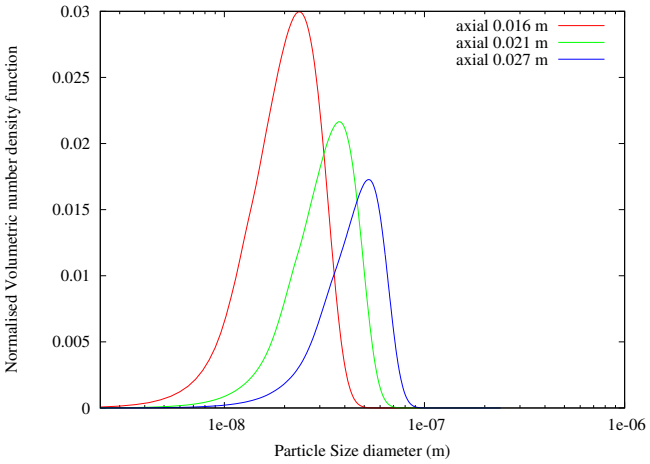

Figure 5.35: Normalised volumetric PSDs number density smoking flame

5.6 Summary and conclusions

In this Chapter, an acetylene-based soot model is used to describe the soot formation rates in the PBE. The time-dependent governing equations of momentum, species, enthalpy and discrete sizes of soot particles are solved in the 2D domain. The PBE predicts the complete PSD of the primary soot particles across the entire flame region for each flame. The model employed is validated against experimental results reported in section 5.1.

The original soot kinetics (without correction factors) that are applied to all the case studies, were very accurate in predicting the peak values of the radial soot volume fraction profiles, both in the smoking and non-smoking flame. Unfortunately, they cannot predict the sooting characteristics of the incipient and smoking flames experiment. The oxidation is very strong, and no soot is emitted from either flame. These findings are in accordance with [25, 53, 86]. However, this problem is alleviated by introducing correction factors to the oxidation rates. As such, the modified oxidation rates are of lower magnitude, and soot is emitted from the flame. The correction factors are initially tested and applied to the monodisperse acetylene-based soot model, found in [53]. In this thesis, the surface rates, combined with the correction factors, are effective in reproducing the integrated soot volume fraction profiles and sooting characteristics of all flames.

However, three results were unsatisfactory: the prediction of the radial temperature profile at 70 mm above the burner (see Figure 5.10), the soot volume fraction on the centreline of the flame (see Figure 5.18) and the sooting characteristics of incipient and sooting flames (see Figures 5.28b and 5.33). The first two problems have been avoided in [83] by applying a modified gas-phase mechanism to describe PAH growth and enhance soot nucleation in the centreline region. Regarding the sooting characteristics, this problem is fixed by applying the suggested correction factors in [53]. Another way to improve the soot kinetics is by modifying the surface reactivity term (similar to correction factors) of the HACA mechanism as implemented in [86], via an age property for the soot particles. Nonetheless, by applying the correction factors, the problem is only alleviated for incipient and smoking flames; in the non-smoking flame, a notable amount of soot is emitted despite the anticipated complete oxidisation. This leads to the suggestion that the employed correction factors, may decrease the strength of the oxidation rates more than expected. In spite of these underpredictions, overall, the flame structure and soot results were well predicted with this PBE formulation and should be applied to turbulent diffusion flames to test its performance.

Number density and volumetric PSDs results are found for all the test cases in the radial position, where the soot volume fraction peaks. In the non-smoking flame, there is a sudden rise in soot and peaks, earlier than the incipient and smoking flames. Thus, the three PSDs in the non-smoking flame are close to each other; in the other two flames, the space between the PSDs have more distance between each other at the same locations. This is because the soot particles had less time to spend in the surface growth region due to the higher inlet velocity. An accurate prediction of the PSD of primary particles is important, as they are the building blocks of predicting the structure of aggregates [14].

Chapter 6

Modelling soot in turbulent flames

In this Chapter two turbulent diffusion flames are investigated numerically. Several experiments exist in the literature, but the Brookes and Moss [10] methane experiment is chosen for study. The other experimental studies that could be investigated are the non-piloted ethylene turbulent flame of Kent and Honnery [161], or a set of piloted preheated propane turbulent flame experiments of Nishida and Mukohara [162].

It would be more appropriate to investigate the Kent and Honnery ethylene flame [161], as all the laminar diffusion flames investigations in Chapter 5 are performed for pure ethylene fuel. Moreover, in the propane flame experiment of Nishida and Mukohara [162] soot concentration and mole fraction of gas-phase species measurements are obtained. The gas species are essential in validating the structure of the flame and the important C_2H_2 species (precursors and main species for surface growth of soot formation). However, the Kent and Honnery experiment [161] is a non-piloted flame. For non-piloted flames, the transported PDF method (to be used and coupled with the PBE in this thesis) is a method that in several studies has demonstrated stabilisation difficulties for turbulent flames [68, 163]. On the other hand, both the ethylene flame and especially the propane flame, due to the higher hydrocarbon content, produce much more soot than the methane flame. Ethylene and propane flames will require a larger PSD domain of possibly many orders of magnitude to capture the particle size spectrum. This will result in a need for more scalars to represent the discrete sizes of soot particles, and will make the simulation far more computationally intensive. As such, the piloted methane flame is a suitable choice. Furthermore, methane is a fuel widely used in the energy industry; it is relatively well-known fuel with mature gas-phase mechanisms and a low number of species and chemical reactions compared to the more complex ethylene and propane gas-phase mechanisms.

6.1 Experimental Study and flame description

Two piloted methane turbulent jet flame experiments are numerically investigated. Both experiments have the same geometrical configuration, issuing the fuel and the oxidiser upwards. The only difference between them is that the first turbulent flame is studied at atmospheric pressure conditions (1 atm) whereas the second is conducted at elevated pressure (3 atm). Details regarding the specifications of both experiments can be found in [10]. In the atmospheric pressure turbulent experiment, the flame is lightly sooting, whilst in the elevated pressure flame the soot yield increases quite significantly. Radial and centreline profiles are measured at several points in the axial direction above the burner height. These measurements are averaged through time. As such, mean mixture fraction profiles, mean temperature profiles and mean soot volume fraction profiles are obtained. Unfortunately, no species concentrations or PSD of soot particles are measured .

The flame is contained inside a Pyrex tube of internal diameter 155 mm. Pure methane fuel is ejected from the central fuel tube. The jet pipe is surrounded by a small annular pilot tube where a rich methane-oxygen mixture is issued. The methane flowrate issued from the pilot tube is kept below 2% of the main fuel flowrate. The pilot burns a rich fuel mix of methane-oxygen in order to prevent any overheating at the burner tip and to avoid any flashback on the pilot tube [10]. A visible flame height of around 0.6 m is observed for the atmospheric jet flame, and approximately 0.4 m is observed for the elevated pressure flame. The dimensions of each component of the experiment are as follows. The central tube has 4.07 mm diameter and the pilot surrounding it has an annular region thickness of 160 μm. A schematic of the experimental configuration is shown in Figure 6.1.

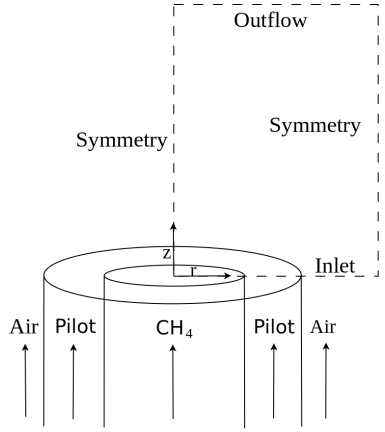

Figure 6.1: Schematic of turbulent flame configuration

It is noted in [10] that even with an annular pilot, the flame could be stabilised only at a Reynolds number of around 5000. For both flames the mean soot volume fraction measurements are subjected to a magnitude error of ± 50%. Moreover, the inlet mass flowrates of the oxidiser and the fuel are kept the same in both experiments. The inlet temperatures of the oxidiser and the fuel are specified at 290 K [10]. A summary of the operating conditions of both flame experiments is found in table 6.1.

Operation	Flame 1	Flame 2
Operating pressure	1 atm	3 atm
Fuel Mass flow rates	0.000172 kg/s	0.000172 kg/s
Air Mass flow rates	0.0118 kg/s	0.0118 kg/s
Fuel velocity	20.3 m/s	6.77 m/s
Air velocity	0.55 m/s	0.18 m/s
Exit Reynolds number	5000	5000

Table 6.1: Turbulent flame conditions of 1 and 3 atm experiments

6.2 Previous numerical studies

Many numerical studies have been performed for both experiments. The first numerical study on this flame is attempted by the same authors who conducted this experiment. The numerical study is found in [164]. The authors solved the Favre-averaged transport equations using a two dimensional parabolic code [164] and a standard k-ϵ turbulence model. The chemistry is modelled via laminar flamelets, with a presumed beta PDF function. The beta function is determined by computing the mean and the variance of the mixture fraction. The flamelet libraries of 1 atm are generated with 90 /s strain rate and the flamelet libraries of 3 atm are generated with 50 /s strain rate [164]. The Brookes and Moss study employed a two-transport equation model wherein the number density and mass fraction of soot particles are solved.

A subsequent numerical study is conducted by Kronenburg et al. [55] on the same flames. Their numerical study focuses on the influence of differential diffusion effects on soot particles. The authors conclude that neglecting differential diffusion can lead at least to a 40% underprediction of soot volume fraction profiles on the turbulent methane flame of Brookes and Moss [10]. As such, the differential diffusion of soot particles (which should be set close to 0) is essential, and should be taken into account in both the atmospheric and elevated pressure experiments.

Later, a numerical study of Roditcheva and Bai [165] employed a flamelet library approach using the one-dimensional counterflow configuration and an assumed PDF shape. A semi-empirical soot model similar to Brookes and Moss [164] along with the flamelet library are used to model soot formation and to account for the turbulence-chemistry interactions on both turbulent flames of Brookes and Moss [10]. Roditcheva and Bai state that the oxidation term is not included on the transport equation of the number density of soot particles (destruction of particles) because they assumed that the influence of oxidation was small.

Another study regarding the turbulent methane flame of Brookes and Moss is found in [19]. Favre-averaged transport equations are used with the k-ϵ turbulence model. The major difference of this study is that the eddy dissipation concept (EDC) is used to express the averaged source terms of the mean enthalpy, mean species and mean soot transport equations. Two semi-empirical soot models are used. The first of Brookes and Moss [164] and the second are similar to the Leung et al. soot model [75].

Another numerical study of Woolley et al. [95] employs the 2TEM approach to predict soot formation. The study of Woolley et al. [95] focuses on the influence of differential diffusion in turbulent methane flames and turbulent propane flames. A detailed gas-phase chemical mechanism is accounted for, with 70 species and 463 chemical reactions, and is an optimised mechanism for the oxidation of C_3 hydrocarbon species. The Woolley et al. study [95] further supports the concept that the differential diffusion of soot particles should be taken into account. Moreover, with the detailed mechanism of the study, a nucleation mechanism can be applied including C_2H_2 and C_6H_6 concentrations.

Later, a numerical study is performed with LES in [94] and model soot formation with the 2TEM approach considering only the atmospheric flame of Brookes and Moss [10]. Martinez and Rigopoulos [94] employed a detailed gas-phase chemical mechanism for methane combustion with 63 species and 415 chemical reactions. A rate-controlled constrained equilibrium (RCCE) approach is used to reduce the number of species in the chemical mechanism. Navarro-Martinez and Rigopoulos [94] manage to obtain good prediction by the reduction of the mechanism to 19 species. Moreover, differential diffusion effects on soot formation are investigated. Similar to the previous numerical studies, the soot distribution in the study of Navarro-Martinez and Rigopoulos [94] with the inclusion of differential diffusion is found to be closer to the experiments.

Another numerical study on both the atmospheric and elevated methane experiment of

Brookes and Moss [10] is found in [20]. A semi-empirical (2TEM) soot model is used similar to the one used by Brookes and Moss [164]. A Lagrange PDF method via Monte-Carlo simulation is used to account for the turbulence-chemistry and turbulence-radiation interactions. The PDF method applied to the study of Stoellinger and Roekaerts [20] is very similar to the PDF method used in this thesis. However, a Reynolds stress model is applied with a round jet correction term and buoyancy effects relative to the standard k-ϵ and a modified $C_{\epsilon 2}$ constant that is applied to model the turbulence in this thesis (see next section). The Lagrange PDF method studies assumed all the transported scalars to be of equal mass diffusivities. However, the study of Stoellinger and Roekaerts [20] includes the differential diffusion effects of soot formation in the micro-mixing term of the scalar PDF method via the scalar mixing frequency. The mixing frequency is kept the same for all the gas-phase scalars, whereas the mixing frequency of soot scalars (soot number density and soot mass fraction) is reduced a hundredfold. Moreover, a more detailed radiation model is applied by using a discrete transfer method to solve the radiative heat transfer equation and to account for the absorption term.

6.3 Computational model description

The in-house CFD code BOFFIN [51] is used to numerically investigate the turbulent methane flame at 1 atm and 3 atm of Brookes and Moss [10]. The Favre-averaged equations of the momentum equations are used as shown in equation (2.32) along with a standard k-ϵ turbulence model from equation (2.35) and (2.36). The k and ϵ transport equations are accompanied by some standard turbulence parameters on the computation of their source terms. The standard values of these parameters are listed in table 2.3, according to the previous numerical studies. However, the $C_{\epsilon 2}$ is set to 1.8 instead of its original value to improve the prediction of the turbulence spreading of the jet. The turbulence-chemistry and turbulence-radiation interactions are modelled using a transported PDF approach. However, a computational domain is still needed to model the micro-mixing term. The 2D computational domain is set at approximately 0.645 m in the axial direction and 0.0775 m in the radial direction. The following Figure shows the dimensions of the computational domain in detail.

The inflow conditions of the 1 and 3 atm turbulent flames are listed in Table 6.1. The turbulent kinetic energy and turbulent dissipation energy are specified at the inlet boundary and are applied with the same expressions mentioned in the original author's work in [7]. The

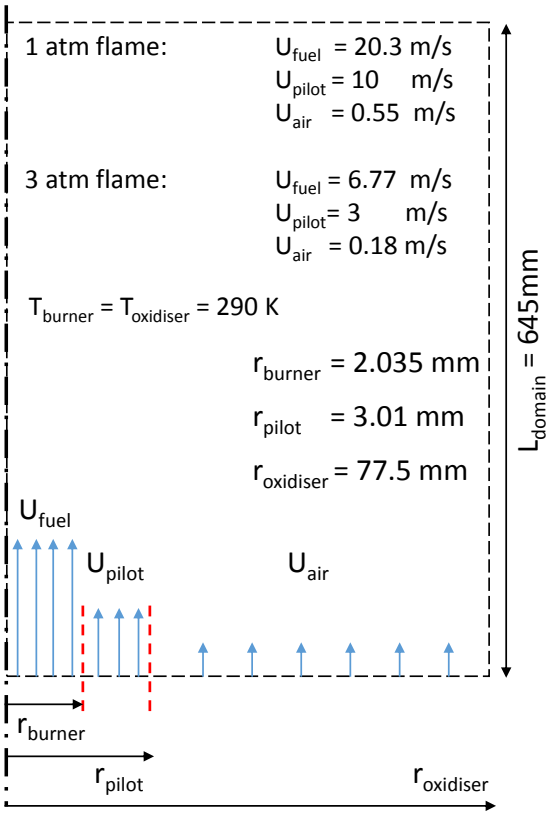

Figure 6.2: Computation domain of turbulent flames

turbulent kinetic energy is specified both at the fuel, pilot and air streams as $k = 0.00375u^2$, where u is the axial velocity. The dissipation rate of the turbulence kinetic energy in fuel, pilot and air streams is specified as $\epsilon = \frac{k^{\frac{3}{2}}}{r_{pipe}}$. The discrete sizes of soot particles are all set to 0 at the inflow boundaries. The Figure 6.3 shows the mesh that is employed in all the turbulent diffusion flames. The mesh similar to the laminar flame is non-uniform and is set up with 80 points in the axial and 50 points in the radial direction with a non-uniform mesh which is finer towards the jet burner exit where larger gradients exist in that area. In the axial direction the non-uniform mesh has a single expansion ratio of 1.03 and in the radial direction the grid has a single expansion ratio of 1.05. Moreover, 500, 000 Lagrangian particles are used to solve the stochastic representations of mixture fraction, species mass fraction, enthalpy and discrete sizes of soot particles. The table 6.2 shows the parameters and models that were used for both $1atm$ and $3atm$ turbulent diffusion flames. The total number of scalars (N_{sc}) in both flames is 234. The N_{sc} is composed by 200 discrete diameters to describe the size of soot particles 32 gas-phase chemical species (GRI 1.2), mixture fraction and enthalpy.

The method employed in this thesis is a PDF-PBE using a Lagrangian framework to solve the particle representations of gas-phase chemistry and the evolution of the PSD of soot particles.

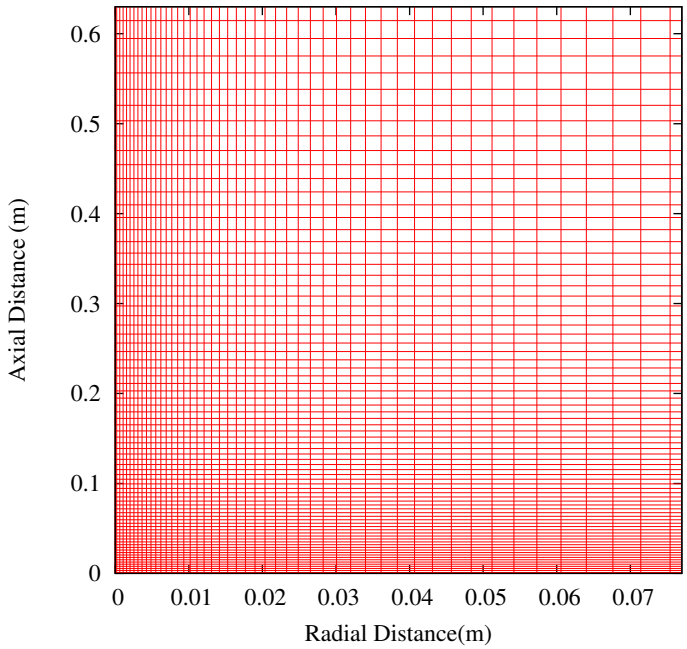

Figure 6.3: Representation of the turbulent flames mesh

Numerical mesh	$80(z) \times 50(r)$
Turbulence model	Standard k$-\epsilon$
Total of stochastic particle	$500,000$
Stochastic particles per cell	125
Mixing model closure	EMST
Mixing coefficient (C_D)	2
Total number of scalars (N_{sc})	234
Gas-phase mechanism	GRI 1.2

Table 6.2: Turbulent flame parameters for 1 and 3 atm experiments

The equations that were solved are shown in the summary of Chapter 2 (see equations (2.115)-(2.117)). It should be noted that full chemistry is employed to this work without any reduction techniques or simplified gas-phase mechanisms and the soot kinetics are exactly the same with the ones employed in the laminar flame and shown in the summary of Chapter 2 (see equations (2.110)-(2.113)). Furthermore, the PSD domain of the soot particles is descritised in the particle diameter space with uniform grid spacing $(\Delta L) = 1.2{\cdot}10^{-9}m$ and nucleus size $d_{p,nuc} = 2.4{\cdot}10^{-9}m$

6.4 Case Study 1: atmospheric flame

The atmospheric pressure flame results will be shown and discussed in this section, and the results of the elevated pressure flame are presented in the next section. The results are compared against the respective experimental results of mixture fraction, temperature and soot volume fraction. Unfortunately, there are no velocity measurements for this experiment to validate the flow field. Temperature, total soot number density and soot volume fraction contour plots are shown in the entire flame region. Figure 6.4 shows the centreline temperature profile of the atmospheric pressure.

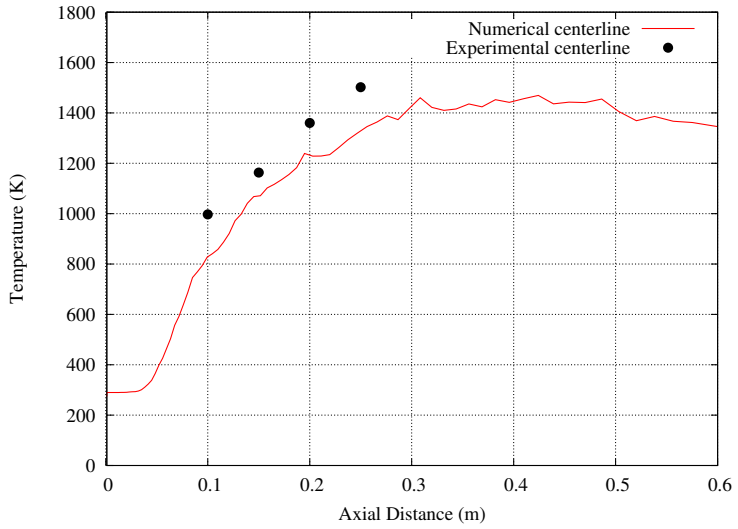

Figure 6.4: Centreline temperature (K) in 1 atm flame

The increase of the temperature from the jet burner exit and the profile across the centreline is well-captured. However, the temperature at 0.250 m is slightly underpredicted. On the other hand, the visible flame length is reported in [10] to be around 600 mm, which is in relatively good agreement with the centreline profile where the centreline temperature slightly drops at 600 mm in relation to the visible flame.

(a)

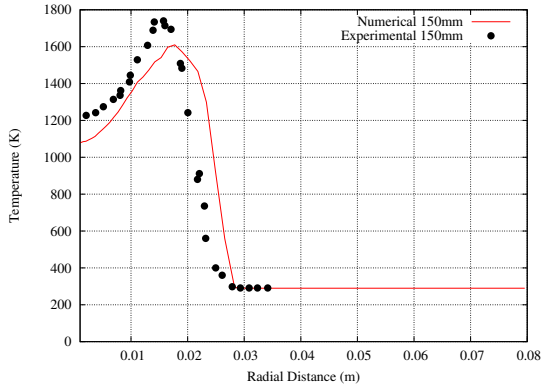

(b)

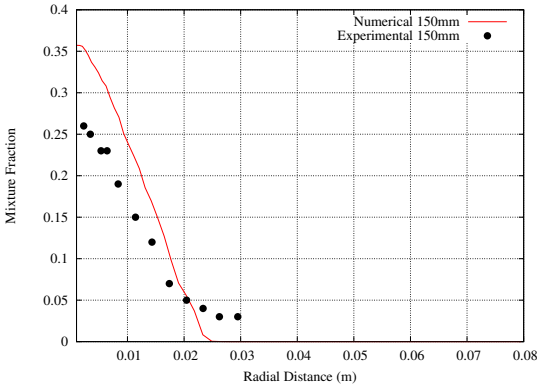

150

(c)

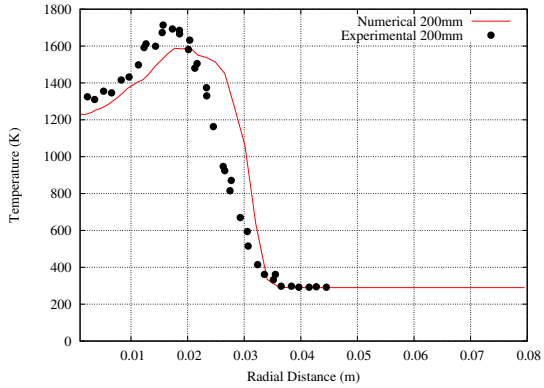

(d)

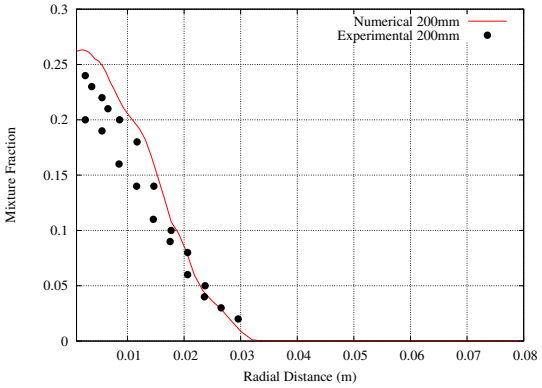

200

(e)

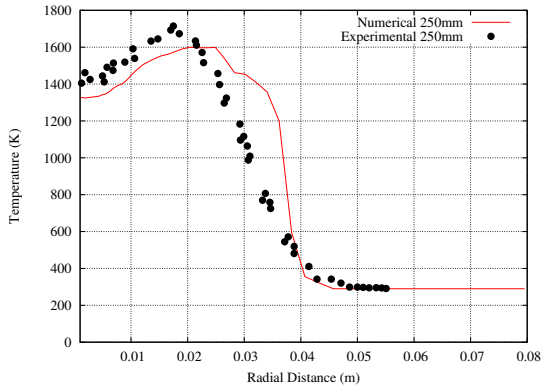

(f)

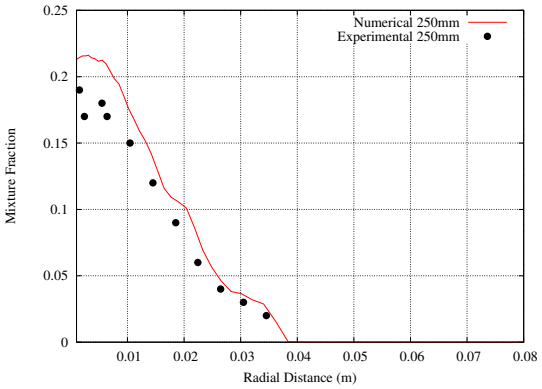

250

(g)

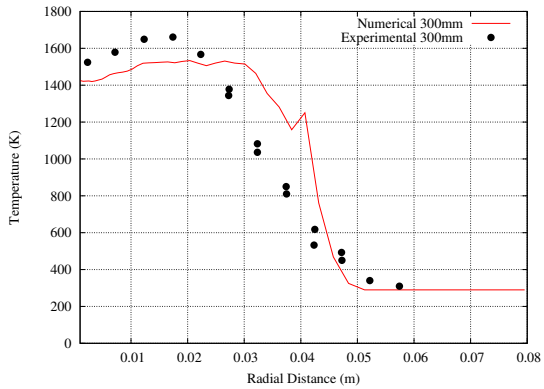

(h)

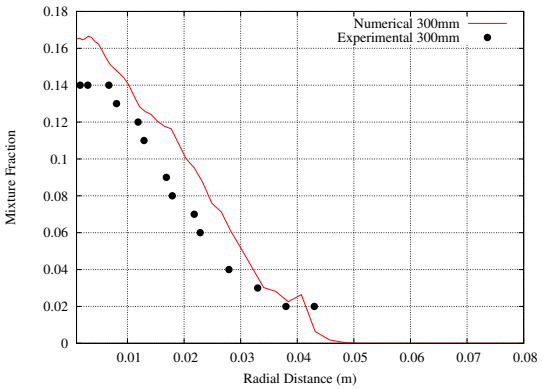

300

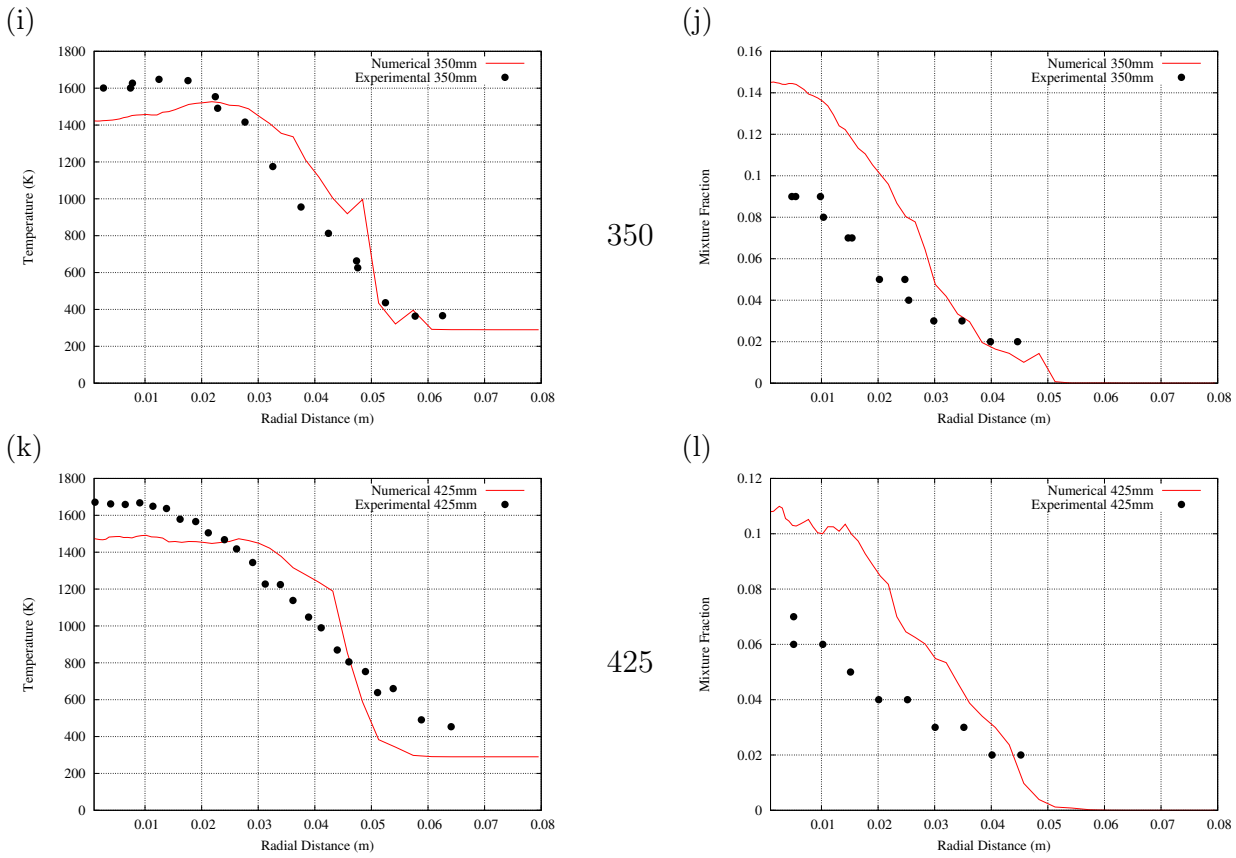

Figure 6.5: Temperature (K) and mixture fraction radial profiles 1atm flame

The Figures 6.5a, 6.5c and 6.5e show the radial temperature profile at 150mm, 200mm and 250mm above the burner. The radial temperature profiles closest to the burner exit have been measured and predicted at 150 mm. The radial temperature profiles at 150mm, 200mm and 250mm are generally well-predicted with an underprediction of approximately 150K at their peak temperature points. Moreover, the width of the flame is well captured at 150 mm, whereas at 200 mm and 250 mm above the burner the radial position of temperature is slightly overpredicted and their peak values are shifted towards the radial direction away from the centreline. More radial temperature profiles across the flame are shown in Figures 6.5g, 6.5i and 6.5k.

The trends of the radial temperature profiles at 300 mm, 350 mm and 425 mm are in reasonable agreement with the experimental results. Even so, the peak temperature values are slightly under predicted. Overall, the temperature profiles seem to be reasonably captured with the optically thin approximation radiation model. However, re-absorption term should be included to improve the temperature underprediction. Figure 6.6 shows a contour plot of temperature across the entire flame region.

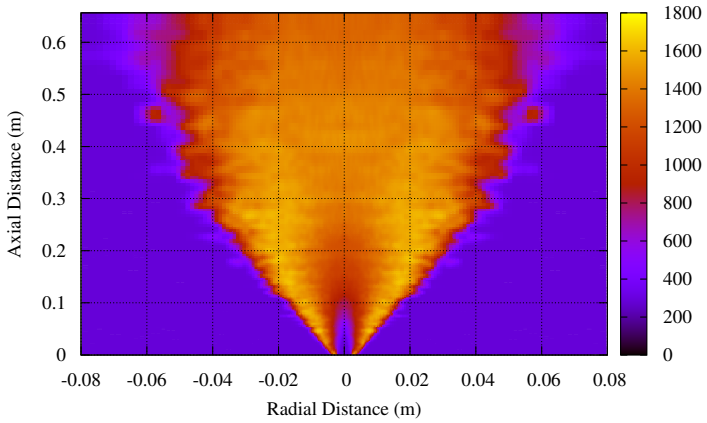

Figure 6.6: Contour plot of temperature (K) in 1 atm flame

It is obvious from the temperature contour plot in Figure 6.6 that the flame's width is increased (in the radial direction). The peak temperatures are located towards the wings of the flame and the near the pilot's region. The next Figure 6.7 show the mixture fraction profile on the centreline of the flame where the measurements are obtained by using a probe to draw gas samples from the flame as it is stated in [10].

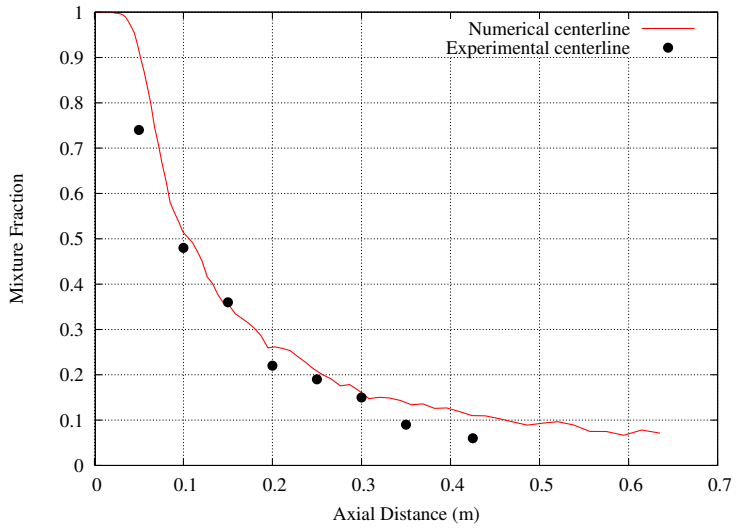

Figure 6.7: Centreline mixture fraction in 1 atm flame

The mixture fraction decay is well-captured along the centreline as shown in Figure 6.7.

Several radial profiles of mixture fraction are presented in the next Figures 6.5b, 6.5d and 6.5f.

Relatively good agreement is observed for most of the parts of the mixture fraction at 150mm, 200mm and 250mm above the burner. A noticeable overprediction of mixture fraction is observed close to the centreline of Figure 6.5b. Additional Figures 6.5h, 6.5j and 6.5l displaying the mixture fraction at 300 mm, 350 mm and 425 mm above the burner are shown.

Reasonable agreement is observed for the rest of the mixture fraction radial profiles at 300 mm, 350 mm and 425 mm. However, there is a significant overprediction in all of them near the centreline. Similar overprediction is observed on the mixture fraction centreline of Figure 6.7. This overprediction increases in the axial direction probably due to the the spreading of the jet that is not accurately predicted across the domain. Figure 6.8a shows the prediction of the coupled PDF-PBE model on soot volume fraction relative to experimental measurements at the centreline of the flame.

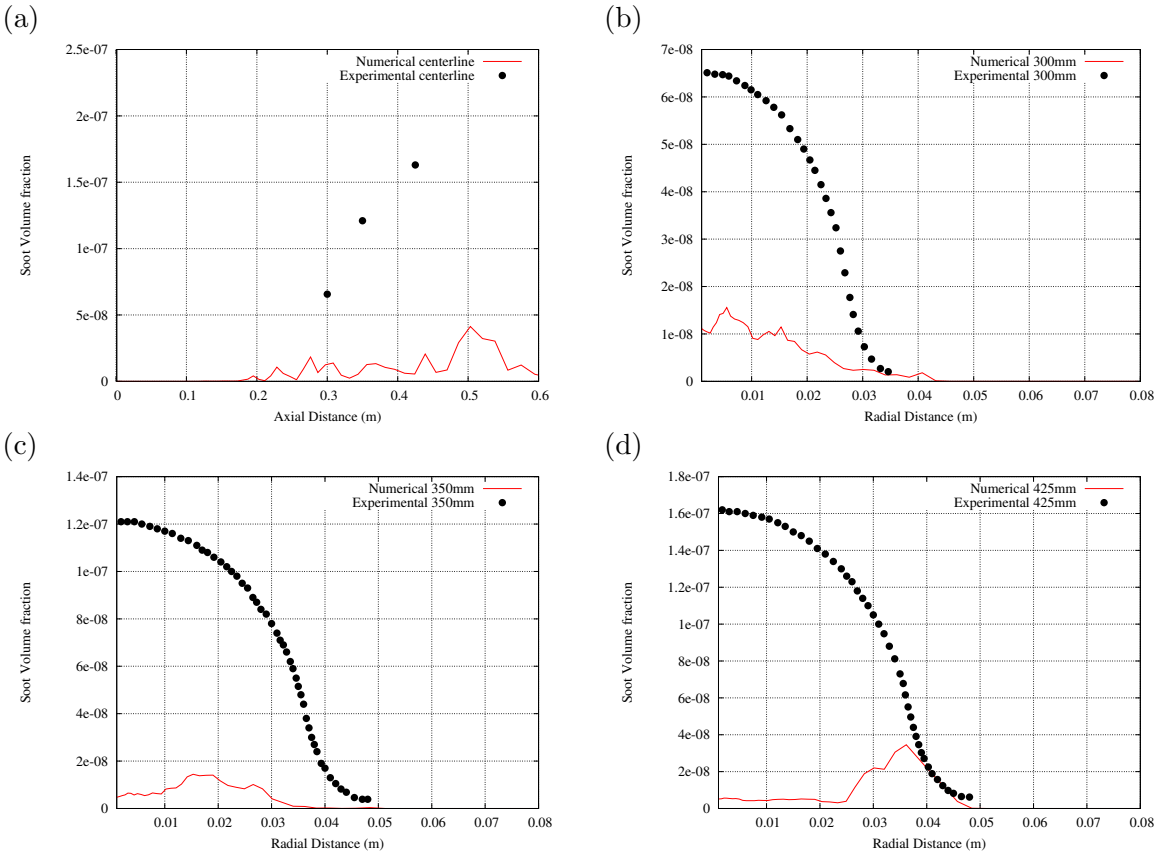

Figure 6.8: Centreline and radial soot volume fraction profiles

The next Figures 6.8 show the centreline and radial profiles of soot volume fraction at 300 mm, 350 mm and 425 mm above the burner. The centreline and radial soot volume fraction profiles exhibit a significant underprediction - a factor of four. To include differential diffusion

effects on soot particles, the micro-mixing term is set to 0, whereas the species have the same mixing frequency. The soot formation study of the same flame [55] used 2TEM approach and pointed out that the underprediction of the soot volume fraction found in their numerical study is due to differential diffusion negligence.

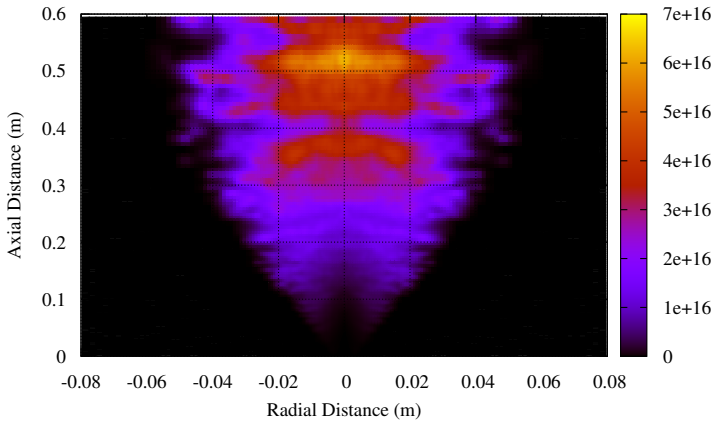

Figure 6.9: Total number density (m^{-3}) of soot particles in 1 atm flame

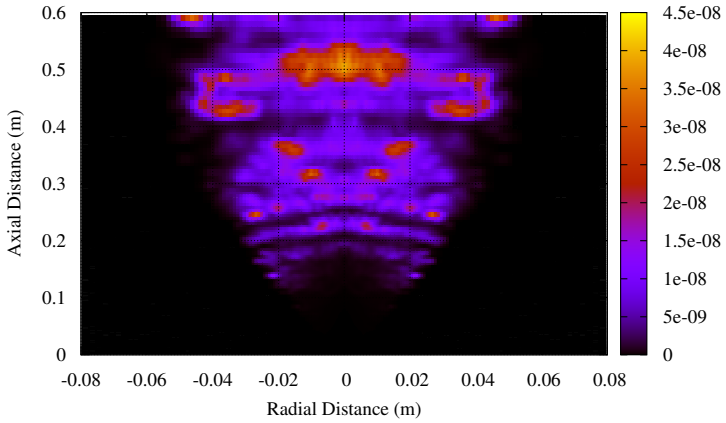

Figure 6.10: Soot volume fraction in 1 atm flame

However, in this study, the underprediction of soot volume fraction is attributed due to the temperature underprediction mainly at the centreline of the flame which the soot formation

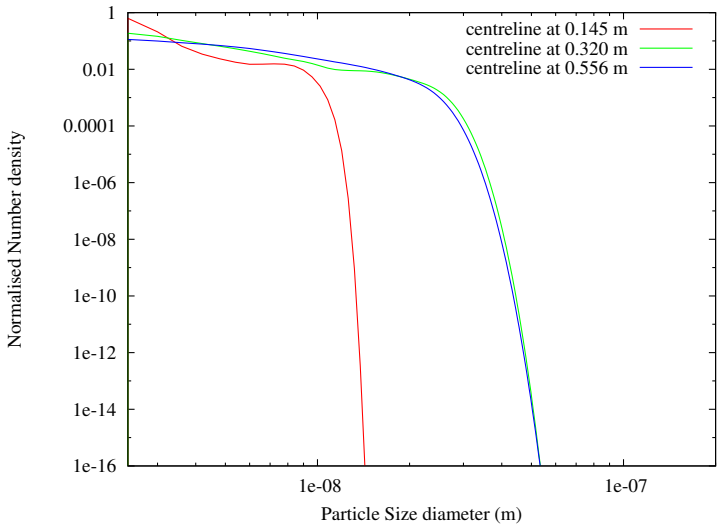

Figure 6.11: Normalised PSD of 1 atm flame

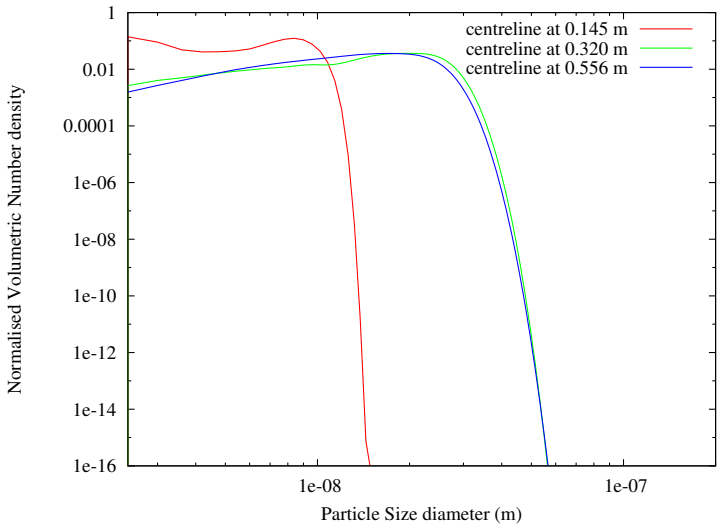

Figure 6.12: Normalised volumetric PSD of 1 atm

processes are very sensitive to it. Thus, the gas-phase chemical mechanism, the nucleation term (which is an incomplete description for this study) or assuming an optically thick instead of optically thin radiation model could further improved the results of this study. Figures 6.9 and 6.10 are contour plots of the total number density of particles and soot volume fraction, respectively. The wavy feature is attributed the micro-mixing term of the soot particles which is set to 0.

Soot volume fraction and number of particles start to form very close to the burner exit.

The soot number density is concentrated and peak around the centreline of the flame, similar to the soot volume fraction results. Figures 6.11 and 6.12 show the normalised PSD of number density and volumetric number density.

Figures 6.11 and 6.12 show the PSD of soot particles at an early axial point on the flame centreline (0.145 m), until an axial point close to the end of the flame length (0.556 m). The PSDs at 0.320 m and 0.556 m seem to be stable and not much difference is observed within this zone. The incipient soot particles in this flame have a diameter of 2.4 nm . The largest soot particles were predicted to be approximately 40 nm.

6.5 Case Study 2: elevated pressure flame (3 atm)

In this section, the same turbulent flame is investigated at an elevated pressure of 3 atmospheres. The boundary conditions are modified accordingly to match the experimental specifications. As with the 1 atm flame, temperature and soot volume fraction results are compared with experimental results without mixture fraction measurements. The next Figure 6.13 shows the temperature profile on the centreline of the flame.

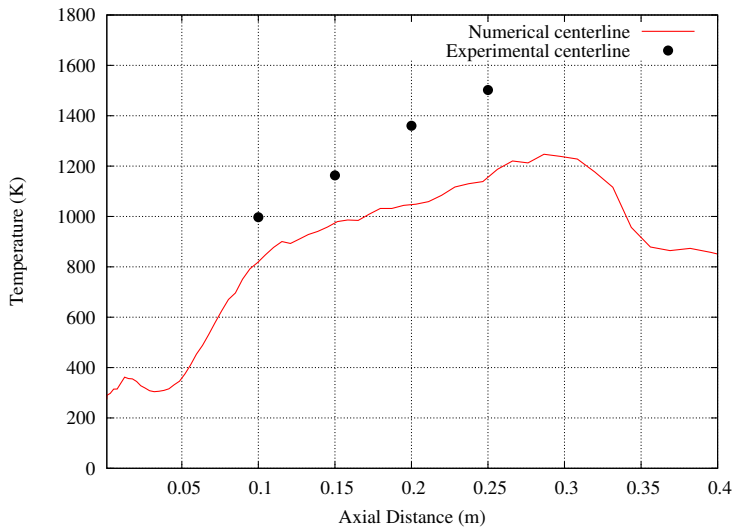

Figure 6.13: Centreline temperature (K) of 3 atm

The evolution of the centreline temperature profile of the 3 atm flame is predicted satisfactorily, although the peak temperature is underpredicted. However, the flame length is reported in [10] to be approximately 400 mm, where the drop in temperature according to Figure 6.13

starts at 0.3 m. Figures 6.14a and 6.14b show the radial temperature profiles at 100 mm and 150 mm above the burner.

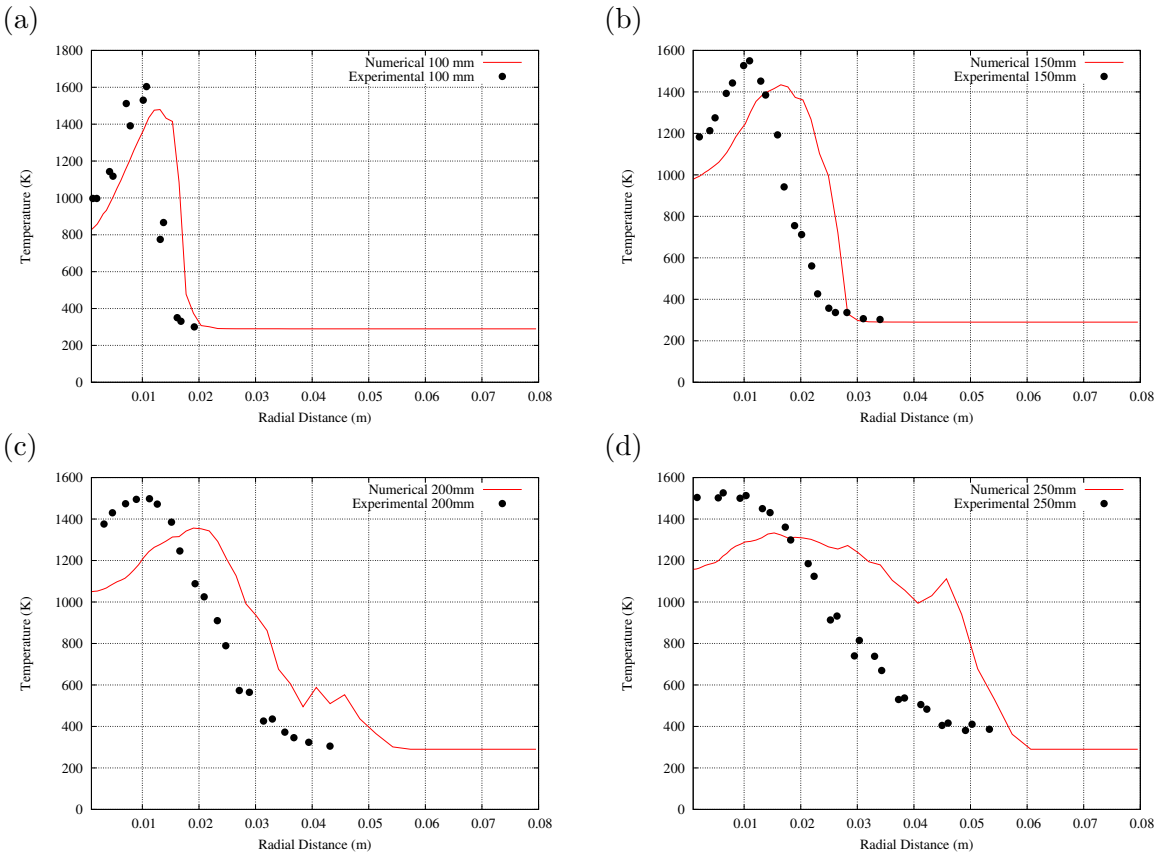

Figure 6.14: Radial temperature (K) profiles 3atm

Reasonable agreement is observed in Figures 6.14a and 6.14b for the radial profiles of temperature at 100 mm and 150 mm close to the burner exit. Further radial temperature profiles are shown in Figures 6.14c and 6.14d. The prediction deviates from the experimental as observed at 200 mm and 250 mm above the burner. The trends, width and peak values of temperature are not well captured implying that significant improvement still is needed such as with the spreading of the jet or a more detailed soot radiation. The temperature contour plot is shown in Figure 6.15.

Compared to the flame at atmospheric pressure, the temperature contour plot of the flame at elevated pressure reveals that the width of this flame is much smaller, and the maximum visible flame height is observer to be close to 400mm. The next Figure 6.16 shows the soot volume fraction on the centreline of the flame.

The peak values of the centreline soot volume fraction profile is overpredicted and peaks at an early stage whereas it is significantly underpredicted by an order of magnitude. Radial soot

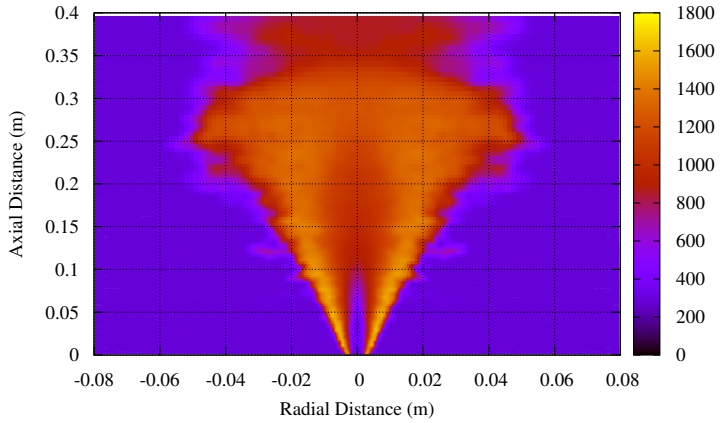

Figure 6.15: Temperature (K) contour plot of 3 atm

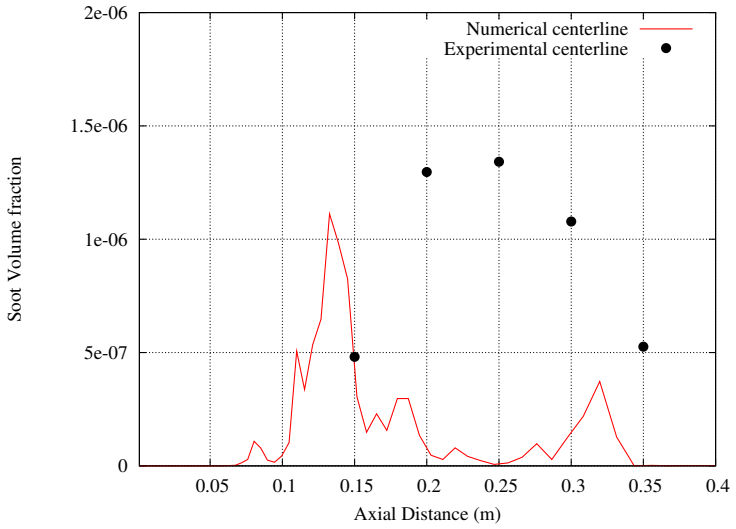

Figure 6.16: Centreline soot volume fraction of 3 atm

volume fraction profiles are compared in Figures 6.17. Reasonable prediction is obtained for the radial soot volume fraction profiles in Figure 6.17a. However, the radial profiles of soot volume fraction in Figure 6.17b exhibit significant underprediction (of an order of magnitude). The next Figures show more radial soot volume fraction profiles.

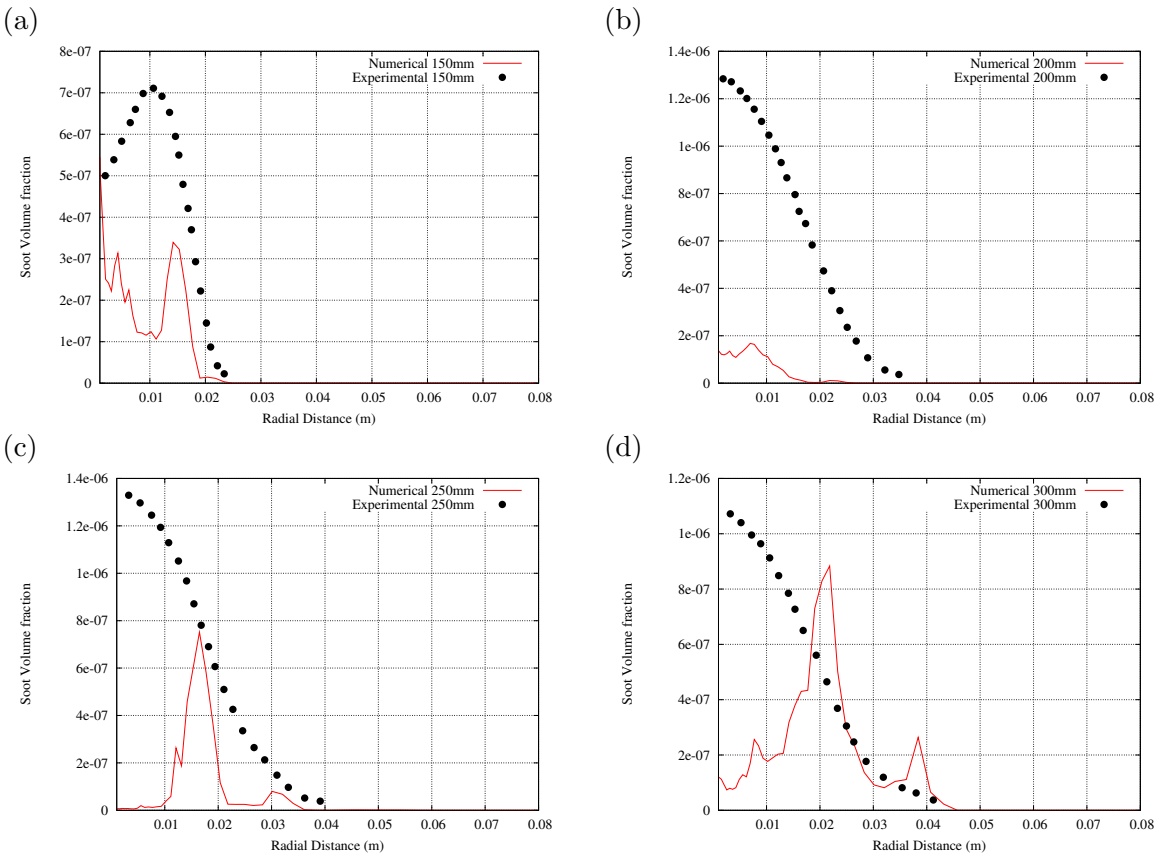

Figure 6.17: Radial soot volume fraction profiles 3atm

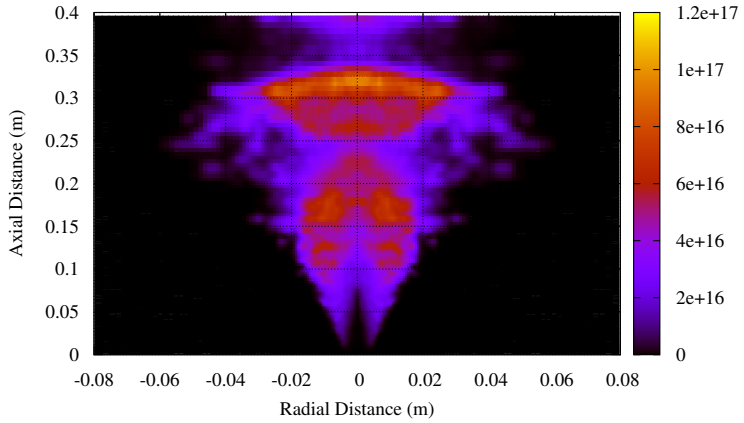

Figure 6.18: Total number density (m^{-3}) of soot particles contour plot of 3 atm

In Figures 6.17 the soot volume fraction is underpredicted in most of the parts and peaks at wrongful locations. Taking into account the radiation absorption and flow field improvements

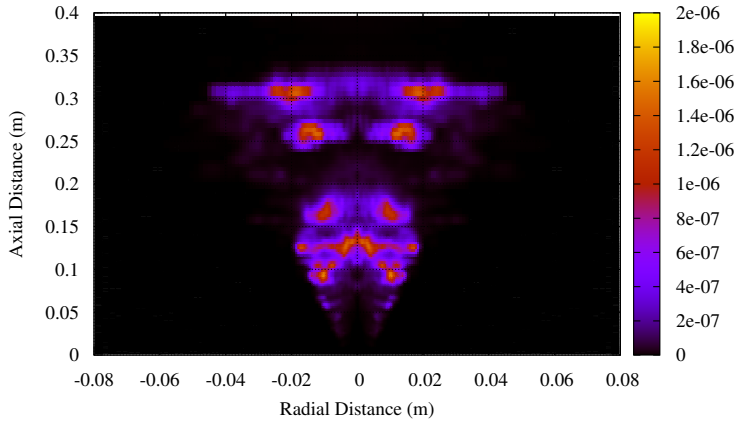

Figure 6.19: Soot volume fraction contour plot of 3 atm

such as improve the spreading of the jet and mixing fields in the domain will result in a better temperature agreement and soot volume fraction results. Total soot number density and soot volume fraction contour plots are shown in the next Figures 6.18 and 6.19, respectively.

The last Figures 6.20 and 6.19 show the evolution of the PSD of this flame at three axial points on the centreline.

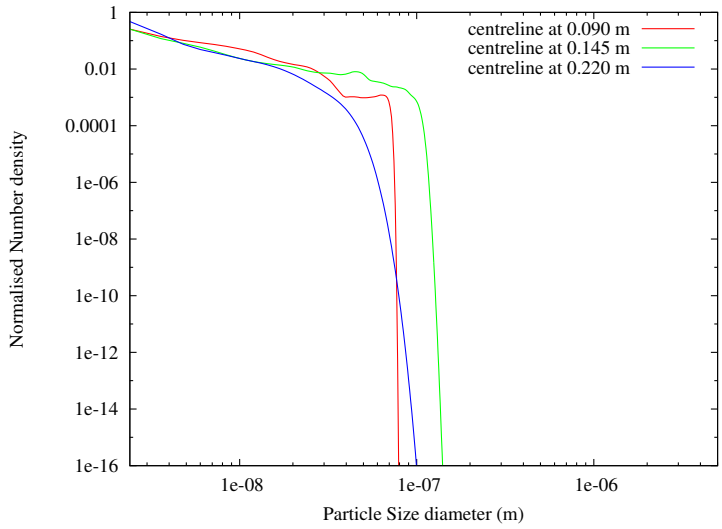

Figure 6.20: Normalised PSD of 3 atm

The normalised PSD is shown for 90mm, 145mm and 220mm above the burner. The PSDs

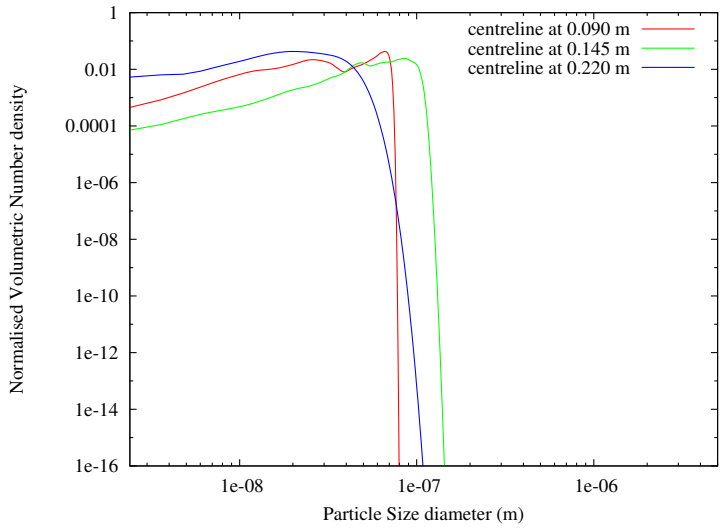

Figure 6.21: Normalised volumetric PSD of 3 atm flame

are steadily increased throughout the flame, reaching a maximum size of particles at approximately 1 μm.

6.6 Summary and conclusions

In this chapter an in-house CFD (BOFFIN) is coupled with a transported PDF-PBE method to resolve the turbulence-chemistry, turbulence-PBE and turbulence-radiation interactions. The PDF-PBE method uses a Lagrangian Monte-Carlo algorithm with stochastic particles, to solve the representations of mixture fraction, species, enthalpy and discrete particle sizes of the soot number density function. The benefit of using the transported PDF approach is that the chemical reaction, radiation emission and soot source terms are in closed form and can be computed directly without any assumptions. The PDF-PBE uses a GRI 1.2 mechanism to obtain the structure of CH_4 flame and an optically thin approximation method to model gas-phase and soot radiation. The EMST mixing model was applied with a mixing coefficient equal to 2.

The PDF-PBE method was employed to two turbulent axisymmetric methane flames. The atmospheric and the elevated pressure turbulent flame experiments are conducted by Brookes and Moss [10]. The mixture fraction and temperature profiles are reasonably predicted compared to the atmospheric flame experimental results. However, the soot volume fraction results

are found to be underpredicted by a factor of four at the centreline. This underprediction is increased in the radial soot volume fraction profiles. Differential diffusion effects of soot formation are included as suggested in [55]. The molecular mixing is set to 0 in this thesis for the soot discrete sizes. Even so, this underprediction still exists, despite the good agreement of the soot kinetics in the laminar flames (see Chapter 5). As such, the results could be improved by implementing a more sophisticated gas-phase mechanism. Another option is to include C_6H_6 species to the nucleation term as it is stated in the study of [166], where a similar underprediction on the centreline is decreased. In the elevated pressure flame, the temperature profiles have a greater discrepancy than those of the atmospheric flame computation. The flame length is predicted to be around 300mm where the reported flame length from the observation of Brookes and Moss experiment [10] is approximately 400mm.

It should be noted that in both flames an optically thin approximation is used where radiation is emitted and no re-absorption of energy takes place. A similar numerical study of [20] accounted for the re-absorption term of radiation and managed to obtain a good temperature agreement on the centreline of both 1 atm and 3 atm flames. Thus, a re-absorption radiation term could improve the profiles of temperature and soot volume fraction in the flame. Another possible improvement to the spreading of the jet would be the the addition of the round jet correction factor.

The PDF-PBE yields a complete PSD of soot particles in the entire turbulent flame region. No experimental data of PSD is available for comparison. The results of the PDF-PBE approach could be improved by applying the aforementioned suggestions.

Chapter 7

Conclusion

7.1 Summary and achievements of thesis

The prediction of soot formation is very complex with chemical and soot kinetics, radiation, soot particle dynamics and turbulence interactions. The work from the preceding Chapters examines the potential of the discretised PBE to obtain the complete PSD as the complexity of the flow is progressively increased from well-mixed systems, laminar and eventually to turbulent reacting flows which are summarised in this Chapter in order to draw some overall conclusions. Any problems and uncertainties regarding the fulfilment of the original objectives of this thesis have been examined and how these objectives have been met. In the end of this Chapter some recommendations for future work are proposed to improve the predictive capability of the models and to incorporate more detail in the representation of the soot particle formation.

The first objective of this thesis was to initially assess the performance of certain numerical methods to obtain the solution of the PBE in an initial distribution test, 0D reactors and a 1D flamelet. The original finite element collocation method provided in Rigopoulos and Jones [24] has been modified into a finite volume method with TVD scheme. The solutions of the new discretised form, such as the first moments and complete PSD, have been validated against exact solutions of moment methods and method of characteristics. It has been shown that for the same mesh resolution in the PSD domain, the prediction of the number density function (i.e. solution of PBE) and its mean properties are significantly improved by using the high resolution finite volume scheme instead of using the finite element suggested in Rigopoulos and Jones [24]. As such, the finite volume method with TVD scheme was found to exhibit the best performance in comparison to others (i.e. finite element collocation type, finite volume

first order and second-order central scheme). It should be further noted that the PBE has been tested for both diameter and volume size as the internal coordinate. In the volume size space, where the growth flux terms are size-dependent, the original finite element method does not converge to the exact solution as the finite volume upwind scheme does. Additionally, the particle domain in volume space requires an enormous number of points compared to diameter space to be accurately represented. The PSD and the 0^{th} moment are underpredicted with the finite element method of Rigopoulos and Jones [24], whereas the finite volume method predicts the PSD correctly. However, the prediction of the first moment of the distribution is very similar for both finite element and finite volume techniques.

The second objective of this thesis was to compare the discretised PBE with widely used soot modelling approaches such as the 2TEM and MoMIC approach in a 1D flamelet system. During the comparison between the approaches, examination was conducted for the feasibility of incorporating a variety of soot kinetics to the PBE. These soot kinetics have already been implemented with a relative success to predict the mean properties of soot formation in laminar and turbulent flames via the 2TEM [55, 78] and the MoMIC approach [79]. It has been shown that the same soot kinetics as applied in the 2TEM approach, in the PBE model introduce significant discrepancy in the mean properties of the PSD, due to the monodispersity assumption where the total surface area is computed by the first two moments. The soot kinetics of the widely-used 2TEM approach have been identified that are not appropriate for the polydisperse PBE model that takes into account the surface area of each particle size section. However, the solutions of the MoMIC and PBE models are found to be in a closer agreement. Therefore, the soot kinetics of the MoMIC code that exhibit reasonable agreement with an experiment can have a very similar level of accuracy when they are applied in the PBE model to describe soot formation. Nonetheless, PAH-based kinetics require more complex gas-phase chemical mechanisms (up to $C_{16}H_{10}$). This is why instead of using PAH-based kinetics, an acetylene-based soot model is preferred and employed in this thesis to reduce the computational cost of the simulations in turbulent flows by using less detailed gas-phase chemical mechanisms. Therefore, neither the soot kinetics of 2TEM and MoMIC approaches are implemented to the PBE to investigate multidimensional laminar and turbulent sooting flames in this thesis. The most appropriate soot kinetics would be the ones who had a reasonable success into a polydipserse soot model and not the ones employed in 2TEM approaches. The origin of the acetylene-based model that is employed in the laminar and turbulent diffusion flames in this thesis comes from

the application of a sectional model study of soot formation in Smooke et al. [81, 167, 49].

The third objective was to apply and validate the discretised PBE with appropriate soot kinetics in a laminar axisymmetric non-premixed flame experiment. The effects of the various elements of the model and their importance are examined before introducing the PBE model into turbulent flames where great uncertainties appear due to turbulence interactions. The implementation of detailed chemistry and complex transport coefficients was found to be important as their negligence will deteriorate the prediction of the structure of the flame and the soot volume fraction results. However, this detailed implementation proved to be very costly for a serial computation. To understand why, an analysis is performed of the time needed in each section of the code. It became evident that an enormous amount of computational time is spent on the calculation of the chemistry source terms of each species, while a lesser amount was dedicated on the PBE section, the transport coefficients and the CFD convection-diffusion processes. According to the time analysis, certain tasks of the code have been parallelised. A significant improvement of the computational speed was achieved by a factor of 8.5 - when 16 processors were used making this computation feasible. In case the total number of the transported quantities is reduced, such as the 400 transport equations of the PBE are not solved, the speed up factor is increased to 11 with 16 processors. Therefore, the parallelisation could be made more efficient by parallelising the computation of the convection-diffusion terms of each transport equation. For simplicity, the convection-diffusion was solved by one CPU (serial process) due to the spatial gradients that require the information of neighbouring grid points in space.

The coupled parallelised CFD-PBE model was employed to solve three laminar diffusion flames (i.e. non-smoking, incipient and smoking flame) without any variation of the modelling parameters between the simulations. The high resolution finite volume PBE model (first objective) was joined with the detailed CFD model and appropriate soot kinetics (second objective) using the particle diameter as the internal coordinate. The experiments of Santoro et al. [8] were found to be suitable for the validation of the CFD-PBE. For illustration purposes, the complete PSDs are shown at three different axial points, indicating the evolution of the PSD in physical space and the dominant soot formation processes.

The non-smoking flame was firstly investigated as it contains a vast data available both experimentally and numerically. Temperature and axial and radial velocity profiles were compared with the experimental, exhibiting relatively good agreement. Mole fractions of C_2H_2

and OH species were reasonably predicted. Soot volume fractions were compared and also displayed good agreement. However, on the centreline, the soot volume fraction was underpredicted by an order of magnitude. This is a common problem for the laminar diffusion flames where very similar underpediction of the same flame can be found in [25, 23, 83]. On the other hand, the temperature prediction on the centreline of the flame is in a better agreement with the experimental data compared to the 2TEM study found in [53]. However, the soot volume fraction prediction on the centreline of the flame is significantly improved as shown in the study of [83] by using a gas-phase chemical mechanism to enhance aromatic formation when using PAH kinetics. In case of the other two flames (incipient and smoking flames), no soot emission was predicted with the original soot kinetics from the tip of the flame similar to the studies of [25, 86]. The soot particles were completely oxidised inside the flame, even in the smoking flame, where a significant amount of soot was emitted according to the experiments. However, in this thesis by applying the correction factors found in [53] to the soot oxidation rates of O_2 and OH, a fraction of soot particles is predicted to escape from the tip of the flame. Integrated soot volume fraction and radial soot volume fraction profiles showed reasonable agreement with the experimental data. The soot kinetics are improved with the correction factors to take into account the sooting characteristics of the flame. The three laminar diffusion flames exhibited a reasonable agreement of the soot amount produced. The soot volume fraction results of the smoking flame are very similar to the 2TEM study of [25] where by applying the correction factors in this thesis the smoking flame results are improved and soot is emitted from the tip of the flame proving that the current CFD-PBE application is successful overall to predict the flame structure and smoking flame characteristics. The coupling of the detailed CFD-PBE model with suitable soot kinetics predicted with a reasonable level and in some parts very good accuracy the soot formation processes in three laminar diffusion flame experiments and the complete PSD was obtained anywhere in the flame region.

The fourth and final objective was to combine the CFD model with a transported PDF-PBE method along with the standard $k-\epsilon$ turbulence model to investigate soot formation in two turbulent diffusion flames. The same soot kinetics and PBE model are employed as the laminar flames (third objective). The representations of all scalars were solved using stochastic particles, where EMST mixing model was employed with a mixing coefficient C_D equal to 2 and an optically thin approximation for computing the divergence of the radiative flux. Two turbulent diffusion flames were experimentally and numerically investigated by the same authors

[10, 164] at 1 atm and 3 atm. In this thesis, reasonable predictions were found for the mixture fraction and temperature at the centreline and several radial profiles. However, the soot volume fraction profiles were significantly underpredicted, almost an order of magnitude. According to few 2TEM soot formation studies [164, 55, 165, 166, 20] for the same flame the mixture fraction, temperature and soot volume fraction results are generally well-captured. Suggestions and implementations according to these numerical studies could be applied to further improve the results. Some of these improvements that have not been applied to this thesis is to use a more detailed gas-phase chemical mechanism compared to the GRI 1.2 and include a C_6H_6 nucleation step as suggested in [166]. However, the implementation of a more detailed gas-phase mechanism will make the simulation more computationally demanding. Another improvement is to use a more detailed radiation model to compute both the radiation emission and absorption terms by solving a radiative heat transfer equation using the discrete transfer method as described in [20]. It should be noted that temperatures are underpredicted on the centreline of the flame and by including the re-absorption term will increase the temperature profiles and produce more soot and could yield better soot volume fraction agreement as shown in [20]. Moreover, great uncertainty exists in this experiment as no velocity measurements exist. Thus, the spreading of the jet and the mixing field cannot be validated easily. Other studies found good agreement by including the buoyancy effects and a round jet correction term in the turbulent dissipation energy rate equation [55, 20]. The PDF-PBE approach was applied to simulate soot formation in two turbulent diffusion flames in order to capture the turbulence-chemistry, turbulence-radiation and turbulence-particle formation interactions. Uncertainties and problems regarding this implementation were expected and are discussed previously to improve the model's prediction. Moreover, for illustration purposes the evolution of the complete PSDs is shown at the three different axial points.

7.2 Future work

This thesis implements a coupled CFD-PBE model to both laminar and turbulent diffusion flames. The PBE is formulated to predict the PSD of the primary soot particles, and not aggregate formation. The PBE model applied in this thesis is one-dimensional (in particle size diameter). More than one internal coordinate can be applied in order to take into account aggregate structure. The laminar diffusion flame of Santoro et al. [8] provides an excellent

experiment for conducting a numerical investigation for validation purposes on soot aggregates and their structure, because measurements of average number of primary particles per aggregate and aggregate number density are available [152].

The soot kinetics applied in this thesis are acetylene-based. Acetylene-based soot models have the benefit of being applicable with relatively small gas-phase mechanisms of C_1 and C_2 hydrocarbons, such as GRI 1.2. A different gas-phase mechanism and by including a C_6H_6 nucleation step could be more appropriate in accurately predicting the precursors of soot formation as shown [166]. This will probably lead to an improved prediction for the soot volume fraction. Also, a different nucleation mechanism that could be described by PAHs could result in better prediction of the soot particles in the centreline region. PAH-based soot kinetics (ABF model) have been found to be accurate in the laminar flames of Santoro et al [8]. Therefore, in the detailed PBE approach the acetylene-based kinetics should also be replaced with PAH-based kinetics. The implementation of PAH-based kinetics will require detailed gas-phase mechanisms for predicting heavy hydrocarbon species up to $C_{16}H_{10}$. As a result, an efficient parallel algorithm is required to speed up the simulations with PAH-based kinetics in the detailed PBE approach. The implementation of PAH-based kinetics in laminar and turbulent flames could be feasible through employing systematic reduction chemical mechanisms via RCCE [94]. This will reduce the computational expense, while keeping the accuracy of the chemistry at sufficient levels.

Moreover, there is an uncertainty in the coagulation rates of soot particles. Further tests should be undertaken with the coagulation mechanism. Coagulation is suspected for the laminar diffusion flames of Santoro et al. [8] to play a major role near the jet burner exit. Moreover, the coagulation mechanism in [167] is set to 0 once the particle size diameter reaches a cut-off maximum size. All these aspects should be investigated.

Finally, fundamental research on soot formation using a variety of soot kinetics combinations could be used in the PSR-jet stirred reactor or 1D laminar premixed flame configuration mentioned in Chapter 2. Measurements of PSD have been obtained, and can be used for the validation of the implementation of any soot kinetics in the PBE. Due to the relatively simple flow model of the 0D reactors, it is much more appropriate to validate the soot kinetics of the PBE using large gas-phase chemical mechanisms before exploring more complex multi-dimensional flames.

Bibliography

[1] EIA, "U.S. Energy Information Administration." `http://www.eia.gov/beta/international/analysis.cfm?iso=GBR`, 2015. Online; accessed: 2015-08-23.

[2] D. O. Lignell, *Direct numerical simulation of soot formation and Transport in Turbulent nonpremixed Ethylene flames*. PhD thesis, University of Utah, 2008.

[3] R. H. Pletcher, J. C. Tannehill, and D. Anderson, *Computational fluid mechanics and heat Transfer*. Taylor and Francis, second ed., 1997.

[4] M. D. Smooke, "The computation of laminar flames," in *Proceedings of the Combustion Institute*, vol. 34, pp. 65–98, 2013.

[5] W. Jones, A. Marquis, and V. Prasad, "LES of a turbulent premixed swirl burner using the Eulerian stochastic field method," *Combustion and Flame*, vol. 159, pp. 3079–3095, 2012.

[6] H. K. Versteeg and W. Malalasekera, *An Introduction to computational fluid dynamics: The finite volume method*. Pearson, Prentice Hall, 2007.

[7] S. J. Brookes, *Soot production and thermal radiation from turbulent jet diffusion flames*. PhD thesis, Cranfield University, October 1996.

[8] R. J. Santoro, H. G. Semerjian, and R. A. Dobbins, "Soot particle measurements in diffusion flames," *Combustion and Flame*, vol. 51, pp. 203–218, 1983.

[9] R. J. Santoro, T. T. Yeh, J. J. Horvath, and H. G. Semerjian, "The transport and growth of soot particles in laminar diffusion flames," *Combustion Science and Technology, 53:2-3*, 1987.

[10] S. J. Brookes and J. B. Moss, "Measurements of soot production and thermal radiation from confined turbulent jet diffusion flames of methane," *Combustion and Flame*, vol. 116, pp. 49–61, 1999.

[11] C. M. Megaridis and R. A. Dobbins, "Soot aerosol dynamics in a laminar diffusion flame ethylene," *Twenty-Second Symposium (International) on Combustion/The Combustion Institute*, pp. 353–362, 1988.

[12] C. M. Megaridis and R. A. Dobbins, "Morphological description of flame-generated materials," *Combustion Science and Technology*, vol. 71, pp. 95–109, 1990.

[13] T. C. Bond, S. J. Doherty, D. W. Fahey, P. M. Forster, T. Berntsen, B. J. DeAngelo, M. G. Flanner, S. Ghan, B. Krcher, D. Koch, S. Kinne, Y. Kondo, P. K. Quinn, M. C. Sarofim, M. G. Schultz, M. Schulz, C. Venkataraman, H. Zhang, S. Zhang, N. Bellouin, S. K. Guttikunda, P. K. Hopke, M. Z. Jacobson, J. W. Kaiser, Z. Klimont, U. Lohmann, J. P. Schwarz, D. Shindell, T. Storelvmo, S. G. Warren, and C. S. Zender, "Bounding the role of black carbon in the climate system: a scientific assessment," *Journal of Geophysical Research: Atmospheres*, vol. 118, pp. 5380–5552, 2013.

[14] Q. Zhang, *Detailed modeling of soot formation/oxidation in laminar coflow diffusion flames*. PhD thesis, University of Toronto, 2009.

[15] B. Quay, T.-W. Lee, T. Ni, , and R. J. Santoro, "Spatially resolved measurements of soot volume fraction using laser-induced incandescence," *Combustion and Flame*, vol. 97, pp. 384–392, 1994.

[16] D. L. Urban, Z.-G. Yuan, P. B. Sunderland, K. C. Lin, Z. Dai, K. Sun, and G. M. Faeth, "Structure and soot properties of nonbuoyant ethylene/air laminar jet diffusion flames," *AIAA Journal, Vol.36, No. 8*, 1998.

[17] A. E. Karatas and Ömer L. Gülder, "Soot formation in high pressure laminar diffusion flames," *Progress in Energy and Combustion Science*, vol. 38, pp. 818–845, 2012.

[18] J. Singh, *Detailed soot modelling in laminar premixed flames*. PhD thesis, University of Cambridge, 2006.

[19] R. N. Kleiveland, *Modelling of soot formation and oxidation in turbulent diffusion flames*. PhD thesis, Norwegian University of Science and Technology, 2005.

[20] M. Stoellinger and D. Roekaerts, "PDF modelling of soot formation in turbulent non-premixed flames using tabulated chemistry," *European Combustion meeting*, 2013.

[21] V. Chernov, Q. Zhang, M. J. Thomson, and S. B. Dworkin, "Numerical investigation of soot formation mechanisms in partially-premixed ethyleneair co-flow flames," *Combustion and Flame 159, 2789-2798*, 2012.

[22] A. Mesbah, H. J. M. Kramer, A. E. M. Huesman, and P. M. J. Van den Hof, "A control oriented study on the numerical solution of the population balance equation for crystallization processes," *Chemical Engineering Science*, vol. 64, pp. 4262–4277, 2009.

[23] Q. Zhang, H. Guo, F. Liu, G. Smallwood, and M. Thomson, "Modeling of soot aggregate formation and size distribution in a laminar ethylene-air coflow diffusion flame with detailed pah chemistry and an advanced sectional aerosol dynamics model," *Proceedings of the Combustion Institute*, vol. 32, pp. 761–768, 2009.

[24] S. Rigopoulos and A. G. Jones, "Finite-element scheme for solution of the dynamic population balance equation," *AIChE Journal*, vol. 49, no. 5, pp. 1127–1139, 2003.

[25] I. M. Kennedy, C. Yam, D. C. Rapp, and R. J. Santoro, "Modeling and measurements of soot and species in a laminar diffusion flame," *Combustion and Flame*, vol. 107, pp. 368–382, 1996.

[26] R. A. Kenneth Kuan-yun Kuo, *Fundamentals of turbulent and multi-Phase Combustion.* John Wiley and Sons, Inc, 2012.

[27] S. Rigopoulos, *Combustion - chemical kinetic and fluid dynamic theory.* Lecture Notes, University of Manchester, 2007-2008.

[28] S. R. Turns, *An introduction to combustion: concepts and applications, 2nd edition.* McGraw-Hill, 1996.

[29] P. F. Caccavale, M. Iamarino, F. Pierri, and V. Tufano, *Control and monitoring of chemical batch reactors.* Springer-Verlag London Limited, 2011.

[30] J. Warnatz, U. Maas, and R. Dibble, *Combustion: physical and chemical fundamentals, modeling and simulation, experiments, pollutant formation 4th Edition.* Springer Berlin Heidelberg New York, 2006.

[31] S. McAllister, J.-Y. Chen, and A. C. Fernandez-Pello, *Fundamentals of combustion processes*. Springer New York Dordrecht Heidelberg London, 2011.

[32] M. E. Davis and R. J. Davis, *Fundamental of chemical reaction engineering*. McGraw-Hill Higher Education, 2003.

[33] D. F. Kronholm and J. B. Howard, "Analysis of soot surface growth pathways using published plug-flow reactor data with new particle size distribution measurements and published premixed flame data," *Proceedings of the Combustion Institute*, vol. 28, pp. 2555–2561, 2000.

[34] J. Z. Wen, M. Thomson, S. Park, S. Rogak, and M. Lightstone, "Study of soot growth in a plug flow reactor using a moving sectional model," *Proceedings of the Combustion Institute*, vol. 30, pp. 1477–1484, 2005.

[35] M. Celnik, R. Patterson, M. Kraft, and W. Wagner, "Coupling a stochastic soot population balance to gas-phase chemistry using operator splitting," *Combustion and Flame*, vol. 148, pp. 158–176, 2007.

[36] D. P. Mishra, *Fundamentals of combustion*. Prentice-Hall of India Private Limited, 2007.

[37] R. J. Kee, J. F. Grcar, M. D. Smooke, J. A. Miller, and E. Meeks, *PREMIX: A FORTRAN program for modeling steady laminar one-dimensional premixed flames*, 1998.

[38] B. Zhao, Z. Yang, M. V. Johnston, H. Wang, A. S. Wexler, M. Balthasar, and M. Kraft, "Measurement and numerical simulation of soot particle size distribution functions in a laminar premixed ethylene oxygen -argon flame," *Combustion and Flame*, vol. 133, pp. 173–188, 2003.

[39] B. Zhao, Z. Yang, Z. Li, M. V. Johnston, and H. Wang, "Particle size distribution function of incipient soot in laminar premixed ethylene flames: effect of flame temperature," *Proceedings of the Combustion Institute*, vol. 30, pp. 1441–1448, 2005.

[40] H. Tsuji, "Counterflow diffusion flames," *Progress in Energy and Combustion science*, vol. 8, pp. 93–119, 1982.

[41] N. Peters, *Turbulent Combustion*. Cambridge University Press, 2000.

[42] C. E. Baukal, ed., *Oxygen-enhanced combustion*. CRC Press, 2nd ed., 2013.

[43] H. Pitsch, M. Chen, and N. Peters, "Unsteady flamelet modeling of turbulent hydrogen-air diffusion fflames," *Twenty-Seventh Symposium (International) on Combustion/The Combustion Institute*, pp. 1057–1064, 1998.

[44] M. Ihme, C. M. Cha, and H. Pitsch, "Prediction of local extinction and re-ignition effects in non-premixed turbulent combustion using a flamelet/progress variable approach," *Proceedings of the Combustion Institute*, vol. 30, pp. 793–800, 2005.

[45] S. Keum, *An improved representative interactive flamelet model accounting for evaporation effect in reaction space (RIF-ER).* PhD thesis, University of Michigan, 2009.

[46] W. E. Mell, V. Nilsen, G. Kosly, and J. J. Riley, "Investigation of closure models for nonpremixed turbulent reacting flows," *Physics of Fluids*, vol. 6, pp. 1331–1356, 1994.

[47] A. Cuoci, A. Frassoldati, T. Faravelli, and E. Ranzi, "Soot formation in unsteady counterflow diffusion flames," *Proceedings of the Combustion Institute*, vol. 32, pp. 1335–1342, 2009.

[48] T. Poinsot and D. Veynante, *Theoretical and Numerical Combustion 2nd Edition.* Edwards, 2005.

[49] M. Smooke, M. Long, B. Connelly, M. Colket, and R. Hall, "Soot formation in laminar diffusion flames," *Combustion and Flame*, vol. 143, pp. 613–628, 2005.

[50] W. P. Jones, F. di Mare, and A. J. Marquis, *LES-BOFFIN: Users Guide.* Imperial College of London, July 2002.

[51] W. P. Jones, *BOFFIN: A Computer program for flow and combustion in complex Geometries.* Imperial College of London.

[52] R. J. Kee, G. Dixon-Lewis, J. Warnatz, M. E. Coltrin, J. A. Miller, and H. K. Moffat, *A FORTRAN computer code package for the evaluation of gas-phase, multicomponent transport properties.* Sandia National Laboratories, March 1998.

[53] F. Liu, H. Guo, G. J. Smallwood, and Ömer L. Gülder, "Numerical modelling of soot formation and oxidation in laminar coflow non-smoking and smoking ethylene diffusion flames," *Combustion Theory and Modelling*, vol. 7, pp. 301–315, 2003.

[54] O. Cabrit and L. Artal, "Direct numerical simulation of turbulent multispecies channel flow with wall ablation," *AIAA Thermophysics Conference*, vol. 39, 2007.

[55] A. Kronenburg, R. W. Bilger, and J. H. Kent, "Modeling soot formation in turbulent methaneair jet diffusion flames," *Combustion and Flame*, vol. 121, pp. 24–40, 2000.

[56] T. Takagi and Z. Xu, "Numerical analysis of laminar diffusion flames effects of preferential diffusion of heat and species," *Combustion and Flame*, vol. 96, pp. 50–59, 1994.

[57] H. Guo, F. Liu, G. J. Smallwood, and Ömer L. Gülder, "A numerical investigation of thermal diffusion influence on soot formation in ethylene/air diffusion flames," *International Journal of Computational Fluid Dynamics*, vol. 18, pp. 139–151, 2004.

[58] R. S. Mehta, *Detailed modeling of soot formation and turbulence-radiation interactions in turbulent jet flames*. PhD thesis, The Pennsylvania State University, 2008.

[59] R. S. Mehta, M. F. Modest, and D. C. Haworth, "Radiation characteristics and turbulenceradiation interactions in sooting turbulent jet flames," *Combustion Theory and Modelling*, vol. 14, no. 1, pp. 105–124, 2010.

[60] C. S. Yoo and G. I. Hong, "Interaction of turbulence, chemistry, and radiation in strained nonpremixed flames," *Journal of Physics: Conference Series*, vol. 16, pp. 91–100, 2005.

[61] Y. Zhang, *Hybrid particle/finite-volume PDF methods for three-dimensional time-dependent flows in complex geometries*. PhD thesis, The Pennsylvania State University, December 2004.

[62] S. A. Elbahloul, *Modelling of turbulent flames with transported probability density function and rate-controlled constrained equilibrium methods*. PhD thesis, Imperial College of London, September 2013.

[63] D. C. Haworth, "Progress in probability density function methods for turbulent reacting flows," *Progress in Energy and Combustion Science*, vol. 36, pp. 168–259, 2010.

[64] W. M. Weerasinghe and W. P. Jones, "Application of lagrangian probability density function approach to a turbulent jet diffusion flame," *Journal of Turbulence*, vol. 11, no. 9, pp. 1–37, 2010.

[65] W. P. Jones, *Closure stategies for turbulent and transitional Flows*, ch. The Joint Scalar Probability Density, pp. 582–625. Cambridge University Press, 2002.

[66] P. A. Nooren, *Stochastic modeling of turbulent natural-gas flames*. PhD thesis, Delft University of Technology, 1998.

[67] C. Celis and L. F. F. da Silva, "Lagrangian mixing models for turbulent combustion: Review and prospects," *Flow Turbulence Combustion*, vol. 94, pp. 643–689, 2015.

[68] B. Merci, D. Roekaerts, and B. Naud, "Study of the performance of three micromixing models in transported scalar pdf simulations of a piloted jet diffusion flame (Delft flame III)," *Combustion and Flame*, vol. 144, pp. 476–493, 2006.

[69] R. R. Cao, H. Wang, and S. B. Pope, "The effect of mixing models in pdf calculations of piloted jet flames," *Proceedings of the Combustion Institute*, vol. 31, pp. 1543–1550, 2007.

[70] G. Y. D. Veroli, *Stochastic modelling of particle formation in turbulent flows via the transported population balance-PDF method*. PhD thesis, University of Manchester, 2009.

[71] M. Muradoglu, K. Liu, and S. Pope, "PDF modeling of a bluff-body stabilized turbulent flame," *Combustion and Flame*, vol. 132, pp. 115–137, 2003.

[72] S. Rigopoulos, "Population balance modelling of polydispersed particles in reactive flows," *Progress in Energy and Combustion Science*, vol. 36, pp. 412–443, 2010.

[73] S. Qamar, *Modelling and simulation of population balances for particulate processes*. PhD thesis, Otto-von-Guericke University Magdeburg, 2008.

[74] I. M. Kennedy, "Models of soot formation and oxidation," *Prog. Energy Combust. Sci.*, vol. 23, pp. 95–132, 1997.

[75] K. M. Leung, R. P. Lindstedt, and W. P. Jones, "A simplified reaction mechanism for soot formation in nonpremixed flames," *Combustion and Flame*, vol. 87, pp. 289–305, 1991.

[76] M. Fairweather, W. P. Jones, H. S. Ledin, and R. P. Lindstedt, "Predictions of soot formation in turbulent, non-premixed propane flame," *Twenty-Fourth Symposium (International) on Combustion/The Combustion Institute*, pp. 1067–1074, 1992.

[77] H. Guo, F. Liu, G. J. Smallwood, and Ömer L. Gülder, "The flame preheating effect on numerical modelling of soot formation in a two-dimensional laminar ethylene-air diffusion flame," *Combustion theory and modelling*, vol. 6, pp. 173–187, 2002.

[78] R. P. Lindstedt, "Simplified soot nucleation and surface growth steps for non-premixed flames," in *Soot formation in combustion: mechanisms and models*, pp. 417–441, Springer-Verlag, 1994.

[79] J. Appel, H. Bockhorn, and M. Frenklach, "Kinetic modeling of soot formation with detailed chemistry and physics: laminar premixed flames of C_2 hydrocarbons," *Combustion and Flame*, vol. 121, pp. 122–136, 2000.

[80] M. Frenklach and H. Wang, "Detailed mechanism and modeling of soot particle formation," in *Soot formation in combustion: mechanisms and models*, pp. 165–192, Springer-Verlag, 1994.

[81] R. J. Hall, M. D. Smooke, and M. B. Colket, *Physical and chemical aspects of combustion: a Tribute to Irvin Glassman*, ch. Predictions of soot dynamics in opposed jet diffusion flames, pp. 189–229. CRC Press, 1997.

[82] J. Nagle and R. A. Strickland-Constable, "Oxidation of carbon between 1000-2000 °C," in *Proc. 5th Conf. on Carbon*, pp. 154–164, London:Pergamon, 1961.

[83] S. B. Dworkin, Q. Zhang, M. J. Thomson, N. A. Slavinskaya, and U. Riedel, "Application of an enhanced PAH growth model to soot formation in a laminar coflow ethylene/air diffusion flame," *Combustion and Flame*, vol. 158, pp. 1682–1695, 2011.

[84] F. Gelbard, *MAEROS User Manual*. Sandia National Laboratories, December 1982.

[85] N. Slavinskaya and P. Frank, "A modelling study of aromatic soot precursors formation in laminar methane and ethene flames," *Combustion and Flame*, vol. 156, pp. 1705–1722, 2009.

[86] A. Khosousi and S. B. Dworkin, "Detailed modelling of soot oxidation by O_2 and OH in laminar diffusion flames," *Combustion and Flame*, vol. 35, pp. 1903–1910, 2015.

[87] M. Frenklach, "Method of moments with interpolative closure," *Chemical Engineering Science*, vol. 57, pp. 2229–2239, 2002.

[88] M. Fairweather, W. P. Jones, and R. P. Lindstedt, "Predictions of radiative transfer from a turbulent reacting jet in a cross-wind," *Combustion and Flame*, vol. 89, pp. 45–63, 1992.

[89] T. Abberger, *Granulation: handbook of powder technology*, vol. 11, ch. Population Balance Modelling of Granulation, pp. 1109–1186. Elsevier, 2007.

[90] S. J. Harris and A. M. Weiner, "Soot particle growth in premixed toluene/ethylene flames," *Combustion Science and Technology*, vol. 38, pp. 75–87, 1984.

[91] K. G. Neoh, J. B. Howard, and A. F. Sarofim, *Particulate carbon: formation during combustion*, ch. Soot oxidation in flames, pp. 261–282. Plenwn Press, New York, 1981.

[92] R. Demarco, J.-L. Consalvi, and A. Fuentes, "Influence of radiative property models on soot production in laminar coflow ethylene diffusion flames," *Journal of Physics: Conference Series*, vol. 369, no. 012011, 2012.

[93] International workshop on measurement and computation of turbulent nonpremixed flames, "Radiation models." `http://www.sandia.gov/TNF/radiation.html`. Online; accessed: 2016-01-06.

[94] S. Navarro-Martinez and S. Rigopoulos, "Differential diffusion modelling in LES with RCCE-reduced chemistry," *Flow Turbulence Combustion*, vol. 89, pp. 311–328, 2012.

[95] R. M. Woolley, M. Fairweather, and Yunardi, "Conditional moment closure modelling of soot formation in turbulent, non-premixed methane and propane flames," *Fuel*, vol. 88, pp. 393–407, 2009.

[96] C. B. B. Costa, M. R. W. Maciel, and R. M. Filho, "Considerations on the crystallization modeling: population balance solution," *Computers and Chemical Engineering*, vol. 31, no. 3, pp. 206–218, 2007.

[97] A. D. Randolph and M. A. Larson, *Theory of particulate processes: analysis and techniques of continuous crystallisation*. Harcourt Brace Jovanovich, 2nd ed., 1988.

[98] H. M. Hulburt and S. Katz, "Some problems in particle technology. a statistical mechanical formulation," *Chemical Engineering Science*, vol. 19, pp. 555–574, 1964.

[99] J. Kumar, M. Peglow, G. Warnecke, S. Heinrich, E. Tsotsas, L. Morl, M. Hounslow, and G. Reynolds, *Modern drying technology: computational tools at different scales*, vol. 1, ch. Numerical Methods on Population Balances, pp. 209–260. Wiley, 2014.

[100] W. T. Scott, "Analytic studies of cloud droplet coalescence," *Journal of the atmospheric sciences*, vol. 25, 1968.

[101] D. Ramkrishna, *Population balances: theory and applications to particulate systems in engineering*. Academic press, 2000.

[102] P. D. Hede, "Modelling batch fluid granulation processes using population balances." Online.

[103] M. J. Hounslow, R. L. Ryall, and V. R. Marshall, "A discretized population balance for nucleation, growth, and aggregation," *AlChe*, vol. 34, no. 11, 1988.

[104] F. Mauss, K. Netzell, C. Marchal, and G. Moréac, *Combustion generated fine carbonaceous particles*, ch. Modelling the soot particle size distribution functions using a detailed kinetic soot model and a sectional method, pp. 465–482. Karlsruhe University Press, 2009.

[105] J. Bhatt and R. Lindstedt, "Analysis of the impact of agglomeration and surface chemistry models on soot formation and oxidation," *Proceedings of the Combustion Institute*, vol. 32, pp. 713–720, 2009.

[106] S. K. Friedlander, *Smoke, Dust, and Haze Fundamentals of Aerosol Dynamics*. Oxford University Press, second ed., 2000.

[107] M. Nicmanis and M. J. Hounslow, "Finite-element methods for steady-state population balance equations," *AlChe*, vol. 44, no. 10, pp. 2258–2272, 1998.

[108] M. Vanni, "Approximate population balance equations for aggregation-breakage processes," *Journal of Colloid and Interface Science*, vol. 221, pp. 143–160, 2000.

[109] M. Kostoglou and A. J. Karabelas, "Evaluation of zero order methods for simulating particle coagulation," *Journal of Colloid and Interface Science*, vol. 163, pp. 420–431, 1994.

[110] R. B. Diemer and J. H. Olson, "A moment methodology for coagulation and breakage problems: part 2moment models and distribution reconstruction," *Chemical Engineering Science*, vol. 57, pp. 2211–2228, 2002.

[111] D. L. Marchisio, J. T. Pikturna, R. O. Fox, , R. D. Vigil, and A. A. Barresi, "Quadrature method of moments for population-balance equations," *AlChe*, vol. 49, no. 5, pp. 1266–1276, 2003.

[112] D. L. Marchisio, R. D. Vigil, and R. O. Fox, "Quadrature method of moments for aggregationbreakage processes," *Journal of Colloid and Interface Science*, vol. 258, pp. 322–334, 2003.

[113] R. O. Fox, "Bivariate direct quadrature method of moments for coagulation and sintering of particle populations," *Journal of Aerosol Science*, vol. 37, pp. 1562–1580, 2006.

[114] M. Mueller, G. Blanquart, and H. Pitsch, "Hybrid method of moments for modeling soot formation and growth," *Combustion and Flame*, vol. 156, pp. 1143–1155, 2009.

[115] V. John, T. Mitkova, M. Roland, K. Sundmacher, L. Tobiska, and A. Voigt, "Simulations of population balance systems with one internal coordinate using finite element methods," *Chemical Engineering Science*, vol. 64, pp. 733–741, 2009.

[116] V. John, I. Angelov, A. A. Öncül, and D. Thévenin, "Techniques for the reconstruction of a distribution from a finite number of its moments," *Chemical Engineering Science*, vol. 62, pp. 2890–2904, 2007.

[117] D. Meimaroglou, A. Roussos, and C. Kiparissides, "Part iv: dynamic evolution of the particle size distribution in particulate processes. a comparative study between monte carlo and the generalized method of moments," *Chemical Engineering Science*, vol. 61, pp. 5620–5635, 2006.

[118] M. M. Attarakih, H.-J. Barta, and N. M. Faqir, "Numerical solution of the spatially distributed population balance equation describing the hydrodynamics of interacting liquidliquid dispersions," *Chemical Engineering Science*, vol. 59, pp. 2567–2592, 2004.

[119] M. Goodson and M. Kraft, "Simulation of coalescence and breakage: an assessment of two stochastic methods suitable for simulating liquidliquid extraction," *Chemical Engineering Science*, vol. 59, pp. 3865–3881, 2004.

[120] W. J. Menz, J. Akroyd, and M. Kraft, "Stochastic solution of population balance equations for reactor networks," *Journal of Computational Physics*, vol. 256, pp. 615–629, 2014.

[121] E. Bayraktar, *Numerical aspects of population balance equations coupled to computational fluid dynamics*. PhD thesis, Der Fakultt fr Mathematik der Technischen Universitt Dortmund, 2014.

[122] S. Kumar and D. Ramkrishna, "On the solution of population balance equations by discretization-i. a fixed pivot techniquw," *Chemical Engineering Science*, vol. 51, no. 8, 1996.

[123] R. Bleck, "A fast, approximative method for integrating the stochastic coalescence equation," *Journal of Geophysical research*, vol. 75, no. 27, pp. 5165–5171, 1970.

[124] R. Batterham, Hall, J.S., and G. Barton, "Pelletizing kinetics and simulation of full scale balling circuits," in *3rd International Symposium on Agglomeration*, pp. A136–A150, 1981.

[125] M. J. Hounslow, *A discretized population balance for simultaneous nucleation, growth and aggregation*. PhD thesis, The Unibersity of Adelaide, 1990.

[126] P. Marchal, R. David, J. Klein, and J. Villermaux, "Crystallization and precipitation engineering - I. An efficient method for solving population balance in crystallization with agglomeration," *Chemical Engineering Science*, vol. 43, no. 1, pp. 59–67, 1988.

[127] F. Gelbard and J. H. Seinfeld, "Simulation of multicomponent aerosol dynamics," *Journal of Colloid and Interface science*, vol. 78, no. 2, pp. 485–501, 1980.

[128] J. D. Litster, D. J. Smit, and M. J. Hounslow, "Adjustable discretized population balance for growth and aggregation," *American Institute of Chemical Engineers*, vol. 41, no. 3, pp. 501–603, 1995.

[129] P. J. Hill and K. M. Ng, "New discretization procedure for the breakage equation," *American Institute of Chemical Engineers*, vol. 41, no. 5, pp. 1204–1216, 1995.

[130] J. Kumar, M. Peglow, G. Warnecke, and S. Heinrich, "An efficient numerical technique for solving population balance equation involving aggregation, breakage, growth and nucleation," *Powder Technology*, vol. 182, pp. 81–104, 2008.

[131] J. Kumar, *Numerical approximations of population balance equations in particulate systems*. PhD thesis, Otto-von-Guericke-Universit at Magdeburg, 2006.

[132] S. Kumar and D. Ramkrishna, "On the solution of population balance equations by discretization-ii. a moving pivot technique," *Chemical Engineering Science*, vol. 51, no. 8, pp. 1333–1342, 1996.

[133] R. Gunawan, I. Fusman, and R. D. Braatz, "High resolution algorithms for multidimensional population balance qquations," *American Institute of Chemical Engineers*, vol. 50, no. 11, p. 27382749, 2004.

[134] F. Gelbard and J. H. Seinfeld, "Numerical solution of the dynamic equation for particulate systems," *Journal of Computational Physics*, vol. 28, pp. 357–375, 1978.

[135] D. Eyre, C. J. Wright, and G. Reuter, "Spline-collocation with adaptive mesh grading for solving the stochastic collection equation," *Journal of Computational Physics*, vol. 78, pp. 288–304, 1988.

[136] H. J. Viljoen, D. Eyre, and C. J. Wright, "Solving dynamic equations for the collection and evaporation of an aerosol," *The Canadian Journal of Chemical Engineering*, vol. 68, pp. 938–943, December 1990.

[137] A. H. Alexopoulos, A. I. Roussos, and C. Kiparissides, "Part I: Dynamic evolution of the particle size distribution in particulate processes undergoing combined particle growth and aggregation," *Chemical Engineering Science*, vol. 59, pp. 5751–5769, 2004.

[138] A. H. Alexopoulos and C. A. Kiparissides, "Part II: Dynamic evolution of the particle size distribution in particulate processes undergoing simultaneous particle nucleation, growth and aggregation," *Chemical Engineering Science*, vol. 60, pp. 4157–4169, 2005.

[139] A. Roussos, A. Alexopoulos, and C. Kiparissides, "Part III: Dynamic evolution of the particle size distribution in batch and continuous particulate processes:a galerkin on finite elements approach," *Chemical Engineering Science*, vol. 60, p. 6998 7010, 2005.

[140] A. H. Alexopoulos, A. Roussos, and C. Kiparissides, "Part V: Dynamic evolution of the multivariate particle size distribution undergoing combined particle growth and aggregation," *Chemical Engineering Science*, vol. 64, pp. 3260–3269, 2009.

[141] S. Qamar, M. Elsner, I. Angelov, G. Warnecke, and A. Seidel-Morgenstern, "A comparative study of high resolution schemes for solving population balances in crystallization," *Computer and Chemical Engineering*, vol. 30, pp. 1119–1131, 2006.

[142] D. L. Ma, D. K. Tafti, and R. D. Braatz, "High-resolution simulation of multidimensional crystal growth," *Ind. Eng. Chem. Res.*, vol. 41, pp. 6217–6223, 2002.

[143] S. Rigopoulos, "PDF method for population balance in turbulent reactive flow," *Chemical Engineering Science*, vol. 62, pp. 6865–6878, 2007.

[144] R. J. Leveque, *Finite-volume methods for hyperbolic problems*. Cambridge, 2002.

[145] B. van Leer, *Upwind-difference methods for aerodynamic problems governed by the Euler equations*, vol. 22, ch. Lectures in applied Mathematics, pp. 327–336. American Mathematical society, 1985.

[146] B. Koren, *Numerical methods for advection-diffusion problems*, ch. A robust upwind discretisation method for advection, diffusion and source terms, pp. 117–138. Braunschweig: Vieweg Verlag, 1993.

[147] H. Wang, "A comprehensive reaction model of ethylene and acetylene combustion." `http://ignis.usc.edu/Mechanisms/C2-C4/c2.html`, 2000. Online; accessed: 2016-13-01.

[148] University of Adelaide, "International Sooting Flames Workshop." `http://www.adelaide.edu.au/cet/isfworkshop/data-sets/laminar/`. Accessed: 2016-01-20.

[149] P. B. SUNDERLAND and G. M. FAETH, "Soot formation in hydrocarbon/air laminar jet diffusion flames," *Combustion and Flame*, vol. 105, pp. 132–146, 1996.

[150] M. C. Megaridis and A. R. Dobbins, "Comparison of soot growth and oxidation in smoking and nonsmoking ethylene diffusion flames," *Combustion Science and Technology*, vol. 66, pp. 1–16, 1989.

[151] A. G. Yazicioglu, C. M. Megaridis, A. Campbell, K.-O. Lee, and M. Y. Choi, "Measurement of fractal properties of soot agglomerates in laminar coflow diffusion flames using thermophoretic sampling in conjuction with transmission electron microscopy and image processing," *Combustion Science and Technology*, vol. 171, pp. 71–87, 2001.

[152] R. Puri, T. Richardson, and R. Santoro, "Aerosol dynamic processes of soot aggregates in a laminar ethene diffusion flame," *Combustion and Flame*, vol. 92, pp. 320–333, 1993.

[153] S. S. Iyer, T. A. Litzinger, S.-Y. Lee, and R. J. Santoro, "Determination of soot scattering coefficient from extinction and three-angle scattering in a laminar diffusion flame," *Combustion and Flame*, vol. 149, pp. 206–216, 2007.

[154] C. P. Arana, M. Pontoni, S. Sen, and I. K. Puri, "Field measurements of soot volume fractions in laminar partially premixed coflow ethylene/air flames," *Combustion and Flame*, vol. 138, pp. 362–372, 2004.

[155] C. S. McEnally, U. O. Koylu, L. D. Pfefferle, , and D. E. Rosner, "Soot volume fraction and temperature measurements in laminar nonpremixed flames using thermocouples," *Combustion and Flame*, vol. 109, pp. 701–720, 1997.

[156] U. O. Koylu, C. S. McEnally, D. E. Rosner, , and L. D. Pfefferle, "Simultaneous measurements of soot volume fraction and particle size / microstructure in flames using a thermophoretic sampling technique," *Combustion and Flame*, vol. 110, pp. 494–507, 1997.

[157] lan M. Kennedy, W. Kollmann, and J.-Y. Ghen, "Predictions of soot in laminar diffusion flames," *AIAA*, vol. 29, no. 9, pp. 1452–1457, 1991.

[158] A. D'Anna and J. Kent, "Modeling of particulate carbon and species formation in coflowing diffusion flames of ethylene," *Combustion and Flame*, vol. 144, pp. 249–260, 2006.

[159] Q. Zhang, M. Thomson, H. Guo, F. Liu, and G. Smallwood, "A numerical study of soot aggregate formation in a laminar coflow diffusion flame," *Combustion and Flame*, vol. 156, pp. 697–705, 2009.

[160] P. Akridis and S. Rigopoulos, "Modelling of soot formation in a laminar coflow nonpremixed flame with a detailed CFD-population balance model," *Procedia Engineering*, vol. 102, pp. 1274–1283, 2015.

[161] J. H. Kent and D. Honnery, "Soot and mixture fraction in turbulent diffusion flames," *Combustion Science and Technology*, vol. 54, pp. 383–397, 1987.

[162] O. Nishida and S. Mukohara, "Characteristics of soot formation and decomposition in turbulent diffusion flames," *Combustion and Flame*, vol. 47, pp. 269–279, 1982.

[163] R. Lindstedt and H. Ozarovsky, "Joint scalar transported pdf modeling of nonpiloted turbulent diffusion flames," *Combustion and Flame*, vol. 143, pp. 471–490, 2005.

[164] S. J. Brookes and J. B. Moss, "Predictions of soot and thermal radiation properties in confined turbulent jet diffusion flames," *Combustion and Flame*, vol. 116, pp. 486–503, 1999.

[165] O. Roditcheva and X. Bai, "Pressure effect on soot formation in turbulent diffusion flames," *Chemosphere*, vol. 42, pp. 811–821, 2001.

[166] Y. Yunardi, D. Darmadi, H. Hisbullah, and M. Fairweather, "Investigation of detailed kinetic scheme performance on modelling of turbulent non-premixed sooting flames," *Journal of Thermal Science*, vol. 20, no. 6, pp. 548–555, 2011.

[167] M. D. Smooke, R. J. Hall, M. B. Colket, J. Fielding, M. B. Long, C. S. McEnally, and L. D. Pfefferle, "Investigation of the transition from lightly sooting towards heavily sooting co-flow ethylene diffusion flames," *Combustion Theory and Modelling*, vol. 8, pp. 593–606, 2004.